Plasma Physics Reports, Vol. 28, No. 10, 2002, pp. 797–801. Translated from Fizika Plazmy, Vol. 28, No. 10, 2002, pp. 867–871.

A Possible Way to Reverse the Impurity Influx by Alfvén Heating in a Tokamak Plasma

D. L. Grekov and S. V. Kasilov

Institute of Plasma Physics, Kharkov Institute of Physics and Technology, National Science Center, ul. Akademicheskaya 1, Kharkov, 61108 Ukraine

Received March 21, 2002

Abstract—A study is made of the effect of local heating on impurity fluxes in the Pfirsch–Schlüter regime. When the effect of the thermoforce on impurity ions is taken into consideration, the impurity flux can be reversed by heating the impurities. This concept may be implemented in experiments on Alfvén heating of plasmas in tokamaks. The RF heating power required to reverse the impurity influx is estimated. © *2002 MAIK "Nauka/Interperiodica".*

1. INTRODUCTION

The development of various methods for reducing the impurity content in the plasma is motivated by the experimentally observed degradation of plasma parameters in the presence of heavy impurities. The impurity ions can be affected by both passive (divertors) and active methods. Among the active methods, which have begun to be developed in [1, 2], are the working-gas puffing (particle source); the heating of the main plasma component (energy source); and the transfer of momentum, e.g., from injected high-energy particles to the plasma. However, in [1, 2] (as well as in more recent papers), no account was taken of a weak thermal force acting on impurity ions, and, accordingly, the heat sources acting on impurities were excluded from consideration.

The distinguishing feature of active methods for affecting impurity fluxes is the need to create a particle (or momentum, or energy) source that is asymmetric with respect to the equatorial plane of the tokamak. While it is fairly easy to design particle and momentum asymmetric sources, a means of creating an asymmetric energy source is still lacking. On the other hand, as early as 1975, Messiaen *et al.* [3] pointed out that, in the ion cyclotron frequency range, the waves with $m = +1$ and $m = -1$ (where m is the azimuthal wavenumber) propagate in different ways. This effect stems from the plasma gyrotropy, and, in the model of a plasma cylinder in a longitudinal magnetic field, it is independent of the sign of the axial wavenumber. However, in a helical magnetic field, it breaks the axial symmetry of the plasma. Jaeger *et al.* [4] proposed to use this effect to control the current profile. Craddock and Diamond [5] showed that Alfvén heating can be used to generate a sheared electric field in a plasma in order to suppress edge plasma turbulence. In this paper, we investigate the possibility of reversing the impurity influx by means of Alfvén heating of a plasma in the Pfirsch–Schlüter regime. The analysis is carried out with allowance for the thermal force acting on impurities.

2. ASYMMETRIC HEATING OF IMPURITY IONS

With allowance for the thermal force acting on impurity ions, the expression for the impurity flux averaged over a magnetic surface in a stellarator was derived in [6]. Following [1, 2] and taking into account the results obtained in [6], we arrive at the following expression for the radial impurity flux Γ_I in a tokamak:

$$\Gamma_I = -\Gamma_i/Z_I = \frac{n_i 2q^2\rho_i^2}{Z_I\tau_{iI}T_i}\left[\left(C_1 + \frac{C_2^2}{C_3}\right)\left(\frac{1}{n_i}\frac{\partial p_i}{\partial r} - \frac{1}{Z_I n_I}\frac{\partial p_I}{\partial r}\right)\right.$$

$$\left. - \frac{5C_2}{2C_3}\frac{\partial T_i}{\partial r} + \frac{5C_2'}{2C_3'}\frac{\partial T_I}{\partial r}\right] - \frac{n_i q^2\rho_i^2}{Z_I\tau_{iI}T_i}\frac{eB_t R}{c}$$

$$\times\left[\left(C_1 + \frac{C_2^2}{C_3}\right)\frac{a_{\tau i}}{n_i} - \frac{C_2}{C_3}\frac{a_{Qi}}{n_i T_i} + \frac{C_2'}{C_3'}\frac{a_{Q1}}{n_I T_I}\right].$$

Here, p_α, $\mathbf{v}_\alpha$, n_α, $Z_\alpha e$, m_α, and T_α are, respectively, the pressure, velocity, density, charge, mass, and temperature of the ions of species α ($\alpha = i, I$); τ_{iI} is the scattering time of the bulk ions by the impurity ions; $q = rB_t/R_0B_p$; a and R_0 are the minor and major radii of the torus; B_t and B_p are the toroidal and poloidal components of the tokamak magnetic field; ρ_i is the Larmor radius of the bulk ions; $a_{Q\alpha}$ and $a_{\tau i}$ are the amplitudes of the components with $\sin\vartheta$ in the Fourier series expansion of the energy source $Q_\alpha(r, \vartheta)$ and the source $\tau_i(r, \vartheta)$ of the main plasma ions; and r and ϑ are the radius and the poloidal angle in the minor cross section (at the inner circumference of the torus, we set $\vartheta = 0$). Hence, under

1063-780X/02/2810-0797$22.00

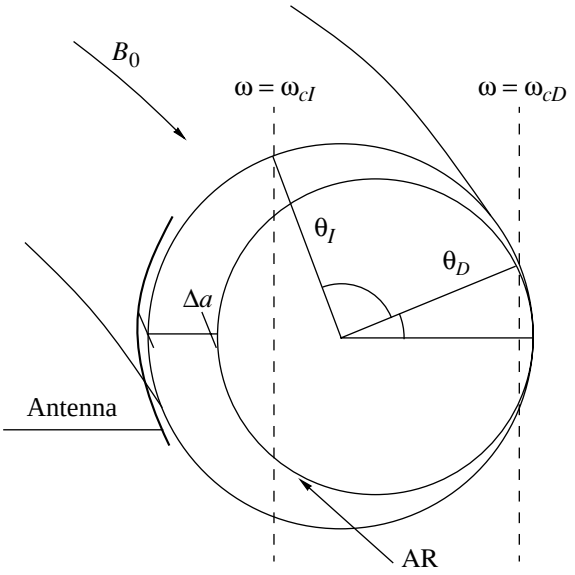

Fig. 1. Minor cross section of a tokamak. Shown are the position of AR and the zones of cyclotron resonances for the main plasma ions ($\omega = \omega_{cD}$) and for the impurity ions ($\omega = \omega_{cI}$).

the condition $B_0 a_{QI}(\bar{r}) < 0$, the impurity influx can be reversed by an asymmetric energy source acting on impurity ions.

Now, we consider whether an asymmetric energy source of this kind can be realized through Alfvén heating of a plasma. Let an antenna exciting the wave magnetic field $B_\parallel$ (which is parallel to the steady-state magnetic field) be positioned at the inner side of the torus. In what follows, we will be interested in the heating of a deuterium plasma. The radial dependence of the cyclotron frequency of deuterium ions is described by the expression $\omega_{cD}(R) = \omega_{cD}(R_0)(1 - \varepsilon_t \cos\vartheta)$. We choose the oscillator frequency ω to be $\omega = \omega_{cD}(R)$ at the outer circumference of the torus (at $\vartheta = \pm\vartheta_D$, where $\cos\vartheta_D = \frac{R_0}{a}\frac{\omega_{cD}(R_0) - \omega}{\omega_{cD}(R_0)}$). For impurity ions, we have $Z_I/M_I < 1/2$. Consequently, relative to the line $\omega = \omega_{cD}(R)$, the region of cyclotron resonance for impurity ions occurs at $\vartheta = \pm\vartheta_I$ in the inner part of the minor cross section of the torus (Fig. 1). For $\omega < \omega_{ci}$, the local Alfvén resonance (AR) zone (Fig. 1) arises in a tokamak on the inner side with respect to the line $\omega = \omega_{ci}$. In a plasma of sufficiently high density, the local AR zone is located in a narrow region of width Δa at the periphery of the plasma column. Since $n_I \ll k_\parallel \rho_{LI} n_e$, the impurities do not affect the propagation of fast Alfvén waves. From the condition $B_p/B_t = \varepsilon_t/q \ll 1$, we have $B \approx B_t$; consequently, the position of the cyclotron resonance is insensitive to the poloidal magnetic field. The AR position is determined by the expression $\varepsilon_1(r, \vartheta) = N_\parallel^2$, where $\varepsilon_1 = \frac{\omega_{pD}^2(r)}{2\omega_{cD}^2\varepsilon_t(\cos\vartheta_D - \cos\vartheta)}$, $N_\parallel = \frac{c}{R\omega}(l + m/q)$, and l and m are the toroidal and poloidal wavenumbers. In our analysis, we do not specify how the field excited by an antenna depends on the poloidal angle. Nevertheless, the bulk of the RF power fed into the plasma is, as a rule, carried by the waves with $|m| \le 2$ (see, e.g., [7]). Since $l \ge 10$, we have $l \gg m/q$, so that the poloidal magnetic field has essentially no impact on the AR position. For typical central plasma densities (10^{13}–10^{14} cm^{-3}), the AR occurs at the plasma periphery in a narrow region with the relative width $\Delta a/a \sim \varepsilon_t N_\parallel^2/N_A^2(0)$ (where $N_A^2 = \omega_{pD}^2/\omega_{cD}^2$). In the hydrodynamic approximation, we set $\varepsilon_1/\varepsilon_3 = 0$ in Maxwell's equations for a tokamak plasma with a zero rotational transform (at this point, the effect of the rotational transform can be neglected). As a result, we arrive at the equation

$$\frac{\omega^2}{c^2}B_\parallel - \left(\nabla \times \left[\frac{i\varepsilon_2}{\varepsilon^2 - \varepsilon_2^2}\frac{1}{R}\nabla(RB_\parallel)\right]\right)_\parallel + R\nabla\cdot\left[\frac{\varepsilon_1 - N_\parallel^2}{\varepsilon^2 - \varepsilon_2^2}\frac{1}{R^2}\nabla(RB_\parallel)\right] = 0, \quad (1)$$

where

$$\varepsilon = \varepsilon_1 - N_\parallel^2,\ \varepsilon_1 = 1 + \sum_i \frac{\omega_{pi}^2(r)}{\omega_{ci}^2(r, \vartheta) - \omega^2},$$

$$\varepsilon_2 = \sum_i \frac{\omega\omega_{pi}^2(r)}{\omega_{ci}(r, \vartheta)[\omega_{ci}^2(r, \vartheta) - \omega^2]},\ \text{and}\ N_\parallel = \frac{cl}{\omega R}.$$

Recall that $\Delta a/a$ is a small parameter in our problem. In order to solve Eq. (1) with the help of this parameter, we multiply Eq. (1) by $\exp(-im\vartheta)$ and integrate over the region S, whose width is $\Delta r \le \Delta a$ and which is bounded by contours L_1 and L_2, as is shown in Fig. 2. Using the Stokes and Gauss theorems, we convert Eq. (1) into the form

$$\frac{\partial}{\partial r}[R(r, \vartheta)B_\parallel(r, \vartheta)] - \frac{i\varepsilon_2(r, \vartheta)}{r\varepsilon(r, \vartheta)}\frac{\partial}{\partial\vartheta}[R(r, \vartheta)B_\parallel(r, \vartheta)]$$

$$= \frac{\varepsilon^2(r, \vartheta) - \varepsilon_2^2(r, \vartheta)}{\varepsilon(r, \vartheta)(N_\parallel^2 - 1)}\frac{aR(r, \vartheta)}{rR(a, \vartheta)}\frac{\partial}{\partial a}[R(a, \vartheta)B_\parallel(a, \vartheta)]$$

$$- \frac{R(r, \vartheta)}{r}\frac{\varepsilon^2(r, \vartheta) - \varepsilon_2^2(r, \vartheta)}{\varepsilon(r, \vartheta)}\left\{\frac{\omega^2}{c^2}\int_a^r r' B_\parallel(r, \vartheta)dr' \right. \quad (2)$$

$$+\frac{\partial}{\partial\vartheta}\int_a^r\frac{dr'}{R(r',\vartheta)}\frac{i\varepsilon_2(r',\vartheta)\dfrac{\partial}{\partial r'}[R(r',\vartheta)B_\parallel(r',\vartheta)]}{\varepsilon^2(r',\vartheta)-\varepsilon_2^2(r',\vartheta)}$$

$$+\frac{\partial}{\partial\vartheta}\int_a^r\frac{dr'}{r'R(r',\vartheta)}\frac{\varepsilon(r',\vartheta)\dfrac{\partial}{\partial\vartheta}[R(r',\vartheta)B_\parallel(r',\vartheta)]}{\varepsilon^2(r',\vartheta)-\varepsilon_2^2(r',\vartheta)}\Bigg\}.$$

Here, we have introduced the notation $\frac{\partial}{\partial r}R(r,\vartheta)B_\parallel(r,\vartheta)\Big|_{r=a}=\frac{\partial}{\partial a}R(a,\vartheta)B_\parallel(a,\vartheta)$. Now, Eq. (2) can be expanded in powers of the small parameter $\Delta a/a$, and the problem can be solved by the narrow layer method. This method was originally developed in [8] for the problem of surface waves. In [9], it was applied to the study of an AR in a one-dimensional plasma, and, in [10], it was generalized to a two-dimensional (r,ϑ) case. We assume that the quantities $B_\parallel(a,\vartheta)$ and $\frac{\partial}{\partial a}B_\parallel(a,\vartheta)$ are specified at the plasma boundary and use the small parameter $\Delta a \ll a, a/m, 1/k_\parallel$. Taking into account the relationships $\frac{\partial\varepsilon}{\partial\vartheta}/\frac{\partial\varepsilon}{\partial r}\sim\frac{\partial\varepsilon_2}{\partial\vartheta}/\frac{\partial\varepsilon_2}{\partial r}\sim\frac{\Delta a}{a}\ll 1$, we expand the wave magnetic field $B_\parallel$ in a power series in the small parameter $\Delta a/a$, $B_\parallel = B_{\parallel 0} + B_{\parallel 1} + \ldots$, to obtain

$$\frac{i\varepsilon_2}{r\varepsilon}\frac{\partial(RB_{\parallel 0})}{\partial\vartheta}-\frac{\partial(RB_{\parallel 0})}{\partial r}=\frac{\varepsilon^2-\varepsilon_2^2}{\varepsilon(N_\parallel^2-1)}\frac{\partial R(a,\vartheta)B_\parallel(a,\vartheta)}{\partial a}, \tag{3}$$

$$\frac{i\varepsilon_2}{r\varepsilon}\frac{\partial(RB_{\parallel 1})}{\partial\vartheta}-\frac{\partial(RB_{\parallel 1})}{\partial r}=-\frac{R}{r}\frac{\varepsilon^2-\varepsilon_2^2}{\varepsilon}\frac{\partial}{\partial\vartheta}\times\left[\frac{1}{R}\left(\int_a^r\frac{i\varepsilon_2}{\varepsilon^2-\varepsilon_2^2}\frac{\partial RB_{\parallel 0}}{\partial r'}dr'+\frac{1}{a}\int_a^r\frac{\varepsilon}{\varepsilon^2-\varepsilon_2^2}\frac{\partial RB_{\parallel 0}}{\partial\vartheta}dr'\right)\right]. \tag{4}$$

Equations (3) and (4) constitute a boundary-value problem of the first kind, which can be solved by the method of characteristics. The equations of characteristics have the form

$$\frac{d\vartheta(r)}{dr}=-i\frac{\varepsilon_2[r,\vartheta(r)]}{r\varepsilon[r,\vartheta(r)]}, \tag{5}$$

$$\frac{d}{dr}RB_{\parallel 0}[r,\vartheta(r)]=\frac{\varepsilon^2[r,\vartheta(r)]-\varepsilon_2^2[r,\vartheta(r)]}{\varepsilon[r,\vartheta(r)](1-N_\parallel^2)}\frac{\partial}{\partial a}RB_\parallel[a,\vartheta(r)]. \tag{6}$$

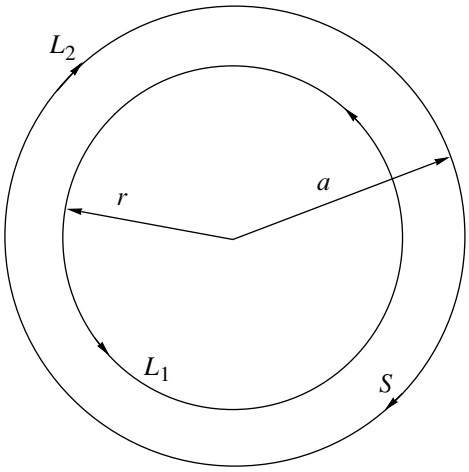

Fig. 2. Domain of integration S for Eq. (8) and contours L_1 and L_2.

An approximate solution to Eq. (5) can be written in the form

$$\Theta(\vartheta_0,a;r)\approx\vartheta_0-i\int_a^r\frac{\varepsilon_2(r',\vartheta_0)}{r'\varepsilon(r',\vartheta_0)}dr'. \tag{7}$$

Hence, we have

$$\vartheta_0(r,\vartheta)=\Theta(\vartheta,r;a)\ \text{ and }\ \vartheta'(r,\vartheta)=\Theta(\vartheta,r;r'). \tag{8}$$

Substituting solution (7) into Eq. (6) and using relationship (8), we obtain

$$R(r,\vartheta)B_{\parallel 0}(r,\vartheta)=R(a,\vartheta_0)B_\parallel(a,\vartheta_0)+\int_a^r\frac{\varepsilon^2(r',\vartheta')-\varepsilon_2^2(r',\vartheta')}{\varepsilon(r',\vartheta')(1-N_\parallel^2)}\frac{\partial}{\partial a}R(a,\vartheta')B_\parallel(a,\vartheta')dr'.$$

Now, we expand the first term on the right-hand side of this equation in a series in $\vartheta-\vartheta_0$ and retain only the first term in the expansion. Setting $\vartheta'\approx\vartheta$ in the second term and introducing the notation $R(a,\vartheta)B_\parallel(a,\vartheta)=R_aB_{\parallel a}$, we arrive at the following equations for the wave magnetic field:

$$R(r,\vartheta)B_{\parallel 0}(r,\vartheta)=R_aB_{\parallel a}+\delta(RB),$$

$$\delta(RB)=i\frac{\partial}{\partial\vartheta}(R_aB_{\parallel a})\int_a^r\frac{\varepsilon_2(r',\vartheta)}{r'\varepsilon(r',\vartheta)}dr'+\frac{\partial}{\partial a}(R_aB_{\parallel a})\int_a^r\frac{\varepsilon^2(r',\vartheta)-\varepsilon_2^2(r',\vartheta)}{(1-N_\parallel^2)\varepsilon(r',\vartheta)}dr'. \tag{9}$$

Equations (9) describe the behavior of the field in a narrow layer between the plasma boundary and the vicinity of the AR. Note that, formally, the integrals in Eqs. (9) have a pole, $\varepsilon(r',\vartheta)=0$, at the AR point. However, when dissipative effects (e.g., Coulomb colli-

sions) are taken into account, the pole actually lies in the region of complex values of r'.

Using Eqs. (9), we can calculate the poloidal RF power flux:

$$S_\vartheta = \frac{c^2}{8\pi\omega R}\mathrm{Re}\left\{\frac{B_{\|a}^*}{\varepsilon}\left[\frac{\varepsilon_2}{N_\|^2-1}\frac{\partial}{\partial a}(R_a B_{\|a}) + \frac{i}{a}\frac{\partial}{\partial\vartheta}(R_a B_{\|a})\right]\right\}. \quad (10)$$

Let us analyze this expression, assuming that $B_\|(a, \vartheta) \sim \exp(im\vartheta)$ at the plasma boundary. Since the quantity ε_2 is proportional to the plasma density and, accordingly, vanishes at the plasma periphery, the second term is dominant near the plasma boundary and we have $S_\vartheta \approx \frac{c^2}{8\pi\omega}\frac{m}{a}\frac{|B_{\|a}|^2}{N_\|^2-1}$. The waves with $m < 0$ carry the RF power in a clockwise direction, and the direction of the power carried by the waves with $m > 0$ is counterclockwise (Fig. 1). As the wave penetrates deeper into the plasma, the first term, which accounts for the plasma gyrotropy, plays an increasingly important role. Taking into account the inequality $\mathrm{Re}\left[B_{\|a}^*\frac{\partial}{\partial a}(R_a B_{\|a})\right] < 0$, we can see that, in this case, the power flux in a counterclockwise direction increases and the power flux in a clockwise direction decreases. This leads to an up/down asymmetric RF power flux in the minor cross section of the torus. The radial power flux can be represented as $S_r = S_{r0} + \delta S_r$, where

$$S_{r0} = \frac{c^2}{8\pi\omega R}\mathrm{Im}\left[\frac{B_{\|a}^*}{N_\|^2-1}\frac{\partial}{\partial a}(R_a B_{\|a})\right],$$

$$\delta S_r = \frac{c^2\omega}{4R^2}\left(\frac{d\omega_{pi}^2}{dr}\bigg|_{r=a}\right)^{-1}\varepsilon_t(\cos\vartheta_D - \cos\vartheta) \quad (11)$$

$$\times\left|\frac{\omega}{\omega_{ci}}\frac{\partial}{\partial a}(R_a B_{\|a}) - \frac{m}{a}R_a B_{\|a}\right|^2.$$

The term δS_r describes the power deposited in the AR zone. Expressions (11) show that, in the lower part of the torus ($m > 0$), the RF power is absorbed more intensely than in the upper part ($m < 0$). In the vicinity of the AR, a fast magnetosonic (FMS) wave converts into a small-scale kinetic wave (KW). When the AR occurs at the plasma periphery, the ion contribution (on the order of $\omega^2\rho_{Li}^2/c^2$) to the dispersion of the KW can be neglected in comparison with the electron contribution (which is on the order of ε_3^{-1}, where $\varepsilon_3 = \frac{\omega_{pe}^2}{k_\|^2 v_{Te}^2}[1 + i\sqrt{\pi}\, z_e W(z_e)]$ with $z_e = \omega/\sqrt{2}\, k_\| v_{Te}$). For the parameters of the present-day tokamaks, we have $\varepsilon_3\omega^2\rho_{Li}^2/c^2 \sim \frac{T_i}{T_e}\varepsilon_t \ll 1$ for $z_e \ll 1$ and $\varepsilon_3\omega^2\rho_{Li}^2/c^2 \sim \frac{v_{Te}^2}{c^2}\varepsilon_t N_\|^2 \ll 1$ for $z_e \gg 1$. The KW propagates along the magnetic field lines toward the inner side of the torus, deviating only slightly from the magnetic surface toward lower plasma densities. Kinetic waves that originate in the sector $-\vartheta_I < \vartheta < \vartheta_I$ will reach the zone of cyclotron resonance for impurity ions and will be completely absorbed there. Hence, we have shown how asymmetric heating of impurities can be realized in tokamak experiments.

3. DISCUSSION OF THE RESULTS OBTAINED

First, we analyze how the process in question is affected by heat exchange between the impurities and the main plasma ions. In [2], it was noted that, with allowance for heat exchange, the change in the impurity temperature (including the change associated with the energy source) decreases by a factor of f, where $f = 1 + \frac{3m_i n_i q^2 R^2}{39 n_I \tau_{iI}\tau_{II} T_I}$. Setting $n_i(a) = 10^{12}$ cm^{-3}, $n_I/n_i = 2\times10^{-3}$, $m_I \approx 60 m_p$, $T_I(a) = T_i(a) = 50$ eV, $Z_I = 4$, $q = 3$, and $R_0 = 150$ cm, we obtain $\tau_{iI} = 2.6\times10^{-3}$ s, $\tau_{II} = 1.3\times10^{-3}$ s, and $f = 2$. We thus can conclude that this effect is of a quantitative (rather than qualitative) character.

Second, we discuss another mechanism for the absorption of a fast Alfvén wave by impurity ions. The impurities make a small contribution to the tensor elements ε_1 and ε_2. The cyclotron absorption of a fast Alfvén wave by impurity ions is described by the imaginary part of this contribution. However, the fraction of the RF power that is absorbed by impurities is small in comparison with that transferred to the KW: $P_{ab}/P_{\mathrm{KW}} \sim n_I Z_I/n_i \ll 1$.

For a KW, the optical thickness τ of the zone of cyclotron resonance for impurity ions is described by the expression

$$\tau \sim \mathrm{Im}(N_\|)\Delta l \sim 9\sqrt{\frac{\pi}{2}}\frac{\omega_{pI}^2}{\omega_{cI}}\frac{Rq}{\varepsilon_t N_\| c},$$

where Δl is the length of the resonance zone along the magnetic field lines. Setting $k_\| = 0.1$ cm^{-1}, we obtain $\tau \geq 1$. Note that, in the resonance zone, we have $z_e \sim 6$, in which case Landau damping of the KW is negligible, $\tau_L \sim k_\| Rq\,\mathrm{Im}\,\varepsilon_3/|\varepsilon_3| \ll 1$. Consequently, the KW is completely absorbed by impurity ions. Denoting the total RF power fed into the plasma by P_{tot}, we can see that the power transferred to the KW is equal to $\frac{\varepsilon_t N_\|^2}{N_A^2(0)}P_{\mathrm{tot}}$, where $N_A^2(0) = \omega_{pi}^2(0)/\omega_{ci}^2(0)$. In order to obtain the

total power absorbed by impurity ions, we must integrate expressions (11) over $\vartheta_D - \vartheta_I$. Note that the optimum position of cyclotron resonance for impurities is between $\vartheta_I = 0.88\pi$ for $Z_I/M_I = 1/4$ and $\vartheta_I = 2\pi/3$ for $Z_I/M_I = 1/3$. Consequently, the quantity Q_I' is equal to

$$Q_I' \approx \frac{\Delta\vartheta_I}{\pi}\frac{\sin\vartheta_I[(\vartheta_I-\vartheta_D)\cos\vartheta_D - \sin\vartheta_I + \sin\vartheta_D]}{(\pi-\vartheta_D)\cos\vartheta_D + \sin\vartheta_D} \times K_{as}\frac{\varepsilon_t N_\parallel^2}{N_A^2(0)}\frac{P_{\rm tot}}{V}, \quad (12)$$

where the quantity $\Delta\vartheta_I = 3k_\parallel\rho_{LI}/\varepsilon_t$, $K_{as} \sim \Delta a/a$ describes the up/down asymmetry of the RF power distribution, $V = 2\pi Ra\Delta\vartheta_I\Delta r$ is the plasma volume in which the impurity ions absorb RF power, and Δr is the radial thickness of the absorption region. For estimates, we adopt $\Delta r \sim \Delta a$. Then, a necessary condition for reversing the direction of the impurity influx has the form

$$Q_I' \approx 2\frac{n_i(0)T_i(0)}{aR}\frac{cT_I(a)}{eB_t}\frac{n_I}{n_i}. \quad (13)$$

Substituting condition (13) into expression (12) yields

$$P_{\rm tot} \approx 7\frac{n_i(0)T_i(0)}{K_{as}}\frac{cT_I(a)}{eB_t}\frac{n_I}{n_i}a.$$

In deriving this estimate, we took into account the fact that the doubled reciprocal of the second fraction in expression (12) is approximately equal to seven. For $n_i(0) = 10^{14}$ cm^{-3}, $n_I/n_i = 2\times10^{-3}$, $T_i(0) = 2$ keV, $B_t = 1$ T, $K_{as} = 0.1$, and $a = 50$ cm, we obtain $P_{\rm tot} \approx 200$ kW.

4. CONCLUSION

Our analysis is based on the assumption that, at the periphery of the plasma column, impurity ions are transported in the Pfirsch–Schlüter regime. It has been shown that, when the small thermoforce affecting the impurities is taken into account, the impurity influx can be reversed by asymmetric (up-down) heating of the impurity ions. To achieve this, we propose to excite RF fields with frequencies lower than the cyclotron frequency of the main (deuterium) plasma ions on the inner side of the torus. We have shown that, after an FMS wave converts into a KW in the vicinity of the AR, the RF power is absorbed by impurity ions. For a medium-size tokamak, the RF power required to reverse the impurity influx is approximately equal to 200 kW. The efficiency of the method proposed here can be increased by displacing the antenna in the poloidal direction. The question of whether the method will prove feasible when heavy impurities are transported in the "plateau" regime or when their transport is anomalous requires a separate study.

ACKNOWLEDGMENTS

We are grateful to K.N. Stepanov for discussing this work.

REFERENCES

1. P. H. Rutherford, Phys. Fluids **17**, 1782 (1974).
2. K. T. Burrell, Phys. Fluids **19**, 401 (1976).
3. A. M. Messiaen, P. E. Vandenplas, R. R. Weynants, and R. Koch, Nucl. Fusion **15**, 75 (1975).
4. E. F. Jaeger, M. D. Carter, L. A. Berry, *et al.*, in *Proceedings of the 24th European Conference on Controlled Fusion and Plasma Physics, 1997*, Rep. P2.122.
5. G. G. Craddock and P. H. Diamond, Phys. Rev. Lett. **67**, 1535 (1991).
6. D. L. Grekov, Fiz. Plazmy **27**, 1070 (2001) [Plasma Phys. Rep. **27**, 1011 (2001)].
7. A. V. Longinov and V. A. Tsurikov, Fiz. Plazmy **16**, 39 (1990) [Sov. J. Plasma Phys. **16**, 22 (1990)].
8. K. N. Stepanov, Zh. Tekh. Fiz. **35**, 1002 (1965) [Sov. Phys. Tech. Phys. **10**, 773 (1965)].
9. D. L. Grekov, K. N. Stepanov, and J. A. Tataronis, Fiz. Plazmy **7**, 752 (1981) [Sov. J. Plasma Phys. **7**, 411 (1981)].
10. S. V. Kasilov, Author's Abstract of Candidate's Dissertation in Physics and Mathematics (Kharkov, 1989).

Translated by I. A. Kalabalyk

Plasma Physics Reports, Vol. 28, No. 10, 2002, pp. 802–805. Translated from Fizika Plazmy, Vol. 28, No. 10, 2002, pp. 872–876.

TOKAMAKS

Fast Measurements of the Limiter Surface Temperature and the Heat Flux onto the Limiter in the T-11M Tokamak by Using an IR Radiometer

V. B. Lazarev, A. G. Alekseev, A. M. Belov, and S. V. Mirnov

Troitsk Institute for Innovation and Thermonuclear Research, Troitsk, Moscow oblast, 142092 Russia

Received March 21, 2002

Abstract—The limiter surface temperature is measured with a high-speed IR radiometer ($\lambda \simeq 3$–6 μm) during a T-11M tokamak discharge. The IR radiometer was absolutely calibrated under steady-state operating conditions: the limiter was heated by a special inner heater, and the limiter temperature was measured with a thermocouple. Based on these measurements, the heat fluxes from the plasma onto the limiter surface during the discharge are determined. The measurement technique is discussed, and the data on the limiter surface temperature and the heat flux to the limiter for different regimes of the T-11M operation are presented. © *2002 MAIK "Nauka/Interperiodica".*

1. INTRODUCTION

The surface temperature and the power of heat release on a tokamak limiter or divertor plates are very important parameters for both tokamak reactors and small-size experimental facilities. The data on the temperature allow one to control the state of the surface material and the heat flux through the surface, the latter being dependent on the parameters of the edge plasma. Recently, the use of lithium capillary–porous structures (CPSs) as a material for the removal of heat energy from the region where the plasma interacts with the facility components has attracted great interest [1, 2]. In this context, experiments on studying the behavior of a tokamak plasma and lithium CPSs at various limiter temperatures (from 20 to 400°C) in helium and hydrogen discharges were previously carried out in the T-11M tokamak [3–5]. In these experiments, it was found that the delivery of lithium in the discharge depends strongly on the initial limiter temperature. Hence, the data on the limiter surface temperature during a discharge are necessary to find out the physical processes responsible for material erosion and the delivery of lithium in plasma.

This study was carried out in the T-11M tokamak under the program of experiments with a lithium limiter [4, 5]. The study was aimed at the time-resolved measurements of the temperature of the lithium limiter surface during a discharge, as well as at the measurements of the specific heat flux onto the lithium limiter surface. The limiter surface temperature was measured by IR emission because, due to the significant temperature gradients in the surface layer (~10 K/mm), the measurements with thermocouples fail to provide the required time resolution and accuracy.

2. SURFACE TEMPERATURE MEASUREMENT TECHNIQUE BY IR RADIATION

An IR radiometer based on an IR detector cooled with liquid nitrogen was used to measure the temperature of the limiter surface. The IR detector was based on a Ge:Au (germanium doped with gold) semiconductor photoresistor with a fairly high sensitivity (~10^3 V/W) in the spectral range 3–6 μm. The optical scheme of measurements is shown in Fig. 1. The IR detector housed in a shielding case was set over the upper branch pipe of the tokamak chamber in the focal plane of a lens. For measurements, we used a BaF_2 window and NaCl lens, which produced a 7.5-times demagnified image of the lithium limiter on the IR detector entrance 2×2 mm in size. In experiments, we measured the output amplifier voltage $U(t)$, which was proportional to the power of IR radiation ($P(t)$) from the 1.5×1.5-cm^2 area of the limiter surface, with a time resolution of ~100 μs. The sampling time was 20 μs. The time resolution of the radiometer was limited by the amplifier of the IR detector.

The radiometer sensitivity dU/dT_s can be determined from the slope of the calibration curve (Fig. 2). It rather rapidly increases with temperature, being equal to ~0.5 mV/K at $T_s \sim 100$°C. The threshold temperature sensitivity of the radiometer $\delta T_s = \delta U_{\text{noise}}/(dU/dT_s)$ is also determined by its self-noise, which is equal to $\delta U_{\text{noise}} \approx 0.5$ mV in the amplifier bandwidth. Thus, at an emitting surface temperature of $T_s > 100$°C, the threshold sensitivity is $\delta T_s < 1$ K. Note that the radiometer sensitivity also depends on the limiter material; e.g., for a graphite limiter, it is much higher because the emissivities of graphite and metals (lithium in our case) are different in the IR region [6, 7].

1063-780X/02/2810-0802$22.00

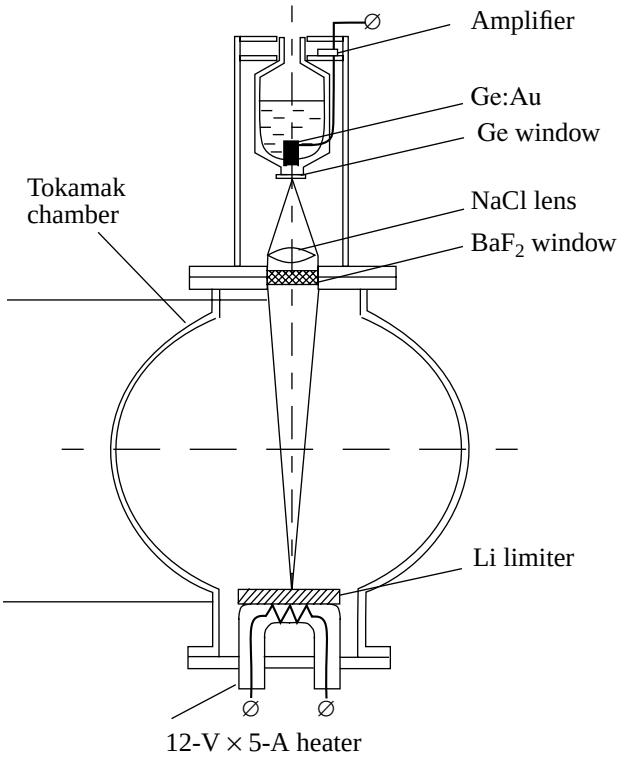

Fig. 1. Location of the IR radiometer in the branch pipe of the T-11M tokamak.

Since the radiometer "sees" the limiter surface through a plasma, the question arises as to how large is the fraction of the recorded IR power related to the plasma emission. Figure 3 presents the calculated ratio of the emission intensity from the plasma to that from the limiter in the range 3–6 μm as a function of the plasma density under the discharge conditions most unfavorable from the standpoint of background plasma emission ($Z_{\text{eff}} = 3$, $T_e = 10$–100 eV). In this spectral range, the main contribution comes from bremsstrahlung. These rough estimates show that, in the range 3–6 μm, the intensity of plasma emission is nearly four orders of magnitude lower than the emission intensity from the limiter surface. Bremsstrahlung from the plasma can be detected only at plasma densities of $n_e = 10^{15}$ cm^{-3} and higher. After placing the limiter into a branch pipe, the detected signal fell to the noise level, which was experimental proof that emission from the plasma column could be neglected under the experimental conditions of the T-11M tokamak.

3. ABSOLUTE CALIBRATION OF THE RADIOMETER

The measured signal $U(t)$ was recalculated into the temperature $T(t)$ by using the calibration curves $P(T)$, which were obtained with a special calibration procedure with the use of a thermocouple in the regime of slow heating of the limiter by an special heater in the absence of plasma.

Figure 2 shows the radiometer calibration curve obtained via approximating the calibration data by a forth-order polynomial for the operational temperature range. Accurate to a constant scaling factor, this curve coincides with a computed curve obtained by integrating the product of the spectral sensitivity and the blackbody radiation spectrum over frequency. Note that this polynomial was also used to extrapolate the calibration curve to the region 400–500°C. The nonlinear behavior of the $U(T)$ dependence stems from the fact that, in the given temperature range of the emitting surface and in the given measurement spectral range, we have

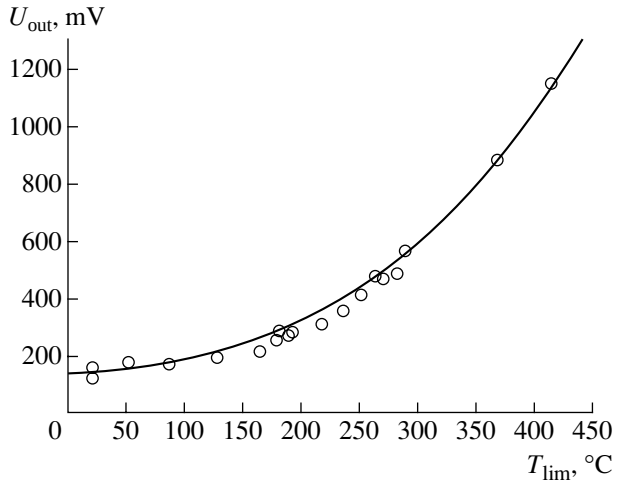

Fig. 2. Calibration curve of the IR radiometer ($T_{\text{lim}} = 300$°C, $Z_{\text{eff}} = 3$).

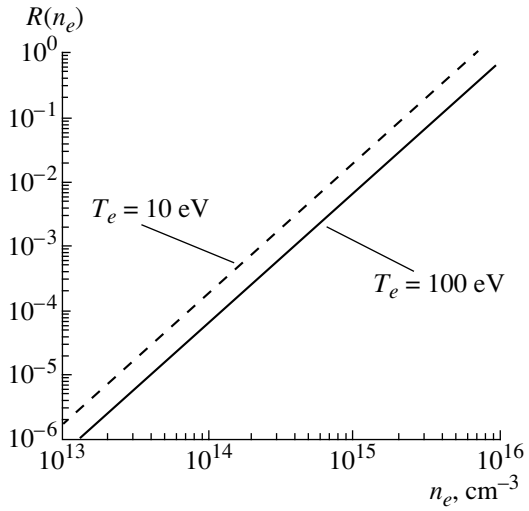

Fig. 3. Ratio of the plasma emission intensity to the intensity of blackbody radiation, $R(n_e)$, as a function of the plasma density n_e ($Z_{\text{eff}} = 3$, $T_e = 10$–100 eV).

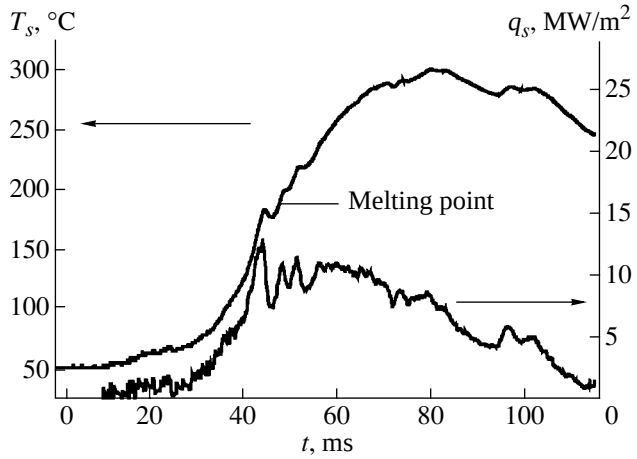

Fig. 4. Time behavior of the surface temperature T_s of a Li limiter and the heat flux q_s onto its surface in a normal L-regime (T-11M, shot no. 12357).

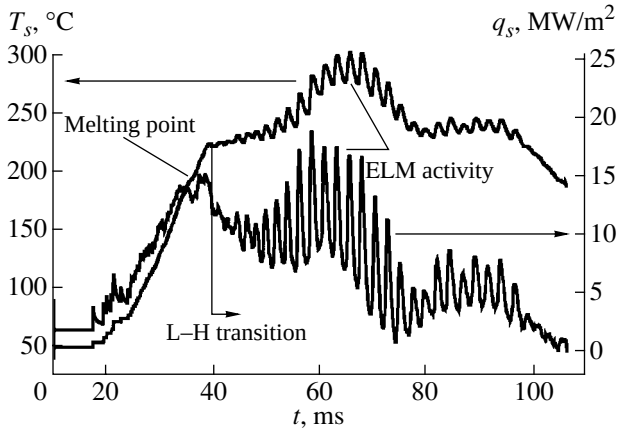

Fig. 5. Time behavior of the surface temperature T_s of a Li limiter and the heat flux q_s onto its surface in the ohmic H-regime after boronization (T-11M, shot no. 13857).

$\hbar\omega \gg kT$; i.e., in this case, the Rayleigh–Jeans law does not work.

The main systematic error in the temperature measurements by this technique is introduced by the drift of the radiometer zero level caused by a change in the temperature background during the calibration procedure. It should also be noted that the apparatus measures the limiter surface temperature averaged over an area of $\sim 1.5 \times 1.5$ cm^2.

4. TEMPERATURE REGIME OF THE LITHIUM LIMITER AND A METHOD FOR HEAT FLUX CALCULATION FROM TEMPERATURE MEASUREMENTS

Strictly speaking, to determine the intensity $Q(t)$ [W/cm^2] of the heat flux onto the limiter surface from the measured temperature $T(t)$ and the known heat capacity and thermal conductivity of the limiter material, one has to solve an inverse problem by using solutions to the heat conduction equation for the entire limiter with allowance for its real geometry. However, under the conditions of our experiment, the problem can be significantly simplified. Let us consider a rail-type limiter employed in the T-11M tokamak. A 5-mm-thick CPS was in contact with a plasma [3–5].

In the course of a discharge, the surface temperature of the CPS lithium element is determined by the specific heat power $Q(t)$ released on its surface; the initial temperature T_0; and the density ρ, heat capacity c, and thermal conductivity λ of the limiter material.

The duration τ of thermal action and the thermal diffusivity $\chi = \lambda/(\rho c)$ of the limiter material determine the depth Δ to which the limiter is heated by the end of the heat pulse. This depth can be roughly estimated from the relationship

$$\Delta \approx (\chi\tau)^{1/2}, \tag{1}$$

which follows from the heat conduction equation.

Estimates by formula (1) show that, at a T-11M discharge duration of $\tau \approx 0.1$ s, the heating depth is on the order of $\Delta \approx 1$ mm. The thickness of the limiter plate is about $D \approx 5$ mm. Thus, the heating depth is approximately five times less than the thickness of the CPS plate.

Since the thickness and radius of curvature of the CPS limiter are much higher than the heating depth Δ, these parameters can be ignored and the time behavior of the surface temperature $T(t)$ can be easily calculated in the thick-plate approximation ($D \gg \Delta$) from the given $Q(t)$ function. Moreover, the inverse problem—the calculation of the specific power $Q(t)$ released on the surface from the given (measured) temperature of this surface $T(t)$—can also be solved rather simply. The well-known solution to the heat conduction equation is

$$T(t) = \frac{1}{\lambda}\sqrt{\frac{\chi}{\pi}}\int_{-\infty}^{t}\frac{Q(\tau)}{\sqrt{t-\tau}}d\tau. \tag{2}$$

The inverse problem can be solved by using the fact that, in our case, the functions $Q(t)$ and $T(t)$ are coupled via Abelian integral equation (2), whose solution is well known:

$$Q(t) = \frac{\lambda}{\sqrt{\pi\chi}}\int_{-\infty}^{t}\frac{dT(\tau)}{d\tau}\frac{d\tau}{\sqrt{t-\tau}}. \tag{3}$$

Figures 4–6 present the power $Q(t)$ restored with formula (3) from the experimental data by using a proper numerical algorithm. Note that, under the conditions of our experiment, the other channels for heat loss

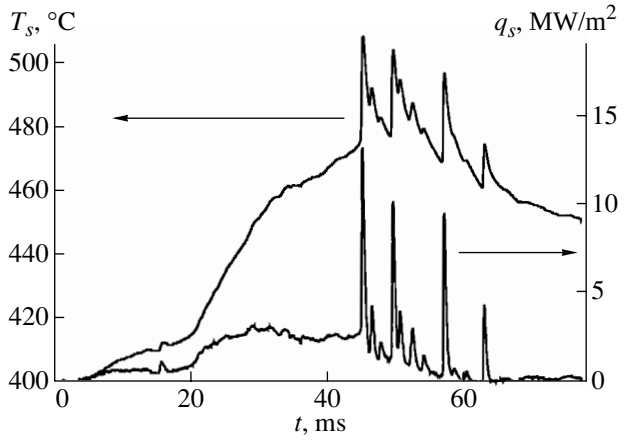

Fig. 6. Time behavior of the surface temperature T_s of a hot Li limiter and the heat flux q_s onto its surface during the disruption instability (T-11M, shot no. 12399).

from the surface (radiation losses and evaporation) can be ignored.

5. MEASUREMENTS OF THE LIMITER TEMPERATURE AND THE HEAT FLUX ONTO THE LIMITER

In T-11M experiments with a lithium limiter, we determined the time behavior of the temperature and the specific heat power in different regimes. Three types of a discharge that differ in the dynamics of energy release at the limiter can be distinguished:

Normal discharge (Fig. 4). In this case, the specific energy release can be as high as ~10 MW/cm^2, which corresponds to an electron temperature on the limiter surface of ~25 eV. A transition of surface lithium into liquid state can be seen in the temperature curve. The temperature of the phase transition is an independent means to verify the absolute calibration of the radiometer; it is in good agreement with the known melting temperature of lithium.

Ohmic H-mode (Fig. 5). This regime is characterized by significant oscillations of the specific energy release on the limiter surface (ELM activity). In this case, the average energy release somewhat decreases. The oscillations of the thermal load reflect the oscillations of the electron temperature near the limiter surface. These oscillations are related to the ELM activity determined by MHD instability at the edge of the plasma column.

Discharge with a disruption instability (Fig. 6). Here, the peak values of the heat release power during the fast disruption processes are somewhat underestimated because of the insufficiently high time resolution and the smoothing procedure used. However, the integral value of the specific energy release during the disruption is determined correctly.

6. CONCLUSION

The results of experiments with a lithium limiter in the T-11M tokamak demonstrate that the IR diagnostics is highly informative. It enables monitoring the most important parameters, such as the surface temperature of the limiter or divertor plate and the specific heat flux onto the limiter (divertor plate) surface, with a fairly high time resolution. It also allows one to estimate the electron temperature near the limiter surface (near the last closed magnetic surface).

The technique used enables studying the dynamics of energy release and the quantitative characteristics of fast MHD processes, such as the disruption instability or ELM activity in the H-mode.

The time resolution of our radiometer can be improved to 10 μs by modifying a preamplifier. However, when studying the problems that require time resolution of ~1 μs (e.g., when investigating the disruption instability), it is reasonable to use an IR detector based on a cooled CHT photodiode (a semiconductor photodiode based on CdHgTe compound) [8]. Further, we plan to use a multichannel matrix CHT detector to study the distribution of energy release at the limiter during the disruption instability with a higher (1–2 μs) time resolution.

REFERENCES

1. V. A. Evtikhin, I. E. Lyublinski, A. V. Vertkov, *et al.*, in *Proceedings of the 16th IAEA Fusion Energy Conference, Montreal, Canada, 1996* (IAEA, Vienna, 1997); Fusion Energy **3**, 659 (1996).
2. V. N. Mikhaĭlov, V. A. Evtikhin, I. E. Lyublinski, *et al.*, in *Lithium in Thermonuclear and Space Power Engineering* (Énergoatomizdat, Moscow, 1999), p. 9.
3. V. Lazarev, E. Azizov, A. Alekseyev, *et al.*, in *Proceedings of the 26th EPS Conference on Controlled Fusion and Plasma Physics, 1999*, Contributed Papers, p. 845.
4. V. A. Evtikhin, I. E. Lyublinski, A. V. Vertkov, *et al.*, Fusion Eng. Des. **56–57**, 363 (2001).
5. V. A. Evtikhin, I. E. Lyublinski, A. V. Vertkov, *et al.*, in *Proceedings of the 18th IAEA Fusion Energy Conference, Sorrento, Italy, 2000*, Book of Abstracts, p. 47.
6. I. D. Anisimova, I. M. Vikulin, F. A. Zaĭtov, *et al.*, in *Semiconductor Photodetectors* (Radio i Svyaz', Moscow, 1984), p. 9.
7. L. Z. Kriksunov, *Handbook on Foundations of Infrared Engineering* (Sov. Radio, Moscow, 1978), p. 30.
8. *Optical and Infrared Detectors*, Ed. by R. J. Keyes (Springer-Verlag, New York, 1977; Radio i Svyaz', Moscow, 1985).

Translated by N. N. Ustinovskiĭ

Plasma Physics Reports, Vol. 28, No. 10, 2002, pp. 806–813. Translated from Fizika Plazmy, Vol. 28, No. 10, 2002, pp. 877–885.

TOKAMAKS

Pulsed Time-of-Flight Refractometry Measurements of the Electron Density in the T-11M Tokamak

A. A. Petrov, V. G. Petrov, A. Yu. Malyshev, V. K. Markov, and A. V. Babarykin

Troitsk Institute for Innovation and Fusion Research, Troitsk, Moscow oblast, 142190 Russia

Received January 16, 2002

Abstract—A new method for measuring the plasma density in magnetic confinement systems—pulsed time-of-flight refractometry—is developed and tested experimentally in the T-11M tokamak. The method is based on the measurements of the time delay of short (with a duration of several nanoseconds) microwave pulses propagating through the plasma. When the probing frequency is much higher than the plasma frequency, the measured delay in the propagation time is proportional to the line-averaged electron density regardless of the density profile. A key problem in such measurements is the short time delay of the pulse in the plasma (~1 ns or less for small devices) and, consequently, low accuracy of the measurements of the average density. Various methods for improving the accuracy of such measurements are proposed and implemented in the T-11M experiments. The measurements of the line-averaged density in the T-11M tokamak in the low-density plasma regime are performed. The results obtained agree satisfactorily with interferometric data. The measurement errors are analyzed, and the possibility of using this technique to measure the electron density profile and the position of the plasma column is discussed. © *2002 MAIK "Nauka/Interperiodica"*.

1. INTRODUCTION

At present, the measurements of the line-averaged plasma electron density are not believed to be a serious problem, because interferometry methods (including multichannel ones) in the optical, submillimeter, and millimeter wavelength ranges are developed quite well. The main problems to be solved in this area are the improvement of the spatial and temporal resolution when reconstructing the density profile evolution and the implementation of multiple-aspect and tomographic systems [1].

Nevertheless, raising the reliability of plasma density measurements in the next-generation tokamaks is an important problem not only because of the increase in the number of the measurement channels. The problem of reliable density measurements is crucial for ITER and other large-scale devices because they must operate with long (longer than 1000 s) pulses, especially when the signals from the density probes will be used to control the equilibrium of the plasma column and the density evolution during the discharge.

In fact, because of the discontinuity of the phase function measured by an interferometer, none of the conventional instruments can avoid fringe "jumps" in measurements, especially under conditions of high MHD activity, in the course of auxiliary heating, pellet injection, etc. These failures may be caused by different things. They may be of technical nature (pickups) or may be related to the physical effects accompanying the measurements (e.g., the refraction of the probing beams). Sometimes, these sources of failures are difficult to prevent or take into account, which leads to the loss of information.

To provide stable measurements, different types of the so-called "unambiguous" interferometers are currently used. In these devices, the problem of obtaining one-to-one correspondence between the density and the phase measured is solved either by the hardware frequency derivation of the phase signal in order to obtain the dependence $\langle nl \rangle \sim \tau$ (where n is the plasma density, l is the length of the measurement chord, and τ is the delay time of an electromagnetic wave propagating through the plasma [2]) or by the differentiation of the phase with respect to the refractive index [3, 4]. It is easily seen that instruments of the former type are, at least, no simpler than usual interferometers. In the latter instruments, a limited access to the measurement object and the dependence of the measured quantity on the magnetic field may hamper the use of Cotton–Mouton and Faraday polarimeters as plasma density probes.

In this paper, we propose to use a pulsed microwave radar (a reflectometer operating as a time-of-flight refractometer when the probing frequency is higher than the plasma frequency) to obtain information on the line-averaged electron density. Previously, this operating mode was used to correct the density profile obtained from reflectometric measurements [5]. It was also proposed to use time-of-flight refractometry to measure the density profile in ITER [6]. It should be noted that, in the pulsed operating mode, valid signals can be relatively easily separated from undesirable spurious retroreflections of the probing radiation from the vacuum windows, flanges, and the chamber wall of the tokamak (time discrimination). Furthermore, with this method, the procedure reduces to direct measurements of the delay time for each probing pulse; the scheme of

1063-780X/02/2810-0806$22.00

measurements is substantially simplified (in comparison with the other methods); and, consequently, the reliability of the diagnostics increases.

The regime of a pulsed time-of-flight refractometer (TFR) was observed in the T-11M tokamak in the current ramp-up and ramp-down phases of the discharge, when the plasma density was rather low [7].

2. PHYSICAL PRINCIPLES OF PULSED TIME-OF-FLIGHT REFRACTOMETRY

Let us consider the propagation of a microwave pulse with an arbitrary shape through a collisionless magnetized plasma. We pass over to the Fourier transform of the signal and write the phase shift of the Fourier component in the form

$$\Phi(\omega)_{o,e} = (\omega/c)\int_{-a}^{a}\eta_{o,e}(\omega, x)dx, \quad (1)$$

where ω is the circular frequency of the Fourier component, a is the minor plasma radius, x is the coordinate counted from the center of the plasma along the beam propagation direction, and $\eta_{o,e}(\omega, x)$ is the refractive index of an ordinary (extraordinary) wave in plasma.

The signal passed through the plasma is delayed by the time (the group time delay)

$$\tau_{gr} = (d\Phi/d\omega) = \Phi'(\omega_0), \quad (2)$$

where ω_0 is the signal carrier frequency. The signal also undergoes spreading, which is determined by the setting time $\tau_{set} = (\pi\Phi''(\omega_0))^{0.5}$. For a transparent plasma, the spreading is negligible [8, 9].

In practice, it is convenient to probe the plasma with ordinary waves whose refractive index is independent of the external magnetic field:

$$\eta_0(\omega, x) = [1 - (\omega_p(x)/\omega)^2]^{1/2}, \quad (3)$$

where $\omega_p(x) = 56.4 \times 10^3 n_e(x)^{0.5}$ is the electron plasma frequency, $n_e(x)$ is the electron density (in cm^{-3}), ω is the circular carrier frequency (in rad/s), and $\omega > \omega_p$.

From expressions (1) and (2), it follows that

$$\tau_{gr} = (1/c)\int_{-a}^{a}\eta_0(\omega, x)dx + (\omega/c)\int_{-a}^{a}\frac{d\eta_0(\omega, x)}{d\omega}dx. \quad (4)$$

Then, for a parabolic density profile, we have

$$\tau_{gr} = (a\omega)/(c\omega_p(0))\ln[(\omega + \omega_p(0))/(\omega - \omega_p(0))]. \quad (5)$$

In the limit

$$\omega \gg \omega_p(0), \quad (6)$$

the expression for the propagation time of the microwave pulse takes the form

$$\tau_{gr} = 2a/c[1 + \omega_p(0)^2/3\omega^2]; \quad (7)$$

i.e., the variation in the propagation time in the presence of plasma (the pulse time delay) is proportional to the line density $\langle nl\rangle$ (where $l = 2a$) and is inversely proportional to the square of the probing frequency f,

$$\tau'_{pl} = \tau_{gr} - 2a/c = (2a/3c)(\omega_p(0)^2/\omega^2) = \gamma\langle nl\rangle/f^2, \quad (8)$$

where γ is a numerical factor and $f = \omega/2\pi$.

From expressions (3) and (4), it follows that, if inequality (6) is satisfied, then formula (8) is valid for any density profile.

When measuring of the pulse delay time in plasma, it is convenient to express time in ns and the distance in cm. Accordingly, the speed of light is equal to 30 cm/ns, the frequency is measured in GHz, and the plasma density is measured in 10^{14} cm^{-3}. In these units, the formula for the delay time in the case of the double pass through the plasma with account for the reflection from the inner wall of the vacuum vessel (when probing is performed in the equatorial plane) takes the form

$$\tau_{pl} = 2\tau'_{pl} = (4a/3c)(\omega_p(0)^2/\omega^2) \approx 270\langle nl\rangle/f^2. \quad (9)$$

Note that, like in interferometric measurements, information obtained in this way is integral in character. However, the phenomenon of interference itself is not used in this approach. For this reason, it is proper to use the term "refractometer," keeping in mind the direct relation between the refractive index and the plasma density.

3. CHOICE OF THE PARAMETERS FOR PULSED TIME-OF-FLIGHT REFRACTOMETRY

The semiempirical criterion for choosing the probing frequency for usual interferometers is well known [10]:

$$f \geq 3f_p. \quad (10)$$

When this condition is satisfied, we can restrict ourselves to the first term in the power series in $\omega_p(x)/\omega$ in expression (3); i.e., the dependence $\varphi \sim \langle nl\rangle$ (where φ is the phase shift) is linear correct to second-order terms. In this case, formula (9) takes the form

$$\tau_{pl} = (4a/3c)(\omega_p^2/\omega^2) \leq (4a/27c). \quad (11)$$

Experiments on pulsed reflectometry show that delay times on the order of 0.5–1 ns [6] can be measured with relatively good accuracy. As follows from equality (11), such delay times correspond to devices with a minor radius of

$$a \geq 27c/8 \approx 100 \text{ cm}. \quad (12)$$

For time-of-flight refractometry can be used in small devices, such as the T-11M tokamak (a = 19–23 cm, R = 70 cm, and $\langle n\rangle \leq 4 \times 10^{13}$ cm^{-3}), it is required to enhance the accuracy of measurements.

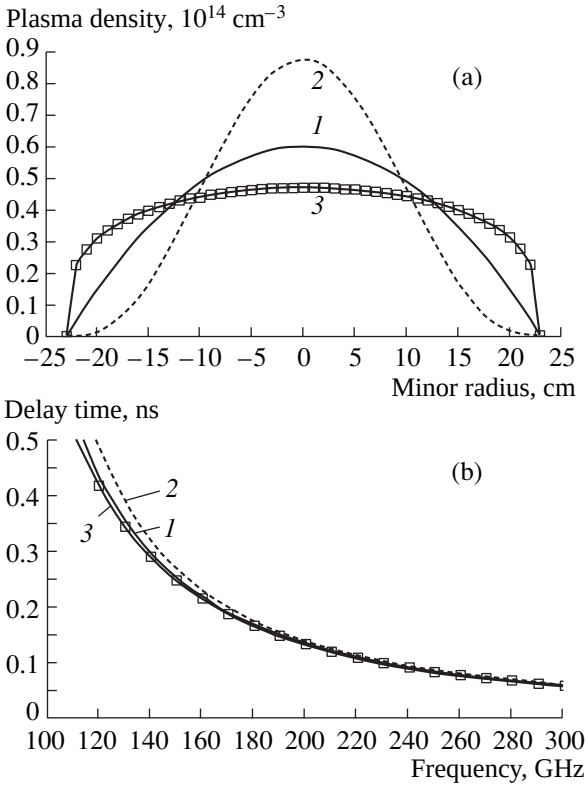

Fig. 1. (a) Density profiles used in calculations and (b) the dependence of the delay time of the TFR signals on the probing frequency for a fixed plasma density ($\langle n \rangle = 4 \times 10^{13}$ cm^{-3}) and different density profiles: (*1*) parabolic profile ($\beta = 1$), (*2*) peaked profile ($\beta = 3$), and (*3*) flat profile ($\beta = 0.3$).

One of the ways to improve the accuracy of density measurements with TFR is probing at a lower frequency, when condition (10) is not satisfied. In this case, the dependence of τ_{pl} on the average density is nonlinear; however, this would not impede measurements if this nonlinearity will be taken into account when calibrating the device. When reducing the probing frequency, we should be assured that the results of measurements are independent of the density profile. To choose a criterion for the probing frequency, we analyzed the dependences of the pulsed TFR output signal (the delay time of the microwave pulse in the plasma) on the probing frequency calculated for different density profiles in the form $n(r) = n_0[1 - (r/a)^2]^\beta$ (Fig. 1). The average density for all these distributions is the same and is equal to 4×10^{13} cm^{-3}. The refractometer curves are obtained from the exact solution of equation (4). From the figure, it is clear that the effect of the profile is negligible for flat profiles and is significant for peaked profiles, because it is flat profiles for which condition (6) is satisfied easier at the same average density.

If we require that the error in the average density due to the profile effect be less than 10%, then, as follows from Fig. 1b, the probing frequency for the T-11M device must be no less than 140 GHz and the propagation time of the microwave pulse through the plasma will be about 0.3 ns.

The accuracy of the measurements in the regime of a pulsed radar reflectometer (PRR) in previous experiments in the T-11M tokamak attained ~50 ps; the repetition rate of probing pulses was 100 kHz, and the measurement results were averaged over a time period of ~1 ms [7]. Consequently, the error in the pulsed TFR measurements of the average electron density will be 15% for the maximum density, which is clearly insufficient.

A relatively simple way to improve the accuracy of density measurements with the same or higher temporal resolution is to increase the repetition rate of the probing pulses and, then, to average the results obtained over many measurements. At present, when operating with pulsed microwave oscillators based on IMPATT diodes, repetition rates of 1–10 MHz are achieved. This makes it possible to attain the limiting accuracy in delay time measurements as high as 5–10 ps. Hence, an accuracy of 1.5% can be achieved if the average density is measured with a temporal resolution of 1 ms. A further improvement of the measurement accuracy is possible with new approaches to the elaboration of the instrumental part of the TFR; these approaches will be described in the next section.

To reduce the influence of the density profile on the measurements of the average electron density, we can use the simultaneous probing at two frequencies that differ substantially from each other. By analogy to Fig. 1b, Fig. 2a shows the dependences of the TFR signal on the probing frequency for a low-density regimes of the T-11M tokamak ($\langle n \rangle = 0.67 \times 10^{13}$ cm^{-3}) for different density profiles. It follows from Figs. 1 and 2 that, for the T-11M tokamak, the higher frequency should be $f_2 \approx 2f_p \approx 170$ GHz and the lower frequency should be close to $f_1 \approx f_p$. In this case, the error due to the effect of the density profile in the measurements of the average density will be less than 1.5%.

Since the possible plasma density profiles are different for different devices, the TFR probing frequency should be chosen individually for each device.

4. TFR EXPERIMENTAL SETUP IN THE T-11M TOKAMAK

The T-11M tokamak was recently modified with the purpose of achieving optimum conditions for experiments with high-power (2 MW) ion cyclotron heating. In particular, the copper liner was removed from the vacuum chamber, a system for controlling plasma equilibrium in the vertical and horizontal directions was put into operation, and an inductor supply system was improved to achieve a longer discharge.

To test the technique proposed, we elaborated a TFR prototype operating at a carrier frequency of 60 GHz.

This device was intended to monitor the average electron density in the T-11M tokamak in the low-density operating mode. In this case, the effect of the profile on the density measurements should be less than 10% (Fig. 2a).

Figure 2b shows the calculated calibrating curve for this refractometer, i.e., the relation between the average plasma-electron density and the measured delay time for different density profiles. For comparison, the same figure shows the dependence obtained from Eq. (9). As the average density increases, the nonlinearity appears earlier than the results of measurements begin to depend on the shape of the density profile. It is seen that the results of measurements are almost independent (within 10%) on the profile shape up to a density of 0.67×10^{13} cm^{-3}.

As was mentioned above, the TFR is very similar to the PRR [7]. The difference is that, in the former instrument, the probing frequency should be higher than the plasma frequency. Moreover, the TFR is expected to be simpler and more reliable in operation and to provide the higher accuracy of measurements of the delay time of a microwave pulse in the plasma as compared to the pulsed reflectometer.

To enhance the TFR sensitivity, we chose the double-pass scheme of probing by ordinary waves in the equatorial plane. It is remarkable that there was no need to install a special retroreflector inside the vacuum chamber in this case, because both the level and quality of the pulses reflected from the inner wall of the T-11M vacuum vessel were quite sufficient to provide a signal-to-noise ratio of ≥20 dB.

The block diagram of the TFR prototype is shown in Fig. 3. An IMPATT diode–based oscillator (*IMPATT*) generated short microwave probing pulses with a power of ~100 mW and a full width at half maximum of 6 ns, the rise and fall times being ~2 ns, respectively. The repetition rate of microwave pulses, which was controlled by a driving oscillator (*DO*), attained 1 MHz; in plasma experiments, this rate was 100 kHz, because an analog-to-digital converter (ADC) with a sampling frequency of up to 100 kHz was used.

The IMPATT diode was preliminarily heated by direct current, and the generation occurred upon applying a specially formed voltage pulse with an amplitude of ~6 V. In this case, variations in the thermal regime of the IMPATT operation were minimal; hence, it was possible not only to obtain microwave pulses with the required time parameters, but also to minimize the chirp of the IMPATT frequency during the pulse. In our case, the frequency drift was no higher than ~100 MHz, which was sufficient to ignore measurement errors related to this drift. It follows from (9) that $\Delta\tau_p/\tau_p = \Delta n/n = 2\Delta f/f_{\text{carrier}} \approx 3 \times 10^{-3}$; i.e., the error in delay-time measurements due to the chirp is no higher than 5 ps.

The use of the direct generation of short microwave pulses allowed us to significantly simplify the design of the apparatus because of the exclusion of fast *p–i–n*

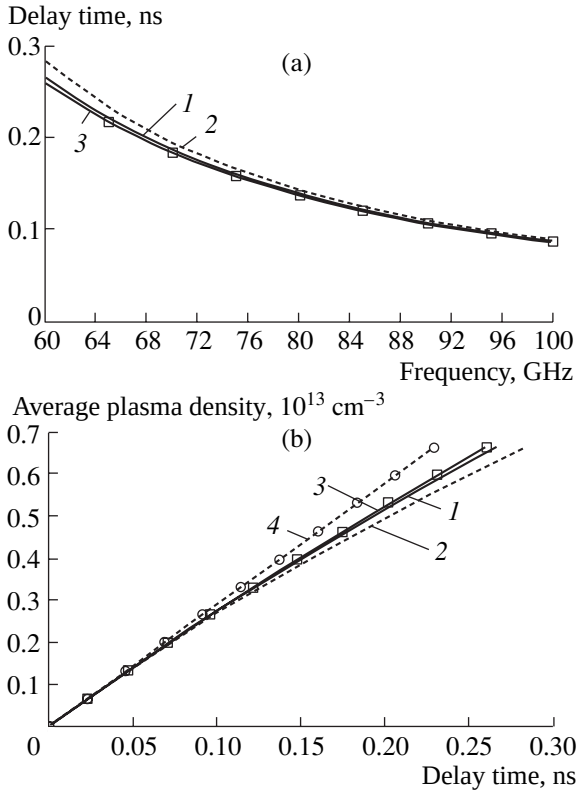

Fig. 2. (a) Dependence of the delay time of the TFR signals in a low-density plasma ($\langle n \rangle = 0.67 \times 10^{13}$ cm^{-3}) on the probing frequency and (b) the average density as a function of the TFR delay time for different density profiles: (*1*) parabolic profile ($\beta = 1$) (*2*) peaked profile ($\beta = 3$), and (*3*) flat profile ($\beta = 0.3$). Curve (*4*) shows calculations by formula (8).

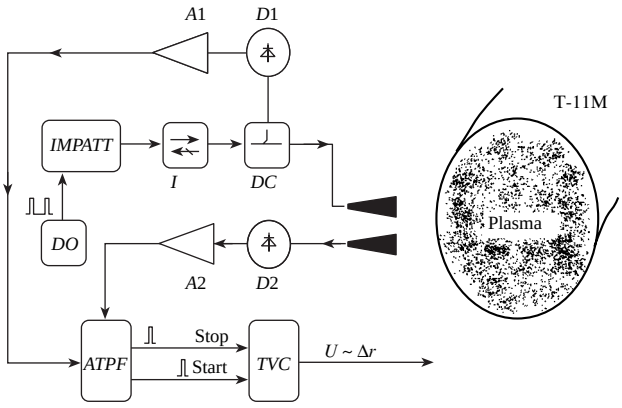

Fig. 3. Block diagram of TFR experiments in the T-11M tokamak: (*IMPATT*) IMPATT diode–based oscillator of microwave pulses; (*DO*) driving oscillator; (*I*) ferrite isolator; (*DC*) directional coupler; (*D*1, *D*2) detectors of the reference and signal channels, respectively; (*A*1, *A*2) amplifiers of the reference and signal channels, respectively; (*ATPF*) adaptive threshold-pulse former; and (*TVC*) time-to-voltage converter.

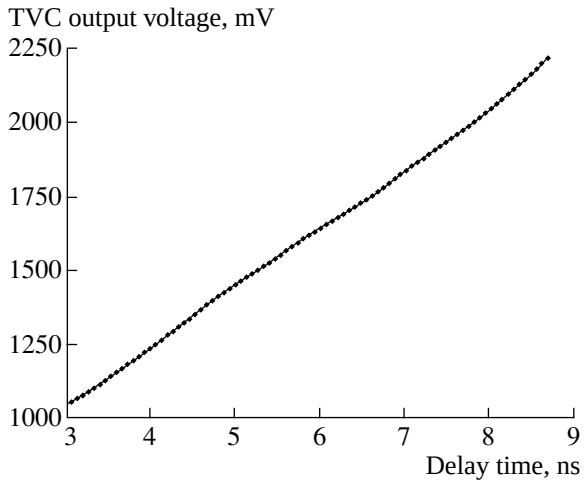

Fig. 4. TFR prototype calibrating curve.

diode modulators and their drivers. Another useful consequence of the design modification is a substantial (by 4–6 dB) decrease in the loss of the microwave signal.

After passing a ferrite isolator (I) and directional coupler (DC), a fraction of the microwave power was directed into reference detector $D1$. Through a 3.6×1.8 mm waveguide, the bulk of microwave radiation fell into an elongated horn antenna with an outlet aperture of $d = 50$ mm and, then, through a dielectric isolator and quartz window, into the tokamak chamber. The reflected signal was received by a similar horn and signal channel detector $D2$. The distance between the antenna axes was 60 mm in the poloidal direction. The transmitting antenna was positioned in the equatorial plane of the tokamak chamber, and the receiving antenna was oriented at an angle of 15° to the transmitting one in order to ensure the optimum overlap of the directional patterns of both antennas. High-sensitivity multidiode detector units based on Schottky barrier diodes ensured a signal-to-noise ratio in the reflected signal of ~20 dB and a sufficient fast response to pulses with the given time characteristics (the noise equivalent power was less than 10^{-11} W/Hz$^{0.5}$). After low-noise pulse amplifiers $A1$ and $A2$ (a rise time of $\tau_f \sim 0.8$–1.0 ns; noise factor of ≤ 2 dB; and voltage gain factors of 10 and 100, respectively), the detected pulses entered an adaptive threshold-pulse former (ATPF), whose design was identical to that used in [9]. Output signals of this unit were referred to the given points at the fronts of the input pulses, which made it possible to compensate for the influence of the amplitude modulation of the received signal (up to 20 dB) onto the accuracy of the formation of the "stop" signal. The start and stop signals generated by the ATPF were fed to the input of a time-to-voltage converter (TVC), whose output voltage was proportional to the delay time between these pulses. The TVC used in the TFR prototype was specially developed to attain an accuracy of 10 ps in delay-time measurements. The TVC signal was filtered by a low-frequency filter with a cutoff frequency of $f \approx 25$ kHz and, then, was fed to a data acquisition system of the T-11M tokamak.

The use of two detectors allowed us to exclude the effect of the time instability of the IMPATT breakdown initiated by a current pulse. In this case, the first reference pulse for the delay-time measuring circuit (the start signal) is formed in response to the signal from detector $D1$, whereas the second signal is formed in response to the signal from detector $D2$. The procedures of forming the start and stop signals from the signals fed from detectors $D1$ and $D2$, respectively, are identical. This allowed us to minimize the possible errors in the pulse locking times and to substantially improve the accuracy of delay-time measurements.

Before the TFR was installed in the tokamak, it was bench tested and calibrated. As a reflecting target, we used a metal cylinder of diameter ~15 cm. The TVC signals were measured by a digital voltmeter with an integration time of ~1 s. The TFR calibrating curve is shown in Fig. 4 (here, we present only a segment of the calibrating curve that was further used for data processing in tokamak experiments). The time resolution in the bench measurements is ~5 ps, and the minimum target displacement traced by the device is ~1 mm.

5. RESULTS OF EXPERIMENTS IN THE T-11M TOKAMAK

In the course of experiments in the T-11M tokamak, along with TFR measurements, the line-averaged electron density was also measured with an "unambiguous" polarization interferometer [3].

Figure 5 shows a typical raw TFR signal for the T-11M plasma with a relatively low density (shot no. 14444). It is seen that delay times of ~0.5 ns are measured with a rather good resolution. The scatter in the TFR signal in the absence of a plasma amounts to ~50 ps. In the presence of the plasma, the scatter increases to nearly 150–180 ps due to plasma fluctuations.

Then, the raw signals were filtered by a median filter with the following statistical averaging, subtracting the constant level, and taking into account the results of calibration. The median filter cut off the measurements with the largest r.m.s. deviations. After statistical averaging over time T, the signal noise decreased by a factor of $1/n^{0.5}$, where n is the number of measurements (during time T) over which the averaging was performed. This also resulted in the deterioration of temporal resolution by a factor of n.

Figures 5b and 5c show the average-density signals after data processing for the central interferometer channel and the refractometer, respectively. On the whole, there is a rather good agreement in the behavior of two signals during the discharge. The increase in the average density observed in the interferometer signal by the end of the discharge is associated with the

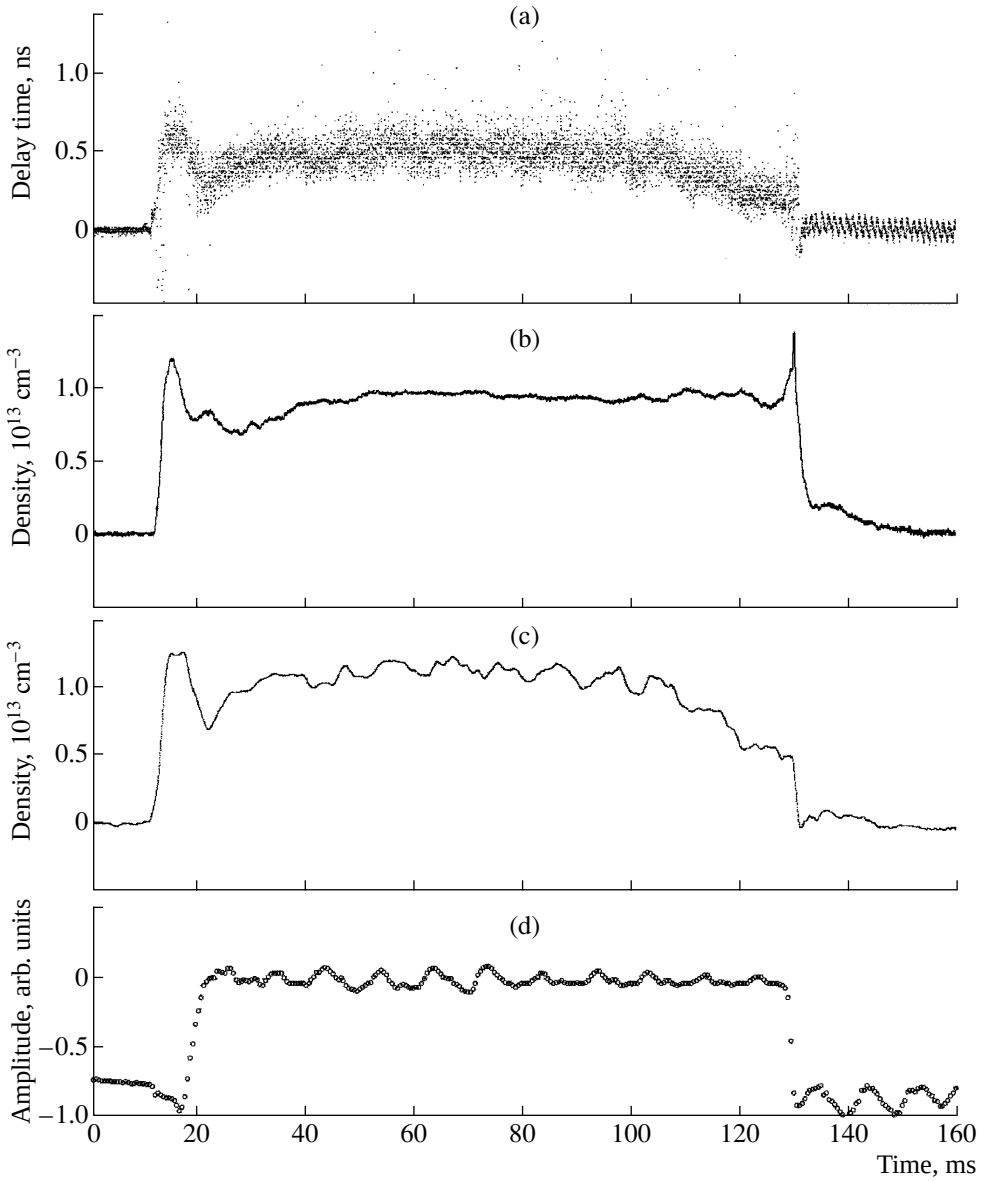

Fig. 5. (a) Raw TFR signal; (b) the time evolution of the average plasma density during the discharge (interferometric measurements); (c) the time evolution of the average density (TFR measurements); and (d) the vertical position of the plasma column measured by magnetic probes (shot no. 14444).

motion of the plasma column in the horizontal direction; in the TFR signal, this increase is absent. The average density determined from the refractometer signal also agrees satisfactorily with the interferometer data. An insignificant discrepancy may be attributed to the different geometry of the plasma column in the vertical and horizontal directions. Large-scale oscillations in the refractometer signal may be attributed to the vertical displacement of the plasma column under the action of a system providing vertical equilibrium in this discharge (Fig. 5d). Therefore, we may conclude that the TFR can be used as a sensitive detector of the vertical displacement of the plasma column.

Taking into account statistical averaging, the temporal resolution of the average-density measurements amounts to ~2–3 ms. In the absence of a plasma, the scatter in the refractometer data corresponds to a minimum measurable density of $\sim 0.2 \times 10^{12}$ cm^{-3}. Consequently, the accuracy of density measurements in these experiments was about 2% for the maximum density.

At plasma densities above the critical value, the refractometer operates as a reflectometer, as is shown in Fig. 6 (shot no. 14440). Here, we see a rather stable operation of the instrument in both the refractometer (up to 35 ms and after 110 ms) and reflectometer (from 45 to 111 ms of the discharge) modes.

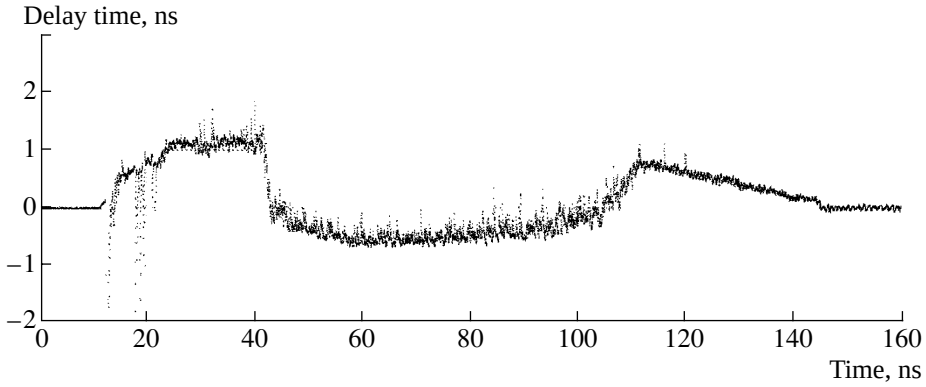

Fig. 6. Raw TFR signal (shot no. 14440). In contrast to shot no. 14444 (Fig. 5), the device operates in the reflectometer mode.

Thus, the TFR method has demonstrated a rather good accuracy of delay time (average density) measurements. The main factors that allowed us to improve the accuracy are the increase in the signal-to-noise ratio in the reflected signal due to the use of more sensitive detectors, the optimization of the instrument design, and the use of a more sensitive TVC circuit.

The increase in the repetition rate of the probing pulses to 1 MHz and the use of an analog-to-digital converter with an appropriate sampling rate allows one, in principle, to increase the resolution of the TFR density measurements by several times as compared to that achieved in these experiments.

6. CONCLUSION

A new method for measuring the plasma density in magnetic confinement systems—pulsed time-of-flight refractometry—is developed. This method is based on the measurements of the propagation time of short (with a duration of several nanoseconds) microwave pulses through the plasma. When the carrier frequency is much higher than the plasma frequency, the measured delay in the propagation time is proportional to the line-averaged electron density regardless of the density profile [see formula (8) and Fig. 1b]. A key problem in determining the delay time is the low accuracy of measurements. It is shown that the available measurement accuracy allows this technique to be applied in large tokamaks [see formula (12)].

For the purpose of implementing this technique in small tokamaks, the following methods of improving the accuracy of delay-time measurements are proposed, analyzed, and used in the tokamak experiments:

(i) the increase in the repetition rate of the probing pulses (up to 1–10 MHz) with the following statistical averaging of measurements;

(ii) the use of lower carrier frequencies of the probing wave, such that condition (6) is not satisfied, i.e., the transition to the nonlinear mode of TFR operation (Fig. 2b);

(iii) the modification of the pulsed microwave oscillator, the reduction of heat loads in the IMPATT diode, and the suppression of the drift of the oscillation frequency;

(iv) the use of identical channels for forming identical start and stop signals at the TVC inputs and the use of an additional detector in the start signal circuit (Fig. 3);

(v) the elaboration and use of a new TVC circuit allowing one to improve the measurement accuracy to 5–10 ps.

The developed TFR prototype operating at a carrier frequency of 60 GHz is calibrated (Fig. 4), and the average density in the T-11M tokamak is measured with the use of this technique.

The results of refractometric and interferometric measurements are in good agreement. Errors in the average-density measurements are reduced to 2% at a temporal resolution of ~2–3 ms, which allows one to use this device to measure the vertical position of the plasma column (Fig. 5). For this purpose, it is planned to equip the device with an additional receiving channel positioned symmetrically in the poloidal direction with respect to the main channel.

The method proposed can also be modified in order to measure the electron-density profile. For this purpose, the probing along several vertical chords with a single radiation pass through the plasma (measurements in the transmitted radiation) can be used. Evidently, in this case, it will be necessary to take into account the possible influence of refraction on the results of measurements. This technique can also be used to determine the horizontal displacement of the plasma column.

The main advantage of the instrument created is the unambiguity of the average-density measurements and, consequently, the reliable results of such measurements. This allows one to use this instrument as a density detector for tokamaks operating with long discharges (ITER, Tore Supra, etc.). The use of the TFR in large devices will certainly require raising its sensitiv-

ity, which can be achieved with the use of a heterodyne scheme of signal detection.

It is also important that, in contrast to interferometers, the instrument does not use the effect of interference. For this reason, it is relatively insensitive to the quality of the transmission line, the presence of standing waves, and the quality of the reflecting surface. The instrument permits simple connection to a tokamak through a quartz window and does not require a vast access to the installation. The simple design of the TFR and its ability to yield reliable and reproducible data allow us to recommend this instrument to be also used as a density detector for the real-time control of the plasma density.

ACKNOWLEDGMENTS

We thank A.P. Chernobaĭ for his assistance in experiments carried out in the T-11M tokamak and A.N. Romannikov for fruitful discussions.

REFERENCES

1. J. H. Donne, Rev. Sci. Instrum. **66**, 3407 (1995).
2. A. W. Morris for the MAST Team, in *Advanced Diagnostics for Magnetic and Inertial Fusion, Varenna, 2001*, Abstracts of Papers.
3. V. F. Shevchenko, A. A. Petrov, V. G. Petrov, and Yu. A. Chaplygin, Fiz. Plazmy **22**, 32 (1996) [Plasma Phys. Rep. **22**, 28 (1996)].
4. R. T. Snider, T. N. Carlstrom, C. H. Ma, and W. A. Peebles, in *Diagnostics for Experimental Thermonuclear Fusion Reactors*, Ed. by P. E. Stott *et al.* (Plenum, New York, 1996).
5. S. H. Heijnen, C. A. J. Hugenholtz, F. C. Schüler, *et al.*, in *Proceedings of the 22nd EPS Conference on Controlled Fusion and Plasma Physics, Bournemouth, 1995*, p. IV-441.
6. V. F. Shevchenko, A. A. Petrov, V. G. Petrov, and Yu. A. Chaplygin, Fiz. Plazmy **22**, 25 (1996) [Plasma Phys. Rep. **22**, 21 (1996)].
7. V. F. Shevchenko, A. A. Petrov, V. G. Petrov, and Yu. A. Chaplygin, Fiz. Plazmy **20**, 33 (1994) [Plasma Phys. Rep. **20**, 27 (1994)].
8. V. L. Ginzburg, *The Propagation of Electromagnetic Waves in Plasmas* (Nauka, Moscow, 1960; Pergamon, Oxford, 1970).
9. V. F. Shevchenko, A. A. Petrov, and V. G. Petrov, Int. J. Infrared Millim. Waves **14**, 1755 (1993).
10. V. E. Golant, in *Handbook of Plasma Physics*, Vol. 2: *Basic Plasma Physics*, Ed. by A. A. Galeev and R. N. Sudan (Énergoatomizdat, Moscow, 1984; North-Holland, Amsterdam, 1984).

Translated by N. F. Larionova

Plasma Physics Reports, Vol. 28, No. 10, 2002, pp. 814–826. Translated from Fizika Plazmy, Vol. 28, No. 10, 2002, pp. 886–897.

PLASMA DYNAMICS

MHD Simulations of Molybdenum X-Pinches

G. V. Ivanenkov* and W. Stepniewski**

**Lebedev Institute of Physics, Russian Academy of Sciences, Leninskiĭ pr. 53, Moscow, 117924 Russia*

***Kaliski Institute of Plasma Physics and Laser Microfusion, Warsaw 49 Hery 23, Poland*

e-mail: ivanenkv@sci.lebedev.ru

Received February 16, 2002

Abstract—The compression of molybdenum X-pinches with paraboloidal and conical initial geometries is investigated using numerical radiative MHD models. The model with conical initial geometry provides a more complete description of the axial plasma motion, better reflects the actual discharge geometry, and applies to molybdenum loads with larger masses. Both models make it possible to describe the main compression stages, including the formation of a "minidiode," the formation of a narrow neck in the constriction, the microexplosion of a "hot spot," and the generation of shock waves followed by the breaking of the constriction. © *2002 MAIK "Nauka/Interperiodica"*.

1. INTRODUCTION

X-pinch, which began to be investigated 20 years ago as an interesting perceptual object, has recently become an important tool in the X-ray diagnostics of dense plasmas. Due to its unique properties (such as the unsurpassed parameters of the compressed matter in the class of discharges through metal wires, submicron sizes of the hot spot, and a picosecond time scale of X-ray burst), X-pinch is widely applied as an instantaneous point source of nearly coherent radiation in the emission spectra of multicharged ions [1]. X-pinches made it possible to experimentally investigate discharges through exploding thin metal wires, in particular, single-wire loads, multiwire arrays, and even X-pinches themselves [2]. In order to interpret the data obtained in those experiments, it became necessary to further develop the previously proposed MHD model [3, 4] of the axisymmetric radiative implosion of a hot dense plasma column.

Our code is based on a mixed Eulerian–Lagrangian approach using the D'yachenko free-point method improved by Jach [5]. A detailed description of the Jach's version, which was adopted for the code, as well as its applications in continuum mechanics can be found in [5]. In turn, the code was further improved by interpolating the local fields from parabolic (rather than linear) profiles. The code, which is analogous to that for single exploding wires, describes the transport phenomena in a magnetic field, radiative–collisional processes, and radiation diffusion. Our code differs from the code for single wires not only in the geometry of the load. Because of the lack of experimental data, we did not introduce any information about the core and the phase transitions (this information is important for a discharge through a wire) into the code and used the configuration of a dense plasma as the initial configuration.

Because of the three-dimensional nature of an X-pinch, its model is not as well developed as that of an individual wire: the task now is to search for the "natural" initial plasma configuration and adequate boundary conditions. The first attempt to implement the model numerically [3] was made for an initially conical X-pinch; however, this attempt was unsuccessful because of an inadequate formulation of the problem and an imperfect algorithm for its solution. Next, an attempt was made to implement a simplified model of a plasma column in the form of a paraboloid of revolution [4, 6] bounded along the axis by end walls. This numerical model was found to be capable of qualitatively describing the main features of the compression of the constriction, in particular, the formation and explosion of the hot spot of an X-pinch. Although the attempts to implement this version of the model were successful, we were not satisfied in the results for the following reasons: (i) the end walls prevented the plasma outflow from the constriction along the axis, so that, in the model, the plasma spread along them, and (ii) it became possible to implement the code only when the plasma motion along the z-axis in the model was artificially suppressed. As a consequence, the longitudinal motion of the plasma became far less intense than its radial motion. In particular, in the slow compression stage, distinct cell structures were observed to appear. Of course, this version of the model also requires improvement.

This paper is devoted to modeling of the MHD compression of an X-pinch that originates from several crossed thin metal wires exploded by a high-power current pulse. We assumed that the role of the initial load is played by two wires. Clearly, the larger the number of wires, the less pronounced the three-dimensional effects; as a result, the range of applicability of the method of averaging over the azimuthal angle to the

1063-780X/02/2810-0814$22.00

constriction of an X-pinch even extends. As the wire material, we chose molybdenum, a metal often used for diagnostic purposes. We restrict our analysis to the constriction because of the autonomous character of the most important region of an X-pinch—the minidiode, which is connected electrically to the electrodes through the remaining parts of the load. First, we will describe the results of calculations based on the model in which the initial shape of the constriction is analogous to that used in [6]. Then, we will present the results obtained for a more realistic (conical) geometry of the pinch. Both of our models have a common physical basis and differ only in the initial pinch geometry and in the initial conditions. In comparison with the model of [6], the algorithms for calculating radiation transport and ionization were significantly improved.

2. MODEL OF A SPATIALLY BOUNDED PLASMA PARABOLOID

First, we carried out simulations for the same geometric pinch configuration as that used in [6], but for another wire material (Mo instead of W). We overcame the drawbacks of numerical implementation of the boundary conditions at the end walls: they were modeled as rigid surfaces impenetrable by the plasma. This allowed us to overcome the disparity in the axial and radial motions of the plasma. As in [6], we considered an initially (at $t = 0$) equilibrium and immobile plasma column in the form of a paraboloid of revolution (Fig. 1) with a length of 400 μm and with a minor cross-sectional radii of 100 μm (at the center) and 150 μm (at the end walls). The plasma density distribution corresponded to a pair of molybdenum wires 10 μm in diameter. The plasma temperature decreased with depth according to a power law from 1.5–1.7 eV at the plasma surface to 1 eV. The onset of the instability was modeled by introducing a random initial scatter in the plasma density and temperature distributions at a level of 1%. The left electrode was an anode, and the right electrode was a cathode. The current at $t = 0$ was set to be 10 kA (instead of 50 kA taken in [6]); then, it increased sinusoidally up to 300 kA over a time of 50 ns.

The basic set of equations of the axisymmetric problem consists of the continuity equation and the equations of motion in the MHD approximation, the equations for heat transport by electrons and ions, the radiation diffusion equation (with allowance for radiation transport from an optically thick plasma to an optically thin outer plasma region), the equations of ionization kinetics in the average ion charge approximation, and the equation describing the generation of a magnetic field. These equations have the following form (see [3, 4] for details):

$$d\rho/dt = -\rho\nabla\cdot\mathbf{v},$$

$$\rho d\mathbf{v}/dt = -\nabla(p + 4\Sigma_{SB}T_\gamma^4/3c) + \nabla\cdot\hat{\mathbf{\Pi}} + \mathbf{j}\times\mathbf{B}/c,$$

$$C_{Ve}n_e d_e T_e/dt + \nabla\cdot\mathbf{q}_e = -(b_e + p_e)\nabla\cdot\mathbf{v}_e + \mathbf{j}^2/\sigma + \hat{\mathbf{\Pi}}_e\colon\nabla\mathbf{v}_e - n_i(C_{Ve}T_e + \varepsilon_Z)dZ/dt - Q_\gamma + \mathbf{R}\cdot\mathbf{j}/en_e - Q_{ei},$$

$$Q_{ei} = 3n_i(T_e - T_i)/2\tau_{ei},$$

$$C_{Vi}n_i d_i T_i/dt + \nabla\cdot\mathbf{q}_i = -(b_i + p_i)\nabla\cdot\mathbf{v}_i + \hat{\mathbf{\Pi}}_i\colon\nabla\mathbf{v}_i + Q_{ei},$$

$$Q_\gamma \equiv 4\Sigma_{SB}(T_e^4 - T_\gamma^4)/l_P = -\nabla\cdot\kappa_\gamma\nabla T_\gamma,$$

$$\kappa_\gamma = 16\Sigma_{SB}l_R T_\gamma^3/3,$$

$$dZ/dt = (R_{\text{ion}} - R_{\text{rec}})Z,$$

$$\partial_t\mathbf{B} = \nabla\times[\mathbf{v}_e\times\mathbf{B} + en_e(\nabla p_e - \nabla\cdot\hat{\mathbf{\Pi}}_e + \mathbf{R})/c],$$

$$\mathbf{j} = 4\pi\nabla\times\mathbf{B}/c.$$

Here, the hydrodynamic time derivative d/dt describes plasma motion with the mass velocity $\mathbf{v}$; $d_{e,i}/dt$ are its analogues for the electron and ion plasma components; $n_{e,i}$, $\mathbf{v}_{e,i}$, and $T_{e,i}$ are the densities, velocities, and temperatures of the electrons and the ions; ρ, Z, p, $p_{e,i}$, $b_{e,i}$, and $C_{Ve,i}$ are the mass density, the mean ion charge number, the plasma pressure, the electron and ion pressures, the electron and ion compression ratios, and the isochoric electron and ion heat capacities; $\mathbf{B}$ is the azimuthal magnetic field; $\hat{\mathbf{\Pi}}$ is the total (electron and ion) viscous stress tensor; ε_Z is the ionization potential; Σ_{SB} is the Stefan–Boltzmann constant; $l_{P,R}$ are the Planck- and Rosseland-averaged photon mean free paths (the quantities referring to radiation will be marked by the subscript γ); and $R_{\text{ion, rec}}$ are the ionization and recombination kinetic rate coefficients. The heat transport by plasma particles was modeled with allowance for all of the magnetic field components, and the current transport was described by the generalized Ohm's law:

$$\mathbf{q}_{Te,i} = -(\kappa_{\perp e,i}\nabla T_{e,i} + \kappa_{\wedge e,i}\mathbf{e}_\theta\times\nabla T_{e,i}),$$

$$\mathbf{R}_T = -(\alpha_\perp\nabla T_e + \alpha_\wedge\mathbf{e}_\theta\times\nabla T_e),$$

$$\mathbf{q}_{\mathbf{u}e} = [(-C_{pe}/e + \alpha_\wedge)\mathbf{j} + \alpha_\wedge\mathbf{e}_\theta\times\mathbf{j}]T_e,$$

$$\mathbf{R}_\mathbf{u} = n_e\mathbf{j}/\sigma,$$

$$\mathbf{E} + \mathbf{v}\times\mathbf{B}/c = \mathbf{j}/\sigma - (\nabla p_e - \mathbf{j}\times\mathbf{B}/c - \nabla\cdot\hat{\mathbf{\Pi}}_e + \mathbf{R})/en_e,$$

where the subscripts T and $\mathbf{u}$ indicate the thermal and current components of the heat fluxes, $\mathbf{q}_e = \mathbf{q}_{\mathbf{u}e} + \mathbf{q}_{Te}$ and $\mathbf{q}_i = \mathbf{q}_{Ti}$, and of the frictional force acting on the electrons, $\mathbf{R} = \mathbf{R}_T + \mathbf{R}_\mathbf{u}$, and the subscripts $\perp$ and $\wedge$ stand

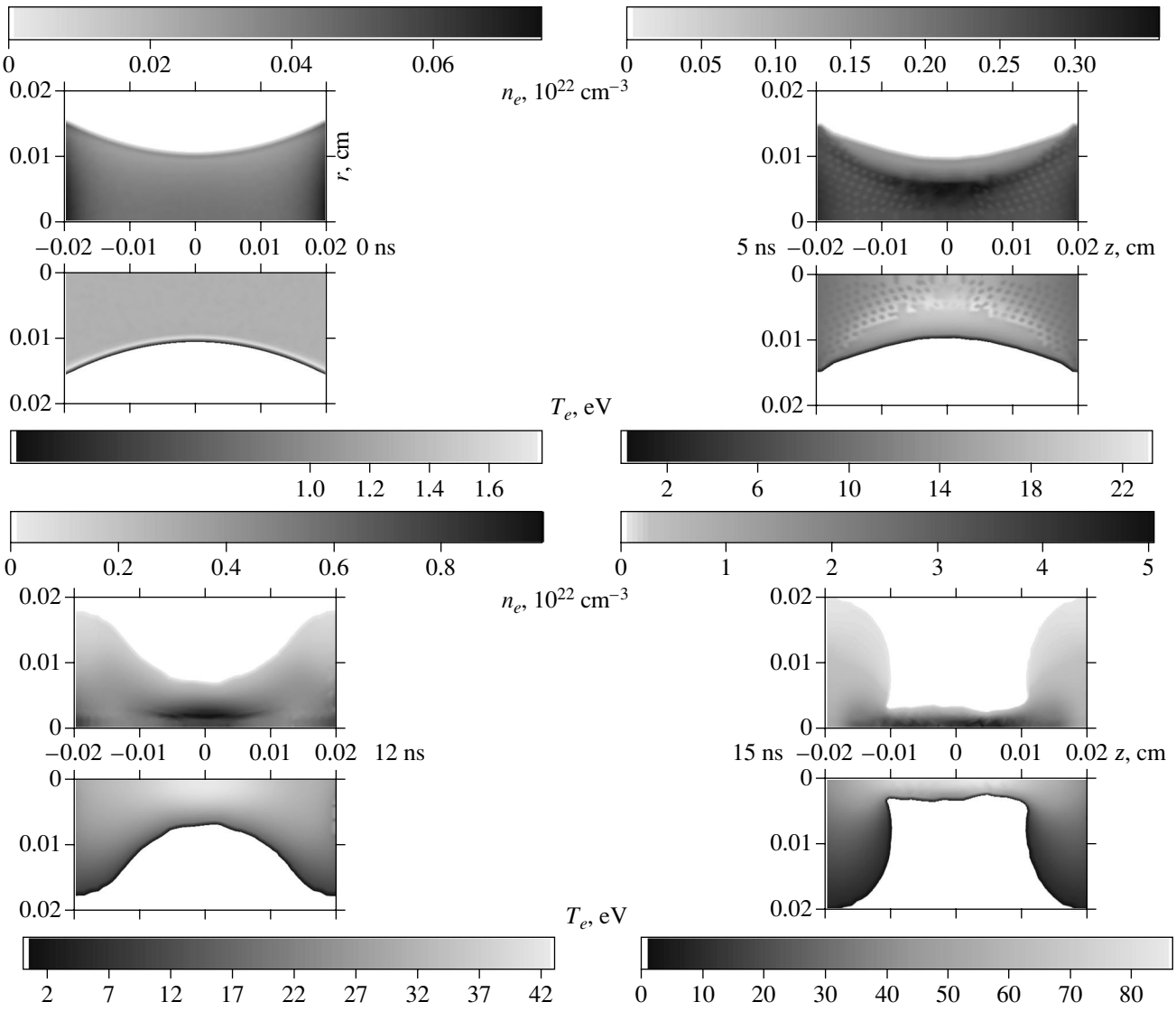

Fig. 1. Evolution of the constriction that forms in an X-pinch during the electric explosion of two molybdenum wires 10 μm in diameter, calculated on the basis of the model of a paraboloidal plasma column. Shown in each of the images are the scales of the variation and the distribution patterns of the electron density (top) and electron temperature (bottom). The last image (referring to the time 15.78 ns) also shows the electron temperature distributions in the regions of the exploding new hot spot (left) and of the cavity that appears in place of the old hot spot after its explosion (right). The structures of light spots that are seen near the cavity boundaries and are stretched across the axis are shock waves propagating away from the place of the explosion of the old hot spot.

for the perpendicular and skew-symmetric components of the coefficients of the thermal conductivity tensor and of the tensor describing the thermoelectric effect. In calculations, the satisfaction of the last three relationships was thoroughly controlled. To do this, we excluded from consideration the region near the plasma–vacuum interface where the plasma is relatively tenuous and the electron current velocity **u** approaches the speed of sound. In this way, however, we could not avoid difficulties in the final computation stage (after the breaking of the plasma column). The particle and radiative heat fluxes were limited to their maximum intensities under free transport conditions. In contrast to the previous versions of the code [2–4], in which the artificial viscosity was incorporated into the ion pressure through the term with the second viscosity, here we included the artificial viscosity into the total viscous stress tensor $\hat{\mathbf{\Pi}}$ as the first viscosity. As in the previous version, the artificial viscosity was involved only in simulations of the compression stage and was described by three pairs of von Neumann-type coefficients, which served to take into account the influence of the magnetic field on the plasma electrons and ions

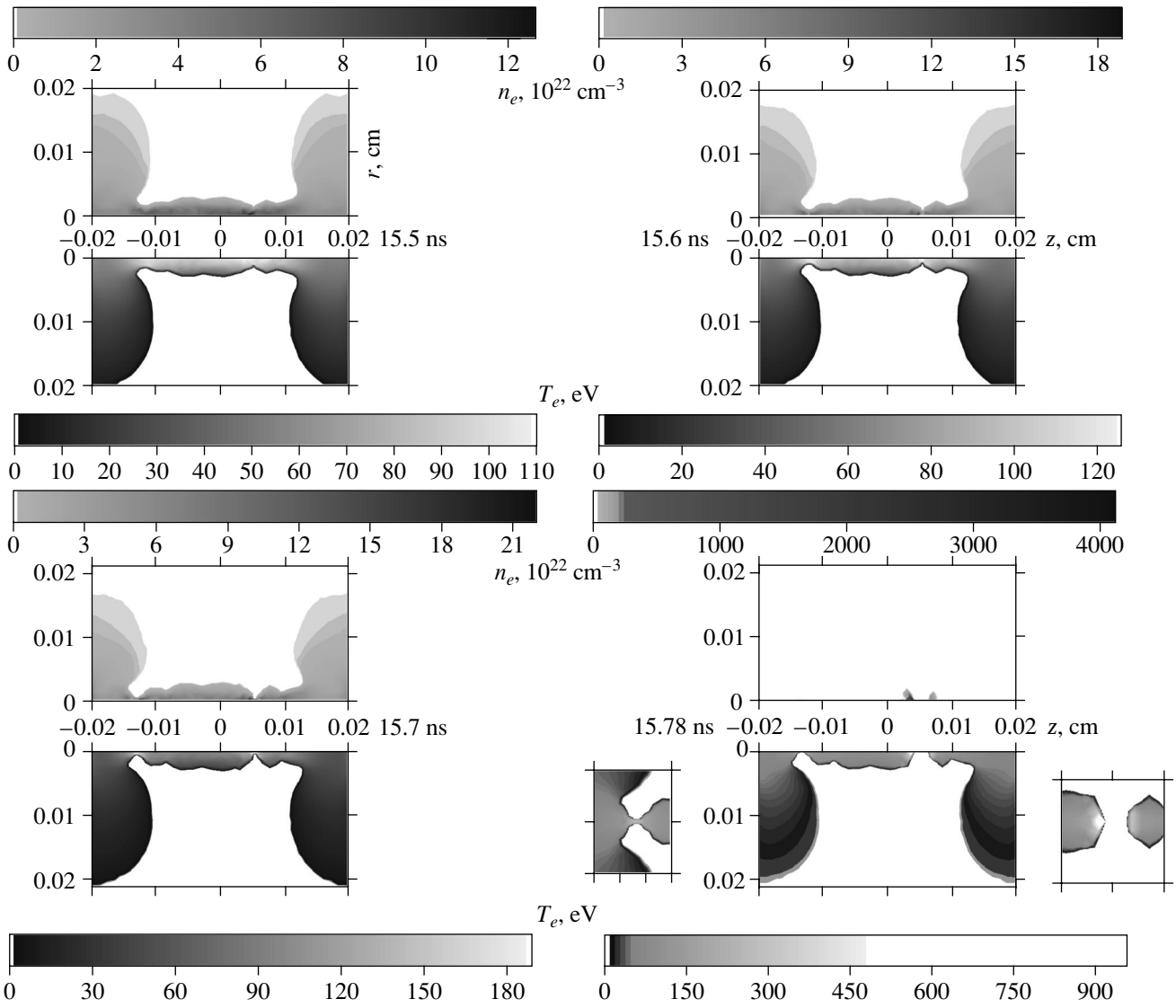

Fig. 1. (Contd.)

and were chosen to be proportional to the corresponding contributions to the physical viscosity.

The equation of state, which was the same as that used in [3, 4, 6], described the effects related to the nonideal character of the ion component and the quantum degeneration of electrons; as in [4, 6], we took into account the radiation pressure. The transport coefficients; the anomalous resistance associated with ion-acoustic, modified Buneman, and lower hybrid turbulence; the electron impact ionization rate; the three-body recombination rate; and the radiative recombination rate were represented in the same form as in [4, 6]. In contrast to [4, 6], the power approximations for the averaged Planck and Rosseland mean free paths of photons were taken from [7]. The dependence of the ionization energy on the ion charge number Z was corrected for the decrease in the ionization threshold and the disappearance of higher excited levels under the action of the microfields of the neighboring ions [8]. The conditions at the plasma surface were taken to be the same as in the previous versions of the code. The symmetric conditions at the end walls ensured that the plasma did not move through them. The calculations were carried on a grid other than that used in [6]: the mesh points at $t = 0$ were chosen to be the intersections of two mutually orthogonal families of parabolas. Usually, we used a grid with 22×60 or 33×90 mesh points.

The experience gained in test simulations showed that to describe the compression process in our model required an additional modulation of the axial mass profile. Specifically, the law according to which the mass per unit length varied along the axis at $t = 0$ was

specified to be $M(z) = \pi\rho_{max}a^2(z)/F(z)$, where $a(z)$ is the local radius of the paraboloid, d is its half-height, and $F(z) = 1 + (z/d)^2[1 - 3(z/d)^2]/8$. This law was obtained by integrating the plasma density distribution $\rho = \rho_{max}\{1 - f[r/a(z)]^2\}/[(1 - f/2)F(z)]$ over the cross section of the plasma column; the factor f used in simulations was taken to be 0.7. Such an approach facilitated the implementation of a simplified model of the ejection of a part of the plasma from the constriction along the axis in an actual X-pinch, specifically, the simulation of plasma flows toward the end walls.

An example of the results obtained from simulations is illustrated in Fig. 1. In accordance with [6], we first observe the slow stage of the evolution of the constriction, whose anode and cathode sides remain almost precisely symmetric. In the dense plasma of the constriction, the shock wave is weak. After 5 ns, we see only an electron heat wave that penetrates from the plasma surface and behind which the plasma is expanding. The current-carrying plasma shell converges to the axis at 12 ns. Then, the plasma temperature and density are fairly rapidly redistributed along the axis, and the plasma spreads over the end walls, thereby contributing to the implosion of the constriction. As a result, by 15 ns, we observe the formation of a fairly symmetric minidiode with a narrow neck along the axis. The electron temperature T_e increases to about 100 eV, and the electron density n_e amounts to 5×10^{22} cm^{-3}. During the evolution, the compression process proceeds on increasingly short time scales and finally occurs on subnanosecond time scales. Later, the previously important plasma flow over the end walls does not have enough time to affect the constriction; hence, the evolution proceeds only inside the constriction by the formation of several necks in a time as short as 500 ps. After 100 ps, the implosion proceeds only in the vicinities of the two narrowest plasma cross sections (necks) in the anode and cathode halves of the minidiode; 100 ps later, the anode neck becomes narrower than the cathode neck. This is the beginning of a new evolutionary stage, which occurs on an extremely short time scale (of about 10 ps). An interesting feature of this example is the formation of two hot spots, which can appear not in every simulation. The first hot spot forms at about 15.7 ns and then evolves in an explosive manner (in a way described in [6]), giving rise to a cavity in its place. The shock fronts that form in a dense plasma around the cavity propagate in both directions along the axis. Soon after the appearance of the first hot spot, a new (second) hot spot forms closer to the anode and evolves in an analogous fashion. In Fig. 1, the inset to the image referring to the time 15.78 ns shows an enlarged fragment of the two hot spots at two times magnification. The plasma compression is the strongest at a short distance to the left from the discontinuity that appears in place of the first hot spot after its explosion. As the shock wave interacts with the plasma, the point at which the electron temperature T_e is maximum is gradually displaced from the axis and the temperature itself increases to about 1 keV, in which case the electron density n_e amounts to 4×10^{25} cm^{-3} and the mean ion charge number becomes as large as 25 or even larger.

In the energy balance of the constriction, the radiation in the slow stage (with a duration of about 10 ns) plays a very minor role in comparison with Ohmic dissipation. However, the situations changes as the compression increasingly becomes faster. By the time at which the constriction is broken, the emitted radiation power is comparable with the Joule heating power. Thus, by the time at which the minimum neck radius is 2 μm, the power density of the emitted radiation in the hottest plasma region and the absorbed power density amount, respectively, to about 10% and 60% of the Joule heating power density. After 50 ps, the minimum neck radius decreases by a factor of 10, the absolute value of the Joule losses increases by a factor of 150, but the relative power densities of the emission and absorption of radiation are nearly the same and are close to 50%. Soon after, the plasma becomes more transparent, and the emission power approaches the ohmic loss power. In this final compression stage, the total power of the radiation emitted from the constriction increases abruptly to a level of 25 GW (in the slow compression stage, this power is slightly lower than 10 MW). This allows us to estimate the radiation energy yield as not larger than several joules. Interestingly, the main contribution to the energy yield comes from a microexplosion with a duration of about 100 ps near the place where the constriction is broken, while the contribution of radiation emitted during the remaining evolutionary stage (with a duration of about 10 ns) is as small as ≈0.1 J.

Let us compare this evolutionary pattern with that obtained in [6]. First, we note that, in both studies, the currents during X-ray bursts from the hot spots were calculated to be nearly the same (about 140–145 kA). As in [6], our simulations revealed a very precise symmetry between the anode and cathode sides of the constriction in the slow compression stage (with a duration up to 12 ns), but the compression was found to be stronger because of the intense axial plasma motion, which was maintained by the fictitious plasma flow over the end walls. However, in the fast compression stage (with a duration of about 12–15 ns), this symmetry is violated by virtue of the predominance of small-scale perturbation modes; as result, the hot spots form in asymmetric positions. Such a behavior of the hot spots indicates an important role of the axial plasma motion in the competition between the necks with small radii during the compression to a state in which their transverse sizes are comparable with the longitudinal sizes.

As was already pointed out, a significant drawback of the model of a paraboloidal plasma column bounded on both sides by the end walls is that it is incapable of describing the actual axial plasma outflow from a constriction. This drawback manifested itself in our

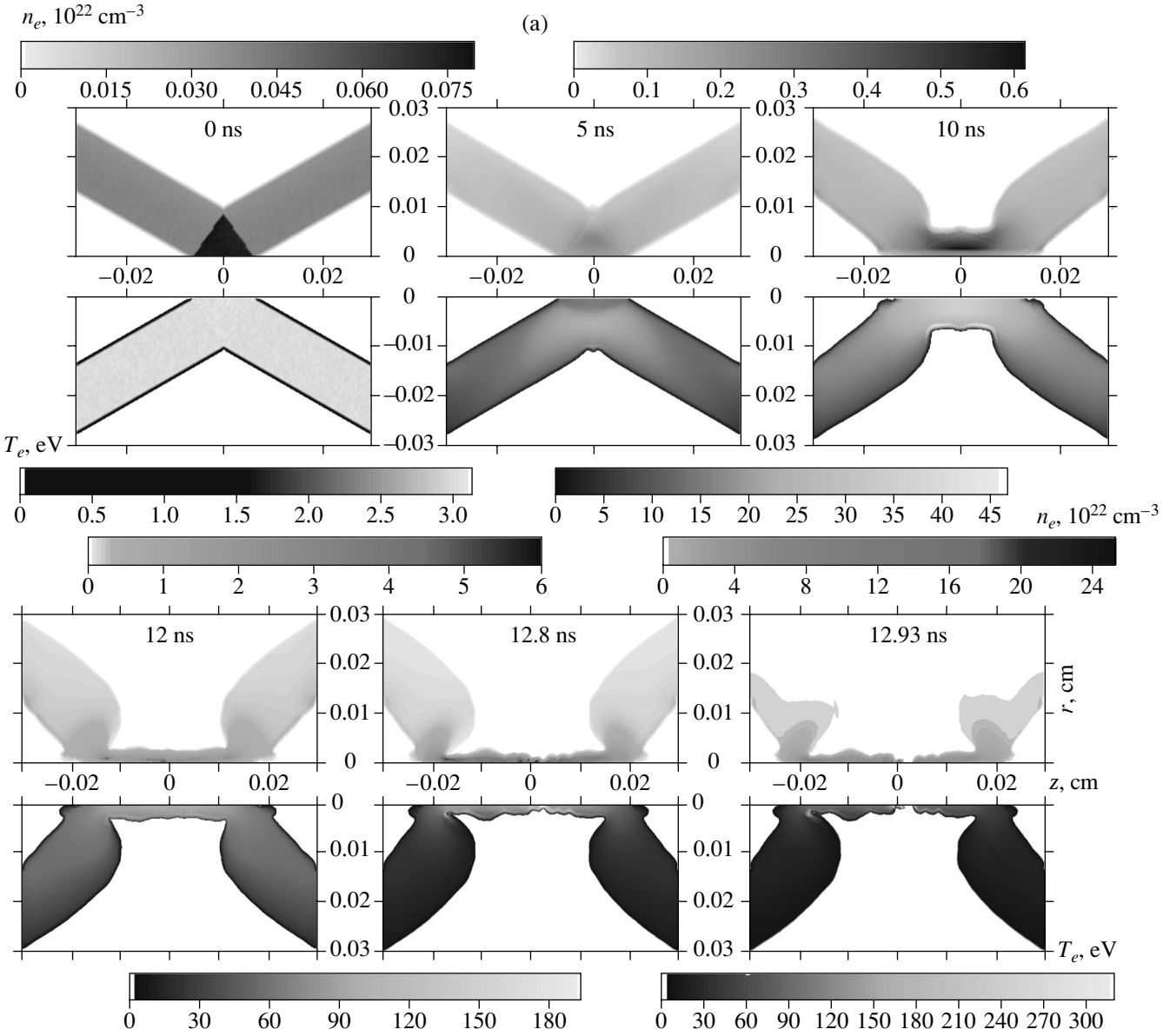

Fig. 2. Evolution of the constriction that forms in an X-pinch during the explosion of two molybdenum wires 12 μm in diameter, calculated on the basis of the model of a conical X-pinch: (a) general evolutionary pattern (the images are given in the same order as in Fig. 1) and (b) detailed evolutionary patterns of the temperature (six images at the top) and density (two images at the bottom) distributions.

attempts to simulate the explosion of wires with diameters greater than 12 μm, in which case the model plasma flow over the end walls can no longer be used to imitate intense axial plasma outflow from the constriction. In that series of simulations, we observed no compression of the X-pinch: although the initial stage of the pinch evolution was similar to the slow implosion stage, the pinch eventually began to expand, resembling the situation with a plasma cylinder (of course, corrected for the short pinch length). These results necessitate the development of a model that will provide a more realistic description of the plasma outflows from the constriction, the more so since X-pinches used for diagnostic purposes are produced by exploding wires 12–25 μm in diameter.

3. MODEL OF A CONICAL SHELL

The important role of plasma outflows from constrictions was pointed out as early as 1982, in the first paper on X-pinches [9]. In order to describe this phenomenon, we chose the model of a conical shell. Phys-

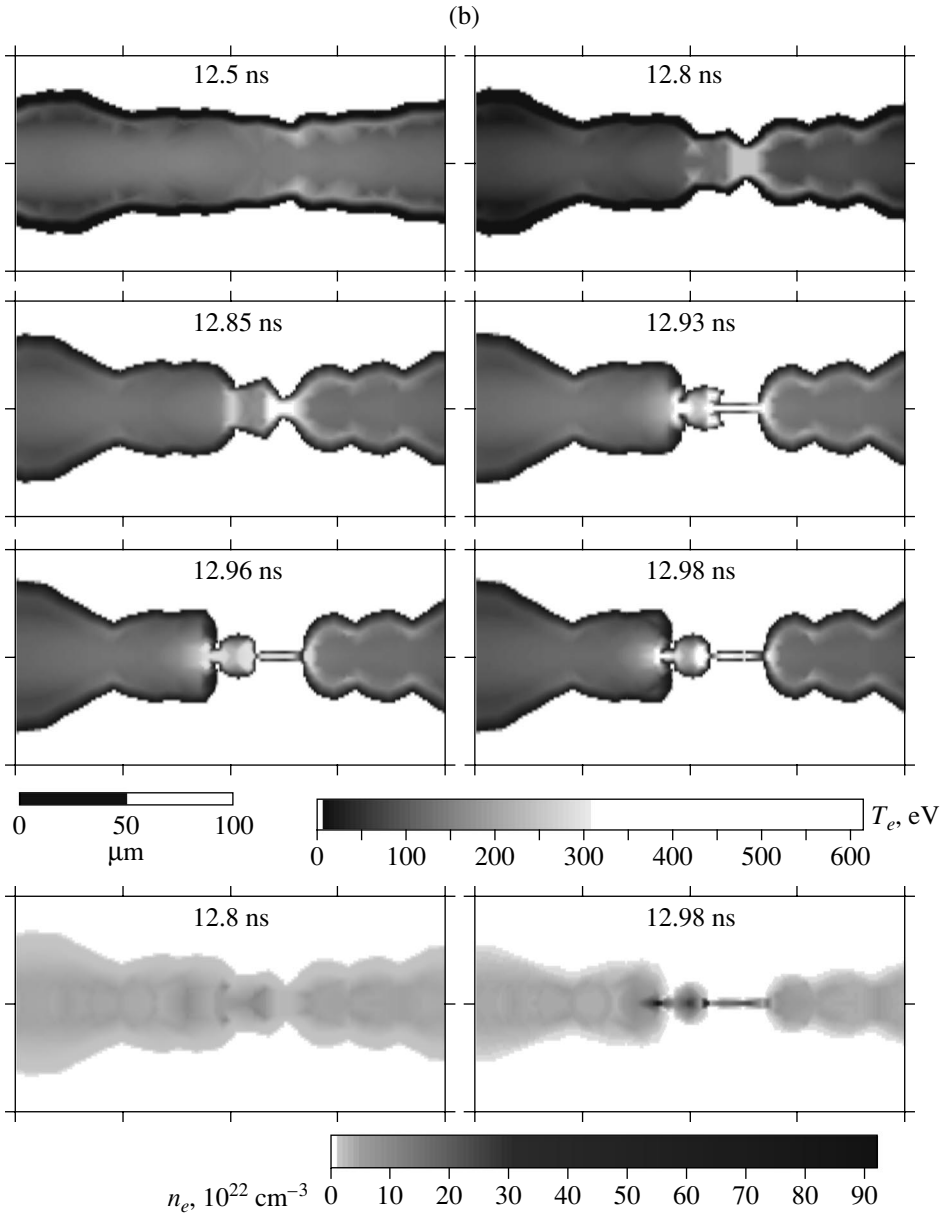

Fig. 2. (Contd.)

ically, this model is identical to that of a paraboloidal plasma column. In a geometric sense, the difference lies in the shape of the region around the constriction (Fig. 2): the load, i.e., a pair of two exploding crossed wires 12 μm in diameter, was modeled by two conical shells, which were oriented in opposite directions and whose apexes were shifted along the axis. The angles of the cones at the vertices are both $\pi/3$, the radius of the narrowest cross section is 100 μm, and the shell thickness is about 130 μm. The mesh points of the initial grid are spaced uniformly along the lines parallel to the boundaries of the cones. The concentration of the mesh points in the most interesting region of the intersection of the cones is two times higher than that at the periphery. Typically, the grid consists of 21 × 165 mesh points. The current is the same function of time as before.

The solution to the problem is illustrated in Fig. 2. We can see that, by 5 ns, the shell surface is substantially perturbed only in the vicinity of the narrowest cross section. However, by this time, the plasma in the main volume of the intersection region is already heated to temperatures of 15–20 eV by electron heat conduction. By 8 ns, the front of the heat wave reaches the surface of the inner cone and expands the plasma in this surface region. This is quite clearly seen in the

image referring to 10 ns, by which time the entire intersection region is already heated and the characteristic structure of a minidiode begins to form as a result of the compression process. By 12 ns, the minidiode becomes more distinct. During the time interval from 10 to 12 ns, the developing constriction stretches along the axis and undergoes deformation; the "electrodes" of the minidiode also undergo deformation and small-scale cumulative jets are generated outside the minidiode. The redistribution of matter occurs (this effect cannot be described in the previous model with end walls): the axial plasma regions of the electrodes of the minidiode move along the axis in opposite directions. As the constriction stretches along the axis, its specific parameters approach those in the previous case. When small-scale fast processes come into play, the anode/cathode symmetry, which is fairly high at $t < 12$ ns, is violated. This effect is analogous to the previous one, but it begins to occur earlier even though the load mass is larger. The reason for this is again the axial plasma motion. The remaining details of the subnanosecond stage are analogous to those obtained in the previous case. The difference between the two cases lies in the burst of one (rather than two) hot spots. However, a more detailed examination of the enlarged fragments of the images in Fig. 2 shows that there also are two hot spots, which are located very close to one another. In the same fragments, we can also see the evolution of these spots, i.e., plasma formations that originated at different times. Near the anode side of the discontinuity, the electron temperature and density become as high as $T_e \approx 490$ eV and $n_e \approx 10^{24}$ cm^{-3}.

Let us consider two more examples, which are not as exotic as that just described. In these examples, the current rises linearly to 250 kA in 40 ns and, then, remains constant.[1] As before, the initial current is taken to be 10 kA. The initial numerical grid is simpler than that in the previous example: the number of mesh points is typically equal to 18×105 (for a pair of wires 10 μm in diameter) and 11×151 (for a pair of wires 16 μm in diameter). The radius of the narrowest cross section also differs from that in the previous case: it is chosen to be 75 μm. The regions in which the pinch evolution was simulated are 1.2 and 1.5 mm in length. The first example of a load in the form of a pair of 10-μm-diameter wires is illustrated in Fig. 3. This example not only demonstrates why the model of a conical X-pinch is more realistic but also shows how the slower current rise delays the explosion of a hot spot. Note, however, that this delay includes the time of the adaptation of numerical results to physical conditions.[2] At 23 ns, the process of jet generation is less pronounced than in the case of 12-μm-diameter wires; the same is true of the perturbations and of the axial displacements of the inner layers of the shell, although these perturbations and displacements are, as before, significant. After a time interval of 0.5 ns, the constriction undergoes small-scale perturbations: the neck that arises at its left edge evolves further into a hot spot on a picosecond time scale. In Fig. 3, the last image (which refers to 23.7 ns) shows the remains of the hot spot after explosion. The highest electron temperature and density obtained in this example ($T_e \approx 370$ eV, $n_e \approx 2 \times 10^{24}$ cm^{-3}) are comparable to those calculated on the basis of the model of a paraboloidal plasma column.

Finally, another example of the explosion of a pair of crossed wires 16 μm in diameter is illustrated in Fig. 4. Since the mass of the wires is larger than that in the previous example by a factor of 2.5, the region in which the pinch evolution was simulated was taken to be longer. The wire material begins to be compressed only after a long-term heating (during a time interval of 20 ns), but the jets begin to be generated and the heated plasma starts to expand in opposite directions along the axis even before the compression. In the next, fairly long, stage (with a duration of up to 39 ns), the wire mass is redistributed in a complicated manner. Only after this stage, the constriction is compressed to the greatest extent. Then, the neck that arises approximately in middle of the constriction evolves into a hot spot. We were succeeded in following the evolution of the hot spot after microexplosion over a fairly long time interval. Although the mass of the load is large, we obtained fairly high electron temperature and density, $T_e \approx 250$ eV and $n_e \approx 1.5 \times 10^{24}$ cm^{-3}. This example served to investigate the role of radiation in the dynamics of an X-pinch. In computations in which the radiation was artificially "switched off" (either from the beginning of the explosion process or shortly before the time at which the neck is broken), the electron temperature and density in the corresponding compression stages were calculated to be lower by a factor of two to three. In this series of computations, we failed to follows the pinch evolution on time scales longer than about 10 ps.

The simulations presented here revealed a wide variety of different possible ways in which the constrictions can form under the action of random factors. However, our model is capable of describing a far wider range of possible scenarios for the evolution of X-pinches.

4. DISCUSSION

Now, we can draw several conclusions about the implosion of plasma loads of the X-pinch type. All of the above examples (and especially a comparative analysis of the results obtained from different models for 10-μm-diameter wires) show that the axial plasma motion is of primary importance in the pinch evolution. Moreover, the larger the mass of the load, the more

[1] The current pulses so shaped correspond to those in experiments on the XP device (Cornell University, Ithaca, N.Y., USA) loaded by a pair of parallel X-pinches.

[2] In the example at hand, this time is about 10 ns, and it is about 20 ns in the example with 16-mm-diameter wires.

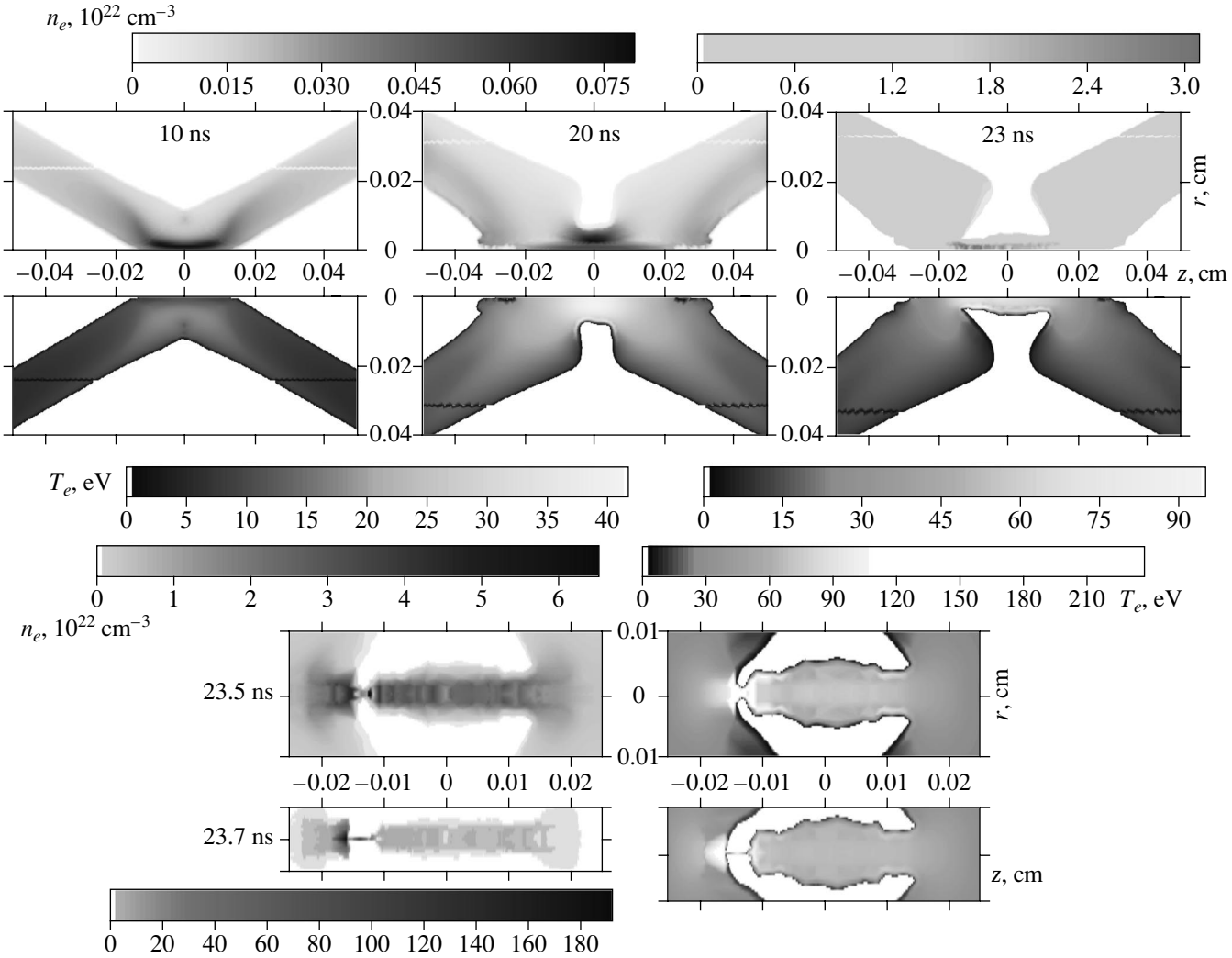

Fig. 3. Same as in Fig. 2, but for wires 10 μm in diameter. The three large-scale images at the top are analogous to those in Figs. 1 and 2a. Shown at the bottom are more detailed distributions of the density (left) and temperature (right) before and after the explosion of a hot spot.

important the role of the axial plasma motion. The examples also illustrate how the current rise time affects the compression dynamics. A special series of test simulations based on the model of a paraboloidal plasma column was carried out for a current rising linearly to 250 kA in 40, 45, and 50 ns. In simulating the explosions of 10-μm-diameter wires, we found that X-ray bursts from hot spots began at 18.2, 20,4, and 21.4 ns, respectively; the currents at these times were calculated to be very close to each other, namely, 114, 113, and 107 kA. In all examples, the resulting plasma parameters of the hot spots (the electron temperature, electron density, and mean ion charges) were close to the experimentally measured values.

We note, however, that the calculated maximum values of these parameters are at the limits of applicability of the numerical method. The D'yachenko free-point method is peculiar in that it eliminates both the mesh points that become too close to each other and the configurations of mesh points that lead to numerical instabilities. When the radial compression becomes so strong that there remains only one mesh point in the narrowest cross section, this peculiarity serves as a serious obstacle to the calculation of the extreme plasma parameters. In this situation, as well as in the situations in which the nonconservative character of the numerical scheme became too pronounced, we had to stop computations when numerical fluctuations became too large because of the small number of mesh points in the region of the strongest compression. In simulations with an inappropriately adjusted code, the calculated parameter values of the compressed plasma are deter-

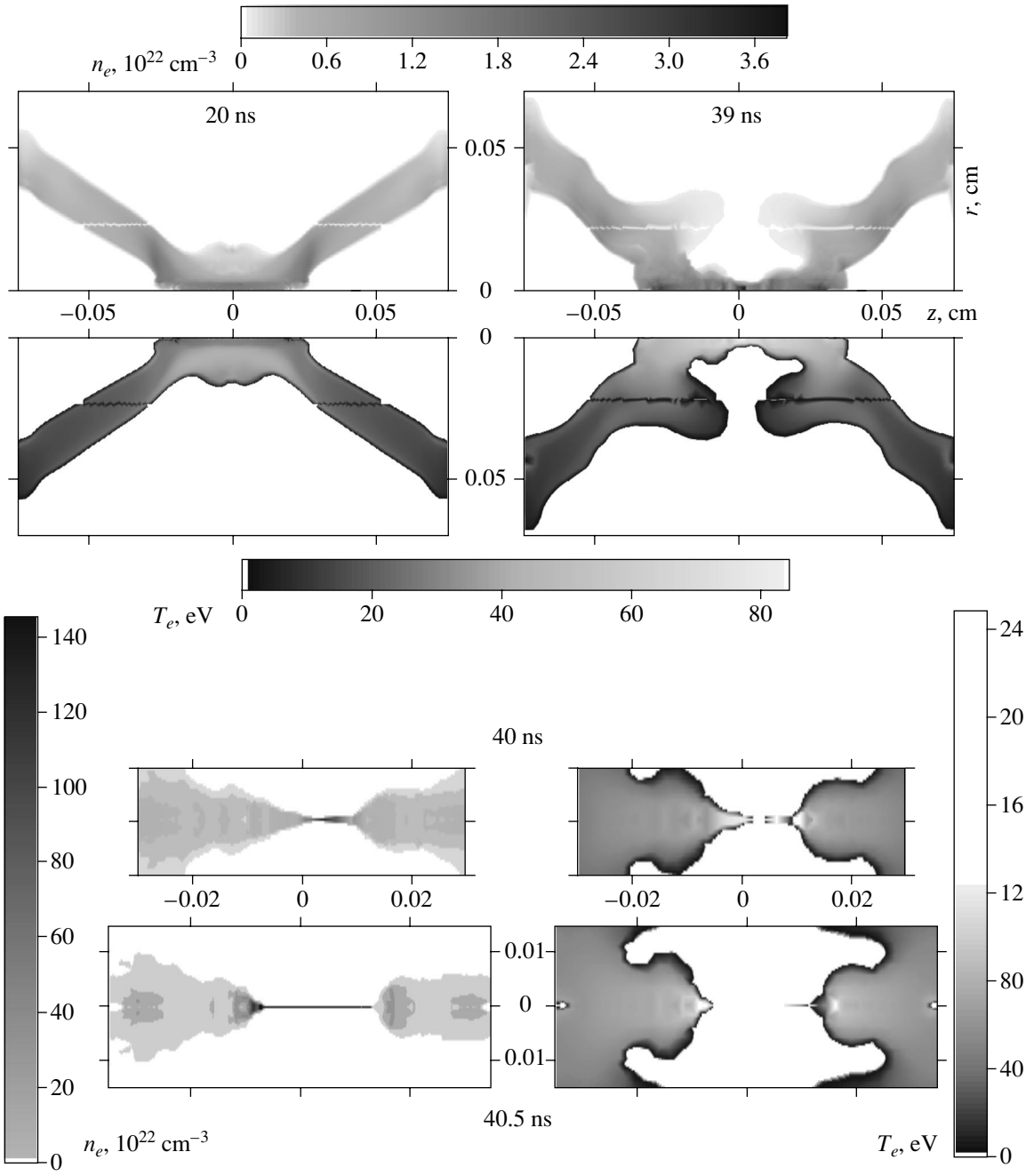

Fig. 4. Results calculated for wires 16 μm in diameter. The four images shown at the top illustrate the final evolutionary stage. Shown at the bottom are enlarged images of the density (left) and temperature (right) distributions around the cavity that appears in place of the hot spot after its explosion.

mined precisely by these numerical (rather than physical) reasons. In order to choose the minimum possible distance between two neighbouring mesh points, which governs the computational speed and, among other things, is responsible for the elimination of the corresponding mesh points, it is necessary to carry out more accurate computations on an increasingly fine grids until the satisfactory results are achieved.

On the whole, our simulations demonstrated some general features of the compression dynamics of X-pinches. As in the simulations based on the model of [6], we observed that, as the current is increased, the space and time scales of the implosion process decrease monotonically from hundreds of microns and tens of nanoseconds (in the initial stage) to fractions of a micron and tens of picoseconds (in the final stage).

Plasma heating in the initial stage can be analyzed on the basis of the same arguments that were presented in [6]. The plasma is heated predominantly by electron heat conduction, while the shock wave generated in a dense medium in the final stage is fairly weak and thus cannot seriously influence the heating. Consequently, the constriction is completely heated for a time of about $\tau = a^2/2\pi\chi_e \approx 10$ ns (where $a \approx 100$ μm is the constriction radius and $\chi_e \approx v_{Te}^2/\nu_{ei} \sim T_e^{5/2}/n_e$ is the electron thermal diffusivity), which agrees well with the hydrodynamic time a_s/c_s (where $c_s = (ZT_e/m_i)^{1/2} \approx 7 \times 10^5$ cm/s is the speed of sound). Note that, in terms of the magnetic viscosity $\chi_m = c^2/4\pi\sigma \sim ZT_e^{-3/2}$, which amounts to about $\approx 5 \times 10^4$ cm^2/s, the time of the diffusive penetration of the current and magnetic field into the plasma has essentially the same form: $\tau_m = a^2/2\pi\chi_m$. Under the conditions adopted in our simulations, the time τ_m is as short as fractions of a nanosecond, which is much shorter than the time τ. This allows us to conclude that the magnetic field diffusion is closely associated with small-scale perturbations in a slowly compressed plasma.

In the slow compression stage, large-scale plasma motion is highly symmetric, whereas small-scale modes do not possess this symmetry. The larger the mass of the load, the more important is the role of the axial plasma motion. The constriction as a whole lengthens, and cumulative jets of matter emerge from the minidiode. The lengthening of the constriction, which occurs at the speed of sound, is an extremely important process for the implosion of a load with a large mass (recall that this process cannot be described by the model of a paraboloidal plasma column). The duration of this process is determined by the time scale on which the compression conditions become favorable for the onset of small-scale unstable plasma modes inside the minidiode. The subsequent complicated evolution of competing processes gives rise to one or two very thin constrictions inside which hot spots are then formed (it is possible that, later, a larger number of constrictions may arise). Each of the hot spots will eventually explode to generate the fronts of a hot dense plasma that propagate in opposite directions along the axis. The plasma between the propagating fronts is fairly tenuous.

The physical mechanism for the explosions of hot spots that were observed in recent experiments with X-pinches [2, 6] is still unclear. According to our simulations, the microexplosion mechanism may be associated with the character of both heat exchange and plasma motion during the convergence of a shock wave toward the axis of a narrow neck in the constriction. The neck radius a satisfies the condition $a < \chi_e/c_s \approx c_s\tau_{ei}$ (where τ_{ei} is the electron–ion energy-exchange time); this indicates that the time scale on which the electron temperature is equalized over the neck is shorter than that of the plasma motion. The entire neck is inside the relaxation zone for the electron and ion temperatures, which thus differ strongly from one another. Then, the electron heat conduction gives rise to nonlinear heat waves propagating from the narrowest cross section in opposite directions along the axis. As the neck further implodes at an increasingly high rate, the pressure in it grows abruptly to a level of about 10 Gbar. As a result, new, highly uniform (over the cross section) shock waves are generated behind the heat fronts. As time elapses, the shock waves leave the neck and occur in the region where the above condition on the neck radius fails to hold. In outward appearance, shock wave's overtaking of heat fronts looks like an explosion.

Let us discuss this point in more detail. Using the relationship $T_e \sim Z^2$, we can determine the critical parameter value corresponding to the condition $a = c_s\tau_{ei}$, specifically, $(n_i a)_{cr} \approx 10^{16}\ (AZ^5)^{1/2}$ cm^{-2}, where A is the atomic mass number. For the values $a = 1$ μm and $Z = 25$, which are typical of the conditions adopted in our simulations, we obtain $n_i \approx 10^{24}$ cm^{-3}. The plasma lifetime in this nonequilibrium state does not exceed the time τ_{ei}, which is as short as tens of picoseconds. During this time, the electron temperature T_e remains significantly higher than the ion temperature T_i. In actuality, such a plasma will intensively emit bremsstrahlung photons. Among the electron–ion relaxation processes that occur during the time τ_{ei}, the ion excitation occurs; hence, the emission lines will appear in the continuum only at the time τ_{ei} after the beginning of emission. In this stage, the line mass of the plasma in a narrow neck gradually decreases and it also continues to decreases after the explosion of a hot spot. The mass ejection intensifies substantially when the microexplosion generates shock waves in the surrounding plasma. As a result, the MHD description and Ohm's law will inevitably fail to hold (see below). In this case, a cavity-like region of a comparatively tenuous plasma (with a density of 10^{17} cm^{-3} and lower) is form, whose resistivity can become anomalous and in which particle beams can be generated. As the beams are decelerated in a dense plasma surrounding the discontinuity, they emit line radiation. Although our model is incapable of describing such a complicated pinch evolution, it is clear that all these processes lead to the generation of an X-ray pulse from the neck region during the breaking of the neck. However, in the region of dense plasma around the discontinuity, one more source producing a hot plasma arises, namely, that associated with the implosion shock wave, which still does not reach the axis and is inclined to it because of the deformation of the shape of the neck. In the interaction of this wave with microexplosion-driven shock waves, the intersecting shock fronts form a region of hot and dense plasma at some distance from the axis. The sizes of this region are larger than the thicknesses of the fronts and are comparable with or even larger than the Planck mean free paths of photons, so that the spectra of the photons

emitted from these region can be expected to be nearly equilibrium. The pulse from this second radiation source dominates the radiation spectrum after the radiative collapse.

The question now arises as to the degree of confidence with which our model of the implosion of an X-pinch reflects the evolutionary pattern of the processes observed in actual experiments. A comparison of our results with the photographs and measurement data presented in [2, 6] shows that our model provides not only a good qualitative but also a fairly good quantitative description of the entire process. However, the finest effects in the dynamics of the explosion of a hot spot clearly require a more thorough analysis. We have already discussed the calculated extreme parameters of matter. Now, we examine how our model describes an expanding cavity. We can see that, in the cavity, there is a thin (fractions of a micron) filament of dense plasma between the anode and cathode sides of the discontinuity. Of course, the presence of this current filament indicates that the model fails to correctly describe current transport in the cavity. The fact that the filament is straight indicates that the approximation of the model becomes very rough because of the low plasma density: in order to continue computations, we had to keep the last remaining mesh point even when it occurred at the shortest possible distance from the axis.[3] This way permitted us to artificially maintain the current through the cavity in the course of a run. Recall that, in real situations, this current can be maintained by electron and ion beams, whose description, however, is beyond the applicability range of our model.

The above analysis necessitate the improvement and refinement of both the model and the algorithm. The easiest way to provide a better approximation is to substantially increase the number of mesh points, which, however, leads to an extreme expenditure of computer time. The available computational means do not allow us to choose this way and require the development of a new numerical algorithm. The model itself, which yields an adequate picture of the pinch evolution up to the explosion of a hot spot, should be improved to provide a more realistic description of the subsequent evolution. Being applicable to a dense bulk plasma, the model fails to describe the cavity. Because of the short spatial and temporal scales of the cavity and the small plasma mass in it, it is of negligible importance for the implosion process. Since the processes occurring in the cavity are yet unknown, we had to prevent the current break in it artificially, thereby distorting the actual situation. However, this approach is supported by the fact that the evolutionary patterns obtained in our model simulations do not contradict the existing experimental photographs [2, 6].

[3] To some extent, this concerns a numerical description of the jets emerging from the plasma minidiode. As a result, the patterns of the jets in our calculations turn out to be less pronounced than the experimentally observed patterns.

5. CONCLUSION

The results from simulations based on the radiative MHD model developed in this paper for X-pinches are in good qualitative agreement with experimental data (see, e.g., [2]). This agreement is supported by the fact that the calculated images of the compression process bear a superficial resemblance to the published photographs taken with present-day laser and X-ray diagnostic systems and also by a comparison between the calculated parameters of hot spots and the experimental findings. We thus can conclude that the model of conical X-pinches has been developed to the extent that it is necessary to carry out a detailed comparison between the numerical and experimental results, so that its further development is supposed to proceed in this way (first, it might be expedient to lower the initial temperature of the matter). On the other hand, our numerical results show that it is necessary to refine the model so as to provide a more realistic description of the evolving cavity after the explosion of a hot spot. In turn, the microexplosion itself, which is observed to occur in our numerical experiments after a complicated evolution of the competing dissipative processes, needs to be investigated in more detail. Out simulations provide evidence that such a microexplosion, which complicates the radiative collapse, may actually take place. At the present stage of investigations, simulations of the evolutionary processes occurring after the microexplosion are aimed exclusively at attempting to gain insight into the situation that is as yet unclear.

We think that the scope of problems arising in experiments with X-pinches is far wider than that associated exclusively with exploding wires. Thus, the model developed here for X-pinches may also be used to simulate the propagation of high-intensity shock waves in hot and dense media. Knowledge of the dynamics of such shock waves, which are generated by the explosion of a hot spot in an X-pinch, is not only important for practical applications but also is crucial to the development of an understanding of, e.g., the dynamic processes occurring in stars. Investigation of these waves under laboratory conditions requires complicated (and often unique) measurement equipment with high temporal resolution (in the picosecond range). Hence, it may be worthwhile to continue to simulate evolutionary processes occurring in an X-pinch after the explosion of a hot spot.

ACKNOWLEDGMENTS

We are grateful to Prof. D.A. Hammer for useful discussions and for providing us with the opportunity to use the computational resources of the Cornell University in Ithaca (N.Y., USA). This study was supported in part by the NATO Scientific Affairs Division (grant no. PST.CLG.976535).

REFERENCES

1. D. H. Kalantar and D. A. Hammer, Phys. Rev. Lett. **71**, 3806 (1993); S. A. Pikuz, T. A. Shelkovenko, V. M. Romanova, *et al.*, Rev. Sci. Instrum. **68**, 740 (1997).
2. G. V. Ivanenkov, S. A. Pikuz, T. A. Shelkovenko, *et al.*, Zh. Éksp. Teor. Fiz. **118**, 539 (2000) [JETP **91**, 469 (2000)].
3. G. V. Ivanenkov and W. Stepniewski, Fiz. Plazmy **26**, 24 (2000) [Plasma Phys. Rep. **26**, 21 (2000)].
4. G. V. Ivanenkov and W. Stepniewski, J. Mosc. Phys. Soc. **9**, 337 (1999).
5. K. Jach, *Komputerowe modelowanie dynamicznych odzialywan cial metoda punktow swobodnych* (PWN, Warsaw, 2001).
6. G. V. Ivanenkov, S. A. Pikuz, D. B. Sinars, *et al.*, Fiz. Plazmy **26**, 927 (2000) [Plasma Phys. Rep. **26**, 868 (2000)].
7. E. Minguez, R. Munoz, R. Ruiz, and Y. Yague, Laser Part. Beams **17**, 799 (1999).
8. V. S. Volokitin, I. O. Golosnoi, and N. N. Kalitkin, Mat. Model. **7** (4), 11 (1995).
9. S. M. Zakharov, G. V. Ivanenkov, A. A. Kolomenskii, *et al.*, Pis'ma Zh. Tekh. Fiz. **8**, 1060 (1982) [Sov. Tech. Phys. Lett. **8**, 456 (1982)].

Translated by G. V. Shepekina

Plasma Physics Reports, Vol. 28, No. 10, 2002, pp. 827–836. Translated from Fizika Plazmy, Vol. 28, No. 10, 2002, pp. 898–907.

PLASMA OSCILLATIONS AND WAVES

Evolution of the Frequency Spectrum of an Extraordinary Wave near the Upper Hybrid Resonance in a Turbulent Plasma

E. Z. Gusakov and A. V. Surkov

Ioffe Physicotechnical Institute, Russian Academy of Sciences, Politekhnicheskaya ul. 26, St. Petersburg, 194021 Russia
e-mail: Evgeniy.Gusakov@pop.ioffe.rssi.ru

Received April 15, 2002

Abstract—A study is made of the formation of the frequency spectrum of an extraordinary wave during its multiple small-angle scatterings along the path to the upper hybrid resonance, in the upper hybrid resonance region, and behind the conversion point. The formation of the spectrum is investigated both approximately (by the eikonal method) and exactly (in the limit of large-scale plasma density fluctuations responsible for small-angle scattering). It is demonstrated that these two approaches yield the same results in the common range of their applicability. It is shown that, in the vicinity of the upper hybrid resonance, the broadening of the frequency spectrum of a probing wave is proportional to its wavenumber. This circumstance and the predicted amount by which the spectrum broadens make it possible to consider small-angle scattering as one of the main effects responsible for a very large spectrum broadening observed in experiments. © *2002 MAIK "Nauka/Interperiodica".*

1. INTRODUCTION

According to current opinion, ion-temperature-gradient driven ion drift waves play a leading role in the anomalous ion energy transport in tokamaks. The same is true of the role played by the electron-temperature-gradient driven electron drift waves in the anomalous electron energy transport. For this reason, there is much current interest in investigating the behavior of the spectra of small-scale low-frequency plasma turbulence during Ohmic and auxiliary heated discharges, as well as during transitions to improved energy and particle confinement modes.

A diagnostic technique based on the effect of enhanced microwave scattering [1] is an efficient tool for studying small-scale plasma density fluctuations. This effect, which is observed when an extraordinary electromagnetic wave is scattered by plasma density fluctuations near the upper hybrid resonance (UHR), is associated with an increase in the potential component of the wave electric field as the UHR is approached.

The enhanced-scattering diagnostic implies that an extraordinary wave is launched into the plasma from the side of the stronger magnetic field along the plasma density gradient. The signals recorded are waves that are scattered backward by small-scale plasma density fluctuations and have the same polarization as the launched waves.

The effect of the increase in the wavenumber of the probing wave in the vicinity of the UHR makes it possible to investigate small-scale plasma density fluctuations. The decrease in the group velocity in this region, accompanied by an increase in the field amplitudes of the probing and scattered waves, leads to the amplification of the scattered signal. That the probing wave is scattered mainly in the UHR region provides high spatial resolution for measurements. The frequency spectrum of the recorded signals contains information about the frequency spectrum of fluctuations, and the wavenumber spectra of fluctuations can be obtained from the time-of-flight and correlation modifications of the enhanced-scattering diagnostic technique [2, 3].

The diagnostic method based on enhanced scattering at the UHR was originally employed to study small-scale oscillations and waves in quiescent plasmas of linear devices [1]. However, in recent years, this method has been widely applied to investigate plasma turbulence and the propagation of microwaves in tokamaks [4]. In tokamak experiments on enhanced scattering by spontaneous plasma density fluctuations, a substantial broadening of the frequency spectra was observed and it was found that this broadening increases in proportion to the wavenumber of the fluctuations by which the probing wave is backscattered [4]. This phenomenon may stem from the fact that, in a tokamak, the probing wave propagates in a turbulent plasma and is scattered primarily by predominant large-scale plasma density fluctuations.

The frequency shift and spectrum broadening may be associated not only with the frequency of the small-scale density fluctuations responsible for backscattering but also with the effects of small-angle scattering of the probing and scattered waves by large-scale plasma turbulence along their paths. The latter conclusion is supported by the fact that, as was shown in recent paper [5], the cross section for small-angle scattering, as well as that for backscattering, increases abruptly when the UHR is approached.

1063-780X/02/2810-0827$22.00

In order to interpret the results of experiments on enhanced scattering, it is very important to understand mechanisms for the formation of the spectra of backscattered signals. In this paper, we study the formation of the frequency spectrum of a probing extraordinary wave during its multiple scatterings in a turbulent plasma. We consider the following three regions: the region where the wave propagates toward the UHR, the UHR region, and the region behind the point at which the wave converts into a Bernstein mode. The analysis is performed by the eikonal method, but the formation of the frequency spectrum in the UHR region is investigated exactly. These two approaches are shown to yield the same results in the common range of their applicability.

2. FREQUENCY SPECTRUM OF A MULTIPLY SCATTERED EXTRAORDINARY WAVE

We consider a collisionless plasma in a magnetic field directed along the z-axis. We assume that the magnetic field and plasma density are both nonuniform in the x direction and that a plane probing wave propagates at a small angle with respect to the plasma density gradient.

In the eikonal approximation, the wave electric field can be represented as

$$\mathbf{E} = \mathbf{E}^0 e^{i\Psi(\mathbf{r})},$$

where $\Psi(\mathbf{r})$ is the eikonal and the harmonic dependence on time is omitted. In this case, the dispersion relation is the following nonlinear first-order partial differential equation:

$$\left| k^2\delta_{\alpha\beta} - k_\alpha k_\beta - \frac{\omega^2}{c^2}\varepsilon_{\alpha\beta} \right| = 0,$$

where $\mathbf{k} = \nabla\Psi(\mathbf{r})$ is the wavenumber of the probing wave, ω is its frequency, and $\varepsilon_{\alpha\beta}$ is the plasma dielectric tensor. In the paraxial approximation, the dispersion relation for an extraordinary wave in a cold plasma has the form

$$k_x^2 + k_y^2 + A(x)k_z^2 = \frac{\omega^2}{c^2}\varepsilon(x) - k_c^2/\varepsilon(x), \qquad (1)$$

with $\varepsilon \equiv \varepsilon_{11}$ and $\eta \equiv \varepsilon_{33}$. Near the UHR, we have $A(x) \approx -\eta/\varepsilon(x)$ and $k_c = \omega_{ce}(x_{UH})/c$, where x_{UH} is the position of the UHR.

Equation (1) is a Hamilton–Jacobi equation,

$$\frac{\partial\Psi}{\partial x} - \sqrt{k^2(x) - \left(\frac{\partial\Psi}{\partial y}\right)^2 - A(x)\left(\frac{\partial\Psi}{\partial z}\right)^2} = 0$$

with the Hamiltonian

$$H(y, z, k_y, k_z, x) = -\sqrt{k^2(x) - k_y^2 - A(x)k_z^2},$$

where $k^2(x) = \varepsilon(x)\omega^2/c^2 - k_c^2/\varepsilon(x)$. The canonical equations

$$\begin{cases} \dfrac{dk_i}{dx} = -\dfrac{\partial H}{\partial q_i} = 0 \\ \dfrac{dq_i}{dx} = \dfrac{\partial H}{\partial k_i} \end{cases} \qquad (2)$$

(with $q_1 \equiv y$ and $q_2 \equiv z$) determine the ray trajectories in space,

$$\begin{aligned} y(x) &= y_0 + \int_0^x \frac{k_y}{\sqrt{k^2(x') - k_y^2 - A(x')k_z^2}}dx', \\ z(x) &= z_0 + \int_0^x \frac{A(x')k_z}{\sqrt{k^2(x') - k_y^2 - A(x')k_z^2}}dx', \end{aligned} \qquad (3)$$

where y_0 and z_0 are the initial coordinates of the trajectory at $x = 0$.

In a Hamiltonian formalism, the eikonal is written as

$$\Psi = \int_0^x L\,dx + \Psi_0(y_0, z_0),$$

where the Lagrangian has the form

$$L = \sum_{i=1,2} k_i\frac{dq_i}{dx} - H = \frac{k^2(x)}{\sqrt{k^2(x) - k_y^2 - A(x)k_z^2}},$$

and the initial phase $\Psi_0(y_0, z_0)$ is specified at the surface $x = 0$.

The turbulent phase change can be calculated using perturbation theory. We can show that, in the general case, a small perturbation δH initiated by large-scale plasma density fluctuations does not affect the ray trajectories in a first approximation. In fact, the associated perturbation of the eikonal has the form

$$\begin{aligned} \delta\Psi &= \int_0^x \left\{ \delta k_i dq_i + k_i d\delta q_i - \frac{\partial H}{\partial q_i}\delta q_i dx \right. \\ &\left. - \frac{\partial H}{\partial k_i}\delta k_i dx - \delta H dx \right\} + \delta\Psi_0 \\ &= \int_0^x \delta k_i\left(dq_i - \frac{\partial H}{\partial k_i}dx\right) + k_i\delta q_i\Big|_0^x \\ &- \int_0^x \delta q_i\left(dk_i + \frac{\partial H}{\partial q_i}dx\right) - \int_0^x \delta H dx + \frac{\partial\Psi_0}{\partial q_i}\delta q_i\Big|_{x=0}. \end{aligned}$$

The first and third terms vanish because Hamiltonian equations (2) with the unperturbed Hamiltonian are satisfied. The second term at the upper limit of integration should be set equal to zero for a ray arriving at a fixed current point.

Taking into account the relationships

$$\delta x|_{x=0} = 0,$$
$$\frac{\partial \Psi_0}{\partial q_i} = k_i|_{x=0},$$

we obtain

$$\delta\Psi = -\int \delta H[q_i(x), k_i(x), x]dx,$$

where the functions $q_i(x)$ and $k_i(x)$ are determined from the unperturbed equations.

In the case under consideration, we have $\delta H \approx -\delta k$ in the paraxial approximation, so that the change in the eikonal associated with large-scale plasma density fluctuations can be calculated from the formula

$$\delta\Psi = \int_0^x \delta k[\mathbf{r}(x')]dx'. \quad (4)$$

Note that, in [6], the perturbation of the eikonal was obtained in an analogous manner but for the particular case of electromagnetic waves propagating in the atmosphere. In contrast, here we have derived expression (4) in the general case.

Let us calculate the turbulent phase change of an extraordinary wave. In the presence of large-scale plasma density fluctuations $\delta n(x, t)$, the perturbation of the projection of the wave vector of an extraordinary wave onto the direction in which the plasma is inhomogeneous,

$$k(x) \simeq \frac{k_c}{\sqrt{-\varepsilon}}, \quad (5)$$

has the form

$$\delta k = -k_c \delta n/(2n\epsilon^{3/2}),$$

where the plasma density profile is assumed to be linear, $\epsilon \equiv -\varepsilon = (x_{UH} - x)/\ell$. The fluctuation-related change in the eikonal is equal to

$$\delta\Psi = -\frac{k_c}{2n}\int_0^x \frac{\delta n(\chi, t)}{\epsilon^{3/2}(\chi)}d\chi. \quad (6)$$

In the expression for the wave electric field, large-scale fluctuations are accounted for by the factor

$$\mathcal{A}(x, t) = e^{i\delta\Psi(x, t)}.$$

In order to obtain the frequency spectrum of a multiply scattered extraordinary wave, we investigate the correlation function

$$\langle \mathcal{A}(x, t)\mathcal{A}^*(x, t+\tau)\rangle = \int_{-\infty}^{+\infty} d\xi_1 \int_{-\infty}^{+\infty} d\xi_2 \mathcal{A}(\xi_1)\mathcal{A}^*(\xi_2)W(\xi_1, \xi_2),$$

where, for brevity, we have introduced the notation $\xi_1 \equiv \delta\Psi(x, t)$ and $\xi_2 \equiv \delta\Psi(x, t+\tau)$. The two-dimensional probability density $W(\xi_1, \xi_2)$ characterizes the fluctuation-related phase changes ξ_1 and ξ_2. The integrand in expression (6) for perturbations of the eikonal $\delta\Psi$ is a random quantity proportional to the level of plasma density fluctuations. If the integration interval is longer than the correlation length of the density fluctuations, then, by the central limit theorem, the distribution of the fluctuation-related phase advances is normal. We assume that, in the opposite case, this distribution is also normal.

The two-dimensional probability density is described by the expression

$$W(\xi_1, \xi_2) = \frac{1}{2\pi\sqrt{\det B}} e^{-\frac{1}{2}(B^{-1})_{ij}\xi_i\xi_j},$$

where summation is implied over the repeated indices ($i, j = 1, 2$) and the covariation matrix has the form

$$\hat{B} = \begin{pmatrix} \langle\xi_1^2\rangle & \langle\xi_1\xi_2\rangle \\ \langle\xi_1\xi_2\rangle & \langle\xi_2^2\rangle \end{pmatrix}.$$

In the general n-dimensional case, the relationship

$$\int_{-\infty}^{+\infty} W(\boldsymbol{\xi})e^{\mathbf{a}\boldsymbol{\xi}}d\boldsymbol{\xi} = e^{\frac{1}{2}\mathbf{a}\hat{B}\mathbf{a}} \quad (7)$$

yields

$$\langle \mathcal{A}(x, t)\mathcal{A}^*(x, t+\tau)\rangle = \exp\left[\langle\xi_1\xi_2\rangle - \frac{1}{2}(\langle\xi_1^2\rangle + \langle\xi_2^2\rangle)\right].$$

Now, we calculate the correlation function $\langle\xi_1^2\rangle$, neglecting the effects associated with the two-dimensional character of wave propagation (below, we will show that, in the paraxial approximation, these effects are small). According to formula (6), we have

$$\langle\xi_1\xi_2\rangle = \frac{k_c^2\ell^3}{4n^2}\int_0^x d\chi \int_0^x d\chi' \frac{\langle\delta n(\chi, t)\delta n(\chi', t+\tau)\rangle}{(x_{UH}-\chi)^{3/2}(x_{UH}-\chi')^{3/2}}. \quad (8)$$

Let us consider two asymptotics of this expression. For a current point x whose distance from the UHR is longer than the correlation length of the large-scale density fluctuations, $x_{UH} - x \gg \ell_c$, the correlation function of the fluctuations determines the change in the

integrand and plays the role of a δ function. Assuming that the plasma density fluctuations are statistically uniform in both space and time, we introduce the notation

$$\Phi(\chi-\chi', \tau) = \langle \delta n(\chi, t)\delta n(\chi', t+\tau)\rangle \quad (9)$$

to write

$$\langle \xi_1\xi_2\rangle = \frac{k_c^2\ell^3}{4n^2}\int_0^x \frac{d\chi}{(x_{UH}-\chi)^3}\int_{\chi-x}^{\chi}\Phi(\delta, \tau)d\delta.$$

Switching to the spectral density of large-scale fluctuations,

$$\Phi(\chi-\chi', \tau) = \int_{-\infty}^{+\infty}\frac{dq_x d\Omega}{(2\pi)^2}\left|\delta n_{q_x,\Omega}\right|^2 e^{iq_x(\chi-\chi')+i\Omega\tau},$$

we find the first of the desired asymptotics:

$$\langle \xi_1\xi_2\rangle = \frac{\ell k_x^4(x)}{8k_c^2n^2}\int_{-\infty}^{+\infty}\frac{d\Omega}{2\pi}\left|\delta n_{0,\Omega}\right|^2 e^{i\Omega\tau}, \quad x_{UH}-x \gg \ell_c. \quad (10)$$

In order to derive the second asymptotic (at $x_{UH}-x \ll \ell_c$), we introduce the function

$$F(q_x, x) = \int_0^x \frac{d\chi}{(x_{UH}-\chi)^{3/2}}e^{iq_x\chi},$$

in terms of which we obtain

$$\langle \xi_1\xi_2\rangle = \frac{k_c^2\ell^3}{4n^2}\int_{-\infty}^{+\infty}\frac{dq_x d\Omega}{(2\pi)^2}\left|\delta n_{q_x,\Omega}\right|^2\left|F(q_x, x)\right|^2 e^{i\Omega\tau}. \quad (11)$$

In the case $x_{UH}-x \ll \ell_c$, we deal with the asymptotic of the function $F(q_x, x)$ at $|q_x|(x_{UH}-x) \ll 1$, when the change in the integrand is determined by a preexponential factor:

$$F(q_x, x) \approx \frac{2}{\sqrt{x_{UH}-x}}e^{iq_x x},$$

in which case the desired correlation function has the form

$$\langle \xi_1\xi_2\rangle = \frac{\ell^2 k_x^2(x)}{n^2}\int_{-\infty}^{+\infty}\frac{dq_x d\Omega}{(2\pi)^2}\left|\delta n_{q_x,\Omega}\right|^2 e^{i\Omega\tau}, \quad x_{UH}-x \ll \ell_c. \quad (12)$$

To determine the frequency spectrum of a multiply scattered extraordinary wave, we introduce the function

$$\mathcal{H}(x, \tau) = \frac{\langle \mathcal{A}(x, t)\mathcal{A}^*(x, t+\tau)\rangle - \langle \mathcal{A}(x, t)\rangle\langle \mathcal{A}(x, t+\tau)\rangle^*}{\langle|\mathcal{A}(x, t)-\langle \mathcal{A}(x, t)\rangle|^2\rangle},$$

where $\langle \mathcal{A}(x, t)\rangle \equiv \langle \mathcal{A}(\xi_1)\rangle = \exp[-\langle \xi_1^2\rangle/2]$. We can show that this function is equal to

$$\mathcal{H}(x, \tau) = (e^{\langle \xi_1\xi_2\rangle}-1)/(e^{\langle \xi^2\rangle}-1),$$

where we dropped the subscript for ξ in $\langle \xi^2\rangle$ because the fluctuations are statistically uniform in time.

Now, the spectral density of the power of the probing wave can be calculated from the formula

$$\mathcal{H}_{\Delta\omega}(x) = \int_{-\infty}^{+\infty} d\tau\mathcal{H}(x, \tau)e^{i\Delta\omega\tau},$$

where Δω should be understood as the shift from the probing-wave frequency (recall that, in our analysis, the harmonic dependence of the field of the probing wave on time is omitted).

In what follows, we will be interested in the linear case

$$\langle \xi^2\rangle, \langle \xi_1\xi_2\rangle \ll 1, \quad \mathcal{H} \approx \frac{\langle \xi_1\xi_2\rangle}{\langle \xi^2\rangle}$$

and the nonlinear case

$$e^{\langle \xi_1\xi_2\rangle} \gg 1, \quad \mathcal{H} \approx e^{\langle \xi_1\xi_2\rangle-\langle \xi^2\rangle}.$$

In the nonlinear case, the correlation time of the field of the probing wave is much shorter than that of the plasma density fluctuations, $\tau/t_c \ll 1$. Assuming that the spectral density of fluctuations is even in frequency and that the corresponding integrals do exist, we expand the exponentials in expressions (10) and (12) to obtain

$$\mathcal{H} \approx \begin{cases} \exp\left\{-\dfrac{\ell k_x^4(x)\tau^2}{16k_c^2n^2}\displaystyle\int_{-\infty}^{+\infty}\frac{d\Omega}{2\pi}\left|\delta n_{0,\Omega}\right|^2\Omega^2\right\}, \\ x_{UH}-x \gg \ell_c \\ \exp\left\{-\dfrac{\ell^2 k_x^2(x)\tau^2}{2n^2}\displaystyle\int_{-\infty}^{+\infty}\frac{dq_x d\Omega}{(2\pi)^2}\left|\delta n_{q_x,\Omega}\right|^2\Omega^2\right\}, \\ x_{UH}-x \ll \ell_c. \end{cases}$$

Introducing the corresponding notation, we can write

$$\mathcal{H} \approx \exp\left\{-\frac{\langle \delta n^2\rangle}{n^2}R(x)\langle \Omega^2\rangle\tau^2\right\},$$

$$R(x) = \begin{cases} \ell\ell_c k_x^4(x)/(16k_c^2), & x_{UH}-x \gg \ell_c \\ \ell^2 k_x^2(x)/2, & x_{UH}-x \ll \ell_c. \end{cases}$$

One can readily see that the expressions derived can be matched at $x_{UH}-x \sim \ell_c$.

This matching allows us to estimate the spectrum width in the nonlinear case:

$$\Delta\omega \approx 2\sqrt{R(x)\langle\Omega^2\rangle\frac{\langle\delta n^2\rangle}{n^2}}. \quad (13)$$

Hence, we have derived expressions describing the frequency spectrum of a multiply scattered extraordinary wave without allowance for the effects associated with the two-dimensional character of wave propagation. Let us estimate the effect of the deviation of ray trajectories in the *y* direction. Since the scale of fluctuations along the plasma magnetic field (the *z*-axis) can be assumed to be very large, the deviation of ray trajectories in this direction will not affect the final result.

Note that the approach developed here makes it possible in principle to take into account the two-dimensional character of ray trajectories. However, as will be clear later, this effect is negligible in the paraxial approximation. In fact, as in the one-dimensional case, we can see that, at distances from the UHR that are much longer than the correlation length of the large-scale fluctuations, the correlation function (9) in expression (8) plays the role of a δ function, because the deviation of ray trajectories in the *y* direction is a function of *x* [see expressions (3)].

Let us consider the effect of the two-dimensional character of wave propagation near the UHR (at $x_{UH} - x \ll \ell_c$). With allowance for the deviation of ray trajectories in the *y* direction, formula (11) becomes

$$\langle\xi_1\xi_2\rangle = \frac{k_c^2\ell^3}{4n^2}\int_{-\infty}^{+\infty}\frac{dq_x dq_y d\Omega}{(2\pi)^3}|\delta n_{\mathbf{q},\Omega}|^2|F_{2D}(q_x, q_y, x)|^2 e^{i\Omega\tau},$$

where the function F_{2D} takes the form

$$F_{2D}(q_x, q_y, x) = \int_0^x \frac{d\chi}{(x_{UH}-\chi)^{3/2}} e^{iq_x\chi + iq_y y(\chi)},$$

and the function $y(\chi)$ is given by the first of expressions (3). However, as in the one-dimensional case, the change in the integrand in the function F_{2D} near the UHR in the paraxial approximation is determined by the preexponential factor, which is the same in the one- and two-dimensional cases:

$$F_{2D}(q_x, q_y, x) \approx \frac{2}{\sqrt{x_{UH}-x}} e^{iq_x x + iq_y y(x)}.$$

This gives

$$|F_{2D}|^2 \approx \frac{4}{x_{UH}-x}.$$

In other words, in the paraxial approximation, the effect of the two-dimensional character of wave propagation has insignificant impact on the above asymptotics of the correlation function (8).

Another consequence of the two-dimensional character of wave propagation is an increase in the projection of the wavenumber of a probing wave, caused by its multiple small-angle scatterings. This consequence may restrict the applicability range of the eikonal approximation, in which we neglected the diffraction of the probing beam. In order to determine the limits of applicability of the eikonal approximation, we obtain the spectrum of a multiply scattered probing wave in transverse wavenumbers with allowance for the dependence of large-scale fluctuations on the *y* coordinate.

The corresponding asymptotics of the correlation function

$$\langle\xi_1\xi_2\rangle = \frac{k_c^2\ell^3}{4n^2}\int_0^x d\chi\int_0^x d\chi' \frac{\langle\delta n(\chi, y, t)\delta n(\chi', y', t+\tau)\rangle}{(x_{UH}-\chi)^{3/2}(x_{UH}-\chi')^{3/2}}$$

have the form

$$\langle\xi_1\xi_2\rangle = \frac{\ell k_x^4(x)}{8k_c^2 n^2}\int_{-\infty}^{+\infty}\frac{dq_y d\Omega}{(2\pi)^2}|\delta n_{0,q_y,\Omega}|^2 e^{i\Omega\tau + iq_y(y-y')},$$

$$x_{UH} - x \gg \ell_c,$$

$$\langle\xi_1\xi_2\rangle = \frac{\ell^2 k_x^2(x)}{n^2}\int_{-\infty}^{+\infty}\frac{dq_x dq_y d\Omega}{(2\pi)^3}|\delta n_{\mathbf{q},\Omega}|^2 e^{i\Omega\tau + iq_y(y-y')},$$

$$x_{UH} - x \ll \ell_c.$$

Then, assuming that the spectral density of fluctuations is even in both q_y and Ω and that the fluctuation amplitude is sufficiently large, we arrive at the following expression for the correlation function of the probing wave:

$$\mathcal{H} \approx \exp\left\{-\frac{\tau^2}{T_c^{\text{eff}^2}} - \frac{(y-y')^2}{L_y^{\text{eff}^2}}\right\},$$

where we have introduced the notation

$$T_c^{\text{eff}} = \begin{cases} \dfrac{4k_c}{k_x^2(x)\sqrt{\ell\ell_c}}\Big/\sqrt{\langle\Omega^2\rangle\langle\delta n^2\rangle/n^2}, & x_{UH}-x \gg \ell_c \\ \dfrac{\sqrt{2}}{k_x\ell}\Big/\sqrt{\langle\Omega^2\rangle\langle\delta n^2\rangle/n^2}, & x_{UH}-x \ll \ell_c, \end{cases}$$

$$L_y^{\text{eff}} = \begin{cases} \dfrac{4k_c}{k_x^2(x)\sqrt{\ell\ell_c}}\Big/\sqrt{\langle q_y^2\rangle\langle\delta n^2\rangle/n^2}, & x_{UH}-x \gg \ell_c \\ \dfrac{\sqrt{2}}{k_x\ell}\Big/\sqrt{\langle q_y^2\rangle\langle\delta n^2\rangle/n^2}, & x_{UH}-x \ll \ell_c. \end{cases}$$

The broadening of the spectrum of the probing wave in transverse wavenumbers can be estimated as

$$\Delta k_y \approx 1/L_y^{\text{eff}}.$$

The condition under which the diffraction of the probing beam at the point x can be neglected should have the form

$$\Delta k_y(x) \int_x^{x_{UH}} \frac{dx'}{k_x(x')} \ll L_y^{\text{eff}}(x),$$

which yields

$$\frac{1}{3}\langle q_y^2\rangle \frac{\langle \delta n^2\rangle}{n^2}\frac{k_c^2 \ell^3}{k_x(x)} \ll 1.$$

As is seen, if this condition is satisfied at the point $x = x^*$ at which the fluctuation-related phase change becomes equal to π so that the spectrum rapidly begins to broaden in both frequency and transverse wavenumber,

$$\langle \delta\Psi^2\rangle = \ell^2 k_x^2(x^*)\langle \delta n^2\rangle/n^2 \sim \pi^2, \quad x_{UH} - x^* \ll \ell_c,$$

then it will be satisfied along the entire wave path from this point to the UHR. This effect is associated with the fact that the rays approaching the UHR propagate almost exactly along the direction in which the plasma is inhomogeneous. For $x_{UH} - x^* \ll \ell_c$, this condition is not too stringent:

$$\frac{1}{3\pi}k_c^2 \ell^4 \langle q_y^2\rangle \frac{\langle \delta n^2\rangle^{3/2}}{n^3} \ll 1.$$

For the case in which the fluctuation-related phase change becomes on the order of π at distances from the UHR that are longer than the correlation length of the large-scale fluctuations, the sought-for condition can be derived in an analogous fashion. In tokamak experiments, however, such a situation is unusual, so we do not present this condition here.

3. FREQUENCY SPECTRUM OF A PROBING WAVE BEHIND THE CONVERSION POINT

It is well known that, near the UHR, an extraordinary wave converts into a Bernstein mode [7], which propagates from the conversion point toward the plasma boundary. Under the condition

$$k_x \sim \frac{\omega}{c}\sqrt{\frac{c}{v_{Te}}},$$

where v_{Te} is the electron thermal velocity, the Wentzel–Kramers–Brillouin (WKB) approximation and the cold plasma approximation, in which the above dispersion relation was derived, both fail to hold. However, behind the conversion point, the Bernstein mode at sufficiently large distances from the UHR can be described in the eikonal approximation. The condition for the validity of this description is

$$\frac{1}{k_x^2}\frac{dk_x}{dx} \ll 1.$$

For the Bernstein mode, this condition should be taken with

$$k(x) = \sqrt{\epsilon}/\ell_T, \tag{14}$$

where the length ℓ_T, associated with electron thermal motion, is on the order of the electron gyroradius. For a linear plasma density profile such that $\epsilon = (x_{UH} - x)/\ell$, substituting relationship (14) into this condition yields the applicability condition of the WKB approximation:

$$\epsilon^{3/2} \gg \ell_T/\ell.$$

For the Bernstein mode, the perturbation of the wavenumber $k(x)$ associated with large-scale plasma density fluctuations has the form

$$\delta k = \frac{1}{2\ell_T}\frac{\delta n(x,t)}{n}\frac{\sqrt{\ell}}{\sqrt{x_{UH}-x}}.$$

We denote the corresponding fluctuation-related phase changes by

$$\xi_1 = \int_{x_{UH}}^{x} \delta k(\chi, t)d\chi, \quad \xi_2 = \int_{x_{UH}}^{x} \delta k(\chi, t+\tau)d\chi.$$

Then, neglecting the two-dimensional character of the propagation of a Bernstein mode, we calculate its correlation function

$$\langle \xi_1\xi_2\rangle = \frac{\ell}{4\ell_T^2 n^2}\int_{x_{UH}}^{x} d\chi \int_{x_{UH}}^{x} d\chi' \frac{\Phi(\chi-\chi', \tau)}{\sqrt{x_{UH}-\chi}\sqrt{x_{UH}-\chi'}}. \tag{15}$$

To do this, we introduce the function

$$G(q_x, x) = \int_{x_{UH}}^{x} \frac{d\chi}{\sqrt{x_{UH}-\chi}} e^{iq_x\chi},$$

which allows us to represent sought-for function (15) in the form

$$\langle \xi_1\xi_2\rangle = \frac{\ell}{4\ell_T^2 n^2}\int_{-\infty}^{+\infty}\frac{dq_x d\Omega}{(2\pi)^2}\left|\delta n_{q_x,\Omega}\right|^2 \left|G(q_x, x)\right|^2 e^{i\Omega\tau}.$$

At distances from the UHR (which serves as a cut-off for the Bernstein wave) that are much shorter than the correlation length of the density fluctuations ($x_{UH} - x \ll \ell_c$), we can set $|q_x|(x_{UH} - x) \ll 1$, which enables us to obtain the following asymptotic of the function $G(q_x, x)$:

$$G(q_x, x) \approx -2\sqrt{x_{UH}-x}\, e^{iq_x x}.$$

In this case, correlation function (15) becomes

$$\langle \xi_1 \xi_2 \rangle = \frac{\ell^2 k_x^2(x)}{n^2} \int_{-\infty}^{+\infty} \frac{dq_x d\Omega}{(2\pi)^2} |\delta n_{q_x,\Omega}|^2 e^{i\Omega\tau},$$

$$x_{UH} - x \ll \ell_c,$$

i.e., it exactly coincides with correlation function (12).

Let us consider correlation function (15) for $x_{UH} - x \gg \ell_c$. To do this, we find the asymptotic of the function $G(q_x, x)$ in the limit $|q_x|(x_{UH} - x) \gg 1$. We make the replacement $x_{UH} - x \equiv u^2$ and use the stationary-phase method to obtain

$$G(q_x, x) = -2e^{iq_x x_{UH}} \int_0^{\sqrt{x_{UH}-x}} e^{-iq_x u^2} du \approx -\sqrt{\frac{\pi}{|q_x|}} e^{iq_x x_{UH} - i\pi/2},$$

$$|q_x| \gg (x_{UH} - x)^{-1}.$$

As a result, we arrive at the following asymptotic of correlation function (15):

$$\langle \xi_1 \xi_2 \rangle = \frac{\pi \ell}{4\ell_T^2 n^2} \int_\Theta \frac{dq_x}{2\pi|q_x|} \int_{-\infty}^{+\infty} \frac{d\Omega}{2\pi} |\delta n_{q_x,\Omega}|^2 e^{i\Omega\tau},$$

$$x_{UH} - x \gg \ell_c,$$

where the domain of integration over q_x is $\Theta = (-\infty, -q^*) \cup (q^*, \infty)$, with $q^* \sim 1/(x_{UH} - x)$. The contribution of the interval $[-q^*, q^*]$, in which the stationary-phase method fails to hold, to this asymptotic is as small as $\ell_c q^* \ll 1$.

In the case at hand, we have $q^* \ell_c \ll 1$, which indicates that the integrand changes mainly at the expense of $1/q_x$. Consequently, we can estimate the integral with logarithmic accuracy:

$$\int_\Theta \frac{dq_x}{2\pi|q_x|} |\delta n_{q_x,\Omega}|^2 \sim 2 \int_{q^*}^{1/\ell_c} \frac{dq_x}{2\pi|q_x|} |\delta n_{q_x,\Omega}|^2$$

$$\sim -\frac{1}{\pi} |\delta n_{0,\Omega}|^2 \ln(q^* \ell_c),$$

which gives

$$\langle \xi_1 \xi_2 \rangle \sim \frac{\ell}{4\ell_T^2 n^2} \int_{-\infty}^{+\infty} \frac{d\Omega}{2\pi} |\delta n_{0,\Omega}|^2 e^{i\Omega\tau} \ln \frac{k_x^2 \ell \ell_T^2}{\ell_c},$$

$$x_{UH} - x \gg \ell_c.$$

Hence, we have obtained two asymptotics of the correlation function of the fluctuation-related changes in the eikonal of a probing wave behind the conversion point. At distances from the UHR that are shorter than the correlation length of the large-scale density fluctuations, the spectrum of the probing wave evolves in the same manner as in the corresponding region along the wave path to the conversion point. In the nonlinear case, the width of the frequency spectrum near the UHR is approximately equal to

$$\Delta\omega \approx \ell k_x(x) \sqrt{2\langle \Omega^2 \rangle \frac{\langle \delta n^2 \rangle}{n^2}}, \quad x_{UH} - x \ll \ell_c. \quad (16)$$

At longer distances from the UHR, the spectrum width behind the conversion point increases much more gradually:

$$\Delta\omega \approx \sqrt{\frac{\ell \ell_c}{\ell_T^2} \ln\left(\frac{k_x^2(x) \ell_T^2 \ell}{\ell_c}\right) \langle \Omega^2 \rangle \frac{\langle \delta n^2 \rangle}{n^2}}, \quad (17)$$

$$x_{UH} - x \gg \ell_c.$$

Formulas (13) and (17) describe how the broadening of the frequency spectrum of a probing wave depends on its wavenumber in the applicability range of the WKB approximation. Hence, we are left with the problem of investigating the immediate vicinity of the conversion point, where this approximation fails to hold.

4. FREQUENCY SPECTRUM OF A PROBING WAVE IN THE UHR REGION

We consider the frequency spectrum of a probing wave in the UHR region, i.e., at distances from the resonance that are much shorter than the scale of the plasma density fluctuations. We use the following exact expression for the electric field of the probing wave in the UHR region [1]:

$$E(\xi) = \sqrt{\frac{8}{\gamma^2 \ell \omega}} \int_0^\infty \exp\left[i\left(\frac{\kappa^3}{3} - \frac{b}{\kappa} + \xi\kappa\right)\right] d\kappa, \quad (18)$$

where we have introduced the dimensionless parameters

$$\gamma = \left(\frac{\ell_T}{\ell}\right)^{2/3}, \quad \xi = \frac{x - x_{UH}(t)}{\gamma\ell}, \quad b = (k_c \ell)^2 \gamma.$$

The change of the UHR position in time is governed by the influence of large-scale density fluctuations. Here, we assume that the fluctuations are coordinate-independent and that their scale is large enough to ignore their effect on the plasma density gradient:

$$x_{UH}(t) = x_{UH} - \ell \frac{\delta n(t)}{n}. \quad (19)$$

Under these assumptions, the correlation function of a probing wave has the form

$$\langle E(t) E^*(t + \tau) \rangle$$

$$= \frac{8}{\gamma^2 \ell \omega} \int_0^\infty d\kappa \int_0^\infty d\kappa' \exp\left[i\left(\frac{\kappa^3}{3} - \frac{b}{\kappa} + \xi\kappa\right)\right]$$

$$\times \exp\left[-i\left(\frac{\kappa'^3}{3} - \frac{b}{\kappa'} + \xi\kappa'\right)\right]$$

$$\times\left\langle \exp\left\{i\left[\frac{\delta n(t)}{\gamma n}\kappa - \frac{\delta n(t+\tau)}{\gamma n}\kappa'\right]\right\}\right\rangle.$$

Assuming that the distribution of the density fluctuations is normal and using formula (7), we obtain

$$\left\langle \exp\left\{i\left[\frac{\delta n(t)}{\gamma n}\kappa - \frac{\delta n(t+\tau)}{\gamma n}\kappa'\right]\right\}\right\rangle$$

$$= \exp\left\{-\frac{1}{2\gamma^2 n^2}[\langle\delta n^2\rangle(\kappa^2+\kappa'^2) - 2\kappa\kappa'\langle\delta n(t)\delta n(t+\tau)\rangle]\right\},$$

which gives

$$K = \langle E(t)E^*(t+\tau)\rangle - \langle E(t)\rangle\langle E^*(t+\tau)\rangle$$

$$= \frac{8}{\gamma^2\ell\omega}\int_0^\infty d\kappa\int_0^\infty d\kappa' \exp\left[i\left(\frac{\kappa^3}{3} - \frac{b}{\kappa} + \xi\kappa\right)\right] \quad (20)$$

$$\times \exp\left[-i\left(\frac{\kappa'^3}{3} - \frac{b}{\kappa'} + \xi\kappa'\right)\right]\exp\left[-\frac{1}{2\gamma^2}\frac{\langle\delta n^2\rangle}{n^2}(\kappa^2+\kappa'^2)\right]$$

$$\times\left\{\exp\left[\frac{\kappa\kappa'}{\gamma^2}\frac{\langle\delta n(t)\delta n(t+\tau)\rangle}{n^2}\right] - 1\right\}.$$

In order to obtain the asymptotics of this expression in the WKB approximation, we apply the stationary-phase method. In each of the two integrals, there are two stationary-phase points

$$\kappa_1 = \sqrt{-\xi}, \quad \kappa_2 = \sqrt{-\frac{b}{\xi}}.$$

Calculating the contributions of these points to the integrals, we obtain

$$K = \frac{8\pi}{\omega}\left\{\frac{1}{\ell_T^2 k_B}\exp\left[-\frac{\langle\delta n^2\rangle}{n^2}k_B^2\ell^2\right]\right.$$

$$\times\left[\exp\left(\frac{\langle\delta n(t)\delta n(t+\tau)\rangle}{n^2}k_B^2\ell^2\right) - 1\right]$$

$$-\frac{k_X^{3/2}}{k_c\sqrt{k_B}\ell_T}\exp\left[-\frac{\langle\delta n^2\rangle}{2n^2}k_B^2\ell^2\right]$$

$$\times\left[\exp\left(\frac{\langle\delta n(t)\delta n(t+\tau)\rangle}{n^2}k_X k_B\ell^2\right) - 1\right]$$

$$\times\sin\left(\frac{2}{3}k_B^3\ell\ell_T^2 - \frac{2k_c^2\ell}{k_X}\right) + \frac{k_X^3}{k_c^2}\exp\left(-\frac{\langle\delta n^2\rangle}{n^2}k_X^2\ell^2\right)$$

$$\left.\times\left[\exp\left(\frac{\langle\delta n(t)\delta n(t+\tau)\rangle}{n^2}k_X^2\ell^2\right) - 1\right]\right\},$$

where k_X stands for wavenumber (5) of an extraordinary wave and k_B denotes wavenumber (14) of a Bernstein mode. Taking into account the inequality $k_B \gg k_X$, we can readily see that the second (oscillating) term is small because the exponentials contain two different wavenumbers. The first and third terms correspond, respectively, to those derived above for a Bernstein mode and an extraordinary wave. Thus, expression (20), which is valid in the UHR region, can be matched with the correlation functions obtained for an extraordinary wave and a Bernstein mode in the eikonal approximation.

Now, we calculate the wave spectrum in the case of a cold plasma, in which expression (18) becomes

$$E = \sqrt{\frac{8\ell}{\omega}}(x - x_{UH} + i\varepsilon^{im}\ell)^{-1},$$

where ε^{im} is the imaginary part of the plasma dielectric function. As before, we consider large-scale plasma density fluctuations. We neglect their dependence on the x coordinate and take into account only their influence on UHR position (19). We begin by calculating the correlation function

$$K \equiv \langle E(t)E^*(t+\tau)\rangle$$

$$= \frac{8}{\omega}\left\langle\left(\varepsilon^r + i\varepsilon^{im} + \frac{\delta n(t)}{n}\right)^{-1}\left(\varepsilon^r - i\varepsilon^{im} + \frac{\delta n(t+\tau)}{n}\right)^{-1}\right\rangle. \quad (21)$$

In what follows, we will omit the superscript r in the real part ε^r of the dielectric function. Assuming that the distribution of the density fluctuations is normal and introducing the notation

$$\xi_1 \equiv \frac{\delta n(t)}{n}, \quad \xi_2 \equiv \frac{\delta n(t+\tau)}{n},$$

$$\zeta_1 \equiv \xi_1 + \varepsilon, \quad \zeta_2 \equiv \xi_2 + \varepsilon,$$

we obtain

$$K = \frac{\exp[-\varepsilon^2/(\langle\xi^2\rangle + \langle\xi_1\xi_2\rangle)]}{2\pi\sqrt{\langle\xi^2\rangle^2 - \langle\xi_1\xi_2\rangle^2}}$$

$$\times\int_{-\infty}^{+\infty}\int_{-\infty}^{+\infty}\frac{d\zeta_1 d\zeta_2}{(\zeta_1 + i\varepsilon^{im})(\zeta_2 - i\varepsilon^{im})}\exp\left\{-\frac{\langle\xi^2\rangle(\zeta_1^2+\zeta_2^2)}{2(\langle\xi^2\rangle^2 + \langle\xi_1\xi_2\rangle^2)}\right.$$

$$\left.+\frac{\langle\xi_1\xi_2\rangle\zeta_1\zeta_2}{\langle\xi^2\rangle^2 + \langle\xi_1\xi_2\rangle^2} + \frac{2\varepsilon(\zeta_1+\zeta_2)}{\langle\xi^2\rangle + \langle\xi_1\xi_2\rangle}\right\}.$$

We take the limit $\varepsilon^{im} \longrightarrow 0$ and use the appropriate contour for circumventing the poles that arise in this limit. After some manipulations, we obtain

$$K = \frac{\exp[-\varepsilon^2/(\langle\xi^2\rangle + \langle\xi_1\xi_2\rangle)]}{2\pi\sqrt{\langle\xi^2\rangle^2 - \langle\xi_1\xi_2\rangle^2}} \times\left\{\pi^2 + 2\pi\left[\int_0^\alpha e^{x^2/2}dx\right]^2 + 2\pi\int_0^k \frac{\exp[\alpha^2/(1-x)]}{\sqrt{1-x^2}}dx\right\}, \quad (22)$$

where we have introduced the notation

$$k \equiv \frac{\langle\xi_1\xi_2\rangle}{\langle\xi^2\rangle}, \quad \alpha^2 \equiv \frac{1-k}{1+k}\delta, \quad \delta \equiv \frac{\varepsilon^2}{\langle\xi^2\rangle}.$$

The parameter k characterizes the degree to which the fluctuations are correlated, and δ is an important parameter determining the relative distance to the UHR. Using expression (22), we can obtain different asymptotics of the correlation function K. Of particular interest is the limit $k \longrightarrow 1$, which corresponds to strongly correlated fluctuations. In this limit, we can readily derive the two asymptotics

$$K \approx \begin{cases} \dfrac{\pi}{\langle\xi^2\rangle\sqrt{1-k^2}}, & \delta \ll 1 \\ \dfrac{\pi}{2\langle\xi^2\rangle\sqrt{1-k^2}}e^{-\delta^2/2} + \dfrac{1}{\varepsilon^2}, & \delta \gg 1. \end{cases} \quad (23)$$

Note that, for $k = 1$, correlation function (21) is calculated to be

$$K_1 = \frac{1}{\sqrt{2\pi\langle\xi^2\rangle}}\int_{-\infty}^{+\infty}\frac{d\xi}{(\xi+\varepsilon)^2 + \varepsilon^{im^2}}\exp\left(-\frac{\xi^2}{2\langle\xi^2\rangle}\right).$$

For $\varepsilon^{im} \ll \sqrt{\langle\xi^2\rangle}$, it takes the form

$$K_1 \approx \begin{cases} \sqrt{\dfrac{\pi}{2\langle\xi^2\rangle}}\varepsilon^{im^{-1}}, & \delta \ll 1 \\ \sqrt{\dfrac{\pi}{2\langle\xi^2\rangle}}\varepsilon^{im^{-1}}e^{-\delta^2/2} + \dfrac{1}{\varepsilon^2}, & \delta \gg 1. \end{cases} \quad (24)$$

The physical meaning of these asymptotics can easily be understood: they are the product of the field amplitude at the resonance, saturated by dissipation, and the probability for the resonance to occur at a given point. A comparison of expressions (23), which were derived in the limit $\varepsilon^{im} \longrightarrow 0$, with expressions (24) shows that dissipation can be neglected up to a certain maximum k value such that

$$1 - k_{\max} \sim \frac{\pi\varepsilon^{im^2}}{\langle\xi^2\rangle}.$$

For $\tau \ll t_c$, we have

$$k = 1 - \left(\frac{\tau}{t_c}\right)^2,$$

where t_c is the correlation time of the fluctuations. Then, for $k \longrightarrow 1$ and $\delta \ll 1$, expressions (23) yield

$$K(\tau) = \frac{\pi t_c}{\sqrt{2}\langle\xi^2\rangle\tau}. \quad (25)$$

This expression is valid up to the time $\tau = \tau_{\min}$, which is defined in terms of $k_{\max}$ as

$$\tau_{\min} = \sqrt{\frac{\pi}{\langle\xi^2\rangle}}\varepsilon^{im}t_c.$$

For $\tau \leqslant \tau_{\min}$, the singularity in expression (25) is saturated at a level determined by expressions (24).

The width of the frequency spectrum of the field in the UHR is estimated as $\Delta\omega \sim \tau_{\min}^{-1}$. This estimate can readily be obtained by taking the Fourier transformation of the dependence $1/\sqrt{\tau^2 + \tau_{\min}^2}$, which approximates both asymptotic (25) and asymptotics (24):

$$K_{\Delta\omega} \propto \int_{-\infty}^{+\infty}\frac{e^{i\Delta\omega\tau}}{\sqrt{\tau^2 + \tau_{\min}^2}}d\tau \propto e^{-\Delta\omega\tau_{\min}}.$$

In this case, the spectrum width is determined not only by the correlation time of the fluctuations but also by dissipation, because the latter governs the width of the resonance when the density fluctuations are time-dependent at a given point.

Hence, we have analyzed the frequency spectrum of a probing wave along its entire path. Note that the calculated behavior of the width of the frequency spectrum in the UHR region agrees with the experimental finding [4] that the width of the spectrum of a backscattered wave is proportional to the wavenumber of the fluctuations responsible for backscattering. Actually, near the UHR, formula (13) reduces to

$$\Delta\omega \approx \ell k_x(x)\sqrt{2\langle\Omega^2\rangle\frac{\langle\delta n^2\rangle}{n^2}}, \quad x_{UH} - x \ll \ell_c.$$

When a probing wave with the wavenumber $\mathbf{k}_i$ is scattered by small-scale fluctuations with wavenumber $\mathbf{q}$, the wavenumber $\mathbf{k}$ of the backscattered wave is determined by the Bragg condition

$$\mathbf{k} = \mathbf{k}_i + \mathbf{q}.$$

For a backscattered wave, we have $\mathbf{k} = -\mathbf{k}_i$, so that the Bragg condition becomes $\mathbf{k}_i = -\mathbf{q}/2$. The width of the frequency spectrum of a probing wave along its path to the point at which it is scattered is determined by formula (13); for $\mathbf{k}_i = -\mathbf{q}/2$, the wave is scattered in the backward direction. Taking into account the fact that

the backscattering is most intense in the UHR region, we arrive at the following estimate for the width of the frequency spectrum of the backscattered wave:

$$\Delta\omega \sim \Omega_0 \frac{\delta n}{n} \ell q_x.$$

Now, we obtain a simple numerical estimate of the amplitude of the density fluctuations for conditions under which experiments on enhanced scattering by spontaneous fluctuations were carried out in the FT-1 tokamak [4]. In those experiments, the frequency spectrum was observed to broaden by an amount of about $\Delta f = \Delta\omega/(2\pi) \approx 2.5 \times 10^6$ Hz at a height equal to 10^{-2} of the spectrum height for $q_x \sim 100$ cm^{-1}, i.e., for $k_i \sim 50$ cm^{-1}.

We set $\ell \sim 1$ cm and assume that the fluctuations are drift fluctuations with $\Omega_0 = v_d q_0$, where $q_0 \sim 2$ cm^{-1} and $v_d \sim 2 \times 10^5$ cm/s.

Under these conditions, we obtain $\delta n/n \sim 0.1$, which is a quite realistic estimate.

Notably, our assumption that the frequency spectra of the scattered and probing waves broaden by the same amount serves merely to obtain estimates. If the small-scale fluctuations are entrained in large-scale turbulent motions, then, along with the frequency shift resulting from the small-scale fluctuations responsible for backscattering (in the approach developed here, this shift is neglected), there may also be Doppler broadening. Allowing for the influence of the Doppler effect on the frequency spectrum of a backscattered wave is the subject of an ongoing investigation.

5. CONCLUSION

We have studied the evolution of the frequency spectrum of an extraordinary wave during multiple small-angle scatterings along its path to the UHR, in the UHR region, and behind the conversion point. The analysis has been performed by the approximate eikonal method, but the formation of the frequency spectrum in the UHR region has been investigated exactly (in the limit of large-scale plasma density fluctuations). We have shown that these two approaches yield the same results in the common range of their applicability.

We have derived expressions describing the frequency spectrum of a probing wave and have calculated the spectrum width. The behavior of the width of the frequency spectrum in the UHR region agrees with the available experimental data. This circumstance and the predicted amount by which the frequency spectrum of a backscattered wave broadens at a fluctuation level of $\delta n/n \sim 0.1$ make it possible to consider small-angle scattering as one of the main effects responsible for the large spectrum broadening observed in experiments on enhanced scattering in the FT-1 tokamak [4].

ACKNOWLEDGMENTS

We are grateful to A.D. Piliya for his interest in this work and critical comments. We also thank D. Gresillon for fruitful discussions. This work was supported in part by the Russian Foundation for Basic Research (project nos. 02-02-17591, 01-02-17926, 00-15-96762, 02-02-17589, and 02-02-06632), INTAS (grant no. 01-2056), and the Netherlands Organization for Scientific Research (project no. NWO.047.009.009).

REFERENCES

1. K. M. Novik and A. D. Piliya, Plasma Phys. Controlled Fusion **36**, 357 (1993).
2. E. Z. Gusakov and A. D. Piliya, Pis'ma Zh. Tekh. Fiz. **18** (10), 63 (1992) [Sov. Tech. Phys. Lett. **18**, 325 (1992)].
3. V. I. Arkhipenko, V. N. Budnikov, E. Z. Gusakov, *et al.*, Pis'ma Zh. Tekh. Fiz. **19** (11), 20 (1993) [Tech. Phys. Lett. **19**, 333 (1993)].
4. D. G. Bulyginskiy, A. D. Gurchenko, E. Z. Gusakov, *et al.*, Phys. Plasmas **8**, 2224 (2001).
5. E. Z. Gusakov and A. V. Surkov, Fiz. Plazmy **27**, 1027 (2001) [Plasma Phys. Rep. **27**, 971 (2001)].
6. V. I. Tatarskiĭ, *Wave Propagation in Turbulent Atmosphere* (Nauka, Moscow, 1967).
7. B. Brüsehaber, E. Z. Gusakov, M. Krämer, and A. D. Piliya, Plasma Phys. Controlled Fusion **36**, 997 (1994).

Translated by I. A. Kalabalyk

Plasma Physics Reports, Vol. 28, No. 10, 2002, pp. 837–846. Translated from Fizika Plazmy, Vol. 28, No. 10, 2002, pp. 908–918.

PLASMA KINETICS

Numerical Modeling of the Formation of Steady-State Nonequilibrium Distributions of Particles Interacting through a Power-Law Potential

V. I. Karas'* and I. F. Potapenko**

**National Science Center Kharkov Institute of Physics and Technology, ul. Akademicheskaya 1, Kharkov, 61108 Ukraine*

***Keldysh Institute of Applied Mathematics, Russian Academy of Sciences, Miusskaya pl. 4, Moscow, 125047 Russia*

Received March 14, 2002

Abstract—The formation of a steady-state nonequilibrium distribution function of particles interacting through the repulsive potential $U \sim \alpha/r^\beta$ $(1 \le \beta \le 4)$, which operates at an infinite range, is studied numerically. The collisional particle dynamics in such a system is investigated using a spatially homogeneous nonlinear collision integral in the Landau–Fokker–Planck form, which is a model Boltzmann collision integral for arbitrary potentials of interaction accompanied by little momentum transfer between particles in collisions. Numerical modeling is based on completely conservative difference schemes. It is shown that the principal condition for the existence of steady-state nonequilibrium distributions is the presence of a particle or an energy flux oriented in the proper manner in momentum space. A steady-state local distribution exists inside the momentum interval between the energy source and sink and has the form of a gradually decreasing function. Since a radical change in the distribution function under nonequilibrium conditions leads to an anomalous enhancement of the conduction of a medium and its emission characteristics, the results obtained can be used, e.g., to predict the behavior of semiconductors with an intrinsic or extrinsic conductivity under the action of particle fluxes or electromagnetic radiation. © *2002 MAIK "Nauka/Interperiodica".*

1. INTRODUCTION

Nonequilibrium states of various physical systems are attracting increased interest in connection with the development and wide use of high-power particle and energy sources.

In physical systems in which the interactions between particles or waves can be described by the kinetic equations for waves, quasi-particles, or particles, the problem of constructing steady-state nonequilibrium distributions reduces to that of solving the kinetic equations. In this case, the local character of the steady-state nonequilibrium distribution corresponds to the convergence of the collision integral (at each point in momentum space, the main contribution to the collision integral comes from collisions between particles with close momenta).

For a classical (nondegenerate) gas, the Boltzmann kinetic equation has the form

$$\begin{aligned}\frac{\partial f(\mathbf{p})}{\partial t} &= \int d\mathbf{p}_1 d\mathbf{p}_2 d\mathbf{p}_3 W(\mathbf{p}, \mathbf{p}_1|\mathbf{p}_2, \mathbf{p}_3) \\ &\times [f(\mathbf{p}_2) f(\mathbf{p}_3) - f(\mathbf{p}) f(\mathbf{p}_1)] \\ &\times \delta(E + E_1 - E_2 - E_3)\delta(\mathbf{p} + \mathbf{p}_1 - \mathbf{p}_2 - \mathbf{p}_3),\end{aligned} \quad (1)$$

where $W(\mathbf{p}, \mathbf{p}_1|\mathbf{p}_2, \mathbf{p}_3)$ is the transition probability due to collisions, $f(\mathbf{p})$ is the particle (electron) distribution function, $\mathbf{p}_i$ and E_i are the momentum of an electron and its energy, and $\delta(x)$ is the Dirac delta function.

The distribution function with which the collision integral vanishes at any time t satisfies the condition

$$f(\mathbf{p}_2) f(\mathbf{p}_3) - f(\mathbf{p}) f(\mathbf{p}_1) = 0 \quad (2)$$

and is a steady solution to Eq. (1). Condition (2) with the energy and momentum conservation laws leads to a thermodynamically equilibrium Maxwellian distribution function f_{Maxw} (or a Fermi–Dirac distribution function in a degenerate gas).

At the beginning of this paper, we briefly review the results concerning the existence of steady-state local isotropic nonequilibrium distributions in a solid-state plasma, which seems to be a convenient object to study because it provides the possibility of controlling the extent to which the system in a stable state is nonequilibrium. The existence of a steady-state nonequilibrium distribution implies that there are particle source and sink in momentum space. The energy (particle) source and sink can be provided by ion beams, high-power laser radiation, emission currents, fluxes of charged particles produced in fusion or fission reactions, etc.

The characteristic feature of systems of charged particles interacting through the Coulomb potential is that the interaction cross section diverges in the limit of a small momentum transferred in a collision. To describe

1063-780X/02/2810-0837$22.00

a gas or a semiconductor plasma for which the Coulomb logarithm is large ($\ln\Lambda = 10$–15), it is sufficient to expand the integrand in powers of the small momentum transferred (the diffusion approximation) and to represent the collision integral in the Landau or Fokker–Planck form [1, 2]. The Landau (Fokker–Planck) kinetic equation, which is an essential element in various physical models, is widely applied in plasma physics. In Section 3, the kinetic equations mentioned above are presented and the formulation of the problem is discussed in detail. The formation of a steady-state nonequilibrium particle distribution function is investigated numerically for a wide range of parameters (different source and sink intensities, localization of the source and sink in momentum space, etc.). The calculated results are discussed, and it is shown that the Landau collision integral provides a correct description of a nonequilibrium distribution function in a plasma in which the main process is a small-angle scattering with little momentum transfer between the particles.

The objective of Section 4 is to consider the features of the conduction and emission characteristics of metals and semiconductors under the action of intense particle fluxes or laser light. As was mentioned in [3], the photoconductivity of a semiconductor irradiated by light whose frequency ω is insufficient to cause the interband transition $\hbar\omega < V_g$ (where V_g is the width of the forbidden band) may become anomalously high because of the formation of a nonequilibrium distribution of electrons and holes. Based on an analysis of the experimental results, Aseevskaya *et al.* [4] arrived at the conclusion that the irradiation of semiconductors by α-particles may substantially change their conduction properties. Some experimental data on the emission current from metals irradiated by lasers (in particular, its dependence on the retarding potential) cannot be explained on the basis of equilibrium distribution functions [5–7], but they are reasonably explicable in terms of the mechanism for the formation of nonequilibrium distributions [6–8].

In our opinion, all these circumstances confirm the above general statement about the formation of nonequilibrium distributions in the presence of external pumping. In this context, the physical effect associated with such fundamental changes in the electron distribution function are discussed.

2. STEADY-STATE NONEQUILIBRIUM ELECTRON DISTRIBUTION WITH AN ENERGY FLUX ALONG THE SPECTRUM

In the theory of the turbulence of incompressible liquids, a universal (independent of the structures of the source and sink) steady-state nonequilibrium energy spectrum ε_k in the wavenumber range between the wavenumbers of the excited and efficiently damped motions was first obtained by Kolmogorov [9]. The well-known Kolmogorov energy spectrum ε_k of the hydrodynamic turbulence has the form

$$\varepsilon_k = AP_1^{2/3}k^{-11/3}, \tag{3}$$

where A is a constant and P_1 is the energy flux along the spectrum. Spectrum (3) was derived on the basis of the hypothesis about the local character of turbulence, i.e., under the assumption that the interaction of perturbations occurring on close spatial scales is the strongest. In the theory of weak turbulence, universal wave spectra in the form of solutions to equations with the wave–wave collision integral were first derived by Zakharov [10].

Universal steady-state nonequilibrium power-law particle distribution functions $f = Ap^{2s}$ that are exact solutions to kinetic equations with the Boltzmann collision integral were first obtained by Kats *et al.* [11]. In order for such distributions to form, there should be a source and sink of particles (or energy) that provide a constant particle (or energy) flux in momentum space.

When the transition probability is an nth-power homogeneous function of momentum, the power s can naturally be determined by expressing the integrand in terms of the variables $\mathbf{p}_i/p$. Then, the right-hand side of Eq. (1) reduces to the product of the factor p^{4s+n+4} and an integral independent of p. In order to determine the particle (I_0) and energy (I_1) fluxes in momentum space, we use the following equations, which relate them to the collision integral:

$$\nabla\cdot\left(j_i(p)\frac{\mathbf{p}}{p}\right) = -E^i\left(\frac{\partial f}{\partial t}\right)_{St}, \tag{4}$$

where $I_i = 4\pi p^2 j_i$ and E is the particle energy. Solving Eqs. (4), we obtain

$$I_i = A^2\alpha^{1-i}\frac{R(s,n)}{4s+n+9+2(i-1)}p^{4s+n+9+2(i-1)}, \tag{5}$$

where α = const and the collision integral contains the factor $R(s, n)$.

From expressions (5), we can see that, if the powers s_i satisfy the conditions

$$\gamma = 4s+n+9+2(i-1) = 0, \quad i = 0, 1, \tag{6}$$

then the fluxes I_i in momentum space are either constant or are equal to zero when $R(s, n)$ has a first-order root at $s = s_i$. In both cases, the collision integral vanishes. In the equilibrium situation, the fluxes obtained from Eqs. (4) are identically zero, because the integrand in spectrum (2) with an equilibrium distribution vanishes at each point p. However, for a nonequilibrium distribution function, there is no need in conditions (6) and only the integral of the collision operator (rather than the operator itself) vanishes.

The distribution function Ap^{2s} corresponds to a steady-state nonequilibrium situation with a constant particle (or energy) flux in momentum space. The

direction of the flux is determined by the sign of the derivative $dR/d\gamma$ at $\gamma = 0$, and A is described by the expression

$$A^2 = I_i \alpha^{i-1} \lim_{\gamma \to 0} \left| \frac{dR}{d\gamma} \right|^{-1}. \quad (7)$$

The collision integral for steady-state nonequilibrium distributions satisfying the above conditions was calculated in a straightforward way in [12, 13]. In those papers, it was shown that the powers s of the local nonequilibrium particle distribution functions (for which the collision integral converges) lie within the intervals

$$-\frac{3}{2} < s_0 < -1; \quad -\frac{3}{2} < s_1 < -\frac{5}{4}. \quad (8)$$

The powers 0 and 1 correspond to the fluxes I_0, I_1 = const, respectively.

In accordance with conditions (6), intervals (8) correspond to the following intervals of the powers of a homogeneous function describing the transition probability:

$$-3 < n < -1, \quad I_0 = \text{const}, \quad (9)$$

$$-4 < n < -3, \quad I_1 = \text{const}. \quad (10)$$

From inequalities (9) and (10), we can see that, in the case of Coulomb interaction ($n = -4$), the collision integral diverges, which corresponds to the well-known singularity of W when the momentum transferred in collisions is small. Note that, in this case, the interaction potential in the coordinate (rather than momentum) space has the form $U = \frac{\text{const}}{r^{-4/n}}$. According to [12, 13], the divergence at $n = -4$ can be eliminated by taking into account the Debye screening. Thus, in [12, 13], it was shown that, for the transition probability corresponding to the screened Coulomb potential $W = 2e^4/(q^2 + a_i^2)^2$ (where q is the momentum transferred in a collision and a_i is the Debye momentum) and for particles with the momenta $p \gg a_i$, taking into account the Debye screening, on the one hand, eliminates the Coulomb divergence and, on the other, does not change the power of the steady-state nonequilibrium particle distribution function with a constant energy flux in momentum space. The power of the distribution function corresponds to the asymptotic behavior of W with the power $n = -4$.

Hence, in [12, 13], it was shown that particles with the momenta $p \gg a_i$ obey a local (in the sense of the convergence of the collision integral) power distribution function, in which case the particle density is determined by the flux intensity in momentum space. The flux conservation is ensured by the source and sink, whose positions should be consistent with the direction of the flux.

The case considered in [14] is more typical of solid-state plasmas; specifically, the electron distribution function is a power function inside the interval (p'', p') between the localized energy source and sink in momentum space and is a thermodynamically equilibrium Fermi–Dirac function outside this interval. It was shown that, under certain conditions on the positions of the source and sink and on their intensities (see below), the steady-state nonequilibrium electron distribution function is close to a universal function ($s = -5/4$ in the case of an unbounded inertial interval). Thus, the power s of the distribution of the filling numbers N_s differs from –5/4 by less than 10% under the conditions

$$|p'' - p'| \approx (5\text{–}6)p_{ch}, \quad N_s(p) \gg 10^{-3}, \quad p_{ch} = (2\text{–}3)a_i. \quad (11)$$

Hence, the electrons may obey a universal nonequilibrium distribution even when the filling numbers are substantially (by one to two orders of magnitude) smaller than the equilibrium numbers.

We have considered the formation of steady-state nonequilibrium distributions with sources and sinks localized in momentum space. Note, however, that it is often necessary to deal with systems in which the source and/or sink are nonlocalized; in particular, ionization by the wake field is described by a nonlocal source in momentum (energy) space.

3. NUMERICAL MODELING OF THE FORMATION OF STEADY-STATE NONEQUILIBRIUM PARTICLE DISTRIBUTIONS

In what follows, we will investigate a spatially homogeneous isotropic gas consisting of a single particle species. The particles are assumed to interact through the power-law potential $U = \frac{\text{const}}{r^\beta}$, where $\beta = -4/n$. Our model is based on the Boltzmann equation with the Landau collision integral [15, 16]. The first three tensor moments and the first four scalar moments of the model collision integral are assumed to coincide with those of the exact collision integral. The particle number and the energy are conserved, and the H-theorem for the Boltzmann equation is satisfied. The equations with the model collision integral provide a correct description of the system in the 20-moment approximation of the Grad method. Finally, an exact solution to the Landau equation for Maxwellian molecules ($\beta = 4$) is the exact solution to the Boltzmann equation.

We will be considering potentials operating at an infinite range ($1 \le \beta \le 4$), in which case a local nonequilibrium particle distribution may form [see inequalities (9) and (10)]. Note that the dynamics of the particles interacting by means of the Coulomb potential ($\beta = 1$) was previously studied using both the Landau kinetic equation and the Fokker–Planck kinetic equation.

For an isotropic distribution function $f(v, t)$, the kinetic equation with the Landau collision integral has the form

$$\frac{\partial f}{\partial t} = I_L[f, f]$$

$$= \frac{\Gamma}{v^2}\frac{\partial}{\partial v}\left\{\frac{1}{v}\int_0^\infty dw Q(v, w)\left[wf(w)\frac{\partial f(v)}{\partial v} - vf(v)\frac{\partial f(w)}{\partial w}\right]\right\},$$

$$Q(v, w) = \frac{a(v, w)(v + w)^{\eta+4} + b(v, w)|v - w|^{\eta+4}}{(\eta + 4)(\eta + 2)(\eta + 6)}, \quad 0 \le v, \quad w < \infty, \quad t \ge 0, \tag{12}$$

$$a(v, w) = [(\eta + 4)vw - (v^2 + w^2)],$$

$$b(v, w) = [(\eta + 4)vw + (v^2 + w^2)], \quad \eta = (\beta - 4)/\beta,$$

where $\Gamma = \dfrac{16\pi^2 e^4 \ln\Lambda}{m^2}$ and the symmetric kernel $Q(v, w) = Q(w, v)$ for the Coulomb potential is described by the expressions $Q(v, w) = (2/3)w^3$ for $w \le v$ and $Q(v, w) = (2/3)v^3$ for $w \ge v$.

Kinetic equation (12) with the Landau collision integral has an equilibrium solution in the form of a Maxwellian distribution function:

$$f_{\text{Maxw}} = \frac{n_p}{\pi^{3/2}} v_T^{-3} \exp\left[-\frac{v^2}{v_T^2}\right], \quad v_T = \sqrt{\frac{2k_B T}{m}},$$

where k_B is Boltzmann's constant and T is the temperature.

In the absence of sinks (or sources), the number of particles in the system and its energy are both constant in time:

$$n_p = 4\pi\int_0^\infty f(v, t)v^2 dv = \text{const},$$

$$n_p E = 2\pi m\int_0^\infty f(v, t)v^4 dv = n_p\frac{3}{2}k_B T = \text{const}.$$

The distribution function $f(v, t)$ is finite at $v = 0$ and decreases fairly rapidly as $t \longrightarrow \infty$ and $v \longrightarrow \infty$.

We introduce dimensionless variables such that the velocity is expressed in units of the thermal velocity $V_T = (3/2)^{1/2}v_T$ and the time is measured in units of the electron–electron relaxation time, which has the form $\tau_{ee} = \dfrac{v_T^3 m^2}{4\pi n_p e^4 \ln\Lambda}$ in the case of Coulomb interaction. In these variables, the parameters of the normalized dimensionless distribution function are $n_p = 1$, $v_T = 1$, $E = 3m/4$, in which case the constant Γ in kinetic equation (12) is equal to unity.

Note that rarefied collisional plasmas ($\beta = 1$) under laboratory conditions and in astrophysical applications are usually simulated using kinetic equations with the Fokker–Planck collision integral:

$$\frac{\partial f}{\partial t} = I_{\text{FP}}[f, f] = \frac{1}{v^2}\frac{\partial}{\partial v}\left[A(v)\frac{\partial f}{\partial v} + B(v)f(v, t)\right],$$

$$0 \le v < \infty, \quad t \ge 0.$$

For numerical modeling, it is most convenient to write the Fokker–Planck equation in symmetric form [17]:

$$\frac{\partial f}{\partial t} = I_{\text{FP}}[f, f]$$

$$= \frac{1}{v^2}\frac{\partial}{\partial v}\left\{\frac{1}{v}\frac{\partial}{\partial v}\int_0^v [f(v)P(x) - f(x)P(v)]x^2 dx\right\}, \tag{13}$$

where $P(x) = 2\int_v^\infty f(x)x dx$.

In modeling the formation of a nonequilibrium distribution on the basis of kinetic equations (12) and (13) with the Landau and Fokker–Planck modified collision integrals, respectively, the particle and energy fluxes in momentum space were taken into account by supplementing the right-hand sides of the kinetic equations with the following terms, which describe the energy (particle) source and sink:

$$\frac{\partial f}{\partial t} = I_{\text{FP, L}}[f, f] + S_+ - S_-.$$

The source and sink functions were modeled by exponential functions localized in different intervals in momentum space, $S_\pm \sim I_\pm \exp\{-\alpha_1(v - v_\pm)^2\}$, and by the localized function (Dirac delta function) $S_\pm \sim I_\pm \delta(v - v_\pm)/v^2$ or

$$S_\pm \sim I_\pm \frac{\delta(v - v_\pm)}{v^2} f(v_-, t). \tag{14}$$

When $I_+ = I_-$, we deal with the energy flux from the source toward the sink, and, when $I_+ = I_-\dfrac{v_-^2}{v_+^2}$, we deal with an analogous particle flux. The direction of the fluxes depends on the ratio of the velocities v_- and v_+.

The initial distribution function was assumed to be either a Maxwellian function or a delta function.

The simulations were carried out on the basis of completely conservative implicit difference schemes [15, 17] for which discrete analogues of the conservation laws are satisfied and which make it possible to perform long-run simulations without accumulating

computational errors. An infinite velocity interval was bounded from above by the highest possible velocities $10v_T$–$14v_T$, at which the distribution function was equal to a computer zero. The initial distribution in the form of a delta function was modeled by the function $\delta(v - v_0)$, which was zero over the entire velocity range used in simulations, except for a single velocity value (usually, $v_0 = 1$).

Since the relaxation problem is, in a sense, a test problem, we began by considering the Cauchy problem for kinetic equations with the initial distribution function $f^0(v) = \delta(v - 1)/v^2$. The corresponding simulations were carried out for kinetic equations (12) and (13) with the Landau and Fokker–Planck collision integrals.

Now, we proceed to a discussion of the results obtained from simulations of the formation of steady-state nonequilibrium distributions in the presence of energy or particle fluxes in momentum space. The right-hand sides of kinetic equations (12) and (13) were supplemented with the source and sink terms S_+ and S_-. First, we consider the results obtained for the case in which the source and sink were consistent with the direction of the collision-related flux in momentum space. Note that an analytic solution of the kinetic equations with a localized source and sink yields a correct flux direction, namely, the flux is directed downward along the velocity axis. From Fig. 1, we can see that, in the presence of an energy flux in momentum space, the initial particle distribution in the interval between the source and sink relaxes to a Kolmogorov steady-state nonequilibrium distribution, while the distribution function outside this interval is in thermodynamic equilibrium. Recall that the positions of the source and sink should be consistent with the flux direction in momentum space. In order to convince ourselves that this condition is very important, we interchanged the source and sink in energy space and performed the corresponding simulations. The results calculated for reversed positions of the source and sink are illustrated in Fig. 2, which shows the logarithm of the distribution function versus the square of the dimensionless velocity. In this case, a change in the flux intensity by several orders of magnitude produces no change in the equilibrium particle distribution.

Figure 3 was calculated for the source and sink terms described by the exponential functions of velocity. The source S_+ is localized in a "narrow" interval of energies corresponding to seven thermal velocities, and the sink S_- is localized in the energy interval corresponding to four thermal velocities. The lengths of the intervals in which the source and sink are localized is controlled by the coefficient α_1 in the exponential functions. In the case at hand, the coefficient is equal to 100; this very large value ensures a strong localization of the source and sink.

In order to investigate how the electron distribution function depends on the extent to which the source and sink are localized in energy space, we carried out a series of computations with a smaller (10 instead of 100) value of the above coefficient in the exponential functions. A comparison between the results presented in Figs. 3 and 4 shows that the character of the steady-state nonequilibrium distribution in the main region between the source and sink is independent of the

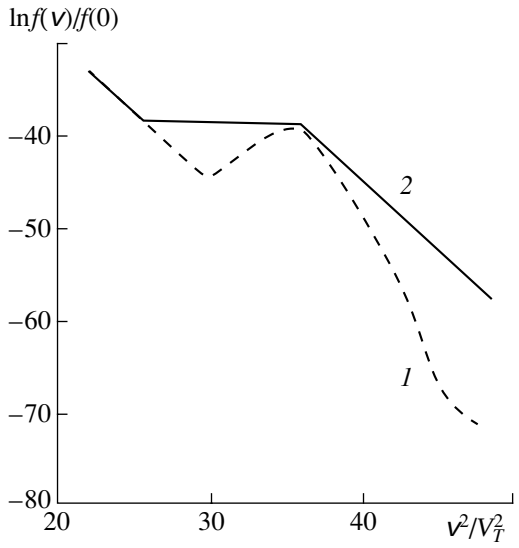

Fig. 1. Logarithm of the steady-state nonequilibrium distribution function normalized to its value at $v = 0$ vs. squared velocity. The computations were carried out for the initial Maxwellian distribution function and the source function with $I = 10^{-16}$, $v_- = 5$, and $v_+ = 6$. The dashed and solid curves were calculated from the Fokker–Planck equation at the times $t_1 = 5$ and $t_2 = 100$, respectively.

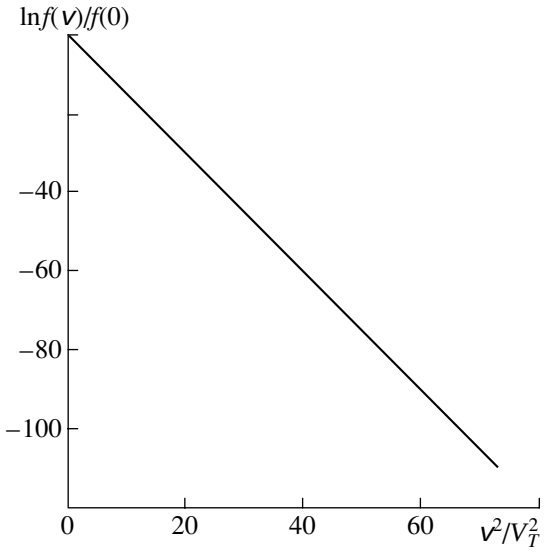

Fig. 2. Steady-state (equilibrium) distribution functions calculated for reversed positions of the source and sink ($v_+ = 5$, $v_- = 7$) from the Fokker–Planck equation and from the Landau equation with $\beta = 1$, 2, and 3.

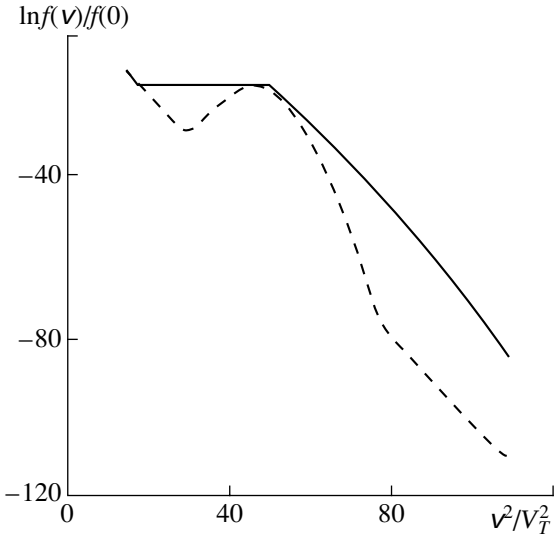

Fig. 3. Distribution function calculated from the Fokker–Planck equation with the source and sink functions $S_\pm \sim I_\pm \exp\{-\alpha_1(v - v_\pm)^2\}$ for $\alpha_1 = 100$, $v_- = 4$, and $v_+ = 7$. The dashed and solid curves refer to the times $t = 25$ and 100, respectively.

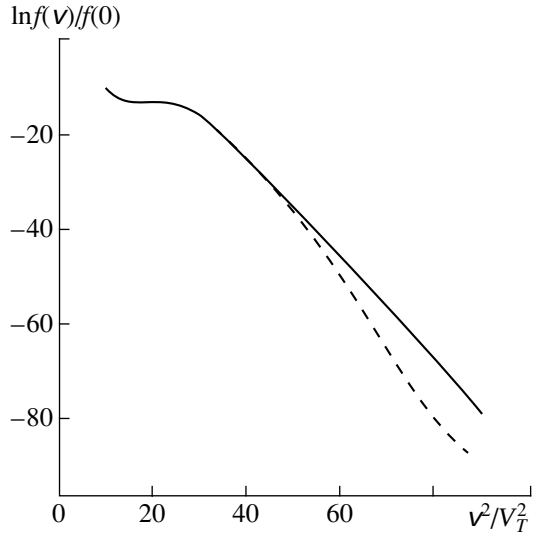

Fig. 4. Distribution function calculated from the Fokker–Planck equation with the source and sink functions $S_\pm \sim I_\pm \exp\{-\alpha_1(v - v_\pm)^2\}$ for $\alpha_1 = 10$, $v_- = 3$, and $v_+ = 5$. The dashed and solid curves refer to the times $t = 25$ and 100, respectively.

extent to which they are localized, thereby providing evidence of the local (universal) character of this solution to the kinetic equation.

Figure 5 shows how the distribution function depends on velocity for different flux intensities. We established that, when the intensities of the source (I_+) and sink (I_-) are both low, a universal nonequilibrium distribution forms in the velocity range $v \le v_+$. The reasons for this are twofold: first, with increasing velocity, the cross section for Coulomb scattering decreases (in proportion to $\sim v^{-3}$) and, second, diffusion due to Coulomb collisions always gives rise to energy and particle fluxes toward the region of the main ("background") equilibrium distribution function. As a result, the higher the intensities of the source and sink, the lower the relative intensity of the particle flux toward the background plasma and, accordingly, the larger the region in which a universal nonequilibrium particle distribution forms between the source and sink. It should be noted that, as the flux becomes more intense, the values of a nonequilibrium distribution function increase. This is because the nonequilibrium distribution function is proportional to the flux intensity [see Eq. (7)]. Some values of the steady-state nonequilibrium distribution function that were obtained by solving the Landau equation numerically are presented in Table 1. These values illustrate the results of a detailed study of the dependence of the solution on the flux intensity in momentum space, which was varied over a wide range. The initial source and sink functions were taken to be functions (14) with $v_- = 4$, $v_+ = 8$, and $dE = 0$.

Now, we consider the formation of a nonequilibrium particle distribution in the case of a constant particle ($dE = 0$, $I_+ = I_-\frac{v_-^2}{v_+^2}$) or energy ($dN = 0$, $I_+ = I_-$) flux. In order to simplify comparisons of the results obtained, it is convenient to normalize the distribution function to

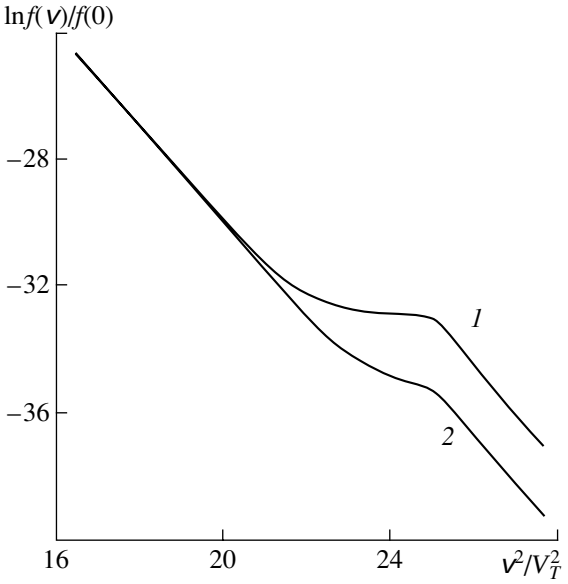

Fig. 5. Steady-state distribution function calculated from the Landau equation with $\beta = 2$ for the source and sink functions in the form of δ functions (14) at different flux intensities $I_1 = 0.01$ and $I_2 = 0.001$ ($v_- = 4$, $v_+ = 5$).

its value at zero, as is done in all figures presented in this paper, and, in particular, in Fig. 6, from which we can see the formation of gradually decreasing distribution functions with close powers s in the cases of a particle and an energy flux.

Let us analyze the shapes of the distribution functions of the particles interacting by means of different potentials with powers in the range $1 \le \beta \le 4$. Note that the power $\beta = 1$ corresponds to the Coulomb interaction potential, the power $\beta = 2$ refers to the dipole interaction potential, and the power $\beta = 4$ describes the interaction between the so-called Maxwellian molecules.

The dependence of the distribution function $f(v_+)$ on the power β for $I = 0.01$ is illustrated in Table 2.

Figure 7 shows nonequilibrium distribution functions calculated for the interaction potentials with $\beta = 1$, 2, and 4 and for an energy flux with the constant intensity $I = 0.01$. As may be seen, the powers s of the distribution functions that form in these three cases are close to each other, in agreement with conditions (8). The larger the power β, the shorter the interval over which the distribution function is nonequilibrium. These calculated results agree qualitatively with the above analytic predictions [see expression (7) and conditions (8)].

Table 1

I	$f(3.95)$	$f(7.95)$	$f(8)$
10	0.393×10^{-9}	0.417×10^{-10}	0.417×10^{-10}
1	0.475×10^{-9}	0.144×10^{-10}	0.144×10^{-10}
0.1	0.508×10^{-9}	0.189×10^{-11}	0.189×10^{-11}
0.01	0.517×10^{-9}	0.197×10^{-12}	0.197×10^{-12}
0.001	0.518×10^{-9}	0.198×10^{-13}	0.198×10^{-13}
0.0001	0.519×10^{-9}	0.196×10^{-14}	0.196×10^{-14}

Note: The values of the distribution function are seen to increase with increasing intensity I: at low intensities (to 0.1), the values of the distribution function increase in proportion to I because of the large contribution of the interaction of nonequilibrium particles (i.e., the particles from the interval between the source and sink) with the background particles, whose distribution is thermodynamically equilibrium; at moderate intensities (from 0.1 to 20), the distribution function is of a universal nature over the entire interval between the source and sink and is proportional to the square root of the intensity I, in agreement with expression (7); and, at higher intensities, the distribution function is no longer proportional to the square root of the intensity because it enters into the sink function in formulas (14).

4. MECHANISM FOR THE FORMATION OF THE ELECTRON DISTRIBUTION FUNCTION IN THE INTERACTION OF ELECTROMAGNETIC RADIATION WITH A SOLID-STATE PLASMA

In this section, we focus on the distinctive features of the conduction and emission characteristics of a semiconductor plasma that is affected by intense particle fluxes or laser radiation.

Let us compare the characteristic times of the electron energy relaxation due to electron–electron and electron–phonon collisions. In the interaction of particle fluxes or fluxes of intense electromagnetic radiation with a semiconductor plasma, ionization processes produce electrons with the energies $E \ge \hbar\omega$, where ω is the radiation frequency. The energy spectrum of the electrons produced by particle fluxes extends from tens of electronvolts to tens of kiloelectronvolts. According to [18], at high temperatures $T > \Theta_D$ (where Θ_D is the Debye temperature), the frequency of collisions between electrons with sufficiently high energies E ($E \gg k_B T$) is described by the expression

$$\gamma^{ee}(E, T) = \gamma_0^{ee}(T)\left[1 + \left(\frac{E}{k_B T}\right)^2\right], \qquad (15)$$

where $\gamma_0^{ee}(T)$ is the classical high-temperature electron–electron collision frequency, which is proportional to T^2. Under the same conditions, the electron–phonon collision frequency has the form [18]

$$\gamma^{ef} = \frac{f(\Theta_D)T}{\Theta_D}, \qquad (16)$$

where $f(\Theta_D)$ is the classical high-temperature electron–phonon collision frequency at $T = \Theta_D$. For the processes

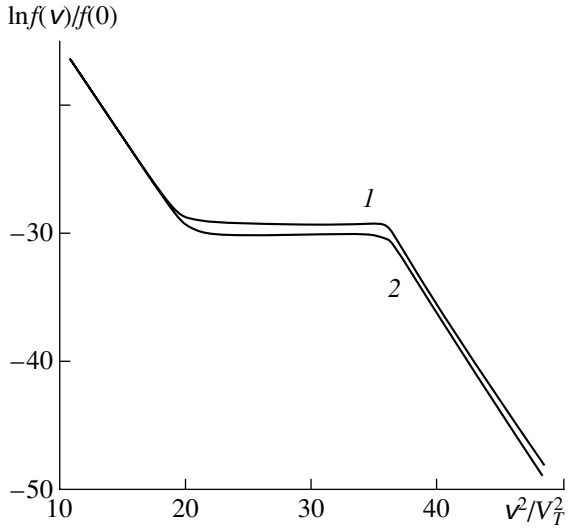

Fig. 6. Steady-state distribution function calculated from the Landau equation with $\beta = 1$ for the source and sink functions in the form of δ functions (14) at $I_{\mp} = 0.01$, $v_- = 4$, and $v_+ = 6$. Curve *1* and *2* correspond to a constant energy flux ($dN = 0$) and a constant particle flux ($dE = 0$), respectively.

Table 2

β	1	1.5	2	3	4
$f(8)$	0.197×10^{-12}	0.123×10^{-13}	0.266×10^{-14}	0.771×10^{-15}	0.384×10^{-15}

under discussion, the conditions under which expressions (15) and (16) are valid hold because we have $E >$ 10 eV, T = 300 K, and Θ_D = 200–300 K. Note that the quantities that are inversely proportional to the collision frequencies (15) and (16) generally differ from the electron energy relaxation times, which depend, in particular, on the number of collisions in which an electron loses its total energy E; therefore, it is necessary to take into account the factor $\xi = E/E_1$ (where E_1 is the energy lost by an electron in a single collision). According to the results obtained in [18], in the case in question, we can write

$$\gamma^{\text{ef}} \approx \gamma_0^{ee}, \quad \gamma^{ee} \gg \gamma_0^{ee}.$$

On the contrary, for electron–electron collisions, the factor ξ can be on the order of unity, and, for electron–phonon collisions, we have $E/k_B\Theta_D > 3 \times 10^2$. Hence, in this case, the time of the electron energy relaxation due to electron–electron collisions is substantially shorter than that due to electron–phonon collisions.

A comparison of the characteristic ionization time with the relaxation times shows that, in our case, the electron distribution function is quasi-steady and is governed primarily by electron–electron collisions. Consequently, this function can be determined from the condition for the Boltzmann (Landau–Fokker–Planck) collision integral to vanish.

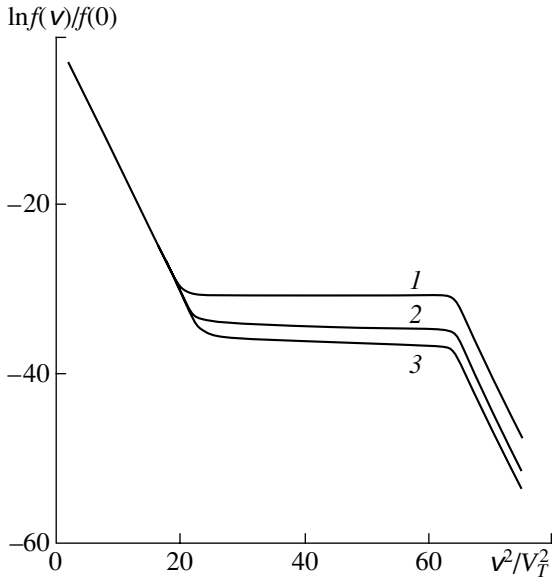

Fig. 7. Steady-state nonequilibrium distribution function vs. squared velocity. The computations were carried out for an energy flux with the constant intensity I = 0.01, for the source and sink functions in the form of δ functions (14), and for v_- = 4 and v_+ = 8. Curves *1*, *2*, and *3* were calculated from the Landau equation with the powers β = 1, 2, and 4, respectively.

The above analysis shows that, in semiconductor plasmas, the power-law distribution function corresponding to a constant energy or particle flux in momentum space can exist in the energy range $(E - E_F) > E_F$. This distribution is formed by both collisions with electrons in the energy range $(E - E_F) > E_F$ and collisions with background (equilibrium) electrons.

As was shown above, the nonequilibrium electron distribution is close to a universal distribution if the intensity of the flux produced by the source and sink in momentum space is sufficiently high.

As an example, we consider a solid-state plasma that is affected by a flux of fast ions (with speeds higher than those of atomic electrons). A typical situation in a single ion track can be described as follows. Let the energy of a helium ion be $\varepsilon_i \approx 5$ MeV, the excitation potential be $\Phi \approx 100$ eV, and the ion mean free path in the target material be $R_{\text{tr}} \approx 10^{-3}$ cm. The number of electrons produced during ionization processes along the path of a helium ion is about 10^4–10^5. The radius of the ionization track of an ion is comparable with the mean free path of the electrons produced ($R_e \approx 10^{-6}$ cm). The electron density in an ionization track is $n_{en} \approx 10^{19}$–10^{20} cm^{-3}, the equilibrium electron density being $n_e \approx 10^{22}$ cm^{-3}. The above analysis shows that, for such ratios of the electron densities, the source and sink are sufficiently intense for the nonequilibrium distribution function to form.

Let us now consider the mechanisms by which a fast ion loses its energy in a solid-state plasma. Note that, under conditions typical of the ion beam–driven inertial confinement fusion, the ion energy loss is independent of the ion density in the beam (cf. [19]). Taking into account this circumstance, we can calculate the energy lost by an ion from the Bethe–Bloch formula. According to [20], the energy of a fast nonrelativistic particle is transferred to a medium by the following two mechanisms. A fraction of the particle energy is expended on the excitation of collective oscillations associated with wake charge density waves, and the remaining fraction is transferred to individual electrons, with a subsequent ionization of the medium. The former fraction corresponds to the macroscopic energy loss in long-range collisions with little momentum transfer, and the latter fraction corresponds to collisions with large momentum transferred. The fraction of the particle energy that is lost through the excitation of collective oscillations is

relatively large. The energy $\Delta\varepsilon_k$ converted into the wake charge density waves can be represented as [20]

$$\frac{\Delta\varepsilon_k}{\Delta\varepsilon} = \frac{\ln(v/10v_0)}{2\ln(v/v_0)}, \quad (17)$$

where $\Delta\varepsilon$ is the total energy lost by an ion and v_0 is the electron speed in the ground state of the hydrogen atom.

From representation (17), we can see that the energy $\Delta\varepsilon_k$ of the wake charge density waves is on the order of the total energy transferred from a particle to the medium.

A fast particle passing through the medium produces slow electrons by two equiprobable mechanisms: by avalanche ionization and by ionization through the excitation of plasma oscillations. The main features of the electron production through ionization by plasma oscillations are associated with long time and spatial scales of the wake charge density waves. Because of the long time scale of the waves, the secondary ionization inside the beam proceeds for a long time after the passage of a beam particle. A substantial number of slow electrons are liberated in cascade ionization caused by a high-energy secondary electron. Since the mean free path of such an electron in a medium is long, most of the slow electrons are produced in cascade ionization along its path. As a result, ionization by the wake field is the dominant process affecting the distribution of liberated electrons near the axis of the particle track, whereas cascade ionization is responsible for the distribution of liberated electrons at distances from the track axis that are on the order of the electron mean free path. Since a charged particle ionizes the medium by its self-field only during its passage and since the wake charge density waves play the role of a linear source of secondary electrons for a long time after the passage of the ionizing particle, the ionization dynamics is governed completely by the secondary electrons.

As was mentioned above, despite the short time required for an ion to pass along the track, the characteristic time of the avalanche ionization by wake charge density waves is fairly long (about 10^{-13} s).

In the interaction with a solid-state plasma, intense electromagnetic radiation with a frequency satisfying the condition $\hbar\omega \gg k_B T$ produces a large number of high-energy electrons, which, according to the above analysis, obey a steady-state nonequilibrium distribution function. Hence, in the case of a plasma irradiated by intense electromagnetic radiation or affected by the fluxes of fast particles, we deal with a nonequilibrium electron distribution, which differs from an equilibrium distribution in that it involves a large number of high-energy electrons. Let us analyze some physical consequences of such a fundamental change of the electron distribution function.

The density of the electron emission current from a solid-state plasma has the form

$$j = B_1 \int_{\varphi + eE_F}^{E_+} Ef(E)dE.$$

From this expression, we can see that, in a plasma with a nonequilibrium electron distribution, the electron emission current density is anomalously high, because, in the inertial interval, the distribution function decreases very gradually. The conduction characteristics of the medium are governed by the density of the current carriers, so that, in a semiconductor plasma with a nonequilibrium electron distribution, this density is very high, in contrast to the case of an exponentially decreasing equilibrium distribution function. That is why, under the action of intense fluxes of electromagnetic radiation or fast particles, the emission and conduction properties of a semiconductor plasma can become anomalous. Note that such anomalies have already been observed in some experiments (see, e.g., [4, 7]).

5. CONCLUSION

In conclusion, we summarize the results obtained from numerical modeling of the formation of steady-state nonequilibrium distribution functions.

For a distribution function computed from the kinetic equation with the Landau collision integral, we have established the following:

(i) In the interval between the source and sink located at certain positions in momentum space, the particles interacting through the Coulomb potential relax to a steady-state nonequilibrium distribution. Moreover, above certain source and sink intensities, the distribution function over almost the entire interval between the source and sink is of a universal nature; i.e., it obeys the same power law.

(ii) The functional dependence of the steady-state nonequilibrium electron distribution is sensitive nether to the extent to which the source and sink are localized in momentum space nor to the length of the inertial interval (i.e., the interval between the source and sink). It is, however, necessary that the positions of the source and sink be consistent with the direction of the energy flux in momentum space. Recall that the flux direction is determined by the nature of the interaction between particles and is entirely independent of the source and sink structures. In other words, the particles relax to universal local distribution functions.

(iii) For Coulomb and dipole interactions between Maxwellian molecules, the power s of the nonequilibrium distribution function that forms in the inertial interval decreases somewhat as the power β increases, in which case the values of the distribution function also become smaller.

(iv) For the source and sink intensities in the interval $0.001 \le I \le 0.1$, the distribution function computed from the Fokker–Planck equation is proportional to the intensity; as the intensity increases from 1 to 10, the values of the distribution function increase only by a factor of 3.

The fundamental change in the electron distribution function under nonequilibrium conditions leads to an anomalous enhancement of the conduction and emission characteristics of the medium. The results obtained in our investigations can be used to predict the behavior of semiconductors with an intrinsic or extrinsic conductivity in the fluxes of fast particles, as well as in intense electromagnetic radiation.

REFERENCES

1. B. A. Trubnikov, in *Reviews of Plasma Physics*, Ed. by M. A. Leontovich (Gosatomizdat, Moscow, 1963; Consultants Bureau, New York, 1963), Vol. 1.
2. V. P. Silin, *Introduction to the Kinetic Theory of Gases* (Nauka, Moscow, 1971).
3. V. I. Karas', Pis'ma Zh. Tekh. Fiz. **1**, 1020 (1975) [Sov. Tech. Phys. Lett. **1**, 438 (1975)].
4. A. S. Assovskaya, E. B. Ivkin, and B. G. Kolomiets, Pis'ma Zh. Tekh. Fiz. **2**, 305 (1976) [Sov. Tech. Phys. Lett. **2**, 44 (1976)].
5. W. L. Knecht, Appl. Phys. Lett. **6**, 96 (1965).
6. W. L. Knecht, Appl. Phys. Lett. **8**, 254 (1966).
7. S. I. Anisimov, Ya. A. Imas, G. S. Romanov, and Yu. V. Khodyko, *High-Power Radiation Action on Metals* (Nauka, Moscow, 1970).
8. V. I. Karas', S. S. Moiseev, and V. E. Novikov, in *Proceedings of the XV International Conference on Phenomena in Ionized Gases, Minsk, 1981*, Vol. 1, p. 73.
9. A. N. Kolmogorov, Dokl. Akad. Nauk SSSR **30**, 299 (1941).
10. V. E. Zakharov, Zh. Prikl. Mekh. Tekh. Fiz., No. 4, 35 (1965).
11. A. V. Kats, V. M. Kontorovich, S. S. Moiseev, and V. E. Novikov, Pis'ma Zh. Éksp. Teor. Fiz. **21**, 13 (1975) [JETP Lett. **21**, 5 (1975)].
12. V. I. Karas', S. S. Moiseev, and V. E. Novikov, Pis'ma Zh. Éksp. Teor. Fiz. **21**, 525 (1975) [JETP Lett. **21**, 245 (1975)].
13. V. I. Karas', S. S. Moiseev, and V. E. Novikov, Zh. Éksp. Teor. Fiz. **71**, 1421 (1976) [Sov. Phys. JETP **44**, 744 (1976)].
14. V. I. Karas', S. S. Moiseev, and A. P. Shuklin, Ukr. Fiz. Zh. **25**, 820 (1980).
15. A. V. Bobylev, I. F. Potapenko, and V. A. Chuyanov, Zh. Vychisl. Mat. Mat. Fiz. **20**, 993 (1980).
16. I. F. Potapenko, A. V. Bobylev, C. A. Azevedo, and S. S. Assis, Phys. Rev. E **56**, 7159 (1997).
17. I. F. Potapenko and V. A. Chuyanov, Zh. Vychisl. Mat. Mat. Fiz. **19**, 458 (1979).
18. J. M. Ziman, *Electrons and Phonons* (Clarendon, Oxford, 1960; Inostrannaya Literatura, Moscow, 1962).
19. M. M. Basko and M. V. Sokolovskiĭ, Preprint No. 177 (Inst. of Theoretical and Experimental Physics, Moscow, 1980).
20. Y.-H. Ohtsuki, *Charged Beam Interaction with Solids* (Taylor and Francis, London, 1983; Mir, Moscow, 1985).

Translated by O. E. Khadin

Plasma Physics Reports, Vol. 28, No. 10, 2002, pp. 847–857. Translated from Fizika Plazmy, Vol. 28, No. 10, 2002, pp. 919–929.

DUSTY PLASMA

Heat Exchange in Dusty Plasma

A. M. Ignatov

Institute of General Physics, Russian Academy of Sciences, ul. Vavilova 38, Moscow, 117942 Russia

Received April 18, 2002

Abstract—The effect of the charge of a dust grain on the exchange of its heat with plasma particles and with neutral gas particles in an anisotropic dusty plasma with dissipative flows is discussed. It is shown, in particular, that nonuniform heating of the grain surface gives rise to the radiometric force, which may be stronger than the ion wind force. Also, the grain charge causes the thermophoretic force to change its sign. © *2002 MAIK "Nauka/Interperiodica".*

1. INTRODUCTION

Much of the diversity of physical processes in gas aerosols is associated with heat and mass exchanges between grains and the gas surrounding them. These processes have been studied for more than a century, and, by now, there is a well-developed body of knowledge about the main effects in the physics of aerosols [1].

A comparatively low degree of gas ionization in an aerosol changes its properties so substantially that it is legitimate to speak of a new medium—a dusty plasma or an aerosol plasma. Since the most distinctive feature of an aerosol plasma is the large grain charge, the vast majority of works in this area deal precisely with plasma phenomena.

The presence of the plasma component can greatly affect heat exchange between the grains and the surrounding medium and, accordingly, influence the associated phenomena. Roughly speaking, in the absence of chemical reactions, the maximum amount by which the grain surface can be heated when the grain is struck by a neutral atom is limited to the atom's kinetic energy. On the other hand, an ion striking the grain will almost inevitably recombine with it, so that essentially all of the ionization energy (which is two to three orders of magnitude higher than the ion thermal energy) goes into heating the grain surface. The ion flux heating the grain surface is intensified by the large negative grain charge, which accelerates the incident ions; as a result, the effective cross section for ion absorption becomes one to two orders of magnitude larger than that for an uncharged grain of the same size. That is why, in a dusty plasma, the heat flux onto the grain surface may be far more intense than that in a gas aerosol, even when the density of the plasma component is comparatively low.

The related problems have been little studied in the literature: among several thousands of works on dusty plasmas that were published during the past decade, only a few papers (almost all of them are cited below) dealt with the effect of plasma on classical aerosol processes. The reason why these problems have been deprived of attention is fairly specific and is apparently associated with the fact that the majority of scientists whose interests lie in this field of research originally worked in plasma physics.

The effect of the neutral gas temperature gradient and the related thermophoresis phenomenon were studied in several papers [2–5]. The essence of this phenomenon, which can be easily observed in everyday life, is that aerosol particles are expelled to the region with a lower gas temperature. At this point, it is worthwhile to make a terminological remark. The thermophoretic force acting on a dust grain should be distinguished from the thermal force used in the hydrodynamic description of a continuous medium. The thermophoretic force depends on the internal grain structure, while the thermal force is governed completely by the gas kinetic coefficients. A good comprehensive review of thermophoresis can be found in [6].

In recent experiments, thermophoresis has been exploited to confine dust grains within the plasma volume [7]. If the temperature of the grain surfaces is for some reason lower than the temperature of the surrounding gas, then each of the grains gives rise to a heat flux converging to it, and thermophoresis may initiate the effective attraction of dust grains and cause them to agglomerate [5, 8, 9]. Thermophoresis has a significant impact on the formation of dust structures in a thermal plasma [10]. The problem of whether thermophoresis may be used for disposing of radioactive wastes from tokamaks was discussed in [11]. Among other phenomena in aerosols, we should mention photophoresis, which serves as a working tool for controlling the motion of individual grains in many experiments with dusty plasmas [12].

Several papers were devoted to studying the influence of the plasma component on heat exchange processes and related phenomena. The heating of grain surfaces in a dusty plasma was investigated experimentally in [13–15]. In some cases (e.g., in an arc discharge plasma), the grain surfaces may be heated so substantially that thermal emission begins to play an important

1063-780X/02/2810-0847$22.00

role, in which case the grain charge is affected not only by electric currents but also by heat fluxes [16]. To the best of my knowledge, the question of thermophoresis in a dusty plasma was first addressed in [17]. Chen [18, 19] developed a theory of thermophoresis that applies to dust grains with sizes larger than the Debye radius and in which plasma recombination is taken into account. Because of the nonuniform heating of the grain surfaces by ion flow, the grain–neutral gas interaction gives rise to the radiometric force [20], which may be stronger than the ion drag force. Of course, the dust component may have an inverse effect on the thermal properties of the surrounding plasma. In particular, because of the large grain charge, the thermal force acting on plasma ions may be governed by ion–grain collisions under certain conditions [21].

The problem addressed in this study is the following. Assume that a certain dissipative flow, e.g., a convective current or a heat flux, have already been formed in a weakly ionized plasma. The intensities of these fluxes are determined by collisional processes on characteristic scales of about several mean free paths l_0, by the boundary conditions, and possibly by the parameters of the external electric circuit. However, this part of the problem is not investigated here, so that the dissipative flows are assumed to be known. In such a plasma, a grain acquires a large negative charge and thus strongly perturbs the surrounding medium on spatial scales of about several electron Debye radii λ_D. If $l_0 \gg \lambda_D$, the dissipative flows on these spatial scales give rise to anisotropic corrections to the equilibrium (Maxwellian) distribution functions of the plasma components. The main questions discussed in this paper are as follows: How does the Debye layer perturb the anisotropic part of the distribution function? How do the heat fluxes change at the grain surface? And what are the forces that arise due to the grain–neutral gas interaction? The main of the results obtained is that the heating of the grain surface is highly nonuniform because of the large negative grain charge. Although the relative temperature difference over the grain surface is relatively small (at most, fractions of a percent), the interaction between the grain and neutral gas gives rise to a fairly strong radiometric force. The force acting on a grain in a dissipative heat flux is antiparallel to the flux vector, so that the grain is expelled to a hotter plasma region.

The interaction of the grain surface with the surrounding medium is described by the following model. The grain absorbs all of the electrons that strike its surface. Each of the ions striking the grain recombines with it to produce a neutral atom and liberates the energy of ionization, which goes into heating the grain surface. The atom produced flies away from the grain in a random direction with a random energy corresponding to the local temperature of the grain surface. A collision between a neutral atom and the grain is described in the same manner; i.e., the approximation of the complete energy accommodation is assumed. The plasma is treated as a free-molecule gas: the characteristic spatial scales satisfy the inequalities $n^{-1/3} \ll a \ll \lambda_D \ll l_0$, where a is the grain radius and n is the density of any of the plasma components.

The paper is organized as follows. In Section 2, the basic equations are formulated and the simplifying assumptions (which are, frankly speaking, the most rough of all possible assumptions) are described. In Section 3, the energy and particle fluxes at the grain surface are calculated. In Section 4, these fluxes are used to determine the temperature distribution over the grain surface. The resulting momentum and force fluxes are analyzed in Section 5. In the Conclusion, the main results obtained in this study are summarized and the questions are discussed of whether the processes under consideration can be observed experimentally and whether they could have been observed in experiments earlier.

2. BASIC EQUATIONS

We consider an individual grain in an anisotropic plasma with the quasi-equilibrium distribution functions $\Phi_\alpha(\mathbf{p})$ ($\alpha = e, i$) of plasma electrons and ions. In particular, the plasma anisotropy may stem from dissipative flows, e.g., an electric current or a heat flux. The details of the distribution functions in the plasma volume are determined by collisions between plasma particles and by their collisions with neutral atoms.

At distances of about several Debye radii from the grain surface, the distribution functions of the plasma particles differ strongly from $\Phi_\alpha(\mathbf{p})$ because of the formation of particle flows that are directed toward the grain surface and, in particular, govern the grain charge.

Under the assumption that the characteristic mean free paths of the plasma particles are longer than their Debye radii, the plasma in the vicinity of the grain can be described by the steady-state Vlasov equation

$$\frac{\mathbf{p}}{m_\alpha}\frac{\partial f_\alpha(\mathbf{p}, \mathbf{r})}{\partial \mathbf{r}} - e_\alpha \frac{\partial \varphi(\mathbf{r})}{\partial \mathbf{r}}\frac{\partial f_\alpha(\mathbf{p}, \mathbf{r})}{\partial \mathbf{p}} = 0 \qquad (1)$$

and Poisson's equation

$$\begin{aligned}\Delta\varphi(\mathbf{r}) &= -4\pi\sum_\alpha e_\alpha n_\alpha(\mathbf{r}) \\ &= -4\pi\sum_\alpha e_\alpha \int d\mathbf{p}\, f_\alpha(\mathbf{p}, \mathbf{r}).\end{aligned} \qquad (2)$$

Here, e_α and m_α are the charge and mass of the corresponding particle species. The boundary conditions for Eq. (1) have the form

$$f_\alpha(\mathbf{p}, \mathbf{r})|_{r = a,\, p_r > 0} = 0 \qquad (3)$$

(where a is the radius of a spherical grain) and

$$f_\alpha(\mathbf{p}, \mathbf{r})|_{r\to\infty} = \Phi_\alpha(\mathbf{p}). \quad (4)$$

Condition (3) describes plasma recombination at the grain surface.

Poisson's equation (2) can be supplemented with the boundary conditions implying that the electric potential is constant at the grain surface and equals zero inside the plasma volume:

$$\varphi(\mathbf{r})|_{r=a} = \varphi_0, \quad (5)$$

$$\varphi(\mathbf{r})|_{r\to\infty} = 0. \quad (6)$$

Condition (6) is consistent with Poisson's equation only when the charge density of the unperturbed plasma is equal to zero, which will be assumed in further analysis.

The grain potential φ_0 can be determined as follows. Having solved Eqs. (1) and (2) with the boundary conditions (3)–(6), we can calculate the radial currents of the plasma components to the grain surface, $j_\alpha(\mathbf{\Omega}) = \mathcal{F}(\mathbf{\Omega}; 1)$. Here and below, the radial flux of any quantity $G(\mathbf{p})$ is denoted by

$$\mathcal{F}(\mathbf{\Omega}; G(\mathbf{p})) = \int d\mathbf{p}\frac{p_r}{m_\alpha} f_\alpha(\mathbf{p}, a\mathbf{\Omega})G(\mathbf{p}) \quad (7)$$

and the angular coordinates are characterized by the unit vector $\mathbf{\Omega} = \mathbf{r}/r$, such that $p_r = \mathbf{p}\cdot\mathbf{\Omega}$. In this notation, the condition that the total electric current vanishes,

$$I(\varphi_0) = \sum_\alpha e_\alpha \int d\Omega\, j_\alpha(\mathbf{\Omega}) = 0 \quad (8)$$

determines the equilibrium floating potential φ_0, in which case the grain charge is to be calculated as the electric field flux through the grain surface

Of course, this formulation of a standard probe problem is so general that the problem cannot be solved analytically and is even very difficult to investigate numerically. System (1)–(6) can be investigated most completely for an isotropic plasma in the so-called orbital motion limit (OML) [22, 23], in which case the potential $\varphi(r)$ is spherically symmetric. The main assumption of the OML theory is that the grain surface is reached by all of the particles for which this is allowed by the conservation laws for energy and angular momentum. For this to occur, it is necessary that the effective potential $U_\alpha^{(\mathrm{eff})}(r) = e_\alpha\varphi(r) + M^2/2m_\alpha r^2$, which determines the particle trajectories, have no positive maxima at any value of the angular momentum M. This is a fairly strong restriction on the dependence $\varphi(r)$. An analysis of self-consistent solutions [24–26] shows that, strictly speaking, the assumptions of the OML theory always fail to hold. Nevertheless, the OML theory is widely used because it provides a good approximate description of the grains whose sizes are small in comparison with the plasma Debye radius, $a \ll \lambda_D$.

In order to estimate how the plasma anisotropy affects the nonuniformity of particle fluxes over the grain surface, several simplifying assumptions need to be made. We consider a weakly anisotropic unperturbed plasma described by the distribution function

$$\Phi_\alpha(\mathbf{p}) = \Phi_{0\alpha}(p^2/2m_\alpha) + (\mathbf{p}\cdot\boldsymbol{\mu})\Phi_{1\alpha}(p^2/2m_\alpha), \quad (9)$$

where $\boldsymbol{\mu}$ is the unit vector of the plasma anisotropy and $\Phi_{1\alpha} \ll \Phi_{0\alpha}$.

It seems that the distribution function $f_\alpha(\mathbf{p}, \mathbf{r}) = f_{0\alpha}(\mathbf{p}, \mathbf{r}) + f_{1\alpha}(\mathbf{p}, \mathbf{r})$, where $f_{0\alpha}(\mathbf{p}, \mathbf{r})|_{r\to\infty} \longrightarrow \Phi_{0\alpha}(p^2/2m_\alpha T_\alpha)$ and $f_{1\alpha}(\mathbf{p}, \mathbf{r})|_{r\to\infty} \longrightarrow (\boldsymbol{\mu}\cdot\mathbf{p})\Phi_{1\alpha}(p^2/2m_\alpha T_\alpha)$, and the self-consistent potential $\varphi(\mathbf{r})$ should also be represented in an analogous manner. However, as was shown in [27], the effect of the deviation of the self-consistent potential from being spherically symmetric is insignificant when $a \ll \lambda_D$. Consequently, instead of solving the complete problem (1)–(6), we can restrict ourselves to investigating Eq. (1) with the boundary conditions (3) and (4) and with the spherically symmetric potential $\varphi(\mathbf{r}) = \varphi(r)$.

However, since the explicit form of the self-consistent potential $\varphi(r)$ is unknown even in the OML approximation, it should be approximated in one way or another. The simplest possible approximation is analogous to that used in deriving the Landau collision integral. Assuming that, inside a sphere of radius R_0, the effect of the self-consistent field is insignificant, we replace the self-consistent potential in Eq. (1) by the Coulomb potential

$$\varphi(r) = \varphi_0\frac{a}{r}. \quad (10)$$

It is reasonable to assume that the radius R_0 is about several Debye radii. Consequently, for $a \ll \lambda_D$, the solutions to Eq. (1) can be analyzed in the limit of infinitely large R_0 values (of course, taking this limit should not lead to singularities). The exact solution to Poisson's equation (2) can also be approximated by another potential, e.g., by the Debye–Hückel potential. In connection with the problem of the drag force exerted by an ion flux on a grain, this point was discussed by Kilgore *et al.* [28], who showed that the final result is weakly sensitive to the particular form of the approximating potential.

Equation (1) with a spherically symmetric potential can be solved most simply by the method of characteristics. We assume that, at the grain surface (at $\mathbf{r} = a\mathbf{\Omega}$), the particle momentum is $\mathbf{p}$ and that, for $r \longrightarrow \infty$, the direction of the particle trajectory is determined by the unit vector $\mathbf{\Omega}'$ and the particle momentum is $\mathbf{p}' = -p_r'\mathbf{\Omega}'$. Using the conservation laws for energy and angular

momentum, we can find the relationship between $\mathbf{p}$ and $\mathbf{p}'$:

$$p_r' = \sqrt{p^2 + 2m_\alpha e_\alpha \varphi_0}, \quad (11)$$

$$\mathbf{\Omega}' = \mathbf{\Omega}\cos\vartheta(\mathbf{p}) - \frac{\mathbf{p}_\perp}{p_\perp}\sin\vartheta(\mathbf{p}), \quad (12)$$

where $\mathbf{p}_\perp = \mathbf{p} - \mathbf{\Omega}(\mathbf{\Omega}\cdot\mathbf{p})$ and the angle by which the particle trajectory turns is equal to

$$\vartheta(\mathbf{p}) = a p_\perp \int_a^\infty \frac{dr}{r^2\sqrt{p^2 + 2m_\alpha e_\alpha(\varphi_0 - \varphi(r)) - \frac{a^2 p_\perp^2}{r^2}}}. \quad (13)$$

In particular, in a Coulomb field with potential (10), the particle trajectory turns by the angle

$$\cos\vartheta(\mathbf{p}) = \frac{m_\alpha e_\alpha \varphi_0 (p_\perp^2 + m_\alpha e_\alpha \varphi_0) - p_\perp^2 p_r \sqrt{p^2 + 2m_\alpha e_\alpha \varphi_0}}{m_\alpha^2 e_\alpha^2 \varphi_0^2 + 2m_\alpha e_\alpha \varphi_0 p_\perp^2 + p_\perp^2 p^2}, \quad (14)$$

moreover, for a repulsive ($e_\alpha\varphi_0 > 0$) potential, we have $0 < \vartheta(\mathbf{p}) < \pi/2$, whereas, for an attractive potential, the angle $\vartheta(\mathbf{p})$ may be larger than $\pi/2$.

Taking into account the fact that the distribution function is constant along the particle trajectories, we solve Eq. (1) with the boundary conditions (3) and (4) and use expressions (11) and (12) to obtain the following solution at the grain surface:

$$f_\alpha(\mathbf{p}, a\mathbf{\Omega}) = \{\Phi_{0\alpha}(E_\alpha) - p_r'(\boldsymbol{\mu}\cdot\mathbf{\Omega}')\Phi_{1\alpha}(E_\alpha)\}\theta(-p_r)\theta(E_\alpha), \quad (15)$$

where $E_\alpha = p^2/2m_\alpha + e_\alpha\varphi_0$ is the total particle energy and $\theta(x)$ is the Heaviside step function. In solution (15), the factor $\theta(-p_r)$ accounts for the condition that charged plasma particles reaching the grain surface are completely absorbed by the grain [see boundary condition (3)]. The factor $\theta(E_\alpha)$, which arises in the OML approximation and is important only in the case of an attractive potential, ensures that, first, there are no trapped particles colliding with the grain and, second, there are no additional potential barriers at finite distances from the grain. In the case of a Coulomb potential, the latter condition is certainly satisfied.

It is also an easy matter to obtain the general solution to Eq. (1) in the plasma volume. This solution is similar in structure to solution (15), but the turning angle of the particle trajectory is described by a somewhat more involved expression, which takes into account the possible scattering of a particle by the grain potential field.

Let us consider two characteristic examples of an anisotropic plasma with dissipative flows. We assume that the unperturbed distribution functions at large distances from the grain are Maxwellian functions with directed velocities $\mathbf{w}_\alpha = w_\alpha\boldsymbol{\mu}$ lower than the corresponding thermal velocities. In this case, the isotropic part of distribution function (9) at infinity has the form

$$\Phi_{0\alpha}(E) = F_{M\alpha}(E) = \frac{n_\alpha}{(2\pi m_\alpha T_\alpha)^{3/2}} e^{-E/T_\alpha}, \quad (16)$$

and the dipole part of the distribution function is

$$\Phi_{1\alpha}(E) = \frac{w_\alpha}{T_\alpha} F_{M\alpha}(E). \quad (17)$$

Another example is that of a plasma with zero current but with nonzero heat fluxes $\mathbf{h}_\alpha = h_\alpha\boldsymbol{\mu}$ of each particle species. In this case, the correction to Maxwellian distribution function (16) has the form (see, e.g., [29], Section 2):

$$\Phi_{1\alpha}(E) = \frac{h_\alpha}{n_\alpha T_\alpha^2}\left(\frac{2E}{5T_\alpha} - 1\right)F_{M\alpha}(E). \quad (18)$$

The dissipative flows $\mathbf{w}_\alpha$ and $\mathbf{h}_\alpha$ are assumed to be given because they are determined by collisional processes occurring on spatial scales of about the mean free path l_0, which is assumed to be much longer than the electron Debye radius λ_D. In the case of heat transport in gases, the quasi-equilibrium temperature in Maxwellian distribution function (16) depends on the coordinates. However, this coordinate dependence can be neglected because $l_0 \gg \lambda_D$.

3. FLUXES AT THE GRAIN SURFACE

At the grain surface, the radial fluxes of plasma particles, $j_\alpha(\mathbf{\Omega})$, and of their kinetic energies, $q_\alpha^{(k)}(\mathbf{\Omega}) = \mathcal{F}(\mathbf{\Omega}; p^2/2m_\alpha)$ [see expression (7)], can be written as the expansions

$$j_\alpha(\mathbf{\Omega}) = j_{0\alpha} + \alpha(\chi_\alpha)\frac{Q_\alpha}{T_\alpha}\boldsymbol{\mu}\cdot\mathbf{\Omega}, \quad (19)$$

$$q_\alpha^{(k)}(\mathbf{\Omega}) = q_{0\alpha}^{(k)} + \beta(\chi_\alpha)Q_\alpha\boldsymbol{\mu}\cdot\mathbf{\Omega}, \quad (20)$$

where we have introduced the dimensionless coefficients α and β, which characterize the nonuniformity of the distribution of fluxes over the grain surface, and the energy scale Q_α of the fluxes.

Using distribution functions (15) and Maxwellian distributions (16), we can readily calculate the mean fluxes. The resulting particle fluxes coincides with those in the OML approximation [22, 23]:

$$j_{0\alpha} = -\frac{n_\alpha v_{T\alpha}}{\sqrt{2\pi}}\begin{cases} e^{-\chi_\alpha}, & \chi_\alpha > 0 \\ 1 - \chi_\alpha, & \chi_\alpha < 0, \end{cases} \quad (21)$$

where $v_{T\alpha} = \sqrt{T_\alpha/m_\alpha}$ are the thermal velocities of the corresponding particle species and $\chi_\alpha = e_\alpha\varphi_0/T_\alpha$ are the

dimensionless grain potentials for different plasma components. The fact that the solution with the Coulomb potential and the self-consistent theory yield the same fluxes is not surprising—in the OML approximation, the currents at the grain surface depend only on the surface potential and are insensitive to the radial potential distribution.

The mean fluxes of the particle kinetic energies are equal to

$$q_{0\alpha}^{(k)} = -\sqrt{\frac{2}{\pi}} n_\alpha v_{T\alpha} T_\alpha \begin{cases} e^{-\chi_\alpha}, & \chi_\alpha > 0 \\ 1 - \chi_\alpha + \dfrac{\chi_\alpha^2}{2}, & \chi_\alpha < 0. \end{cases} \quad (22)$$

Since the radial coordinate is assumed to increase in the direction away from the grain center, fluxes (21) and (22) are negative.

The energy scale Q_α in expressions (19) and (20) and the dimensionless coefficients α and β all depend on the explicit form of the correction to distribution function (16). For a plasma with convective fluxes, this correction is given by expression (17) and the energy scale has the form

$$Q_\alpha^{(c)} = n_\alpha w_\alpha T_\alpha. \quad (23)$$

For a plasma with heat fluxes, this correction is described by expression (18) and the energy scale is

$$Q_\alpha^{(h)} = h_\alpha. \quad (24)$$

In what follows, the quantities calculated from expressions (17) and (18) will be distinguished by superscripts (*c*) and (*h*), respectively.

The dimensionless coefficients α and β in expressions (19) and (20) are represented in terms of integrals, which cannot be calculated in a closed form. Nevertheless, they can be calculated in the limits of small and large (positive and negative) χ_α values. For a plasma with convective currents that give rise to corrections (17) to the particle distribution functions, the coefficient $\alpha(\chi)$, which characterizes the nonuniformity of the distribution of particle fluxes over the grain surface and is defined by expression (19), has the following form in the above three limits:

$$\alpha(\chi) = \alpha^{(c)}(\chi) \approx \begin{cases} \dfrac{1}{2} - \dfrac{\chi}{4}, & |\chi| \ll 1 \\ \sqrt{\chi/\pi}\exp(-\chi), & \chi \longrightarrow \infty \\ \dfrac{16}{15}\sqrt{-\chi/\pi}, & \chi \longrightarrow -\infty. \end{cases} \quad (25)$$

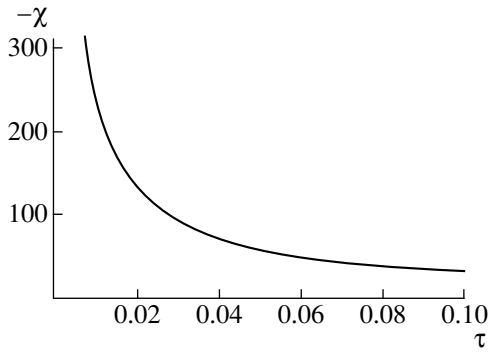

Fig. 1. Dependence of the dimensionless potential $-\chi_i$ on the temperature ratio $\tau = T_i/T_e$ for argon.

In the same limits, the analogous coefficient $\beta(\chi)$ in expression (20) is

$$\beta(\chi) = \beta^{(c)}(\chi) \approx \begin{cases} \dfrac{5}{4} - \dfrac{7}{8}\chi, & |\chi| \ll 1 \\ 2\sqrt{\chi/\pi}\exp(-\chi), & \chi \longrightarrow \infty \\ \dfrac{16}{15}(-\chi)^{3/2}/\sqrt{\pi}, & \chi \longrightarrow -\infty. \end{cases} \quad (26)$$

For a plasma with heat fluxes that give rise to corrections (18) to the particle distribution functions, these coefficients are described by the asymptotic expressions

$$\alpha(\chi) = \alpha^{(h)}(\chi) \approx \begin{cases} \dfrac{\chi}{10}, & |\chi| \ll 1 \\ \dfrac{2\chi^{3/2}}{5\sqrt{\pi}}\exp(-\chi), & \chi \longrightarrow \infty \\ -\dfrac{16}{75}\sqrt{-\chi/\pi}, & \chi \longrightarrow -\infty, \end{cases} \quad (27)$$

$$\beta(\chi) = \beta^{(h)}(\chi) \approx \begin{cases} \dfrac{1}{2} - O(\chi^2), & |\chi| \ll 1 \\ \dfrac{4\chi^{3/2}}{5\sqrt{\pi}}\exp(-\chi), & \chi \longrightarrow \infty \\ -\dfrac{16(-\chi)^{3/2}}{75\sqrt{\pi}}, & \chi \longrightarrow -\infty. \end{cases} \quad (28)$$

In order to determine how the coefficients α and β in expressions (19) and (20) depend on the plasma parameters, it necessary to find the grain floating potential φ_0 from the condition for the total electric current to vanish, $j_{0e} = j_{0i}$, where the currents $j_{0\alpha}$ are given by expressions (21), and then to evaluate the corresponding integrals with the help of expressions (17) and (18). An example of relevant numerical calculations carried out

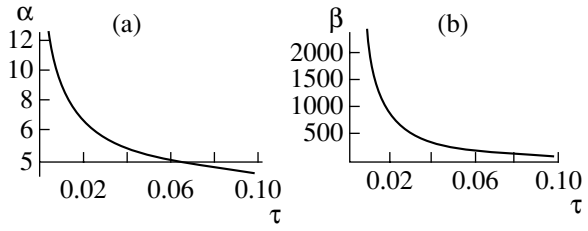

Fig. 2. Dependence of the coefficients (a) $\alpha_i^{(c)}$ and (b) $\beta_i^{(c)}$ on the temperature ratio $\tau = T_i/T_e$ for a plasma with a convective current.

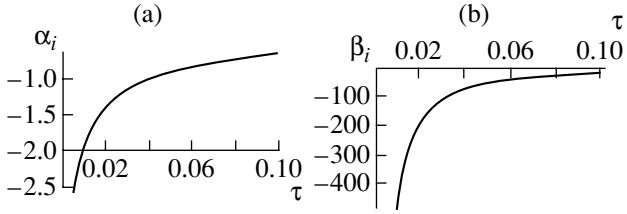

Fig. 3. Dependence of the coefficients (a) $\alpha_i^{(h)}$ and (b) $\beta_i^{(h)}$ on the temperature ratio $\tau = T_i/T_e$ for a plasma with a heat flux.

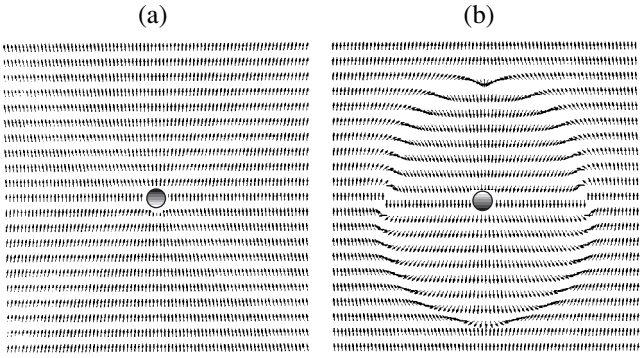

Fig. 4. (a) Direction field of the dipole component of the ion current and (b) direction field of the dipole component of the energy flux.

for the electron-to-ion mass ratio $\mu = m_e/m_i$ corresponding to argon is illustrated in Fig. 1, which shows the plot of $-\chi_i$ versus the ion-to-electron temperature ratio $\tau = T_i/T_e$. Note that, for $\mu \ll \tau$, the expression $\chi_i \approx -1/(2\tau)\ln(\tau/\mu)$ provides a good approximation for the floating potential. Figure 2 shows the plots of $\alpha_i^{(c)} = \alpha^{(c)}(\chi_i)$ and $\beta_i^{(c)} = \beta^{(c)}(\chi_i)$ versus τ, and Fig. 3 shows the same plots but obtained for a plasma with heat fluxes.

From Figs. 1–3, we can see that, for τ values typical of gas discharges, the dimensionless potential $|\chi_i|$ increases to several hundred; the effective cross section for ion absorption by the grain surface is seen to increase in the same proportion. For a plasma with convective currents, the nonuniformity of the ion current distribution over the grain surface, determined by the coefficient $\alpha_i^{(c)}$, is higher by about one order of magnitude than that for an uncharged grain, while the nonuniformity of the energy flux distribution over the grain surface is higher by about three orders of magnitude. It may be said that, because of its large negative charge, the grain focuses the ion flux onto itself and thus "feels" the plasma anisotropy at distances far larger than its size. Clearly, the situation with electrons is opposite: the electron flux distribution over the surface of a charged grain is nonuniform to a far lesser extent than that over the surface of an uncharged grain.

Comparing Fig. 3 and expressions (27) and (28) with Fig. 2 and expressions (25) and (26), we can see some interesting distinctions between them. First, in a plasma with a heat flux, the convective current described by expressions (27) is nonzero at the grain surface and vanishes at infinity. Second, because of the high dimensionless negative grain potential χ_i for the ions, the coefficients $\alpha_i^{(h)}$ and $\beta_i^{(h)}$ are negative, in contrast to a plasma with a convective current, for which the analogous coefficients $\alpha_i^{(c)}$ and $\beta_i^{(c)}$ are positive. Thus, if the ion heat flux is directed from bottom to top, then the grain is heated most intensely from above. This rather unusual phenomenon resembles reverse photophoresis in neutral aerosols[1] and stems from the fact that the effect of the grain's electric field on the ion fluxes is similar to that of the focusing lens.

An understanding of what are the processes in the grain's vicinity and of how different are the effects of a convective current and a heat flux can be derived from Fig. 4. As has been pointed out, it is possible to obtain a general solution to Eq. (1) in the plasma volume. Using this solution, we can (of course, numerically) calculate the ion current and the energy flux $\mathbf{q}(\mathbf{r}) = \int d\mathbf{p}\,\frac{\mathbf{p}}{m_i}\frac{p^2}{2m_i} f(\mathbf{p}, \mathbf{r})$. Obviously, they both can be represented as the sums of the monopole and dipole components, e.g., $\mathbf{q}(\mathbf{r}) = \mathbf{q}_0(r) + \mathbf{q}_1(r)(\boldsymbol{\mu}\cdot\boldsymbol{\Omega})$. The monopole components are always directed along the radius and are proportional to $\propto 1/r^2$. Figure 4a shows the direction field of the dipole component $\mathbf{j}_1(r)(\boldsymbol{\mu}\cdot\boldsymbol{\Omega})$ for a plasma with a convective ion current described by correction (17), and Fig. 4b shows the same field for the dipole component $\mathbf{q}_1(r)(\boldsymbol{\mu}\cdot\boldsymbol{\Omega})$ for a plasma with a heat flux described at infinity by correction (18). In both cases,

[1] In a light ray, the dark side of the grain can be heated stronger due to diffraction or refraction.

the dimensionless grain potential for the ions is $\chi_i = -50$. As may be seen in Fig. 4, the ion current is focused by the negative grain charge; however, the overall pattern of the ion current does not change qualitatively. In the case of a plasma with a heat flux, we observe a qualitative redistribution of the energy flux, resulting in the formation of something like a toroidal vortex. It should be noted that, at the grain surface, the monopole components of the fluxes are always larger than their dipole components; it is for this reason that there are actually no radial plasma fluxes from the grain.

4. HEATING OF THE GRAIN SURFACE

From the expressions derived in the previous section, we can see that the electron contribution to the total heat balance can be neglected. An ion striking the grain almost inevitably recombines with it. The energy released in each recombination event is $\epsilon = E_i - E_{wf}$, where E_i is the ionization energy and E_{wf} is the work function for emission of an electron. For argon, we have $E_i = 15.7$ eV; hence, ϵ is at least 10 eV. Obviously, all other contributions to ϵ, such as those from the absorption of an ion and the desorption of a neutral atom, can also be neglected. However, along with the energy released in recombination reactions, we must take into account the ion kinetic energy. If the electrical conductivity of a grain is sufficiently high (i.e., if the nonuniformity of the electric current distribution does not affect the recombination process), then the total heat flux generated in the plasma interaction with the grain can be written as

$$q^{(p)}(\mathbf{\Omega}) = \epsilon j_i(\mathbf{\Omega}) + q_i^{(k)}(\mathbf{\Omega}) = q_0^{(p)} + \gamma Q_i(\boldsymbol{\mu}\cdot\mathbf{\Omega}), \quad (29)$$

where $q_0^{(p)} = -n_i v_{Ti}/\sqrt{2\pi}\,(\epsilon|\chi_i| + T_i\chi_i^2)$ and

$$\gamma = \gamma^{(c)} = \frac{16}{15}\sqrt{\frac{-\chi_i}{\pi}}\left(\frac{\epsilon}{T_i} + |\chi_i|\right) \quad (30)$$

for a plasma with a convective current and

$$\gamma = \gamma^{(h)} = -\frac{1}{5}\gamma^{(c)} \quad (31)$$

for a plasma with a heat flux.

In deriving these formulas, we took into account the inequality $|\chi_i| \gg 1$ and used the asymptotic expressions (25) and (26). The above estimates show that, under conditions typical of gas discharges, the quantities ϵ/T_i and $|\chi_i|$ are of the same order of magnitude.

Now, we consider the energy exchange between the grain and neutral gas. In the simplest case of a Knudsen gas, which is typical of most experiments, the mean free path of neutral atoms is large in comparison with the grain size and the distribution function of the atoms that strike the grain surface is independent of its temperature. In the complete energy accommodation approximation, the neutrals scattered by the grain obey a Maxwellian distribution function with a temperature equal to the temperature of the grain surface. Consequently, at $r = a$, we have

$$f_n(\mathbf{p}, a\mathbf{\Omega}) = \begin{cases} F_{Mn}(p^2/2m_n), & \mathbf{p\Omega} < 0 \\ F_{Ms}(p^2/2m_n), & \mathbf{p\Omega} > 0, \end{cases} \quad (32)$$

where $F_{Ms}(p^2/2m_n)$ is the Maxwellian distribution function (16) with the local surface temperature $T_s(\mathbf{\Omega})$ and the density $n_s(\mathbf{\Omega})$.

Under the additional assumption that the temperature of neutral atoms produced in recombination reactions is equal to the local surface temperature, we can determine the density $n_s(\mathbf{\Omega})$ of the atoms flying away from the grain from the condition that the total flux of neutral atoms is equal to the flux of the ions recombining at the grain surface:

$$n_s(\mathbf{\Omega}) = n_n\sqrt{\frac{T_n}{T_s(\mathbf{\Omega})}} + n_i\sqrt{\frac{T_i}{T_s(\mathbf{\Omega})}}|\chi_i| - \alpha_i\sqrt{\frac{2\pi M}{T_s(\mathbf{\Omega})}}\frac{Q_i}{T_i}\boldsymbol{\mu}\cdot\mathbf{\Omega}. \quad (33)$$

Here, for simplicity, the masses of an ion and of a neutral atom are assumed to be the same, $m_n = m_i = M$. As a rule, the degree of ionization in the plasma volume is low ($n_i \ll n_n$); however, because of the large negative grain charge ($|\chi_i| \gg 1$), the density of the recombined ions, which is described by the last two terms in expression (33), can be comparable with n_n near the grain surface.

Hence, the flux of the energy carried by neutral atoms away from the point with the angular coordinates $\mathbf{\Omega}$ at the grain surface is equal to

$$q^{(n)}(\mathbf{\Omega}) = -n_n\sqrt{\frac{2T_n^3}{\pi M}} + n_s(\mathbf{\Omega})\sqrt{\frac{2T_s(\mathbf{\Omega})^3}{\pi M}}. \quad (34)$$

When analyzing the total energy balance, we must also take into account the radiative cooling of the grain surface. In the literature, it was often said that this effect may play an important role. Since little is known about the optical properties of the actual dust grains, there are no serious reasons for considering the grain as a completely absorbing (black) body. Moreover, since the grain sizes are, as a rule, smaller than the wavelength of thermal radiation, the radiative cooling of the grain surface may become far less intense. Nevertheless, we assume for simplicity that the radiative flux is equal to σT_s^4, where σ is a certain constant, which characterizes the optical properties of the grain substance and depends on the grain size. We also assume that the plasma surrounding the grain is transparent to thermal electromagnetic radiation and that the radiative heating of the grain surface by plasma thermal radiation is negligible. It is in the latter assumption that the model

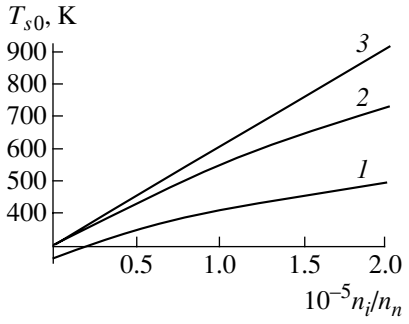

Fig. 5. Dependence of the mean grain temperature T_{s0} on n_i/n_n for $T_n = T_i = 300$ K, $n_n = 3 \times 10^{15}$ cm^{-3}, and $\epsilon = 10$ eV at $\sigma/\sigma_0 =$ (*1*) 1, (*2*) 0.1, and (*3*) 0.

developed here differs from the model in which the radiative heating of the grain surface was accounted for in the overall heat balance (see the discussion in [15]).

Hence, the total heat flux onto the grain surface is represented as the sum of three terms:

$$q(\mathbf{\Omega}) = q^{(p)}(\mathbf{\Omega}) + q^{(n)}(\mathbf{\Omega}) + \sigma T_s(\mathbf{\Omega})^4, \qquad (35)$$

where the heat fluxes of plasma particles and neutral atoms, $q^{(p)}$ and $q^{(n)}$, are given by expressions (29) and (34), respectively.

Now, we can determine the grain surface temperature $T_s(\mathbf{\Omega})$. To do this, it is necessary to solve the heat-conduction equation

$$\nabla \kappa(\mathbf{r}) \nabla T(\mathbf{r}) = 0 \qquad (36)$$

inside the grain, i.e., for $r < a$. The boundary condition for this equation implies that the heat fluxes inside and outside the grain are the same:

$$-\kappa(a\mathbf{\Omega}) \frac{\partial T(\mathbf{r})}{\partial r}\bigg|_{r=a} = q(\mathbf{\Omega}), \qquad (37)$$

where $T_s(\mathbf{\Omega}) = T(a\mathbf{\Omega})$ and $\kappa(\mathbf{r})$ is the coordinate-dependent thermal conductivity of the grain substance. Note that most experiments are carried out with grains whose thermal conductivity can be assumed to be constant. However, in some experiments, the grains may be thin-walled hollow spheres [30] or even may possess a fractal structure. Putting aside the question about the thermal conductivity of the fractal grains (this discussion goes far beyond the scope of the present work), we consider a hollow grain. In other words, we assume that

$$\kappa(r) = \begin{cases} \kappa = \text{const}, & \xi a < r < a \\ 0, & r < \xi a, \end{cases} \qquad (38)$$

where $\xi < 1$.

Since the grain heating is assumed to be only slightly nonuniform, we can solve the heat-conduction equation in the dipole approximation by expanding total heat flux (35) in powers of the unit vector $\mathbf{\Omega}$. We describe the nonuniformity of the temperature distribution over the grain surface by an as-yet-unknown small coefficient ζ:

$$T_s(\mathbf{\Omega}) = T_{s0}(1 + \zeta \boldsymbol{\mu} \cdot \mathbf{\Omega}). \qquad (39)$$

From expansion (39) in powers of $\mathbf{\Omega}$, we obtain

$$q(\mathbf{\Omega}) = p_0 + (\gamma Q_i + p_1 \zeta) \boldsymbol{\mu} \cdot \mathbf{\Omega}, \qquad (40)$$

where the isotropic component of the heat flux is equal to

$$p_0 = 2\frac{n_n v_{Tn}}{\sqrt{2\pi}}(T_{s0} - T_n) - \frac{n_i v_{Ti}}{\sqrt{2\pi}}(\epsilon|\chi_i| + T_i \chi_i^2) + \sigma T_{s0}^4 \qquad (41)$$

and

$$p_1 = \sqrt{\frac{2}{\pi}} T_{s0}(n_n v_{Tn} + n_i v_{Ti}|\chi_i|) + 4\sigma T_{s0}^4. \qquad (42)$$

When writing expressions (41) and (42), we took into account the inequality $|\chi_i| \gg 1$ and assumed that the grain surface temperature and the temperatures of the plasma ions and neutral atoms are all low in comparison with the energy ϵ released in each recombination event.

We can readily solve Eq. (36) with boundary condition (37) and thermal conductivity (38) and thus determine the mean surface temperature T_{s0} and the coefficient ζ. It is obvious that the mean temperature can be determined from the condition that mean energy flux (41) is zero, $p_0 = 0$. Figure 5 shows several plots of the mean temperature versus the ratio n_i/n_n, calculated for different values of σ/σ_0, where σ_0 is the Stefan–Boltzmann constant. We can see that, because of the recombination-related heating, the mean temperature T_{s0} of the grain surface can be appreciably higher than the temperature of the surrounding gas even when the degree of gas ionization is comparatively low (about 10^{-6}) and the radiative cooling is as intense as possible.

The coefficient ζ, which is defined by expression (39) and characterizes the nonuniformity of the grain surface heating, can be written as

$$\zeta = -\frac{\gamma Q_i}{p_1 + \tilde{\kappa} T_{s0}/a}, \qquad (43)$$

where we have introduced the effective thermal conductivity of the grain with allowance for its internal structure:

$$\tilde{\kappa} = \frac{2\kappa(1 - \xi^3)}{2 + \xi^3}. \qquad (44)$$

The form of expression (43) is quite typical in the problems of heat exchange in aerosols. The numerator in this expression characterizes the nonuniformity of the external heating source (in the case at hand, the nonuniformity of the heating of the grain surface by plasma particles). There are two processes reducing the nonuniformity of the temperature distribution over the

grain surface. The first process is the thermal conduction of the grain substance, described by the term $\tilde{\kappa}T_{s0}/a$, and the second one is the heat exchange of the grain with the surrounding gas and the radiative cooling described by the quantity p_1 in expression (42). For typical experimental parameters ($\kappa \sim 10^4$ erg/(cm s K), $a \sim 10^{-3}$ cm, $\xi = 0$, and $w \sim 0.1v_{Ti}$), we have $p_1 \ll \tilde{\kappa}T_{s0}/a$ and $\zeta \sim 10^{-4}$. For hollow grains, the effective thermal conductivity may be two to three orders of magnitude lower, in which case we have $p_1 \geq \tilde{\kappa}T_{s0}/a$, and the coefficient ζ may be as large as 0.03. Hence, depending on the experimental conditions and the grain structure, the temperature difference over the grain surface can vary from fractions of a degree to about ten degrees.

5. MOMENTUM FLUX

In order to determine the force acting on the grain, it is necessary to calculate the momentum flux tensor at its surface. Expressions (32) implies that, at the point $\mathbf{r} = a\mathbf{\Omega}$, the neutral gas pressure is isotropic and thus can be described by the tensor

$$\Pi_{ij}^{(n)} = \delta_{ij}P^{(n)}(\mathbf{\Omega}) = \delta_{ij}\frac{1}{2}[n_nT_n + n_s(\mathbf{\Omega})T_s(\mathbf{\Omega})]. \quad (45)$$

Here, we are interested only in the pressure component that depends on the vector $\mathbf{\Omega}$. Using expression (33) and expansion (39), we can write this component as

$$P^{(n)}(\mathbf{\Omega}) = (\boldsymbol{\mu}\cdot\mathbf{\Omega})\frac{1}{4}\sqrt{T_nT_{s0}} \times\left\{\zeta\left[n_n + n_i|\chi_i|\sqrt{\frac{T_i}{T_n}}\right] - \frac{2\sqrt{2\pi}\alpha_i}{v_{Tn}}\frac{Q_i}{T_i}\right\}. \quad (46)$$

The last term in braces accounts for the pressure of the recombination-produced neutral atoms. The nonuniformity of the grain surface heating gives rise to the radiometric force, which is described by the term proportional to ζ. Recall that the ζ value is substantially smaller than unity. Nevertheless, the radiometric pressure can be fairly high because it is determined by the product of the relative temperature difference ζ and the neutral gas pressure, which is higher than the pressure of each of the plasma components.

The plasma pressure at the grain surface is easy to calculate using distribution function (15). Clearly, the ion pressure is always (in particular, in the case $|\chi_i| \gg 1$) dominant; hence, we can write

$$\Pi_{ij}^{(p)}(\mathbf{\Omega}) = -\lambda\frac{|\chi_i|^{3/2}}{\sqrt{\pi}}\frac{Q_i\sqrt{2\pi}}{v_{Ti}}(\mu_i\Omega_j + \mu_j\Omega_i), \quad (47)$$

where the dimensionless coefficient is equal to $\lambda = 2/15$ for a plasma with convective currents described by Eq. (17) and to $\lambda = -4/75$ for a plasma with heat fluxes described by Eq. (18). In expression (47), the $\mathbf{\Omega}$-independent isotropic pressure component is omitted.

The force acting on the grain can be written as the following integral over the grain surface:

$$F_i = -a^2\oint d\Omega_j(\Pi_{ij}^{(n)}(\mathbf{\Omega}) + \Pi_{ij}^{(p)}(\mathbf{\Omega})). \quad (48)$$

This integral is easy to evaluate analytically. As a result, we arrive at the following expression, in which the force is conveniently represented as the sum of two components:

$$\mathbf{F} = \boldsymbol{\mu}(F^{(rm)} + F^{(p)}). \quad (49)$$

With allowance for expression (43), the radiometric force has the form

$$F^{(rm)} = \frac{\pi a^2}{3}\frac{\gamma Q_i}{p_1 + \tilde{\kappa}T_{s0}/a}\sqrt{T_nT_{s0}}\left[n_n + n_i|\chi_i|\sqrt{\frac{T_i}{T_n}}\right]. \quad (50)$$

The last term in parentheses in expression (49) is the force associated with plasma pressure (47) plus the reactive force of neutral atoms, which is described by the last term in expression (45):

$$F^{(p)} = \frac{\pi a^2}{3}\frac{Q_i\sqrt{2\pi}}{v_{Ti}}\left[\lambda\frac{16|\chi_i|^{3/2}}{\sqrt{\pi}} + 2\alpha_i\sqrt{\frac{T_{s0}}{T_i}}\right]. \quad (51)$$

Since $\alpha_i \sim |\chi_i|^{3/2}$, the two terms in square brackets in expression (51) are of the same order of magnitude.

Let us compare expressions (50) and (51). Radiometric force (50) depends sensitively on the thermal conductivity of the grain substance. If the grain thermal conductivity is high, then, in expression (50), we have $p_1 \ll \tilde{\kappa}T_{s0}/a$; therefore, the drag force associated with plasma pressure (51) is dominant. In the opposite limit, the ratio of forces (50) and (51) can be estimated as $F^{(rm)}/F^{(p)} \sim \epsilon/(T_n|\chi_i|)$, which may be appreciably larger than unity.

For a plasma with convective currents, the coefficients γ, λ, and α_i in expressions (50) and (51) are all positive, which indicates that the drag force acting on the grain is parallel to the current. In a plasma with heat fluxes, these coefficients are all negative; hence, the force acting on the grain is directed oppositely to the heat flux vector. It is in this point that thermophoresis in dusty plasmas differs from thermophoresis in neutral aerosols, in which the corresponding force expels a grain to the colder gas region.

6. CONCLUSION

To conclude, let us draw an overall picture of heat fluxes in an aerosol plasma. The interaction of a convective current or a heat flux with the grain's electric field in the plasma volume, on the one hand, substantially increases the pressure gradient at the grain surface and, on the other hand, leads to a nonuniform heating of the surface because of the plasma recombination.

The scattering of neutral atoms by a grain with a nonuniform surface temperature gives rise to the radiometric force, which is comparable with or even stronger than the ion wind force. This is the main difference between aerosol plasmas and neutral aerosols, in which the nonuniformity of the temperature distribution over the grain surface can be neglected provided that the Knudsen number is large [6]. In aerosol plasmas, the effect of the large negative grain charge on both the drag force exerted by ion fluxes on the grain and thermophoresis is of great importance; in particular, the thermophoretic force may reverse direction.

Let us try to guess what will happen in a situation with several (rather than one) grains. Since each grain forms "its own" converging flux of plasma particles, every other grain will experience a drag force. The total effect of these drag forces is to produce an effective force that attracts the grains toward each other [31]. Since, in this case, there are no ion heat fluxes, the effect of neutral atoms (see the discussion in the body of the paper) and the associated radiometric force make the attraction even more intense.

On the other hand, the difference between the grain surface temperature and the temperature of the surrounding gas leads to the formation of a heat flux of neutral atoms. As was already mentioned, this effect also gives rise to attraction between the grains provided that their cooling is sufficiently efficient [5, 8, 9]. An analysis of heat fluxes illustrated in Fig. 5 shows that the recombination-related heating of the grain surfaces is more intense than their radiative cooling. Consequently, the agglomeration mechanism associated with the formation of heat fluxes of neutral atoms is more typical of neutral aerosols and high-pressure thermal plasmas or flames [10], in which the grain acquires a positive charge as a result of thermal emission.

The main qualitative result obtained in this study is that the thermophoretic force in an aerosol plasma reverses direction. However, the reverse thermophoresis in gas discharges can be suppressed by the heat fluxes of the neutral gas component. The question of the relationship between the heat fluxes of neutral atoms and plasma ions under actual conditions is fairly complicated because this relationship is governed by both the discharge geometry and the nature of collisions. Presumably, the reverse thermophoresis manifests itself in plasmas with a sufficiently high degree of ionization (e.g., in the edge plasma of a tokamak), but almost nothing is known about the dust properties under these conditions (the only reliable information is that the dust indeed exists).

The above analysis has been carried out for small grains that do not affect the properties of the surrounding plasma. The larger the grain size, the more complicated is the situation, because the Knudsen number becomes on the order of unity. The attraction of two closely spaced parallel plates in a gas discharge was observed in experiments carried out by Dubinov *et al.* [32]. The plate sizes were comparable with the mean free path, while the distance between the plates was substantially smaller. The measured excess pressure, which brings the plates closer together, is, on the one hand, about two orders of magnitude lower than the neutral gas pressure and, on the other, it is three to four orders of magnitude higher than the pressure of the plasma component. In order for this excess pressure to be produced by the radiometric effect, it is sufficient to maintain the temperature drop across the plates at a level of about one degree. This drop is likely to be provided by a nonuniform heating of the plates by the plasma component. Hence, at present, the radiometric force driven by the plasma recombination seems to be the most fitting candidate to explain this effect.

ACKNOWLEDGMENTS

I am grateful to Sh.G. Amiranashvili for fruitful discussions. This study was supported in part by the Russian Foundation for Basic Research (project no. 02-02-16439) and the Netherlands Organization for Scientific Research (grant no. NWO.047.008.013).

REFERENCES

1. H. L. Green and W. R. Lane, *Particulate Clouds: Dusts, Smokes, and Mists* (Spon, London, 1964; Khimiya, Leningrad, 1972).
2. G. M. Jellum, J. E. Daugherty, and D. B. Graves, J. Appl. Phys. **69**, 6923 (1991).
3. O. Havnes, T. Nitter, V. Tsytovich, *et al.*, Plasma Sources Sci. Technol. **3**, 448 (1994).
4. J. Perrin, P. Molinàs-Mata, and P. Belenguer, J. Phys. D **27**, 2499 (1994).
5. A. Brattli and O. Havnes, J. Vac. Sci. Technol. A **14**, 644 (1996).
6. L. Talbot, R. K. Cheng, R. W. Schefer, and D. R. Willis, J. Fluid Mech. **101**, 737 (1980).
7. H. Rothermel, T. Hagl, G. Morfill, and H. Thomas, physics/0110045.
8. V. N. Tsytovich, Ya. K. Khodataev, G. E. Morfill, *et al.*, Comm. Plasma Phys. Control. Fusion **18**, 281 (1998).
9. V. N. Tsytovich and J. Winter, Usp. Fiz. Nauk **169**, 899 (1998) [Phys. Usp. **41**, 815 (1998)].
10. V. E. Fortov, A. P. Nefedov, O. F. Petrov, *et al.*, Zh. Éksp. Teor. Fiz. **116**, 1601 (1999) [JETP **89**, 864 (1999)].
11. K. Yuuki, T. Torikai, T. Kusakabe, *et al.*, J. At. Energy Soc. Jpn. **40**, 323 (1998).
12. A. Melzer, Plasma Sources Sci. Technol. **10**, 303 (2001).
13. J. E. Daugherty and D. B. Graves, J. Vac. Sci. Technol. A **11**, 1126 (1993).
14. D. B. Graves, J. E. Daugherty, M. D. Kilgore, and R. K. Porteous, Plasma Sources Sci. Technol. **3**, 433 (1994).
15. G. H. P. M. Swinkels, H. Kersten, H. Deutch, and G. M. W. Kroesen, J. Appl. Phys. **88**, 1747 (2000).
16. A. V. Kozyrev and A. N. Shishkov, Pis'ma Zh. Tekh. Fiz. **28** (12), 33 (2002) [Tech. Phys. Lett. **28**, 504 (2002)].

17. J. R. Brock, Nature **207**, 69 (1964).
18. X. Chen, J. Phys. D **30**, 826 (1997).
19. X. Chen, Plasma Chem. Plasma Process. **19**, 33 (1999).
20. A. M. Ignatov and Sh. G. Amiranashvili, Phys. Rev. E **63**, 017402 (2001).
21. V. N. Tsypin, S. V. Vladimirov, M. Tendler, *et al.*, Phys. Lett. A **239**, 94 (1998).
22. I. B. Bernstein and I. N. Rabinowitz, Phys. Fluids **2**, 112 (1959).
23. J. G. Laframboise and L. W. Parker, Phys. Fluids **16**, 629 (1973).
24. J. E. Allen, B. M. Annaratone, and U. de Angelis, J. Plasma Phys. **63**, 299 (2000).
25. M. Lampe, G. Joyce, and G. Ganguli, Phys. Scr. T **89**, 106 (2001).
26. M. Lampe, V. Gavrishchaka, G. Joyce, and G. Ganguli, Phys. Rev. Lett. **86**, 5278 (2001).
27. J. E. Daugherty, R. K. Porteous, and D. B. Graves, J. Appl. Phys. **73**, 1617 (1993).
28. M. D. Kilgore, J. E. Daugherty, R. K. Porteous, and D. B. Graves, J. Appl. Phys. **73**, 7195 (1993).
29. V. P. Silin, *Introduction to the Kinetic Theory of Gases* (Nauka, Moscow, 1971).
30. C. Arnas, M. Mikikian, and F. Doveil, Phys. Rev. E **60**, 7420 (1999).
31. A. M. Ignatov, Fiz. Plazmy **22**, 648 (1996) [Plasma Phys. Rep. **22**, 585 (1996)].
32. A. E. Dubinov, V. S. Zhdanov, A. M. Ignatov, *et al.*, Pis'ma Zh. Tekh. Fiz. **25** (13), 73 (1999) [Tech. Phys. Lett. **25**, 538 (1999)].

Translated by O. E. Khadin

Plasma Physics Reports, Vol. 28, No. 10, 2002, pp. 858–865. Translated from Fizika Plazmy, Vol. 28, No. 10, 2002, pp. 930–938.

LOW-TEMPERATURE PLASMA

Cathode Fall Parameters of a Self-Sustained Normal Glow Discharge in Atmospheric-Pressure Helium

V. I. Arkhipenko, S. M. Zgirovskiĭ, A. A. Kirillov, and L. V. Simonchik

Institute of Molecular and Atomic Physics, Belarussian Academy of Sciences, pr. F. Skoriny 70, Minsk, 220072 Belarus

Received February 8, 2002; in final form, April 4, 2002

Abstract—Results from comprehensive studies of a high-current self-sustained glow discharge in atmospheric-pressure helium are presented. The main parameters of the cathode fall, namely, the electric field profile, cathode fall thickness, current density, gas temperature, and heat flux to the cathode are determined. The results obtained are discussed using one-dimensional models of the cathode fall with allowance for volumetric heat release. *© 2002 MAIK "Nauka/Interperiodica".*

1. INTRODUCTION

Low- and medium-pressure glow discharges are widely used in lighting techniques, communication devices, and atomic-absorption and atomic-emission methods of material analysis. They are also employed for film deposition, photoresist removal, ion implantation, modification of metal surfaces, etc. However, more extensive employment of low-pressure discharges in science and technology is limited by two main disadvantages: the low power deposition in the discharge plasma and the necessity of expensive vacuum apparatuses. These disadvantages can be avoided by using atmospheric-pressure glow discharges (APGDs), which have recently attracted great interest [1–5].

The APGDs were first observed and studied in the 1930s [6–8]; then, the studies were continued in the 1950s [9]. It was found that an increase in the gas pressure leads to a decrease in the dimensions of the characteristic glow discharge regions and the sharp increase in the heat release in the cathode region. The related change in the gas density leads to a change in the normal current density corresponding to the given gas pressure. Moreover, the high temperature gradients, high charged particle densities, and high electric fields in the cathode region result in a significant deviation of the discharge conditions from being equilibrium. All this promotes the onset of various instabilities and the contraction of a glow discharge with a subsequent transformation into an arc discharge. For this reason, it is commonly believed that self-sustained glow discharges with a normal current density can only operate at low or moderate pressures and discharge currents in the range 100 μA–1 A [10–14].

Experiments [15–17], started in 1968, dealt with dc discharges in atmospheric-pressure helium at currents of up to 3 A. These discharges were stable and did not resemble an arc discharge. However, the authors were not able to unambiguously identify these discharges as normal glow discharges at atmospheric pressure. After 1992, these studies were continued at the Institute of Molecular and Atomic Physics of Belarussian Academy of Sciences [18–22].

The small sheath length in an APGD (tens of microns) presents difficulties for experimental studies of the electrode regions and modeling of the plasma processes near the cathode. In the literature, there are no reliable experimental data on both the electrophysical parameters of the APGD cathode fall and the elementary processes in it. In review [14], it was shown that, even at low pressures, the lack of knowledge on the cathode electron emission properties during the discharge operation leads to a weak correlation between the experimental and theoretical results. At atmospheric pressure, the modeling encounters even more serious problems because of the lack of the data on the cathode fall parameters and insufficient measurement inaccuracy. For instance, the measured cathode fall thickness and the current density in an atmospheric-pressure helium discharge (at a repetition rate of 10 kHz and maximum voltage of 1.5 kV) were equal to ~0.3 mm and several mA/cm^2, respectively [3]. The developed self-consistent one-dimensional fluid model of this discharge readily describes the above parameters and, according to the authors, the calculated electric field profile and the charged particle densities in the cathode region correspond to a normal glow discharge. However, taking into account the low gas heating in this discharge and making allowance for scaling laws [6], such a cathode fall thickness in a normal glow discharge at atmospheric pressure seems to be highly overestimated.

This paper is devoted to comprehensive studies of the cathode fall of an APGD with a steel cathode in helium. The main parameters of the cathode fall, namely, the electric field, fall thickness, gas temperature, current density, and heat flux to the cathode are

1063-780X/02/2810-0858$22.00

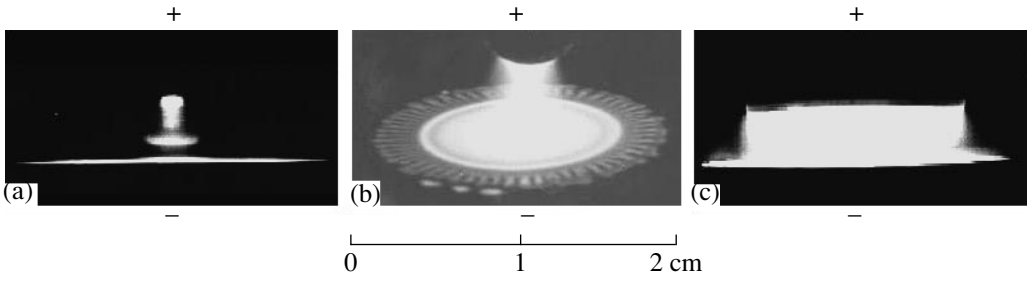

Fig. 1. Photographs of an APGD in helium in the planes (a, c) parallel and (b) tilted with respect to the cathode surface for (a, b) rounded anode–plane and (c) plane–plane electrode configurations.

determined. The data obtained are discussed using one-dimensional models [6, 23, 24] with allowance for volumetric heat release in the cathode region.

2. CATHODE FALL PARAMETERS OF AN APGD

A glow discharge was ignited between two electrodes in a sealed chamber with quartz windows. The anode was made of 6-mm-diameter tungsten rod with an apex radius of 3 mm, and the 36-mm-diameter cathode was made of type-45 steel. Two cathode designs were used: an uncooled cathode and a cathode with forced cooling. Heat removal from the uncooled 10-mm thick disc-shaped cathode was hampered because it was accomplished through a holder from the opposite side of the cathode. In this case, the cathode temperature depended on the discharge current, and, already at a current of 2 A, the cathode got red hot.

The cooled cathode was a cylindrical cup whose outer bottom surface acted as a cathode working surface. The cup was hermetically closed with a lid to which the tubes with cooling water were soldered. This design ensured efficient cooling of the cathode working surface; as a result, its temperature increased just slightly even at currents of several amperes. The interelectrode distance was 4 mm. The working gas was helium at atmospheric pressure. The impurity (H_2, N_2, O_2, Ar, CO_2, CO, Ne, and H_2O) contents did not exceed 0.02%. The discharge was fed by a dc power supply with an output voltage of up to 600 V.

As is seen in Fig. 1a, the structure of the glow discharge is as follows: a thin (less than 1-mm thick) disc of glow emission resides above the cathode surface, whereas the glowing column is adjacent to anode. Between these glow regions, there is the Faraday dark space. The anode surface is covered with a glowing layer. The positive column contracts to a diameter of about 3–5 mm (Figs. 1a, 1b). The discharge can also run when both electrodes are flat (see Fig. 1c). However, in this case, the electrode surfaces must be polished and strictly parallel. The discharge was observed at currents of up to 1.5 A. When determining the cathode fall parameters, a more stable APGD with a rounded anode was used.

For a cooled cathode, the current–voltage APGD characteristic (Fig. 2, solid curve) is slowly rising in the current and voltage ranges 0.05–15 A and 200–280 V, respectively [19]. For an uncooled cathode (Fig. 2, crosses), at currents of several amperes, the discharge becomes unstable and transforms into an arc. As is seen in [17], the potential profile along the discharge gap has a shape typical of conventional glow discharges [10–14]: the main voltage drop (150–200 V) occurs in the cathode region, whereas the minor voltage drop (40–50 V) is shared between the positive column and the anode region.

Current density. The current density was defined as the ratio of the discharge current I to the area of the negative glow S (Fig. 3). For a cooled cathode, the intensity of the negative glow varies slightly along the radial direction, which seems to be indirect evidence that the current density is constant over the main part of the area occupied by the negative glow. The area occupied by the negative glow depends linearly on the discharge

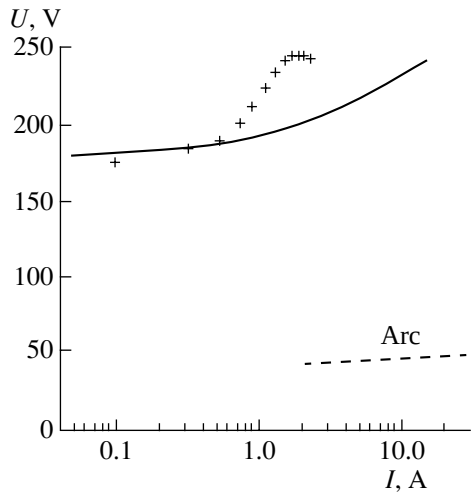

Fig. 2. APGD current–voltage characteristic.

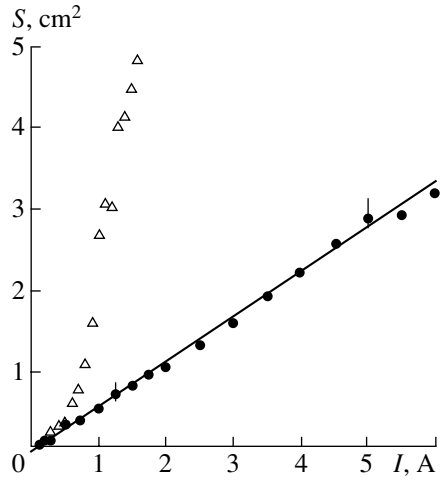

Fig. 3. Negative glow area vs. discharge current for cooled (circles) and uncooled (triangles) cathodes.

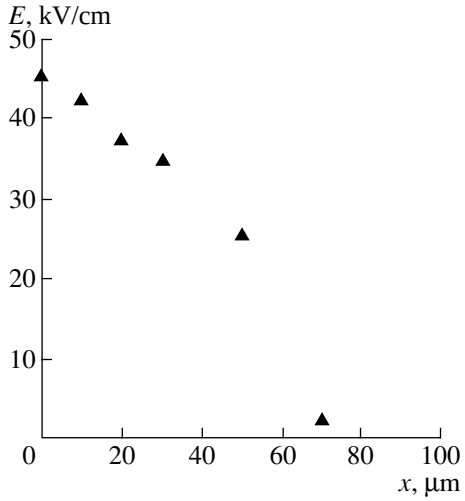

Fig. 4. Axial profile of the electric field.

current (Fig. 3, solid curve). This linearity indicates that, within the cathode fall region, the current density is constant, as in the case of a normal glow discharge. The normal current density determined from the curve slope is equal to 1.8 ± 0.1 A/cm^2.

For an uncooled cathode, the area of the negative glow depends linearly on the current only at currents of no higher than 0.3–0.5 A (Fig.3, triangles). A further increase in the current results in the more rapid growth of the negative glow area, which is related to the cathode heating. At a current of 1.5–2 A, the negative glow occupies the entire cathode area. In this case, the negative glow becomes nonuniform in the radial direction: its intensity in the peripheral area is several times lower than in the central region. Seemingly, the current density also decreases with distance from the discharge axis. Hence, the cathode fall parameters were compared with the predictions of one-dimensional models [6, 23, 24] described in the next section only for a cooled steel cathode. We used a steel cathode because, in [10–13], there are data on the cathode fall parameters in a low-pressure glow discharge (LPGD) in helium with an iron cathode, which are needed to apply theoretical models [6, 23, 24].

To this end, we determined the following APGD parameters: the current density J, the cathode fall voltage V_c, the gas temperature T_g, the electric field profile $E(x)$, the cathode fall thickness d, and the heat flux to the cathode Q_c. The measurements were carried out at a discharge current of 1 A.

Cathode fall voltage. The cathode fall voltage V_c was measured with the help of a tungsten probe 50 μm in diameter. The length of the uninsulated part of the probe was 7 mm. The potential was measured with respect to the grounded cathode at the instant just before the probe touched (or just after it detached) the cathode. At a current of 1 A, the cathode fall voltage was $V_c \approx 155 \pm 2.5$ V.

Electric field profile. The electric field profile $E(x)$ in the cathode fall region of an APGD in helium with a steel cathode was determined using a spectropolarization technique [20, 22]. To this end, the effect of the Stark splitting of the hydrogen energy levels in the external electric field was used. The shape of the H_β 486.128-nm hydrogen line was recorded in the direction perpendicular to the discharge axis; thus, the line of sight was parallel to the cathode surface. The measurements were carried out at a minimum possible aperture of ~0.02 with a resolution at the discharge axis of ~20 μm. This resolution can be regarded as a compromise one, because, as the aperture decreases further, the resolution becomes comparable with the cathode fall thickness. Several such measurements of the electric field were carried out. The measured electric field profile along the discharge axis is shown in Fig. 4. It is seen that the cathode fall thickness is $d \sim 70$ μm and the maximum electric field near the cathode surface is 46 ± 2.5 kV/cm.

Gas temperature profile. The gas temperature profile $T_g(x)$ in an APGD was determined from the spectrum of molecular nitrogen [25], which is present in helium as a minor impurity. The (0–1) $N_2^+ (B^2\Sigma_u^+)$ band (λ = 427.81 nm) from the first negative system of molecular nitrogen ion served as a working band. The technique of determining the gas temperature T_g is based on the measurements of the relative intensities of corresponding bands under the assumptions that the rotational level populations of N_2^+ molecules in the excited electronic state obey Boltzmann distribution and that the measured rotational temperature T_{rot} corresponds to the gas temperature T_g. Estimates show that $\tau_c \gg \tau_{rot}$, where $\tau_c = 63.1$ ns is the lifetime of the excited

electronic state ($B^2\Sigma_u^+$) and $\tau_{rot} = 0.67$ ns is the time of rotational relaxation of nitrogen molecules in atmospheric-pressure helium at a temperature of 300 K. The obtained axial profile of the gas temperature in an APGD is shown in Fig. 5. Unfortunately, we failed to determine the gas temperature in the cathode fall region by using this technique. However, as is seen in Fig. 5, at the end of the cathode fall region (~0.01 cm), the temperature can be estimated at 600–650 K. The temperature increases with distance from the cathode, the temperature gradient being 2500 ± 250 K/cm.

Heat flux to the cathode. The heat flux to the cathode Q_c was determined by a calorimetric method. For this purpose, we determined the amount of water flowing through the cooled cathode and measured the water temperature at the entry into and exit from the cathode. Based on these data, one can calculate the heat power removed from cathode with water. The heat flux to the cathode Q_c was determined by dividing this power by the area of the negative glow.

3. CATHODE FALL MODELS ACCOUNTING FOR VOLUMETRIC HEAT RELEASE

At present, there is a variety of the models of normal and anomalous glow discharges. A recent analysis [14] shows that, even at low pressures, the predictions of the available models significantly disagree in the cathode fall parameters. This stems from the lack of knowledge on the cathode emission properties and scatter in the data on the cross sections for elementary processes in plasma. At atmospheric pressures, the situation becomes even more complicated because of the lack of the experimental data and because applying some numerical models, e.g., those based on the Monte Carlo method, is highly hypothetical under these conditions. Moreover, according to [14], only a few models of a low-pressure glow discharge took into account the effects of gas heating and, besides, this account only slightly affected the simulation results.

Having recognized the complicity of the kinetic models of an APGD and having estimated the reliability of the results that could be obtained from these models, we decided on simple one-dimensional models [6, 23, 24] to determine the cathode fall parameters of an APGD in helium and to compare the calculated results with the experimental data. These models take into account the effect of ohmic gas heating on the discharge characteristics and do not require the knowledge of elementary kinetic processes in the cathode region. With these models, one can go over from the well-known parameters of a glow discharge at pressures of 1 torr [10–13, 26] to the APGD parameters via scaling laws for a normal glow discharge. Let us consider the specific features of these models.

The model of [6] is based on the following assumptions:

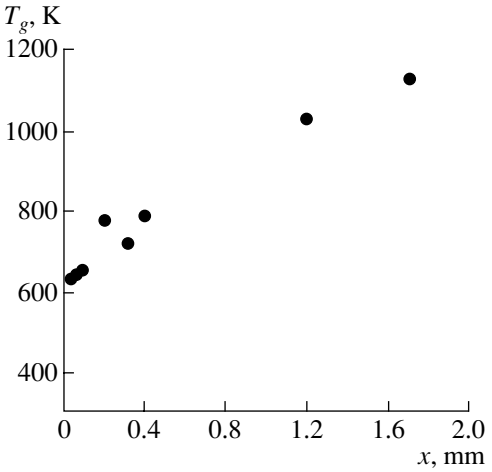

Fig. 5. Axial profile of the gas temperature.

(i) Gas heating in the cathode fall is caused by collisions between the positive ions and neutral gas atoms.

(ii) Both the electric field and the ion current density decrease linearly with distance from the cathode.

(iii) The gas thermal conductivity is proportional to the gas temperature, $\lambda(T) = \alpha T$.

(iv) The cathode fall region, which is nonuniform in temperature, is replaced by a sheath with a uniform average temperature $\langle T \rangle$, and the electric parameters of the cathode fall are determined by using scaling laws for a normal glow discharge.

In this model, the heat conduction equation for the gas in the cathode fall has the form

$$T\frac{d^2T}{dx^2} + \left(\frac{dT}{dx}\right)^2 + \frac{E_{max}J}{\alpha}\left(1 - \frac{x}{d}\right)^2 = 0; \quad (1)$$

where J is the current density, E_{max} is the electric field near the cathode surface, and d is the cathode fall thickness. In [6], the solution to Eq. (1) with the boundary conditions

$$T = T_c \quad \text{at} \quad x = 0,$$
$$\frac{dT}{dx} = 0 \quad \text{at} \quad x = d \quad (2)$$

was found in the form

$$T = T_c\left[1 + \sqrt{q}\left(\frac{2x}{d} - \frac{x^2}{d^2}\right)\right]. \quad (3)$$

After averaging the temperature over x, we have

$$\langle T \rangle = T_c\left(1 + \frac{2}{3}\sqrt{q}\right), \quad (4)$$

where the dimensionless parameter q

$$q = \frac{V_c J d}{3\lambda_c T_c} \quad (5)$$

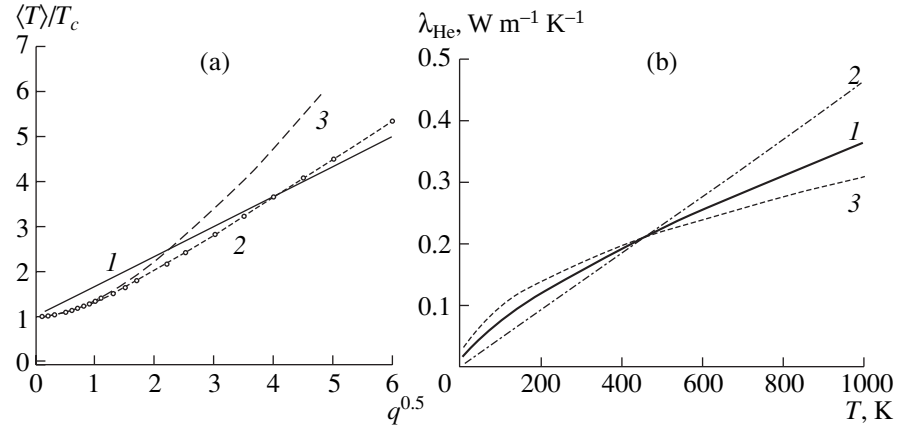

Fig. 6. (a) Average temperature $\langle T\rangle$ in the cathode fall region vs. heat release: (*1*) approximate calculations at $\lambda \propto T$, (*2*) exact calculations at $\lambda \propto T$, and (*3*) exact calculations at $\lambda \propto \sqrt{T}$ [formula (12)]; (b) the helium heat conductivity vs. temperature: (*1*) measured heat conductivity λ_{He} [27], (*2*) linear approximation $\lambda_L(T) = \alpha T$, and (*3*) square-root approximation $\lambda_{1/2}(T) = \beta\sqrt{T}$.

is the heat release power in the cathode fall normalized to the heat flux with a gradient near the cathode surface of $2T_c/d$. Here, V_c is the cathode fall voltage and λ_c is the gas thermal conductivity at the temperature T_c.

With allowance for the scaling laws for a normal glow discharge [26],

$$J = J_l\left(\frac{PT_l}{P_l\langle T\rangle}\right)^2, \quad d = d_l\frac{P_l\langle T\rangle}{PT_l}, \tag{6}$$

the authors of [6] obtained the dependence of the current density on pressure in the form

$$\frac{P}{P_l} = \frac{T_c}{T_l}\sqrt{\frac{J}{J_l}} + \frac{2}{3}\sqrt{q_l}\left(\frac{J}{J_l}\right)^{3/4}. \tag{7}$$

Here, the quantities with index *l* correspond to a low-pressure discharge. Expression (7) describes the well-known power-law dependence (with a power index of 4/3) of the current density on pressure, which is valid for a gas discharge with a large heat release power q and a cathode kept at a constant temperature T_c.

However, it is easily seen that the solution to Eq. (1) is described by the expression

$$T = T_c\sqrt{1 + q(1-\xi^4)} \tag{8}$$

(where $\xi = 1 - x/d$), rather than formula (3). Then, we have

$$\langle T\rangle = T_c\left[\frac{1}{3} + \frac{\sqrt{2}}{3}\sqrt{1+q}\sqrt[4]{1+\frac{1}{q}}F\left(\varphi, \frac{1}{\sqrt{2}}\right)\right]; \tag{9}$$

where $F(\varphi, k)$ is the elliptic integral of the first kind and

$$\varphi = \arcsin\frac{\sqrt{2}}{\sqrt{1+\sqrt{1+\frac{1}{q}}}}. \tag{10}$$

Let us analyze the difference between solutions (4) and (9). The related dependences of the average temperature of a uniform cathode sheath on $\sqrt{q}$ are shown in Fig. 6 (curves *1* and *2*). It is seen that, under intense heat release ($\sqrt{q} > 2$), the temperature increases linearly with $\sqrt{q}$ for both approximate solution (4) and exact solution (9) (both of them result in the 4/3 power law). The average temperatures determined by formulas (4) and (9) differ at most by 25% (at $\sqrt{q} \approx 0.7$).

Both in the model of [6] and in deriving exact solution (9), it was assumed that the gas thermal conductivity depended linearly on the temperature. In the model of [23], the square-root dependence $\lambda \sim \sqrt{T}$ was assumed. In this case, the gas temperature depends on the distance from the cathode as

$$T = T_c\sqrt{1 + \frac{3}{4}q(1-\xi^4)}, \tag{11}$$

and, to within 2%, the average temperature can be expressed in the form

$$\langle T\rangle = T_c(1 + 2.475q_c + 0.366q_c^2)^{1/5}, \tag{12}$$

where q_c is determined by formula (5), in which the current density and the cathode fall thickness d are recalculated for the temperature T_c. The dependence of the average temperature in the cathode fall region on $\sqrt{q}$ given by formula (12) is shown by curve *3* in

Fig. 6a. For $\sqrt{q} \leq 1.5$, the mathematically correct expressions for $\langle T \rangle$ obtained from the models with both linear and square-root dependences of the thermal conductivity on the temperature lead to nearly the same results. At high q, according to the model of [23] with $\lambda \sim \sqrt{T}$, the average temperature in the cathode fall is $\langle T \rangle \sim q^{2/3}$; consequently, the current density is a power function (with a power index of 6/5) of the pressure.

The experimental data on the helium thermal conductivity λ_{He} as a function of the gas temperature are given in [27] and are shown by curve *1* in Fig. 6b. Here, the linear, $\lambda_L(T) = \alpha T$ (curve *2*), and the square-root, $\lambda_{1/2}(T) = \beta\sqrt{T}$ (curve *3*), approximations are also shown. The coefficients α and β are chosen such that $\lambda_L(T_c) = \lambda_{1/2}(T_c) = \lambda_{He}(T_c)$. We can see that the real thermal conductivity of helium lies between the linear and square-root approximations.

In [24], an attempt was made to calculate the parameters of the cathode fall with allowance for a nonuniform temperature distribution in it. According to [24], the local characteristics of the cathode fall at atmospheric pressure can be expressed in the form

$$dx = \delta(x)\frac{P_l T(x)}{P T_l} dx_l, \quad E(x) = \varepsilon(x)\frac{P T_l}{P_l T(x)} E_l(x_l); \quad (13)$$

where $\delta(x)$ and $\varepsilon(x)$ are the corrections related to the deviation of the current density J from the normal local value $J_n(x)$ determined from the scaling law. To calculate the corrections $\delta(x)$ and $\varepsilon(x)$, we used formulas

$$\frac{J}{J_n(x)} = \frac{1}{\delta(x)[1 + \ln\delta(x)]^2}, \quad \varepsilon(x) = \frac{1}{1 + \ln\delta(x)}. \quad (14)$$

The temperature profile in the cathode fall is calculated from the heat conduction equation

$$\frac{d}{dx}\left[\lambda(T)\frac{dT}{dx}\right] + E J_T = 0, \quad (15)$$

where J_T is the fraction of the current density that causes gas heating. For a normal glow discharge, the current density J is believed to correspond to the minimum of the cathode fall voltage.

In [24], in contrast to [6, 23], it was suggested that the electron current also contributes to gas heating in the cathode fall along with the ion current. In the cathode fall, the power of the ion current W_i is approximately twice the electron current W_e. When estimating the fraction of the power W_e spent on gas heating, we should take into account that, in a monatomic gas, which is the case of helium, elastic collisions between electrons and atoms are nearly the only channel for transferring the electron energy into the atomic thermal energy. The average energy fraction transferred in one collision is $2m_e/M_{He}$, where m_e and M_{He} are the masses of an electron and a He atom, respectively. At distances of a few tens of the electron mean free paths, this inefficient mechanism for the energy transfer is definitely not capable of conveying a significant fraction of the electron current power to gas heating. The power W_e is mainly spent on the ionization and excitation of helium atoms; it is easily seen that the former takes about one-half of W_e. Hence, the ion current makes the main contribution to gas heating in the cathode fall region.

We note that, in all the above models, the ion current density at the end of the cathode fall region was assumed to be zero, which is not the case. This assumption somewhat lowers the temperature at the end of the cathode fall region. Thus, calculations with the use of the ion and total currents determine the lower and upper temperature limits at the end of the cathode fall region. The experimental data should be compared with the cathode fall parameters calculated under the assumption that only the ion current contributes to gas heating in the cathode fall.

4. DISCUSSION

The measured and calculated parameters of the cathode fall are listed in the table. The experimental data obtained at a discharge current of 1 A are presented in the first row of the table. Note that almost all the cathode fall parameters required for a comparison with the theoretical results were determined as was described in Section 2. The only parameter that we were not able to measure here is the cathode surface temperature T_c.

To determine T_c, we will use the above models. We will require that the calculated electric parameters of the cathode fall of an APGD coincide with the experimental data. At the same temperature T_c, the models assuming that gas heating is caused by the ion current should give the lower gas temperature T_d at the end of the cathode fall region than the measured one. In contrast, the models assuming that both the ion and electron currents contribute to gas heating give T_d much higher than the measured one. The data for a normal glow discharge with an iron cathode in helium at a pressure of 1 torr [26] are shown in the second row of the table (LPGD [26]). It turns out that the use of these values as cathode fall parameters of an LPGD in calculations by the models of [6, 23, 24] gives the APGD parameters that differ from the measured ones by several times. To fit the calculated data to the experimental ones, the LPGD cathode fall thickness must be increased twice, whereas the current density must be increased by a factor of 5.5 for models with the ion current and 6.5 for models with the total current. The described procedure of determining the cathode surface temperature gives $T_c \sim 450$ K, which seems to be reasonable taking into account that the thickness of the cathode plate is 2.5 mm and the thermal conductivity of steel is $\lambda_{st} = 46$ W m^{-1} K^{-1} at $T = 400$ K [28].

The cathode fall parameters calculated by different models are shown in the next rows of the table. Except

Measured and simulated cathode fall parameters of an APGD in helium

	V_c, V	J, A/cm^2	E_{max}, kV/cm	d, cm	T_c, K	T_d, K	dT/dx, K/cm	Q_c, W/cm^2
$APGD_{expt}$	155 ± 2.5	1.8 ± 0.1	46 ± 2.5	0.0070 ± 5		625 ± 25	2500 ± 250	250
LPGD [26]	150	2.2×10^{-6}		1.3	290	290		
$LPGD_{calc}$ ion current	150	1.21×10^{-5}		2.6	290	290		
total current		1.43×10^{-5}						
APGD [9]	150	1.81	44.7	0.0067	450	578	0	225
APGD [4]	150	1.24	36.9	0.0081	450	781	0	200
APGD [23]	150	1.72	43.5	0.0070	450	584	0	215
APGD [24], ion current	150.2	1.87	48.6	0.0066	450	582	0	233
	150.2	1.84	48.4	0.0067	450	599	2500	236
APGD [24], total current	150.6	1.74	45.0	0.0076	450	709	0	261
	150.6	1.71	44.7	0.0077	450	726	2500	265

for the model [6] based on the approximate solution, all the other models assuming that only the ion current contributes to gas heating give nearly the same results. In the model [6] based on the exact solution (APGD [9]) and the model of [23] (APGD [23]), an agreement between the cathode fall parameters stems from the fact that the given experimental conditions correspond to $\sqrt{q} \approx 0.8$ (Fig. 6a). Since the use of the approximate formulas in the model of [6] at $\sqrt{q} \approx 0.8$ results in a significant error (Fig. 6a), the cathode fall parameters determined in this way (APGD [4]) were not used to analyze the experimental data. The absence of an appreciable difference between the results calculated by the models in which a nonuniform sheath is replaced by a uniform one with a certain average temperature and those calculated by the model [24], in which the ion current is assumed to be responsible for gas heating and the temperature variations across the sheath are taken into account (APGD [24], ion current), stems from fact that the sheath is nearly uniform: the parameter of local anomaly varies from 0.7 to 1.2.

The assumption that gas heating is caused by the total current rather than the ion current leads to a significant increase in the calculated temperature T_d at the end of the cathode fall region (APGD [24], total current). Calculations by the model of [24] were carried out with two boundary conditions at the end of the cathode fall region: $dT/dx = 0$ and 2500 K/cm. The latter condition is taken from the experimental data and corresponds to heat flux $Q_d \approx 6.5$ W/cm^2 to the cathode fall region from the positive column.

It is seen from the table that the calculated electric parameters of the APGD cathode fall (V_c, J, E_{max}, and d) are in good agreement with the experimental data. The measured T_d value lies between the temperatures calculated by the models with the ion and total currents. The measured and calculated heat flux densities Q_c to the cathode are close to each other. When calculating the heat flux density Q_c to the cathode by the models assuming that only the ion current contribute to gas heating, the energy released due to the neutralization of ions on the cathode surface was also taken into account.

5. CONCLUSION

In this study, a self-sustained normal glow discharge in atmospheric-pressure helium is investigated at currents of up to 15 A. In the course of comprehensive experiments, the main parameters of the cathode fall of a normal glow discharge in atmospheric-pressure helium with a steel cathode, namely, the electric field profile, cathode fall thickness, current density, gas temperature, and heat flux to the cathode are determined. The measured current density and cathode fall thickness differ from those calculated by one-dimensional models with allowance for volumetric heat release [6, 23, 24] by a factor of 5–6 and 2, respectively. This discrepancy can be related to both the scatter in the data on the LPGD in helium with an iron cathode [10–13, 26] and some difference between the conditions of our experiment (steel instead of iron and the presence of impurities in helium) and those at which the LPGD parameters were measured. The difference between the balances of elementary processes in the LPGD and APGD plasmas, which can limit the applicability of scaling laws (6), also cannot be ruled out. For example, it was found that the density of metastable atoms in the APGD cathode fall was almost one order of magnitude lower than the electron density [21], whereas for the LPGD in helium [29], the situation was opposite.

Nevertheless, the experimental and theoretical results obtained are in reasonable agreement, the calculated cathode fall parameters being strictly related to each other. The best agreement is achieved when the ion current is assumed to be responsible for gas heating in the cathode fall. Note that the models of [6, 23] and [24], which are quite different in that they assume the temperature distributions in the cathode fall to be uni-

form and nonuniform, respectively, give almost identical results when the ion current is supposed to be responsible for gas heating in the cathode fall.

These one-dimensional models are unlikely to be applied to a discharge with an uncooled cathode seems because the cathode fall parameters are significantly nonuniform in the radial direction. Nevertheless, in this case too, the discharge is a glow discharge, whose description, however, requires more complicated two-dimensional models.

REFERENCES

1. S. Kanazawa, M. Kogoma, T. Moriwaki, and S. Okasaki, J. Phys. D **21**, 838 (1988).
2. F. Massines, A. Rabehi, P. Decomps, *et al.*, J. Appl. Phys. **83**, 2950 (1998).
3. R. B. Gadri, J. R. Roth, T. C. Montie, *et al.*, Surf. Coat. Technol. **131**, 528 (2000).
4. A. P. Napartovich, Plasma Polym. **6**, 1 (2001).
5. K. Becker, in *Proceedings of the XIII Symposium on Atomic, Cluster, and Surface Physics, 2002*, p. 129.
6. A. Engel, B. Seeliger, and M. Steenbeck, Z. Phys. **85**, 144 (1933).
7. G. Suits, J. Appl. Phys. **10**, 648 (1939).
8. H. Y. Fan, Phys. Rev. **55**, 769 (1939).
9. W. A. Gambling and H. Edels, Br. J. Appl. Phys. **7**, 376 (1956).
10. G. Francis, *Handbuch der Physik*, Ed. by S. Flugge (Springer-Verlag, Berlin, 1956), Vol. 22, p. 53.
11. J. M. Meek and J. D. Craggs, *Electrical Breakdown of Gases* (Clarendon, Oxford, 1953; Inostrannaya Literatura, Moscow, 1960).
12. V. L. Granovskiĭ, *Electric Current in a Gas: Steady-State Current*, Ed. by L. A. Sen and V. E. Golant (Nauka, Moscow, 1971).
13. Yu. P. Raizer, *Gas Discharge Physics* (Nauka, Moscow, 1987; Springer-Verlag, Berlin, 1991).
14. A. V. Phelps, Plasma Sources Sci. Technol. **10**, 329 (2001).
15. L. I. Kiselevskiĭ and D. A. Solov'yanchik, Zh. Anal. Khim. **23**, 829 (1968).
16. L. I. Kiselevskiĭ, D. A. Solov'yanchik, and I. I. Suzdalov, Zh. Prikl. Spektrosk. **16**, 969 (1972).
17. L. I. Kiselevskiĭ, S. L. Mazurenko, A. N. Makarevich, and D. A. Solov'yanchik, Zh. Prikl. Spektrosk. **54**, 682 (1991).
18. V. I. Arkhipenko, S. M. Zgirovskiĭ, A. K. Kapanik, *et al.*, Zh. Prikl. Spektrosk. **64**, 711 (1997).
19. V. I. Arkhipenko, A. K. Kapanik, L. V. Simonchik, and S. M. Zgirovskiy, in *Proceedings of the 1998 International Conference on Plasma Physics and 25th EPS Conference on Controlled Fusion and Plasma Physics, Prague, 1998*; ECA **22C**, 2671 (1998).
20. V. I. Arkhipenko, S. M. Zgirovskiĭ, and L. V. Simonchik, Zh. Prikl. Spektrosk. **66**, 362 (1999).
21. V. I. Arkhipenko, S. M. Zgirovskiĭ, and L. V. Simonchik, Zh. Prikl. Spektrosk. **67**, 530 (2000).
22. V. I. Arkhipenko, S. M. Zgirovskiĭ, N. Kon'evich, *et al.*, Zh. Prikl. Spektrosk. **67**, 658 (2000).
23. S. Ya. Bronin, V. M. Kolobov, V. N. Sushkin, *et al.*, Teplofiz. Vys. Temp. **18**, 46 (1980).
24. G. A. Baranov and S. A. Smirnov, Zh. Tekh. Fiz. **69** (11), 49 (1999) [Tech. Phys. **44**, 1305 (1999)].
25. V. I. Arkhipenko, S. M. Zgirovskiĭ, A. A. Kirillov, *et al.*, in *Proceedings of the Conference on Physics of Low-Temperature Plasma, Petrozavodsk, 2001*, Vol. 1, p. 285.
26. A. von Engel and M. Steenbeck, *Elektrische Gasentladungen, Ihre Physik und Technik* (Springer, Berlin, 1934; ONTI, 1936), Vol. 2.
27. *Handbook on Heat Conductivity of Liquids and Gases*, Ed. by N. B. Vargaftik, L. P. Filippov, A. A. Tarzimanov, *et al.* (Énergoatomizdat, Moscow, 1990).
28. V. S. Chirkin, *Thermophysical Properties of Materials for Nuclear Plants* (Atomizdat, Moscow, 1968).
29. E. A. Den Hartog, D. A. Doughty, and J. E. Lawler, Phys. Rev. A **38**, 2471 (1988).

Translated by N. N. Ustinovskiĭ

Plasma Physics Reports, Vol. 28, No. 10, 2002, pp. 866–870. Translated from Fizika Plazmy, Vol. 28, No. 10, 2002, pp. 939–944.

LOW-TEMPERATURE PLASMA

Development of a Linear Corona Torch Discharge

G. V. Ashmarin, V. M. Lelevkin, and A. V. Tokarev

Kyrgyz–Russian Slavic University, Bishkek, 720000 Kyrgyzstan

Received October 29, 2001

Abstract—An anomalous kind of the positive corona—a linear corona torch discharge—is investigated. The discharge is nearly steady-state and operates with various electrode configurations, e.g., wire–plane, needle–plane, wire–cylinder, and two or more wires placed in parallel. It is found that the discharge exists in the form of a pulsed corona or an ordinary positive corona, which alternatively change each other under the action of a spark-gap switch. *© 2002 MAIK "Nauka/Interperiodica".*

1. INTRODUCTION

Corona discharges are widely used to modify the surface of composite materials in plasmochemistry, to clean gases of aerosols and chemically-active fogs (e.g., in sulfuric acid production), etc. [1–4]. In corona discharges, active plasmochemical reactions related to gas ionization and dissociation proceed within a narrow region near the corona electrode (the inner region of the discharge). The main voltage drop occurs in the rest of the discharge gap (the outer region), where the current is carried by heavy ions, the ionization and chemical processes are of minor importance, and the electric power is lost uselessly. The inner corona region can be expanded over the entire discharge gap by igniting a pulsed nanosecond corona discharge [5] with the help of either a special high-voltage pulsed generator or a torch discharge [6]—an anomalous kind of the positive corona [6–9]. In the presence of a disc-shaped positive corona electrode placed in parallel to the grounded plane surface, a corona torch discharge is ignited at discharge gap lengths of 15–30 mm and voltages of 15–30 kV [10–12].

In this study, we investigate a linear corona torch discharge (LCTD), which combines the useful properties of an ordinary corona discharge, a pulsed corona, a torch discharge, and a corona torch discharge [13].

2. EXPERIMENTAL SETUP

A schematic of the experimental setup used to study the linear corona torch discharge is shown in Fig. 1. The power supply consists of an autotransformer T_1, from which the voltage is applied to the primary coil of a high-voltage transformer T_2. The high voltage from the secondary coil is applied to the voltage-doubling circuit, consisting of diodes D_1 and D_2 and capacitors C_1 and C_2. The power supply provides an output voltage of up to 25 kV at a current in the load of I = 10 mA. The discharge unit, which serves as a load for the power supply, consists of a 220-mm-long 0.5-mm-diameter Nichrome wire (anode) placed in parallel to the cathode plate at the distance of d = 20–30 mm. The high voltage of positive polarity is applied to the wire.

The electrical and power parameters of the discharge were determined by measuring the power in the primary coil of the power supply with the help of a wattmeter. The average discharge current was measured simultaneously with the help of a microammeter and an oscilloscope, taking into account both the pulsed and dc current components. A comparison of the data obtained showed ~5% discrepancy between these measurements over almost the entire current and voltage ranges. In oscilloscope measurements of the discharge current, a noninductive shunt R_3 was set in series with the microammeter. In this case, the microammeter was short-circuited to prevent the distortion of the measured current pulse shape. The discharge voltage was measured by an electrostatic voltmeter.

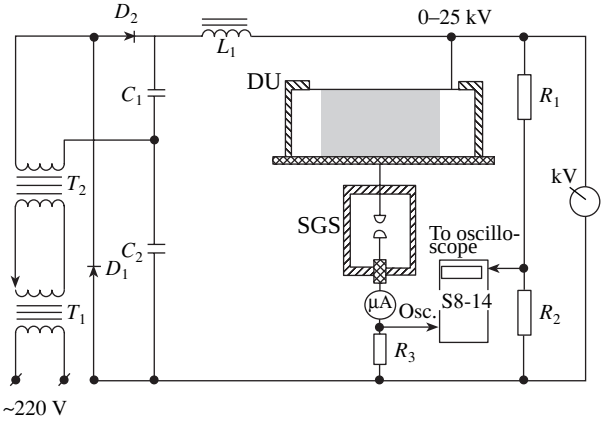

Fig. 1. Schematic of the experimental setup: (T_1) autotransformer, (T_2) high-voltage transformer, (D_1, D_2, C_1, C_2) voltage-doubling scheme, (L_1) choke, (R_1, R_2) voltage divider, (kV) kilovoltmeter, (μA) microammeter, (S8-14) S8-14 storage oscilloscope, (SGS) spark-gap switch, and (DU) discharge unit.

1063-780X/02/2810-0866$22.00 © 2002 MAIK "Nauka/Interperiodica"

The power supply cathode was grounded through a spark-gap switch (SGS). The gap length between the SGS electrodes was varied in the range $h = 0$–5 mm. At $h = 0$, either an ordinary corona or a corona torch discharge occurred, depending on the shape of the corona electrodes. Otherwise, an LCTD was ignited between the corona wire and the parallel conducting plate. For an LCTD to occur, the cathode must be electrically separated from the power supply by an SGS and an inductance L should be introduced in the discharge circuit at the anode side. A choke consisting of two 20000-turn coils wound on an electrical-steel core acted as a variable inductance L. A U-type magnetic core with a cross-sectional area of 950 mm^2 and 440-mm-long mean line was used. To change L, the controlled dc bias current was passed through two 250-turn windings wound in series round the choke. The L value was determined by the voltmeter–ammeter method at a frequency of 50 Hz [14]. The inductance measured without biasing was compared with the calculated L value for a toroidal core taken from [15]:

$$L_p = \frac{\mu_0 \mu}{2\pi} \omega^2 a \ln \frac{D + r}{D - r},$$

where μ_0 is the permeability of free space; μ is the relative permeability of the core material; ω is the number of turns; D is the average core diameter; and a and r are the average axial and radial dimensions of the turn, respectively. A comparison of the results shows that $L \approx L_p$.

3. LCTD DEVELOPMENT

Visual and photographic studies revealed the following stages in the LCTD development. The increase in the voltage (up to the SGS breakdown) is accompanied by a weak glow characteristic of an ordinary positive corona. After the first SGS breakdown, the corona discharge rapidly expands into the discharge gap. At $U = 15$ kV and $d = 30$ mm, the entire interelectrode gap is occupied by the LCTD plasma with a diffuse violet glow (Fig. 2). On the wire, there are a number of spots that the discharge contracts. As the voltage increases to $U = 17$ kV, the glow intensity rises and the current increases to 600 μA. At $U = 18.5$ kV and $I = 1000$ μA, the LCTD becomes almost uniform throughout the entire volume and over the entire wire length (Fig. 3). The discharge cross section looks like an oval curve whose vertex is located on the corona wire, whereas the branches of the curve enter the other electrode at right angles to its surface. Inside the oval curve, the glow is of pale-blue color in the central region and of violet color at the periphery. The main discharge current flows within the oval curve; in the outer region, the current is carried by slowly drifting N^+, O^+, O^-, and other ions. When the SGS is short-circuited ($h = 0$), the situation is quite different. In this case, an ordinary positive corona ($U = 18.5$ kV and $I = 100$ μA) with a characteristic weak glow around the wire is observed in the discharge gap. All other factors being the same, the LCTD current is by one order of magnitude higher than the positive corona current.

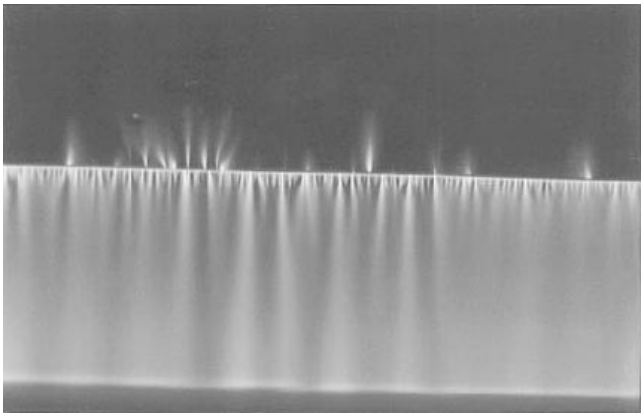

Fig. 2. Linear corona torch discharge: $U = 17$ kV, $d = 30$ mm, $h = 0.5$ mm, $L = 3640$ H, and $I = 0.1$ mA.

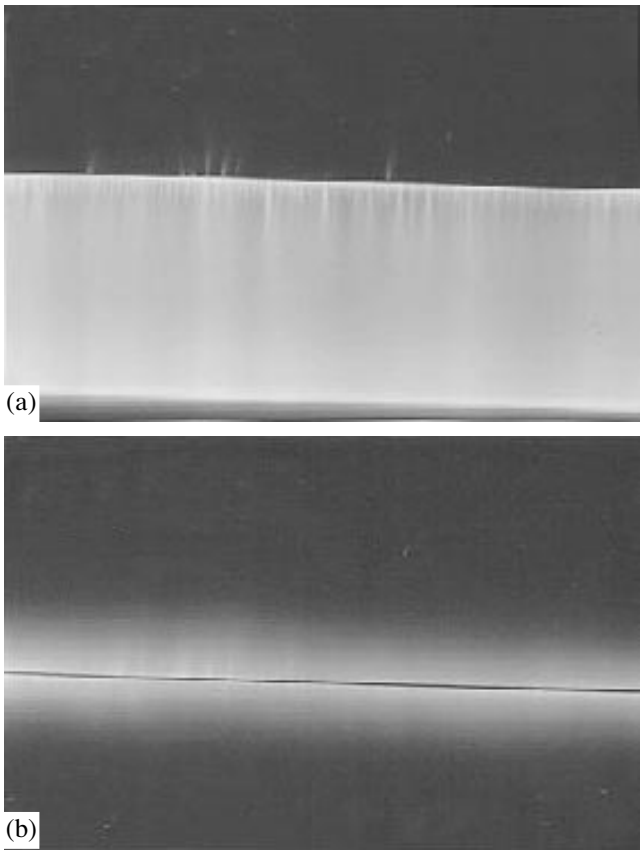

Fig. 3. (a) Side and (b) top view of a linear corona torch discharge: $U = 18.5$ kV, $d = 30$ mm, $h = 0.5$ mm, $L = 3640$ H, and $I = 3.4$ mA.

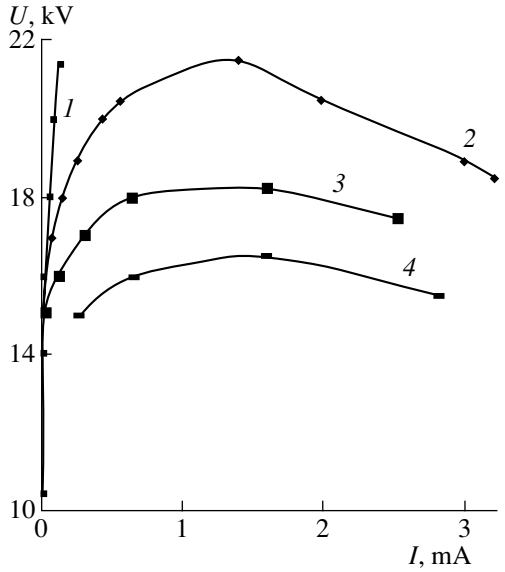

Fig. 4. Current–voltage characteristics measured using an ammeter for h = 0.5 mm and L = 3640 H: positive corona (*1*) and LCTD with d = (*2*) 30, (*3*) 25, and (*4*) 20 mm.

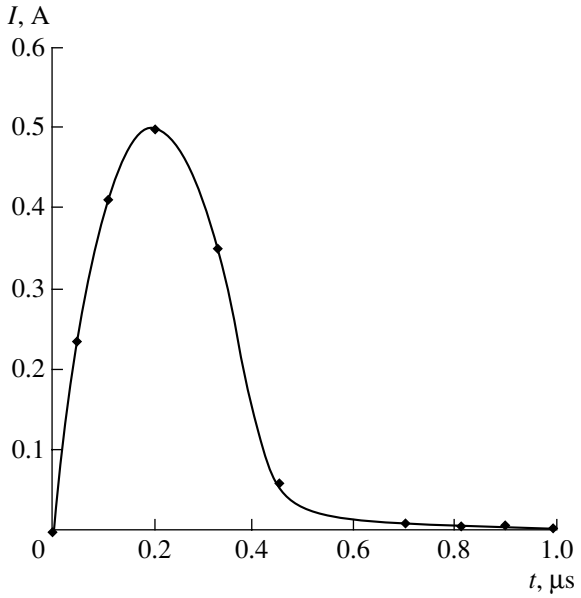

Fig. 5. LCTD current pulse for U = 18.5 kV, I = 2.8 mA, ν = 14 kHz, L = 3640 H, d = 30 mm, and h = 0.5 mm.

4. DISCHARGE CHARACTERISTICS

Figure 4 presents the LCTD current–voltage characteristics for different interelectrode distances. It is seen that the voltage decreases as d decreases from 30 to 20 mm. At I = 1250 μA, the ascending branch of the current–voltage characteristic passes over to the descending one. Nevertheless, the discharge remains almost steady-state throughout the entire range of discharge voltages. For reference, at d = 30 mm, an ordinary positive corona is characterized by a maximum current of 135 μA, power of up to 3 W, and voltage of up to 21.5 kV.

In an LCTD, the product of the gas pressure by the interelectrode distance amounts to pd = 1520–2280 torr cm; i.e., the streamer mechanism for the breakdown of the gas gap is dominant, and the transition from the classical positive corona to an LCTD is not smooth. The LCTD occurs to be stable at any configuration of the corona electrode.

Oscilloscope studies of the LCTD (Fig. 5) show that the LCTD current is pulsed. The pulse duration and amplitude slightly increase with the discharge current. The pulse repetition rate increases linearly from 10 Hz to 14 kHz as the discharge current increases from 5 to 2800 μA due to a decrease in the resistance of the discharge gap. As the voltage increases, the pulse repetition rate, the current, and the discharge power vary substantially, although the charge transmitted per one pulse increases insignificantly (from 0.12 to 0.17 μC). Along with the ac current component I_{osc} (Fig. 6), there is also the dc component I_{const}. Altogether, these two components constitute the current I_a measured with the ammeter. The I_{const} fraction amounts to 10% of the total discharge current. Actually, I_{const} is the current of an ordinary positive corona that runs during the pauses between the current pulses. This corona current charges the capacitance of the cathode plate and the input oscilloscope capacitance, which is connected in series with the cathode. A small current can flow through the spark gap due to the residual conductance of the gap after the preceding pulse.

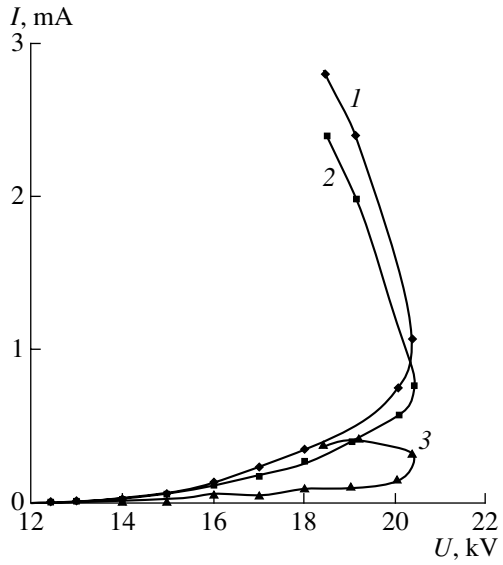

Fig. 6. Discharge current–voltage characteristics for d = 30 mm, h = 0.5 mm, and L = 3640 H. Curve *1* shows the current I_a measured with an ammeter, curve *2* shows the pulsed current component I_{osc} measured with an oscilloscope, and curve *3* shows the dc current components I_{const} measured with an oscilloscope.

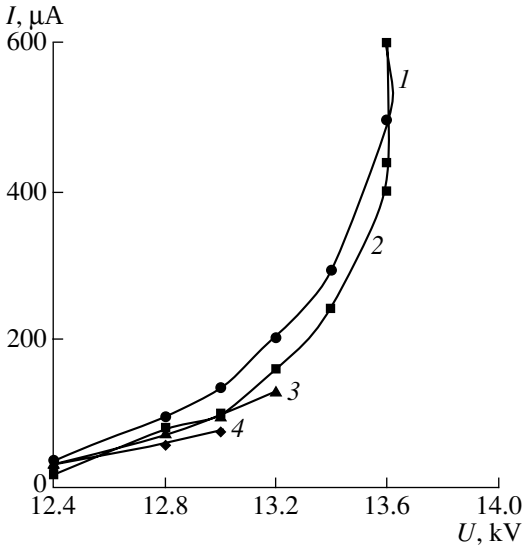

Fig. 7. Current–voltage characteristics for d = 15 mm; h = 0.5 mm; and an anode inductance of L = (*1*) 3640, (*2*) 3092, (*3*) 1990, and (*4*) 198 H.

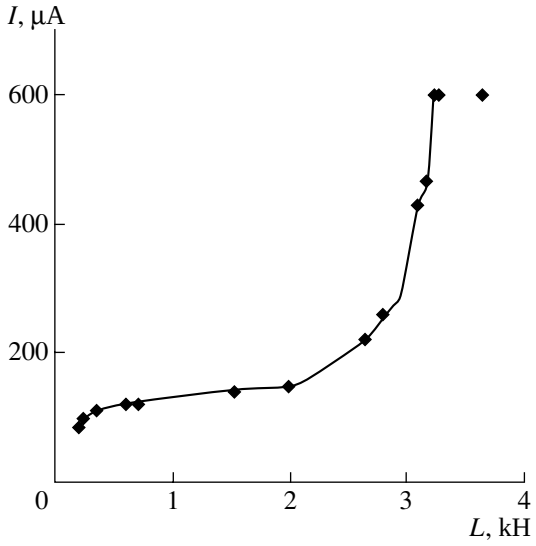

Fig. 8. Maximum LCTD current vs. inductance for d = 15 mm and h = 0.5 mm.

5. EFFECT OF INDUCTANCE

Along with the SGS, the inductance L introduced in the discharge circuit is of importance for the LCTD formation. The influence of L on the discharge characteristics was studied for a main discharge gap of 15 mm. At d = 15 mm, the LCTD transforms into an arc discharge at voltages and prebreakdown currents lower than those at d = 30 mm.

Varying the value of L in the anode circuit of LCTD within the range 150–3640 H substantially affects the discharge processes (Fig. 7). At L = 200 H, U = 13 kV, and a discharge current of lower than 50 μA, the LCTD transforms into an arc discharge. At higher L values of up to 3640 H, a stable LCTD is feasible at voltages of up to 13.6 kV and currents of I = 40–600 μA. The increase in the inductance not only increases the maximum discharge current, but also enlarges the region of stable LCTD operation within the voltage range 0.6–1.2 kV. The generalized dependence of the maximum LCTD current on the inductance at constant SGS parameters (Fig. 8) is very nonlinear. The maximum current changes from 100 to 600 μA, and the saturation occurs at L = 3200 H, which allows one to increase the current by several times, the other main discharge parameters being unchanged.

6. LCTD PHYSICS

The LCTD formation and operation are determined by the charging of the cathode plate. On applying the high voltage, the positive charge is transported onto the cathode surface by the positive ions residing in the outer region of an ordinary positive corona. The weak electric field of the remote cathode only slightly affects electron multiplication. The reproduction of electrons is ensured by the secondary processes near the corona electrode [16]. The positive ions approaching the cathode are neutralized by the electrons knocked-out from the electrode. The excitation energy is lost due to emission and collisions with the ambient gas molecules. The coefficient of secondary emission at the cathode surface is small. The neutralization of ions proceeds until the cathode acquires a potential sufficient to prevent electron emission from the metal under the action of incident ions. The charging of the capacitor goes on because the incident ions are held near the cathode due to electrostatic attraction. This results in the formation of a positive space charge sheath near the cathode surface. The space charge density in the sheath exceeds that in the discharge gap. As soon as the voltage at the cathode plate reaches the breakdown value, the cathode discharges to a low potential. The SGS breakdown is accompanied by the injection of a large amount of electrons into the discharge gap. Some of these electrons recombine with the positive space charge near the cathode; another electrons are attached to oxygen; and the rest ones participate in the formation of electron avalanches, which then transform into anode-directed streamers. The recombination of space charge at the cathode plate increases the conductance of the discharge gap due to the following processes:

(i) At the instant of SGS breakdown, the emission coefficient γ increases significantly because the probability of transferring the recombination energy to the metal electrons increases.

(ii) After breakdown, the positive charge in the immediate vicinity of the cathode becomes neutralized, whereas the space charge in the cathode sheath as a whole shifts only slightly. Hence, a kind of a capacitor is formed whose plates are the cathode and the layer of

positive ions over the cathode surface. This situation is similar to that with a charged dielectric film at the cathode surface, where cold emission starts at $E \approx 10^6$ V/cm, and its intensity rapidly increases with electric field; e.g., at $E \approx 10^7$ V/cm, the current density becomes as high as 10^6 A/cm^2 [17]. Due to electron emission, the conductance of the discharge gap sharply increases, the space charge decreases and fails to limit the corona discharge current. In a time of ~300 ns, the capacitors formed by the corona electrode with both the cathode and the earth discharge through the conducting gap. This discharge current is added to the current of an ordinary positive corona. The large inductance in the anode circuit decreases the growth rate of the discharge current; as a result, Joule heating decreases and the resistance increases.

The repetition rate of the discharge current pulses depends on the power supply voltage, the SGS breakdown voltage, and the cathode plate capacitance. The pulse repetition period can be estimated using the common expression $\tau = R_x C_2 \ln \frac{U_p}{U_p - U_2}$, where R_x is the total resistance of the charging circuit of the cathode plate capacitance C_2, U_p is the power supply voltage, and U_{br} is the SGS breakdown voltage [18]. Applying a dc voltage from the power supply results in the pulsed LCTD current. The pulse amplitude, duration, and repetition rate can be controlled by varying the inductance and the SGS breakdown voltage. A steady-state LCTD acquires the properties of a pulsed corona discharge.

7. CONCLUSION

An anomalous kind of the positive corona—a linear corona torch discharge—is investigated. A steady-state LCTD can be excited in regime of self-excited oscillator with an inductance introduced in the anode circuit and with an SGS in the cathode circuit. The discharge parameters can be varied over a wide range by changing the inductance in the anode circuit.

REFERENCES

1. A. F. Pershin and A. V. Fedorova, in *Proceedings of the 3rd International Congress "Water: Ecology and Technology," ECWATECH-98, Moscow, 1998*, p. 671.
2. V. N. Uzhov, A. Yu. Val'dberg, B. I. Myagkov, and K. K. Reshidov, *Industrial Gas Cleaning against Dust* (Khimiya, Moscow, 1981).
3. Yu. V. Gorin, F. Kh. Kulakhmetov, É. D. Kurbanov, *et al.*, Élektron. Obrab. Mater., No. 1, 41 (1986).
4. Ch. M. Dzhuvarly, Élektron. Obrab. Mater., No. 1, 51 (1987).
5. R. Kh. Amirov, I. S. Samoĭlov, and A. V. Shepelin, in *Proceedings of the Conference "Plasma Physics and Technology"* (Akad. Nauk Resp. Belarus', Minsk, 1994), p. 321.
6. V. I. Popkov and N. B. Bogdanova, Izv. Akad. Nauk SSSR, Énerg. Transp., No. 1, 79 (1968).
7. N. B. Bogdanova and V. I. Popkov, Dokl. Akad. Nauk SSSR **129** (2), 21 (1959).
8. N. B. Bogdanova and B. G. Pevchev, Zh. Tekh. Fiz. **45**, 97 (1975) [Sov. Phys. Tech. Phys. **20**, 58 (1975)].
9. R. L. Andrianova, N. B. Bogdanova, and B. G. Pevchev, Izv. Akad. Nauk SSSR, Énerg. Transp., No. 4, 102 (1980).
10. V. M. Lelevkin, A. V. Tokarev, and V. A. Yudanov, in *Hakone 5: International Symposium on High-Pressure Low-Temperature Plasma Chemistry, Milovy (Czech Republic), 1996*, Contributed papers, p. 273.
11. A. V. Tokarev, V. A. Yudanov, and K. S. Kim, in *Collection of Scientific Articles* (Kyrgyzsko-Rossiĭskiĭ Slavyanskiĭ Univ., Bishkek, 2000), Vol. 2, p. 12.
12. A. V. Tokarev, V. A. Yudanov, and K. S. Kim, in *Collection of Scientific Articles* (Kyrgyzsko-Rossiĭskiĭ Slavyanskiĭ Univ., Bishkek, 2000), Vol. 2, p. 24.
13. K. S. Kim, V. M. Lelevkin, A. V. Tokarev, and V. A. Yudanov, in *Collection of Scientific Articles* (Kyrgyzsko-Rossiĭskiĭ Slavyanskiĭ Univ., Bishkek, 2000), Vol. 3, p. 23.
14. *Electric Measurements* (Vysshaya Shkola, Moscow, 1972), p. 288.
15. P. L. Kalantarov and L. A. Tseitlin, *Inductance Calculation* (Énergoatomizdat, Leningrad, 1986), p. 368.
16. Yu. P. Raizer, *Gas Discharge Physics* (Nauka, Moscow, 1987; Springer-Verlag, Berlin, 1991).
17. V. L. Granovskiĭ, *Electric Current in Gas* (Gostekhteoretizdat, Moscow, 1952), p. 200.
18. G. I. Izyurova and M. S. Kaufman, *Instruments and Facilities in Industrial Electronics* (Vysshaya Shkola, Moscow, 1975), p. 317.

Translated by N. N. Ustinovskiĭ

Plasma Physics Reports, Vol. 28, No. 10, 2002, pp. 871–876. Translated from Fizika Plazmy, Vol. 28, No. 10, 2002, pp. 945–951.

LOW-TEMPERATURE PLASMA

Microwave Cellular Discharge in Fine Powder Mixtures

G. M. Batanov*, N. K. Berezhetskaya*, V. A. Kop'ev*, I. A. Kossyi*, A. N. Magunov*, and V. P. Silakov**

**Institute of General Physics, Russian Academy of Sciences, ul. Vavilova 38, Moscow, 119991 Russia*

***Keldysh Institute of Applied Mathematics, Russian Academy of Sciences, Miusskaya pl. 4, Moscow, 125047 Russia*

Received February 21, 2002

Abstract—The excitation of microwave discharges in fine semiconductor powders and powder mixtures of metals and dielectrics is studied. The plasma is produced due to local sparks generated in microsecond microwave pulses. The time delay in the onset of a discharge amounts to several milliseconds for intensities on the order of 10 kW/cm^2. As the discharge develops, both microwave absorption and the discharge glow intensity increase. Intense nonuniform heating of the powder is observed. *© 2002 MAIK "Nauka/Interperiodica".*

1. In early experiments on the irradiation of solid targets with high-power microwave beams (see [1, 2]), the excitation of low-threshold discharges on dielectric surfaces with metal inclusions in the form of grains with characteristic dimensions no larger than 1 mm was observed (Fig. 1a). The number density of the metal grains randomly distributed over the surface was such that the grains did not form a solid conducting layer and the target as a whole was transparent to low-power microwave radiation. However, starting from a certain intensity of the microwave beam, a discharge was excited on the metal–dielectric surface, which resulted in the perturbation (reflection and absorption) of a microwave beam incident on the target. The threshold density of the discharge depended slightly on the gas pressure and fairly well satisfied the relationship

$$\Psi_{\text{thr}}\tau_f \simeq 0.1 \text{ J/cm}^2, \quad (1)$$

where Ψ_{thr} is the threshold intensity of microwave radiation focused on the target surface (in W/cm^2) and τ_f is the microwave pulse duration (in s).

When a metal–dielectric surface is in a rarified gas or in a vacuum, the surface slipping discharge produces a dense collisionless plasma [3] expanding into the surrounding space and filling the vacuum chamber. In a high-pressure gas ($\nu_{\text{eff}} > \omega$, where ω is the microwave angular frequency and ν_{eff} is the effective frequency of electron–neutral collisions), a non-self-sustained gas discharge is excited near the surface of the metal–dielectric target; in this case, the dominant ionizing factor is UV radiation from the microwave surface discharge (see [2, 4]).

Microwave discharges on targets with metal–dielectric surfaces are widely used, e.g., to heat and melt metal inclusions [2], to generate dense collisionless plasmas in the converters of microwave energy into the energy of dc electric field [3], and to produce an excess pressure on the target [4]. However, until recently, mechanisms responsible for surface breakdown have been unknown and a physical model for the phenomenon revealed in [1, 2] has been lacking.

This paper is aimed at studying the excitation of a microwave discharge in a configuration different from that shown in Fig. 1a. Specifically, we studied mixtures of fine powders (with a grain size on the order of 1–40 μm) of dielectric and metal (semiconductor) materials irradiated with a microwave beam, as is shown in Fig. 1b. These experiments are important from the standpoint of both fundamental (the explanation of the mechanisms for the plasma formation on metal–dielectric interfaces) and applied (the search for new technological possibilities provided by the processes of local plasma formation) physics. It should be noted that the possibility of plasma formation under the microwave irradiation of fine powder mixtures is problematic. First of all, it is not clear whether the mechanisms providing the excitation of a microwave discharge on a free metal–dielectric surface will work in this case. Indeed, the small distance (~10 μm) between neighboring powder grains (i.e., the sizes of the pores in the irradiated target) should result in significant diffusion losses of charged particles in the gas and, accordingly, the low probability of plasma formation in the pores.

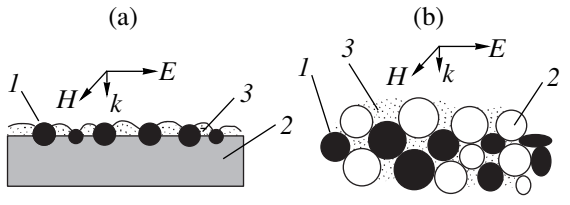

Fig. 1. Schematic representation of metal–dielectric structures initiating a low-threshold microwave discharge: (a) (*1*) a dielectric substrate with (*2*) metal inclusions on its surface and (*3*) electric-discharge plasma; (b) a mixture of (*1*) metal and (*2*) dielectric powders and (*3*) electric-discharge plasma.

1063-780X/02/2810-0871$22.00 © 2002 MAIK "Nauka/Interperiodica"

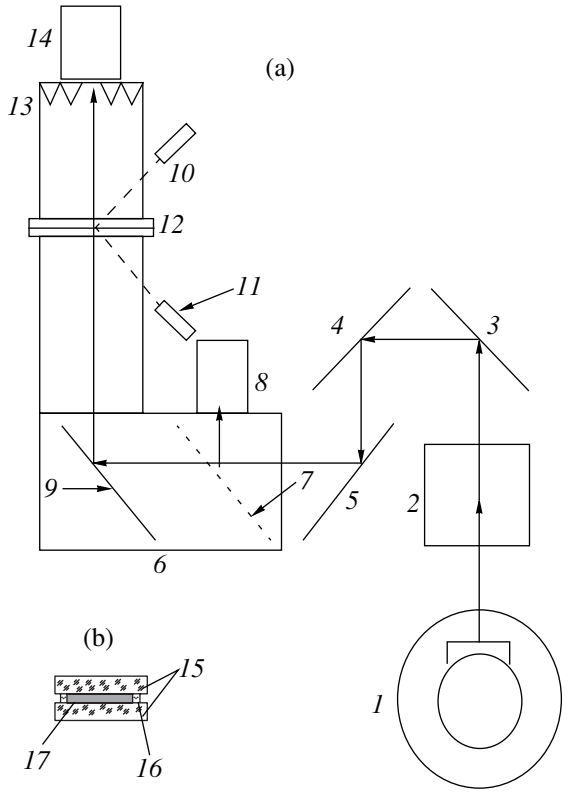

Fig. 2. (a) Schematic of the Svecha testing device: (*1*) gyrotron with a cryomagnet, (*2–5*) mirrors of the quasioptical transmission line, (*6*) target unit, (*7*) quasioptical coupler, (*8*) detector section, (*9*) deflecting mirror, (*10*, *11*) photodiodes, (*12*) sample holder, (*13*) ceramic absorbing loads, and (*14*) detector of the transmitted signal; (b) a schematic representation of a sample (target) irradiated with a high-power microwave beam: (*15*) quartz plates, (*16*) quartz ring, and (*17*) powder-mixture layer.

2. A schematic of the experimental setup is shown in Fig. 2a. A quasioptical system forms a high-power microwave beam acting on a thin layer of a powder mixture. In the experiments, we used a gyrotron with a wavelength of $\lambda_0 = 4$ mm. The gyrotron power was varied from 60 to 240 kW, and the pulse duration was varied from 2 to 10 ms. Sandwich-type samples consisted of three quartz disks 80 mm in diameter. The upper and lower disks were 1 mm thick; the middle 0.5-mm-thick disk was shaped as a ring with an inner diameter of 40 mm to form a cavity between the outer disks (Fig. 2b). The cavity was filled with powders of different compositions. Samples were clamped in a holder and placed in the center of the focal region of a Gaussian microwave beam. The radiation intensity at the beam axis in the sample plane varied from 5 to 20 kW/cm^2.

The signals of radiation incident on the sample and reflected from it were measured with the help of a quasioptical coupler. In addition, we measured the envelop of the microwave radiation transmitted through the sample. The glow of the sample discharge was detected by two collimated photodiodes; one of them was positioned on the side of the incident beam, and another one was positioned behind the sample.

The reflection and transmission coefficients of the samples were preliminarily measured in a special testing device at a low microwave power (30 mW). The minimum absorption coefficients that can be resolved are estimated at $A \approx 0.03$–0.05.

The average size of powder grains was 30–40 μm. We used semiconductor (SnO_2, SnO, CrO_3) and dielectric (Al_2O_3, PbO) powders; glass powder; and also their mixtures with Al, Fe, Ti, and Si powders.

3. The main results obtained in experiments on the irradiation of the samples with a high-power microwave beam in the atmospheric air are the following:

(i) Throughout the entire range of the radiation intensities used in the experiments, the action of a microwave beam on the mixtures of *metal* powder with *dielectric* or *semiconductor* powders (Al + Al_2O_3, Si + Al_2O_3, Ti + PbO, etc.) was accompanied by the excitation of a discharge (the production of a plasma in the powder mixture) at reduced electric fields on the order of $E_{\text{eff}} = E/n_m\sqrt{2} \simeq 10^{-16}$ V cm^2, which was well below the breakdown intensity for air at atmospheric pressure (here, E is the amplitude of the oscillating electric field and n_m is the molecule number density).

(ii) The excitation of a discharge under the action of a microwave beam was also observed when the target was a single-component *semiconductor* (Si, SnO_2, SnO, or CrO_3) powder layer.

(iii) No breakdown occurred (even in microwave pulses with the maximum duration and intensity) when the target was a single-component *dielectric* (Al_2O_3, glass, etc.) powder layer.

First, let us consider in more detail the processes occurring in a metal/semiconductor–dielectric powder mixture irradiated with a high-power microwave beam. As an example, we consider experiments with an Al powder mixed with an Al_2O_3 or PbO powder in the proportions 1 : 1 or 1 : 3. Powder samples of this kind appear to be almost noninteracting with low-power microwaves: the microwave absorption coefficient at low radiation powers ($\leq$30 mW) is below an accessible measurement level ($A \leq 0.05$) and the reflection coefficient does not exceed a value of $R \simeq 0.1$–0.15. However, the propagation of electromagnetic waves changes significantly when the same samples are irradiated with high-power microwave beams. Figure 3 shows the signals of radiation transmitted through the sample and reflected from it, as well as the photodiode signals. During several first milliseconds, there is no significant difference in the behavior of the reflected and transmitted signals as compared to those measured at low microwave powers. Further, the transmitted signal decreases monotonically till the end the microwave pulse, whereas the reflected signal varies only slightly. This

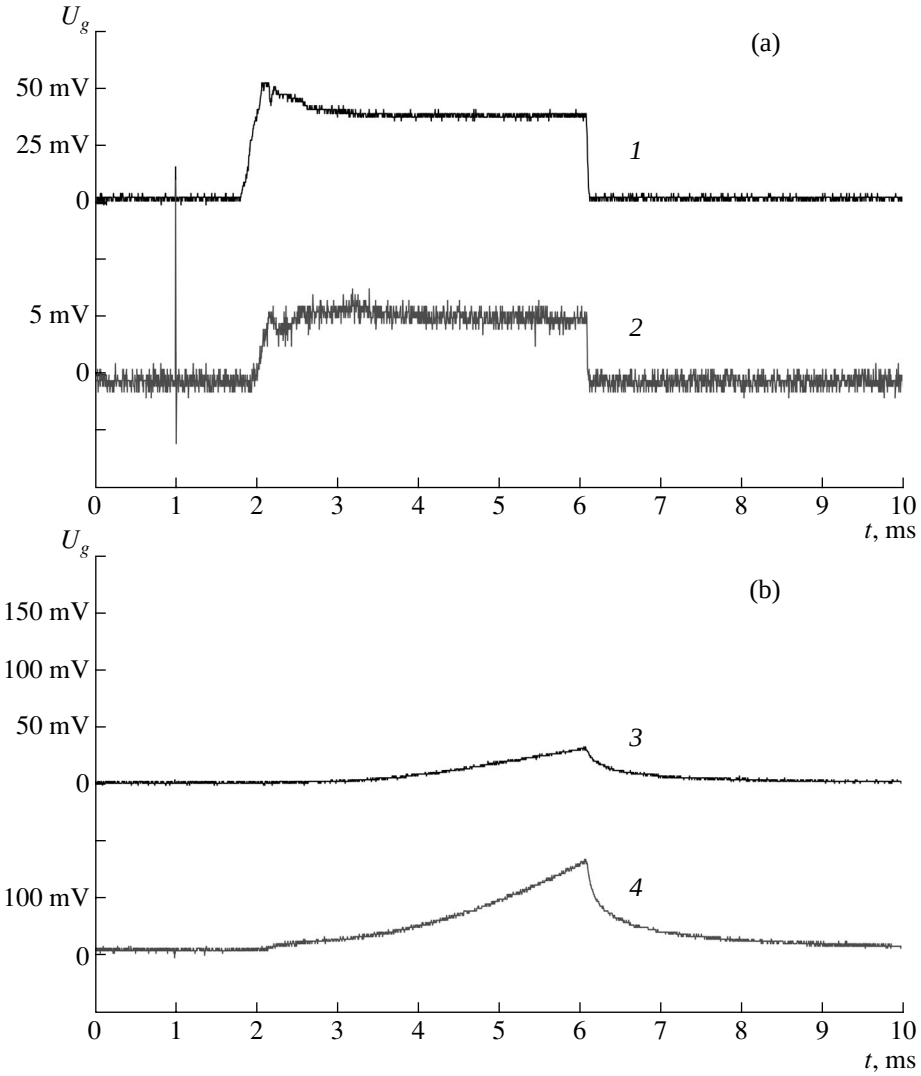

Fig. 3. Typical waveforms of the signals recorded when a target with a metal–dielectric powder mixture was irradiated with a high-power microwave beam (Al + SNO powder mixture): (a) signals from the detectors of (*1*) transmitted and (*2*) reflected microwave power and (b) signals from photodiodes positioned (*3*) in front and (4) behind the sample.

indicates a substantial (up to $A \simeq 0.6$) absorption of microwave energy by the sample. The intensity of the sample glow starts growing with some delay with respect to the time when the transmitted signal begins to fall. After the end of the microwave pulse, the sample glow decays with a characteristic time of 0.3–0.5 ms. In subsequent pulses, the time behavior of the signals is qualitatively the same; however, the initial level of the transmitted signal, as well as the delay times after which the transmitted signal begins to fall and the glow intensity begins to grow, decreases.

The beginning of the glow was detected by both photodiodes simultaneously. Both the sample glow and a substantial increase in the microwave absorption coefficient indicate that a plasma is produced in the powder volume.

The time-integrated spectra of discharge emission for metal/semiconductor–dielectric mixtures of different compositions were studied with the help of an Avantis S-2000 spectrograph (Fig. 4). It can be seen in the figure that the discharge emits a continuous spectrum, which can also contain individual spectral lines and bands. The presence of a continuous spectrum allows us to compare it with a Planckian blackbody spectrum and, thus, to determine the brightness temperature of the discharge. For this purpose, the spectrograph was calibrated with the help of an SI-8 standard lamp in the spectral range 0.45–0.65 μm. The brightness temperature of the discharge turned out to be ~2.5 kK.

Hence, low-threshold microwave discharges can be excited not only in a dielectric target with metal grains introduced into its surface layer (Fig. 1a), but also in a

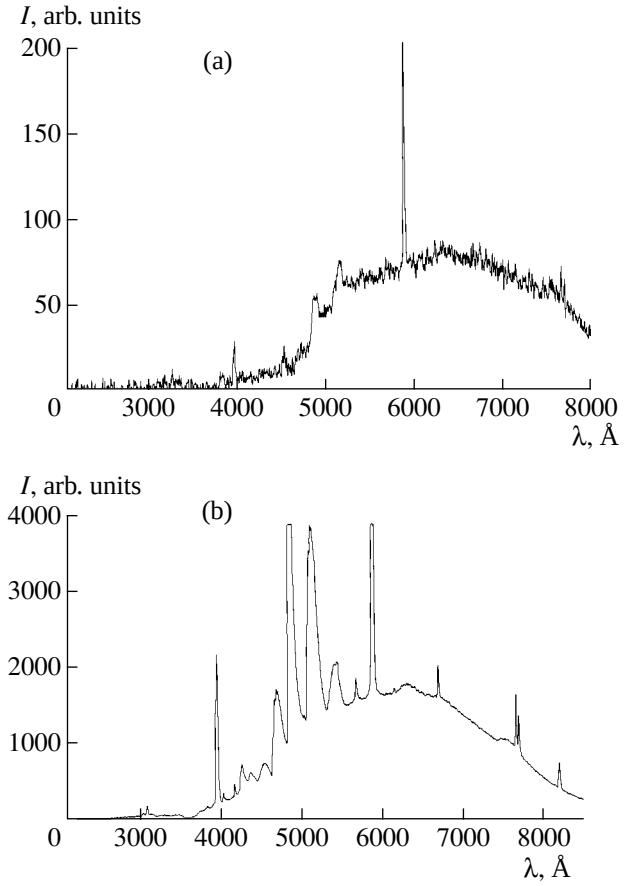

Fig. 4. Typical spectra of optical radiation from a microwave discharge initiated in (a) Si + Al_2O_3 and (b) Al + Al_2O_3 powder mixtures.

layer of a metal/semiconductor–dielectric powder mixture (Fig. 1b).

Experiments show that a low-threshold microwave discharge can also be excited in layers consisting purely of a semiconductor powder. As an example, we consider an experiment on the irradiation of samples containing an SnO_2 powder. At low microwave powers, no appreciable reflection and absorption was detected in these samples. However, when a powder layer was irradiated with a high-power microwave beam, we observed the same features as for metal/semiconductor–dielectric powder mixtures: a delay of the breakdown by several milliseconds, a decrease in the amplitude of the transmitted signal, an increase in the radiation intensity by the end of the microwave pulse, small fluctuations in the signal reflected from the sample, and changes in the signal characteristics in subsequent pulses.

Note that, in some powder mixtures (e.g., in the 1 : 1 mixture of SnO with PbO) exposed to a high-power microwave beam, the mixture components were melted. In this case, we observed a change in the radiophysical properties of the target: being almost completely transparent to low-power microwaves in the initial state, the target began to efficiently absorb microwaves after treating by a sequence of high-power plasma-producing microwave pulses (the absorption coefficient of the powder mixture treated by a high-current microwave beam attains $A \sim 0.4$–0.6; i.e., it increases by one order of magnitude from its initial value). It is interesting that the powder is melted nonuniformly over the layer depth. This indicates that the length on which high-power microwave radiation is absorbed during the pulse appears to be shorter than the powder layer thickness (≤ 0.05 cm).

In some powder layers, a change in the structure of the powder, namely, the material sputtering in the radial direction along quartz plates from the beam axis to the periphery, was observed even after the irradiation by a single microwave pulse accompanied by a discharge. This indicates that the gas pressure inside the layer increases substantially during the discharge. The shorter the microwave pulse, the weaker the effect of gas-dynamic action of the discharge.

4. When analyzing possible mechanisms for plasma production during the microwave irradiation of metal–dielectric systems, we address the paper [2], in which a mechanism for low-threshold breakdown in the version shown in Fig. 1a was proposed. The authors think that of crucial importance in the onset of a microwave discharge may be the injection of electrons from the metal into the conduction band of the dielectric where it is in contact with metal inclusions. The electron emission at the metal–dielectric interface can be enhanced due to a decrease in the electronic work function of metal; in addition, the electric field of the electromagnetic wave is enhanced on metal grains.

Electron injection into the dielectric substrate increases the conductivity of the dielectric in a narrow layer adjacent to the metal; as a result, the conductivity of the dielectric reaches a level typical of semiconductors (see [5]). The absorption of microwave power in the dielectric with an enhanced conductivity is accompanied by the heating of dielectric regions around the metal grains. Both the conductivity of the dielectric and the flux of electrons injected into the dielectric from the metal increase with increasing temperature of the metal–dielectric contact. As a consequence, an explosive energy release in the contact region can occur due to the development of thermal instability [5], which is accompanied by a solid–plasma phase transition.

Probably, in metal/semiconductor–dielectric powder mixtures, an analogues process in the form of a surface discharge (sparking) in the sites of contacts of metal and dielectric grains takes place. Indeed, when metal–dielectric powders were irradiated with 5-μs pulses with intensities of ~10 kW/cm^2 at a radiation wavelength of 2.5 cm, local radiation bursts were observed in the powder in some places of the sample. In millisecond pulses, the area of these local discharges can increase, e.g., because of UV radiation from sparks,

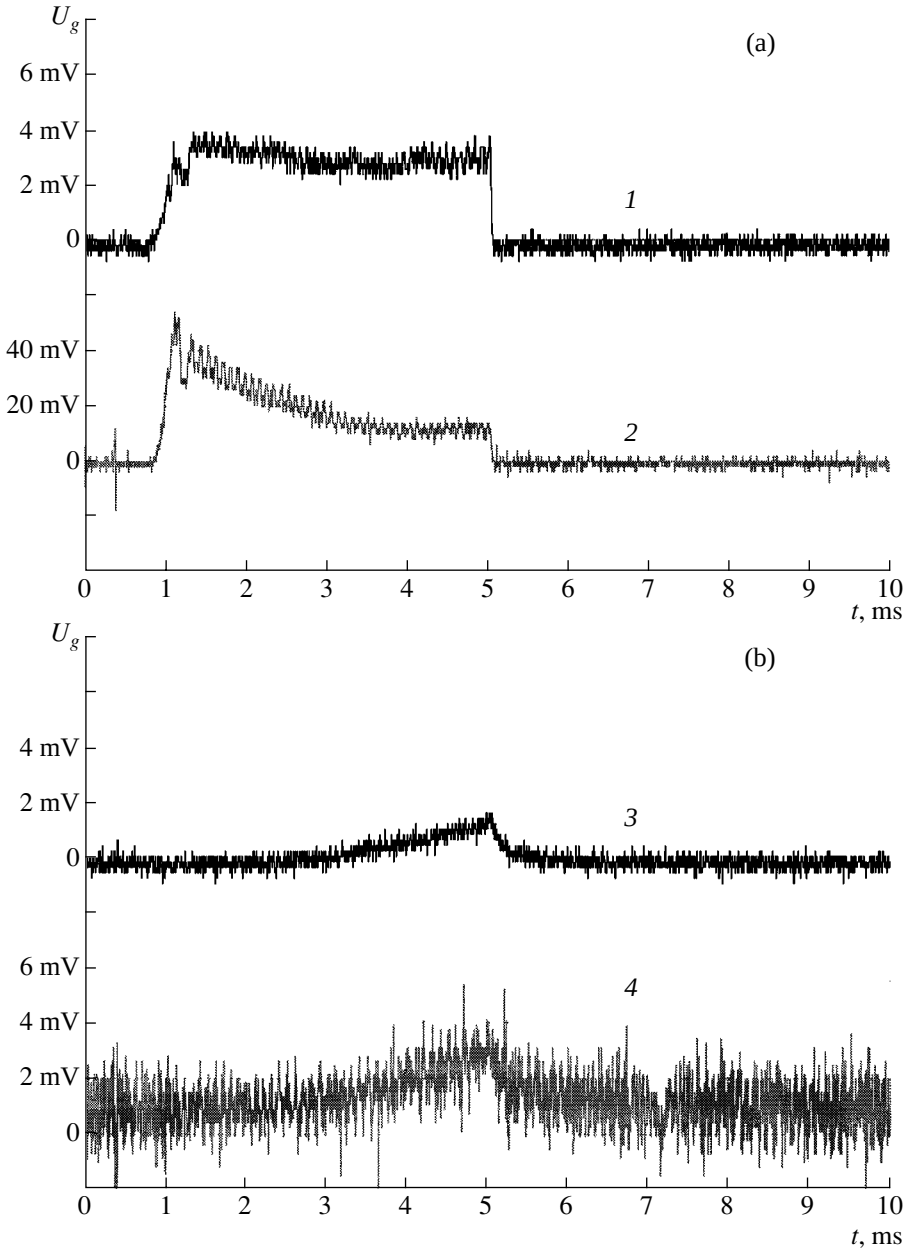

Fig. 5. Typical waveforms of the signals recorded when a siliceous powder was irradiated with a high-power microwave beam: (a) signals from the detectors of (*1*) reflected and (*2*) transmitted microwave power and (b) signals from photodiodes positioned (*3*) in front and (4) behind the sample.

which ultimately results in an efficient absorption over all the sample area exposed to microwaves.

The effect of plasma production under the action of high-power microwave radiation in a one-component semiconductor powder may be regarded as being contradictory to the above assumption about a decisive role of sparking on metal–dielectric contacts. However, this may be merely an apparent contradiction. First of all, we are to take into consideration the presence of the contacts of semiconductor grains with the surfaces of the quartz plates confining the powder layer. Sparking on these contacts may produce an initial plasma and may promote the creation of a microwave-absorbing plasma layer throughout the sample.

At the same time, it is probable that mechanisms different from those operating in a metal–dielectric powder may come into play in the case of a semiconductor powder. Thus, we can assume that free electrons in the conduction band play an important role in the onset of a discharge and that the main effect initiating the discharge is the emission of "hot" electrons from semiconductor due to electron heating by a strong microwave

field penetrating into the semiconductor grains [6]. The emitted electrons are trapped in surface traps, and double electric layers form at the gas–solid interface. Inside pores (cells), the induced conductivity produced by the heating of the emitted electrons in a microwave field can be very nonuniform, which results in the local enhancement of the microwave field and local sparking on the surfaces of some grains. Indeed, no discharge occurs on a uniform single-crystal siliceous plate, whereas in a siliceous powder, a discharge develops with a delay time of 1 ms (Fig. 5).

As a trivial mechanism for plasma production, one could consider the heating of the solid phase by microwaves with a subsequent rarefaction of air in pores, which is accompanied by breakdown because of a decrease in the electric strength of the interparticle gas gaps. However, simple estimates show that the semiconductor powder grains are heated during the discharge delay time by no higher than 100–200 K, which is certainly insufficient for the breakdown of air inside the pores.

5. In summary, we have experimentally discovered a class of solid targets initiating low-threshold microwave discharges in air at atmospheric pressure. In the initial state, the targets are microwave-transparent thin layers of mixtures of fine metal (or semiconductor) and dielectric powders or one-component semiconductor powder. Just as the previously investigated discharge initiators in the form of dielectric plates with metal inclusions on their surfaces, solid initiators are capable of concentrating a substantial amount of energy transferred by microwave beams in fairly small volumes of atmospheric air.

The unique possibility of concentrating the energy release of high-power pulsed microwave beams is of interest for solving a number of technological and engineering problems. In particular, with the use of powder initiators, it is possible to weld dielectrics (even those having different temperature expansion factors). Due to the high gas temperature in discharges occurring in powder, these discharges can be used to initiate solid-state reactions in mixtures at a controlled heat supply.

ACKNOWLEDGMENTS

We thank L.V. Kolik, V.A. Plotnikov, and A.A. Pshenichnikov for maintaining the operation of the gyrotron complex and N.M. Tarasova for advice on optical spectral measurements. This work was supported in part by the International Science and Technology Center (contract no. 908) and the Russian Federal Program “Leading Scientific Schools” (project no. 00-15-66676).

REFERENCES

1. G. A. Askar’yan, G. M. Batanov, N. K. Berezhetskaya, *et al.*, Pis’ma Zh. Éksp. Teor. Fiz. **29**, 706 (1979) [JETP Lett. **29**, 648 (1979)].
2. G. M. Batanov, E. F. Bol’shakov, A. A. Dorofeyk, *et al.*, J. Phys. D **29**, 1641 (1996).
3. *Generation of Nonlinear Waves and Quasi-Steady Currents in Plasma*, Ed. by L. M. Kovrizhnykh (Nauka, Moscow, 1988), Tr. Inst. Obshch. Fiz. Akad. Nauk SSSR, Vol. 16.
4. G. M. Batanov, S. I. Gritsinin, I. A. Kossyĭ, *et al.*, Tr. Fiz. Inst. Akad. Nauk SSSR **160**, 174 (1985).
5. Yu. N. Vershinin, *Electric Breakdown of Solid Dielectrics* (Nauka, Novosibirsk, 1968).
6. V. Denis and Yu. Pozhela, *Hot Electrons* (Mintis, Vilnius, 1971).

Translated by N. F. Larionova

Plasma Physics Reports, Vol. 28, No. 10, 2002, pp. 877–881. Translated from Fizika Plazmy, Vol. 28, No. 10, 2002, pp. 952–956.

LOW-TEMPERATURE PLASMA

High-Power Gas-Discharge EUV Source

V. M. Borisov, A. Yu. Vinokhodov, A. S. Ivanov, Yu. B. Kiryukhin, S. V. Mironov, V. A. Mishchenko, A. V. Prokof'ev, and O. B. Khristoforov

Troitsk Institute for Innovation and Fusion Research, State Scientific Center of the Russian Federation, Troitsk, Moscow oblast, 142090 Russia

Received February 1, 2002

Abstract—The results from studies aimed at creating a high-power high-repetition-rate gas-discharge EUV source based on xenon Z-pinch are presented. In a liquid-cooled EUV source prototype, an average output power of 10 W for the burst mode (~1 s) and 5 W for continuous operation, emitted into a solid angle of 0.25 sr and 2% bandwidth around 13.5 nm is attained at a repetition rate of ~1 kHz. Operating wavelength of the source corresponds to XeXI 13.5-nm ion emission band. It is experimentally shown that the size of the emitting hot plasma can be decreased to ~2 mm without loss in the average output power. The radiation characteristics were determined by using standard techniques and calibrated metrology tools, which allowed a comparison of the absolute values of the measured parameters with the available data on other EUV sources developed for the next-generation lithography with a resolution of ~50 nm. The attained level of an average EUV power of 10 W at $\lambda = 13.5$ nm into the 0.25-sr solid angle and 2% bandwidth is one of the highest at the moment. © *2002 MAIK "Nauka/Interperiodica".*

1. INTRODUCTION

The application of EUV radiation in lithography optical systems requires the development of reliable high-power sources emitting in the spectral range corresponding to efficient reflection from multilayer mirrors. One of the most promising EUV projection systems can be created based on Mo/Si multilayer mirrors, which efficiently (by ~70%) reflect radiation at wavelengths around $\lambda = 13.5$ nm [1].

One of the approaches to creating an EUV source is based on the use of a hot plasma capable of efficiently emitting at $\lambda \sim 13.5$ nm. Such a plasma can be produced either at the focal spot of a laser beam [2] or in a discharge. In the latter case, a direct conversion of the electric energy stored in a capacitor bank into the energy of emitting plasma can increase the source efficiency and simplify technology. To ensure efficient emission in the spectral range near 13.5 nm, the electron temperature of both laser and discharge plasmas should be in the range 20–30 eV. To date, a plasma emitting in 13.5-nm band of XeXI or LiIII ions was obtained, e.g., in Z-pinches [3], plasma focus [4], capillary discharges [5], and pseudospark discharges with a hallow cathode [6]. In all the experiments, it was demonstrated that the discharge plasma can emit intense EUV radiation at $\lambda = 13.5$ nm.

To employ an EUV source in industrial lithographic systems for manufacturing next-generation microchips with critical dimensions near ≤50 nm, one needs an EUV source capable of emitting 13.5-nm radiation with an average power of 50–100 W into the ≥1.8-sr solid angle and $\Delta\lambda/\lambda \le 2\%$ bandwidth [7].

This paper presents the results of studies aimed at creating a high-power EUV source with the parameters needed for EUV lithography.

The studies on high-power gas-discharge EUV sources are being conducted at the Troitsk Institute for Innovation and Fusion Research in cooperation with the XTREME Technology GmbH (under the auspices of the International Science and Technology Center, project no. 1727). In the initial stage of research, a gas-discharge EUV source prototype based on xenon Z-pinch was created [8]. Under continuous operation, the source provided an EUV in-band power of 1 W emitted into the 0.25-sr solid angle at a repetition rate of 100 Hz. The size of the emitting plasma pinch was (1–2) × 20 mm, depending on the input energy (30–35 J/pulse) and the geometry of the electrodes. Below, the second source prototype with a modified cooling system and a more efficient excitation system is described. These improvements allowed us to increase the repetition rate and to significantly raise the average power of EUV radiation as compared to the first prototype.

2. DESIGN OF A GAS-DISCHARGE EUV SOURCE BASED ON XENON Z-PINCH

A schematic of the source is shown in Fig. 1. A hot xenon plasma was produced by using preionization from an surface discharge on a cylindrical dielectric. Preionization ensures the ignition of the discharge in the main discharge gap, improves the pulse-to-pulse stability of the radiated EUV energy, and increases the efficiency of EUV emission from the plasma at the final stage of the pinch discharge. A 15-mm-diameter cylin-

1063-780X/02/2810-0877$22.00

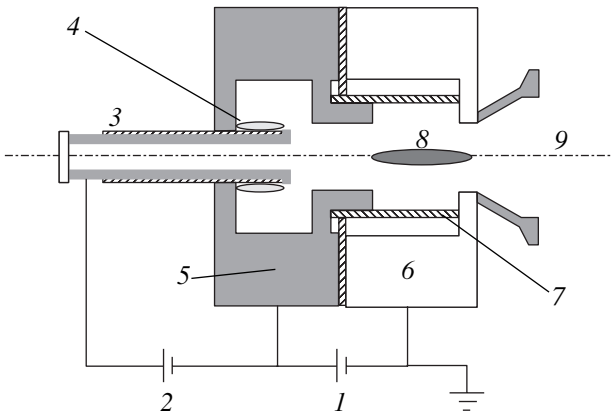

Fig. 1. Schematic of a EUV source based on xenon Z-pinch: (*1*) main discharge power circuit, (*2*) preionizer power circuit, (*3*) preionizer, (*4*) surface discharge, (*5*) cathode, (*6*) anode, (*7*) dielectric tube, (*8*) plasma pinch, and (*9*) output flange for EUV radiation.

drical plasma shell created in the course of preionization contracts to a hot dense plasma column on the axis of the discharge gap under the action of the pulsed magnetic-field pressure produced by the main discharge current with an amplitude of several tens of kiloamperes. To ignite a high-current xenon Z-pinch discharge with an interelectrode distance of 15 mm, we used a pumping scheme with a two-stage pulsed magnetic compression circuit and stored energy from 15 to 40 J. To ensure the source operation at high (up to ~10 kW) input powers, the elements of the discharge chamber were intensely cooled with liquid coolants. A specific feature of one of the versions of the source was the use of dielectric fluid for both cooling and the electrical insulation between the cathode and anode units of the discharge chamber.

A two-channel measurement system was used to determine the energy and temporal evolution of EUV radiation. The energy of EUV radiation was measured in a channel with a Mo/Si mirror (with a reflectance of 73% at λ = 13.5 nm for 4.8% reflectance bandwidth) and an AXUV-100 photodiode with Mo/Si coating. The measurement system was calibrated by using synchrotron radiation of a known intensity; the calibration method is described in [9]. In our experiments, there was an option to set the measurement system at a spe-

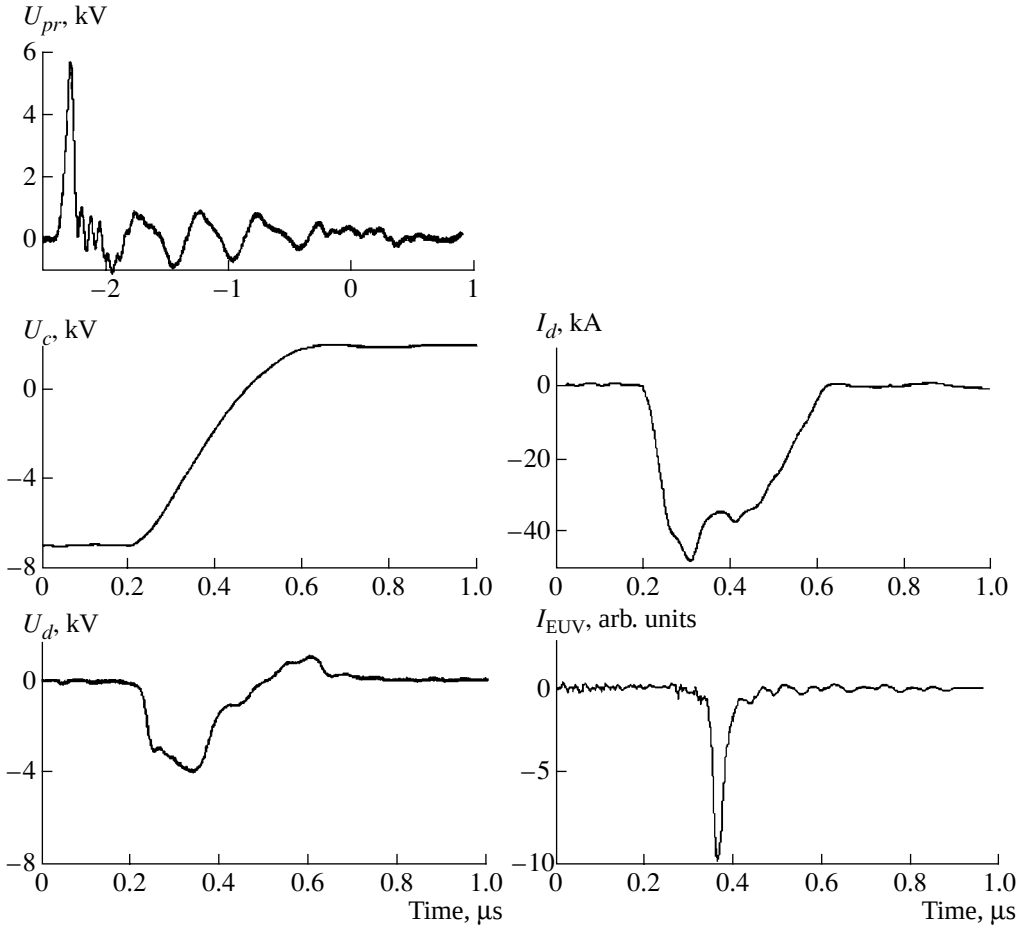

Fig. 2. Waveforms of the voltages across the preionizer (U_{pr}) and storage capacitor (U_c), the discharge voltage U_d, the discharge current I_d, and the intensity I_{EUV} of a 13.5-nm EUV pulse.

cial swing whose axis traversed the discharge region perpendicular to the *Z*-axis. The measurements at various displacements of the measurement system from the discharge axis allowed us to determine the angular distribution of EUV radiation within the 0.25-sr solid angle, in which radiation was emitted.

The other channel was used to determine the waveform of the EUV pulse. This channel consisted of a filter made of a 1-μm-thick Be foil and a Mo/Si mirror reflecting radiation to an SPPD 11-04 photodiode with high (0.5 ns) time resolution. To ensure the linear regime of the high-speed photodiode operation, neutral attenuators of radiation in the form of grids with different mesh sizes were used.

3. OUTPUT PARAMETERS OF THE EUV SOURCE

Figure 2 shows typical waveforms characterizing the operation of the Z-pinch EUV source. In the source, the highest voltage of ≈6 kV (see the waveform of the voltage at the preionizer) is used to ignite an auxiliary discharge located outside the main discharge chamber. One of the main advantages of the preionizer employed is that it ensures the possibility of using much lower voltages (≤4 kV) across the main discharge gap (Fig. 2). This reduces electrodynamic loads on the ceramic tube of the discharge chamber and on the insulation between the cathode and anode units and helps to attain a longer lifetime of the EUV source. It is seen from Fig. 2 that the pumping scheme with a stored energy of 34 J ensures the discharge current with an amplitude of up to 50 kA and a pulse duration of 400 ns, which are required to produce at the discharge axis a hot dense xenon plasma efficiently radiating at λ = 13.5 nm. The front of the EUV signal (Fig. 2) coincides with the onset of a singularity in the waveform of the discharge current. The FWHM duration of the EUV pulse is 40 ns.

The amplitude, duration, and energy of the EUV pulse are governed to a great extent by the gas pressure. Figure 3 shows the peak intensity and energy of 13.5-nm EUV pulses as functions of the Xe pressure. Note that the maximum peak intensity of the EUV pulse is attained at a pressure higher than that at which the maximum energy is attained. At the highest peak intensity, the pulse energy is 17% less than the maximum one.

The dependences of the average EUV power of the second EUV source prototype on the pulse repetition rate for different energies deposited in the discharge are shown in Fig. 4. With a power supply providing an input energy of E_{in} = 32.5 J/pulse (curve *1*), an average EUV power of 10 W/0.25 sr into 2% bandwidth was attained in the demonstration mode (5-s-long running followed by a 10-s pause) at a repetition rate of f = 500 Hz. In the continuous several-hour operation mode

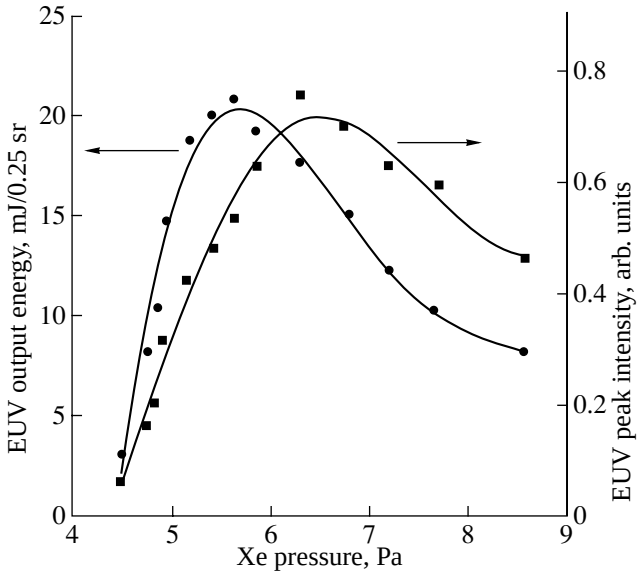

Fig. 3. Energy and the peak intensity of a 13.5-nm EUV pulse vs. Xe pressure.

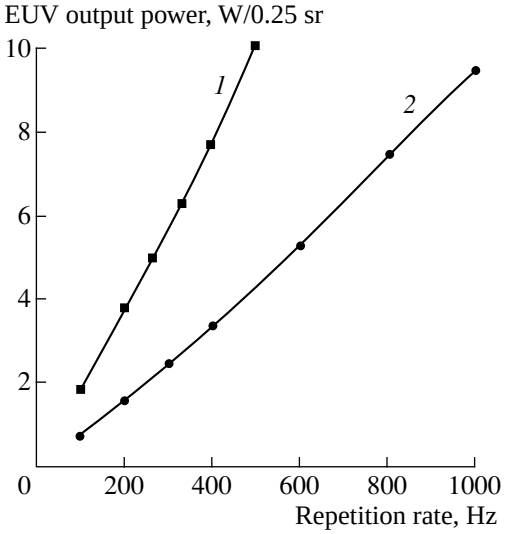

Fig. 4. EUV output power vs. repetition rate for schemes with different input energies of (*1*) 32.5 and (*2*) 17.2 J/pulse.

with f = 260 Hz, the output power was 5 W/0.25 sr into 2% bandwidth. It is seen from Fig. 4 (curve *2*) that the source is capable of operating at f = 1000 Hz without considerable loss in the efficiency due to the reduction in the input energy.

Figure 5 presents a sequence of signals from an AXUV-100 photodiode under continuous operation at f = 300 Hz. It is seen that the energy of the generated EUV pulses is fairly stable (σ = 3–4%). The signals were recorded with a Tektronix TDS-520 D oscilloscope.

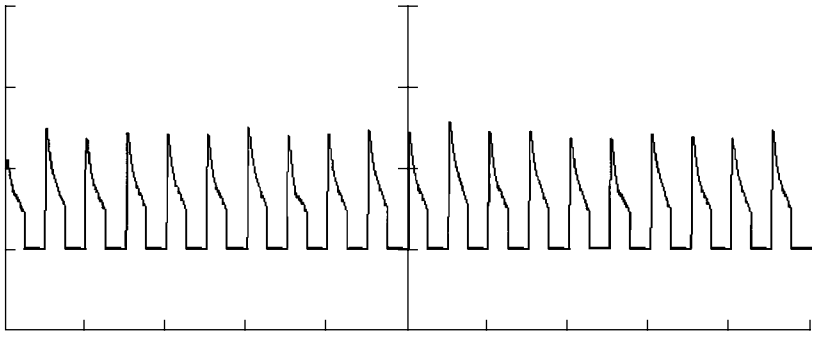

Fig. 5. Sequence of EUV pulses at a repetition rate of f = 300 Hz (measurements with an AXUV-100 photodiode).

4. EFFECT OF GEOMETRICAL FACTORS ON THE SOURCE CHARACTERISTICS

Some optical systems require the use of EUV sources with a smaller size of the emitting zone and a larger angular width of emission as compared to those in the second source prototype under study. To find out whether it is possible to create an EUV source with a small-size emitting zone (<2 mm), we carried out experiments with a modified second prototype.

Figure 6 shows the relative input energy E_{in}/E_0 as a function of the distance h_z between the electrodes. Here, E_0 is the energy stored in the capacitor connected to the source electrodes and E_{in} is the energy deposited in the discharge during the discharge current pulse.

It is seen from Fig. 6 that a good matching between the gas-discharge load and the power circuit is achieved at an electrode distance of 13 mm, used to form a Z-pinch in the second EUV source prototype. In this case, 86% of the energy stored in the capacitors is deposited in the discharge. The shorter the electrode distance, the lower the energy fraction E_{in}/E_0 dissipated in the discharge. Nevertheless, even at an electrode distance as low as h_z = 2 mm, the energy deposition in discharge can comprise a significant fraction of the stored energy: E_{in}/E_0 = 45%. The results obtained show that the creation of an efficient gas-discharge EUV source with a small-sized emitting zone requires the development of a pumping scheme that is better matched to the electric-discharge load and that is capable of using the energy left in the capacitors after an EUV pulse to pump the following pulses.

Figure 7 presents the measured energies of EUV pulses from a modified source with an electrode distance of 2 mm and the waveform of the 13.5-nm EUV radiation pulse with an FWHM duration of 38 ns. It is

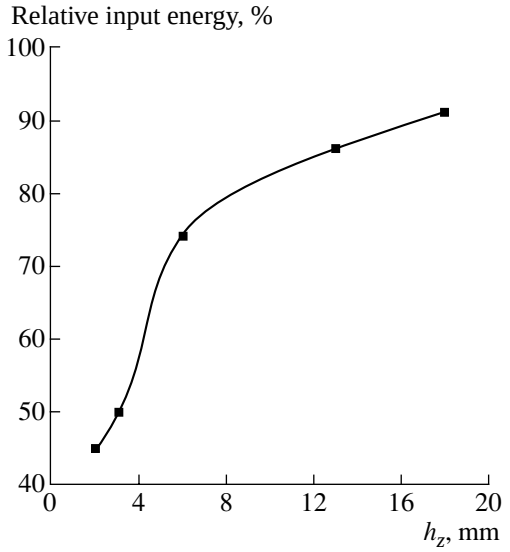

Fig. 6. Relative input energy E_{in}/E_0 vs. electrode distance h_z.

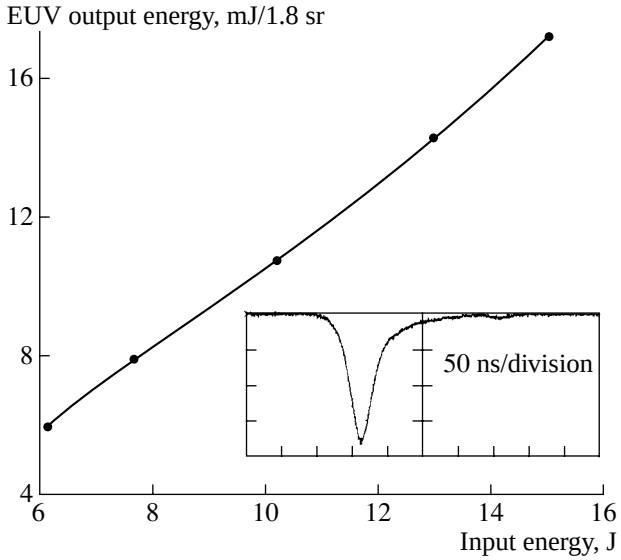

Fig. 7. EUV in-band energy vs. energy deposited in the discharge with an electrode distance of 2 mm and the waveform of the EUV pulse.

seen that, at input energies in the range 6–15 J/pulse, the in-band EUV pulse energy amounts to 6–17 mJ/1.8 sr.

5. CONCLUSION

An average output power of 5 W at $\lambda \sim 13.5$ nm is obtained using the second Z-pinch EUV source prototype with an emitting region of ~1.5×15 mm in the continuous operating mode at the optimized energy deposition and pulse repetition rate. The source is shown to be capable of operating with a repetition rate of 1000 Hz.

Under continuous operation, the average power deposited in the discharge during the successive 2×10^6 pulses was $W_{in} = 9$ kW.

An EUV source with an electrode distance reduced to 2 mm has been studied. The extrapolation of the data obtained shows that, at $W_{in} = 9$ kW, a source with a small-size emitting plasma is capable of generating radiation with an average power of 10 W into a solid angle of 1.8 sr within a spectral range of $\lambda = 13.5 \pm 0.135$ nm dictated by the requirements of the next-generation EUV lithography.

REFERENCES

1. J. P. Benchop, A. J. van Dijsseldonk, W. M. Kaiser, and D. Ockwell, J. Vac. Sci. Technol. B **17**, 2978 (1999).
2. G. Shriever, K. Bergmann, and R. Lebert, J. Appl. Phys. **83**, 4566 (1998).
3. M. W. McGeoch, Proc. SPIE **3997**, 861 (2000).
4. W. Partlo, I. Fomenkov, R. Oliver, and D. Birx, Proc. SPIE **3997**, 136 (2000).
5. M. A. Klosner and W. T. Silfast, Appl. Opt. **39**, 3678 (2000).
6. K. Bergmann, O. Rosier, W. Neff, and R. Lebert, Appl. Opt. **39**, 3833 (2000).
7. V. Banine, J. P. H. Benschop, M. Leenders, and R. Moors, Proc. SPIE **3997**, 126 (2000).
8. V. M. Borisov, O. B. Khristoforov, A. Yu. Vinokhodov, *et al.*, Proc. SPIE **4146**, 113 (2000).
9. G. Shriever, R. Lebert, A. Naweed, *et al.*, Rev. Sci. Instrum. **68**, 33011 (1997).

Translated by N. N. Ustinovskiĭ

Plasma Physics Reports, Vol. 28, No. 10, 2002, pp. 882–883. Translated from Fizika Plazmy, Vol. 28, No. 10, 2002, pp. 957–958.

COMMENTS

Comment on the paper by V.V. Tirskiĭ, V.G. Ledenev, and V.M. Tomozov, *Spectra of Electromagnetic Radiation from a Hot Plasma with Langmuir Turbulence in a Magnetic Field*, Fiz. Plazmy 27, 423 (2001) [Plasma Physics Reports 27, 398 (2001)]

In the paper, the generation of electromagnetic waves due to the merging of two high-frequency (Langmuir) plasmons in a weak magnetic field ($\omega_{Pe}^2 \gg \omega_{Be}^2$) is considered. Unfortunately, when deriving simplified expressions (6) and (14) for the wave frequency in the long-wavelength limit ($\omega^2 \gg k_\parallel^2 V_{Te}^2$, $\omega_{Be}^2 \gg k_\perp^2 V_{Te}^2$), the authors made an error that led them to a wrong conclusion about the opportunity of the existence of high-frequency longitudinal waves with frequencies lower than the plasma electron frequency, $\omega < \omega_{Pe}$. Here, ω is the plasma wave frequency, ω_{Pe} is the plasma electron frequency, ω_{Be} is the electron cyclotron frequency, V_{Te} is the thermal electron velocity, and $k_\parallel$ and $k_\perp$ are the longitudinal and transverse (with respect to the magnetic field) components of the wave vector of the plasma wave. The error automatically resulted in a wrong conclusion about the opportunity of generating electromagnetic waves due to the merging of two plasmons in the frequency range from 1.6 to 2.2 plasma electron frequencies. Actually, the frequency of the waves generated in this process (in the long-wavelength limit considered by the authors) cannot be lower than $2\omega_{Pe}$. The incorrectness of the result obtained by the authors is qualitatively illustrated by Figs. 1 and 2 of the paper. In fact, as the ratio $\omega_{Be}/\omega_{Pe} = a$ decreases (as ω_{Be} tends to zero), the results should tend to those for a plasma without an external magnetic field. In particular, the dependence of the wave frequency on the angle θ between the wave vector and the magnetic field should become less pronounced. Figures 1 and 2 of the paper demonstrate the opposite effect: as a decreases, the wave ω frequency at angles θ close to $\pi/2$ decreases appreciably, and it varies only slightly at angles close to 0 (longitudinal propagation).

The authors' error is as follows. In order to derive the dispersion relation for longitudinal (potential) high-frequency plasmons (Section 2), the authors use the expressions for the permittivity tensor taken from the book by V.L. Ginzburg and A.A. Rukhadze *Waves in Magnetoactive Plasmas*. These expressions are represented as an infinite sum over s, each term of which is the product $\frac{\omega}{\omega - s\omega_{Be}} J_+\left(\frac{\omega - s\omega_{Be}}{k_\parallel V_{Te}}\right) I_s\left(\frac{k_\perp^2 V_{Te}^2}{\omega_{Be}^2}\right)$, where s is the number of the harmonic (integer), $J_+\left(\frac{\omega - s\omega_{Be}}{k_\parallel V_{Te}}\right)$ is the plasma function, and $I_s\left(\frac{k_\perp^2 V_{Te}^2}{\omega_{Be}^2}\right)$ is the modified Bessel function of the first kind. When deriving approximate expressions for the components of the permittivity tensor in the long-wavelength limit, the authors, as can be seen from formulas (2)–(4) of the paper, restricted themselves to the terms with $s = 0, \pm 1$ and retain the terms up to $\left(\frac{k_\parallel V_{Te}}{\omega}\right)^6$ and $\left(\frac{k_\perp V_{Te}}{\omega_{Be}}\right)^6$. As a result, the terms up to $(kV_{Te})^4$ remain in the dispersion relation. As is known, to obtain the correct result, it is necessary to take into account *all terms of the same order*. An approach in which only terms with $s = 0, \pm 1$ are kept is valid only in the so-called "cold limit," in which the total dispersion relation does not contain the terms proportional to V_{Te}^2 at all! To derive the dispersion relation to within $(kV_{Te})^2$, it is necessary to take into account terms with $s = \pm 2$; to derive the dispersion relation to within $(kV_{Te})^4$, the terms with $s = \pm 3$ should be kept; etc. Thus, it can be easily shown that, in the cold limit at $\omega_{Pe}^2 \gg \omega_{Be}^2$, the frequency of high-frequency potential oscillations exceeds the plasma electron frequency ($\omega > \omega_{Pe}$) at *any* direction of the wave vector. If the thermal corrections are correctly taken into account, then, along with the dependence of the frequency of high-frequency waves ω on $k^2 V_{Te}^2$ and θ (for these waves, the inequality $\omega > \omega_{Pe}$ is always satisfied), new roots of the dispersion relation—the so-called Bernstein modes—appear, whose dispersion relation at $k_\parallel = 0$ (strictly transverse propagation) has a simple form $\omega \approx s\omega_{Be}$ in three cases: (i) $\omega \gg \omega_{Pe}$,

1063-780X/02/2810-0882$22.00

(ii) $\left(\frac{k_\perp V_{Te}}{\omega_{Be}}\right)^2 \ll 1$ (at $s > 1$), and (iii) $\left(\frac{k_\perp V_{Te}}{\omega_{Be}}\right)^2 \gg 1$. For finite values of $\frac{k_\perp V_{Te}}{\omega_{Be}}$ and $\omega < \omega_{Pe}$, these solutions occupy almost all the frequency interval between the sequential harmonics of the electronic cyclotron frequency. Thus, it seems that the authors exceeded the calculation accuracy, because the required accuracy can only be achieved by incorporating the terms with $s = 0, \pm 1$ in the initial dispersion relation, or, in other words, they did not take into account the terms that are necessary to correctly derive the dispersion relation with the required accuracy. It is this circumstance that led the authors to an erroneous result.

To be acquainted in more detail with the dispersion properties of high-frequency plasmons with the allowance for spatial dispersion, see the books by V.L. Ginzburg and A.A. Rukhadze *Waves in Magnetoactive Plasmas*, A.I. Akhiezer *et al. Plasma Electrodynamics*, V.V. Zheleznyakov *Radiation in Astrophysical Plasma*, and others.

Yours sincerely, S.M. Grach,
Doctor of Sciences
Assistant Professor at the Faculty of Radiophysics,
Nizhni Novgorod State University
Chief Scientist at the Radiophysical Research Institute

Plasma Physics Reports, Vol. 28, No. 10, 2002, p. 884. Translated from Fizika Plazmy, Vol. 28, No. 10, 2002, p. 959.

COMMENTS

The answer to the comment of Prof. S.M. Grach to the paper by V.V. Tirskiĭ, V.G. Ledenev, and V.M. Tomozov, *Spectra of Electromagnetic Radiation from a Hot Plasma with Langmuir Turbulence in a Magnetic Field*, Fiz. Plazmy 27, 423 (2001) [Plasma Physics Reports 27, 398 (2001)]

The author of the comment asserts that our error stems from neglecting the terms corresponding to the higher cyclotron harmonics in the expression for the dielectric tensor. In his opinion, when the terms corresponding to the higher harmonics are taken into account, the frequency of high-frequency longitudinal waves cannot be lower than the plasma electron frequency, regardless of the angle at which they propagate with respect to the magnetic field. However, as is seen from the comment, the author arrives at this conclusion based on the dispersion relation for a cold plasma; as to a hot magnetoactive plasma, it seems that no consistent calculations were performed.

When preparing our paper, we estimated the contribution of different terms in the sum over cyclotron harmonics in the expression for the dielectric tensor of a hot magnetoactive plasma. These estimates allowed us to conclude that, in the approximation adopted, the main contribution comes from the terms with the cyclotron harmonics $s = 0, \pm 1$. To check the correctness of these estimates, we have recently performed calculations with allowance for higher harmonics (up to tenth harmonic). The results of calculations show that the effect of the reduction of the frequency of high-frequency longitudinal waves becomes more pronounced as the propagation direction approaches the transverse direction with respect to the magnetic field. It is important that this effect manifests itself for wavelengths longer than the electron gyroradius. At present, we are preparing a paper in which the spectra of high-frequency longitudinal waves in a hot magnetoactive plasma will be considered in more detail.

Sincerely, V.V. Tirskiĭ, V.G. Ledenev, and V.M. Tomozov

1063-780X/02/2810-0884$22.00

Plasma Physics Reports, Vol. 28, No. 10, 2002, p. 885. Translated from Fizika Plazmy, Vol. 28, No. 10, 2002, p. 960.

COMMENTS

Comment on the book by A.F. Nikiforov, V.G. Novikov, and V.B. Uvarov *Quantum-Statistical Models of a High-Temperature Plasma and Methods for Computing Rosseland Mean Free Paths and Equations of State* (Fizmatlit, Moscow, 2000)

The book is devoted to the problem of plasma opacity, i.e., to the methods for calculating the spectral coefficients of photon absorption and Rosseland mean free paths in a dense high-temperature plasma. The problem of opacity is one of the fundamental physical problems, because an adequate description of the interaction of radiation with matter is of crucial importance when considering various astrophysical objects; solving practical problems of the physics of powerful explosions; studying the action of laser, electron, and ion beams on matter; and simulating the operation of high-energy-density devices, in particular, high-power X-ray sources.

To better understand the processes occurring in a high-temperature plasma, it is necessary to know its thermodynamic and radiation properties, such as the equations of state, absorption coefficients, and plasma emittance as functions of the plasma parameters and the characteristics of radiation interacting with the plasma.

In the book, the widely used Thomas–Fermi, Hartree–Fock, and Hartree–Fock–Slater quantum-statistical models of a high-temperature plasma are generalized to arbitrary temperatures and densities of matter in the average atom approximation. It is demonstrated how these models can be applied to compute the spectral coefficients of photon absorption, Rosseland mean free paths, and the equations of states, which are necessary for mathematical modeling of hydrodynamic processes with allowance for radiation transport in high-temperature plasmas.

Special attention is given to absorption in spectral lines, because, in a dense high-temperature plasma (in which absorption in spectrum lines can be more intense than absorption in continuum by several orders of magnitude), ion states with even very low probability must also be taken into account, which results in searching for an enormously large number of configurations. By using high-performance supercomputers, the authors managed to considerably update the existing models, to carry out calculations with relativistic wave functions, and to take into account ion configurations more correctly, with allowance for the fine structure of energy levels in the intermediate-type coupling model. Unfortunately, the approach proposed is not justified based on the first principles. However, it should be noted that such a justification is hardly possible in the framework of the modern theory of strongly nonideal systems. It would also be useful to discuss the possible reasons for the discrepancy between theory and experiment, in particular, when describing states with two or more centers, whose spectra are observed in experiments on the collision of exploding foils.

The book can be very useful for specialists working in this field, because, to the best of our knowledge, no analogous books have yet been published.

Almost half of the book is based on the lectures that one of the authors, Prof. A.F. Nikiforov, has given over many years for the students of the Physics Faculty of Moscow State University. Therefore, the book will also be useful for students who wish to become more proficient in a number of problems of quantum mechanics, statistical physics, and computation mathematics.

V.S. Lisitsa and A.N. Starostin

1063-780X/02/2810-0885$22.00 © 2002 MAIK “Nauka/Interperiodica”